Neutrino Production of Opposite Sign Dimuons in the NOMAD Experiment

S. B. Boyd

A thesis
submitted for the degree of
Doctor of Philosophy
at the
University of Sydney

September, 1998

Abstract

The NOMAD experiment is a neutrino oscillation experiment at the CERN SPS. The experiment is described with particular emphasis given to the construction and calibration of the Front Calorimeter of NOMAD. The absolute energy scale is determined to be

$$1[\mathrm{GeV}] = (2.95 \pm 0.02(stat) \pm 0.27(sys))[\mathrm{mip}]$$

from comparison of the Monte Carlo simulation with the data. About 3,500,000 charged current events are found to be useful for analysis. The reconstruction of the various kinematic quantites is shown to be in good agreement with the Monte Carlo prediction. The energy resolution of the FCAL is estimated to be

$$\frac{\sigma}{E} = \frac{104\%}{\sqrt{E/1GeV}} \tag{0.1}$$

The production of charm quarks via the formation of opposite sign dimuon events in neutrino interactions is investigated. Analysis of the opposite sign dimuon data yields determinations of the charm quark mass, the strange sea content of the nucleon and the average semileptonic branching ratio. An opposite sign dimuon sample of 4,953 events is reconstructed from the sample of charged current neutrino interactions. After accidental overlaps of beam muons with charged current events have been eliminated, 35 % of the sample, after cuts, are found to be background events from muonic hadron decays and hadron punchthrough. The numbers of neutrino and antineutrino induced opposite sign dimuon events, after background subtraction, are estimated to be (2966 ± 236) and (263 ± 24) respectively. FADE, a dedicated dimuon simulator of dimuon interactions in the FCAL is constructed. This is shown to describe the dimuon data well. Using FADE, the rate of opposite sign dimuon production with respect to the production of charged current events is measured to be $(4.14 \pm 0.05) \times 10^{-3}$ after correction for experimental acceptance.

The charm quark mass, the strange sea content of the nucleon and the average semileptonic branching ratio are estimated to be $1.3^{+0.2}_{-0.3}{}^{+0.3}_{-0.3}$, $0.46^{+0.09}_{-0.07}{}^{+0.15}_{-0.09}$ and $0.095 \pm 0.007^{+0.015}_{-0.013}$ repectively. Suggested improvements on and extensions to these results are then discussed.

Acknowledgements

In the course of this work I have been fortunate to receive assistance from many people.

I would, first of all, like to thank my supervisors, Dr. Kevin Varvell and Dr. Juris Ulrichs, for all the suggestions, guidance and assistance that they have provided over the course of the degree and for patiently explaining the simple things when I (frequently) confused myself. Thanks, in great measure, go to the members of the Falkiner High Energy Physics Department : Assoc. Prof. Laurie Peak, Dr. Andy Bakich and Dr. Reza Hashemi-Nezhad for listening while I tried to explain things and for general advice.

I would like to extend my thanks to Mr. Bruce Yabsley, with whom I shared an office and who contributed new and interesting ideas to this analysis when he didn't have to, and to Dr. Paul Soler, who offered useful ideas and suggestions and was continually interested in what I was doing. Thanks go to the other postgraduate students in the department : Mr Malcolm Ellis, Mr Andrew Godley, and Mr Aldo Saavedra for help, friendship, and (occasionally) sheer frustration. To all the above, thanks for making the Falkiner High Energy Physics Department an interesting and stimulating working environment.

From the University of Melbourne, I would like to thank Dr. Fawzi Fares and Mr. Lyle Winton (who is the only person I know whose sense of humour approaches mine - God help him).

My thanks go to all of the members of the NOMAD collaboration. In the context of the FCAL analysis, I would especially like to thank Mr. Dirk Geppert, Dr. Burkhard Schmidt, Dr. Sanjib Ratan Mishra, Mrs. Sylvie Geppert, Dr. Patrick Nedelec, Dr. Dario Autiero and Dr. Achim Geiser for discussions, conclusions, encouragement, arguments, ideas and criticisms at various places and times. Thanks go to all those involved in the construction of the FCAL: you know who you are, even if I don't.

For making my time spent in NOMAD an enjoyable one I have to thank Dr. Peter Hurst, Dr. Fred Weber, Dr. Kai Züber, Dr. Josh Long, Dr. David Steele, Dr. Emmanuel Tsesmelis and especially Dr. Malica Tareb and Ms. Anna Lupi. Thanks for everything!

Although they have been mentioned above, special thanks go to the Dörtmund group with whom we Australians formed a close working relationship. They are : Dr. Burkhard Schmidt, Mr. Dirk Geppert and Dr. Thomas Weisse. Thanks for the enlightening discussions and the good company.

Lastly, but certainly not least, I would like to warmly thank my parents, Barry and Carole, for their unreserved support and encouragement during this degree. It couldn't have been done without them.

To all of the above, and anyone I have managed to leave out : Ta!

P.S. I've been told to mention cows. Please don't ask why. You wouldn't thank me.

Author's Contribution

The construction, testing and relative calibration of the FCAL was carried out by members of the Univeristy of Dortmund, as was production of all Monte Carlo samples generated with the NOMAD simulation programs. The author was responsible for the absolute calibration and for the reconstruction of the data used in this thesis.

The resolution studies in Chapter 4 were performed by the author. The development of the dimuon selection algorithm and its implementation and testing was carried out by the author. The author was responsible for construction, implementation and running of the alternative NOMAD Monte Carlo, FADE.

The analyses in Chapters 5 and 6 are the sole responsibility of the author.

Preface

This thesis is a report of work carried out for the degree of Doctor of Philosophy at the University of Sydney in the Falkiner High Energy Physics Department. It describes the NOMAD experiment in general and the construction and calibration of the NOMAD Front Calorimeter in particular. Data taken with this detector is then analysed for the presence of opposite sign dimuons and several charm production parameters are determined within the framework of Leading Order QCD.

The first chapter describes the phenomenon of deep inelastic scattering in general and charm quark production in particular.

Chapter 2 describes the NOMAD experiment. The theory of neutrino oscillations and techniques for oscillation searches are detailed, followed by a description of the WANF beam line at the CERN SPS, the NOMAD detector and the NOMAD software environment.

Chapter 3 focuses upon the Front Calorimeter of NOMAD. The construction of the calorimeter is outlined and the energy calibration is discussed.

A study of muon identification begins Chapter 4. The selection of ν_μ^{CC} events is then discussed and the reconstruction and resolution of the various kinematic variables is described. An estimate of the energy resolution of the Front Calorimeter is presented and a cross check on the calibration carried out in Chapter 3 is investigated.

Chapter 5 describes the algorithm developed for the recognition of opposite sign dimuon events. Selection efficiencies are calculated and the background subtraction method is discussed. The issue of whether the NOMAD Monte Carlo program adequately simulates the kinematics of charm quark production is investigated and an alternative Monte Carlo program proposed, constructed and tested. Finally, the observed rate of opposite sign dimuon to ν_μ^{CC} production is measured and compared with previous experiments.

Chapter 6 utilises the data discussed in Chapter 5 to determine several of the charm production parameters. The mass of the charm quark, the strange content of the nucleon sea and the average semileptonic branching ratio are determined. Opportunities for expansion upon the present study are then listed and discussed.

Contents

Abstract I
Acknowledgements II
Author's contribution III
Preface IV
Contents VII
List of Figures XVI
List of Tables XX

1 Theory **1**
1.1 Introduction 1
1.2 The Description of Neutrino-Nucleon Collisions 3
1.3 The Charged Current Neutrino-Nucleon Interaction 6
1.4 The Quark-Parton Model 8
1.5 Charm Quark Production 11
1.5.1 Slow Rescaling in Heavy Quark Production 12
1.6 Opposite Sign Dimuon Production 14

2 The NOMAD experiment **16**
2.1 Introduction 16
2.2 Neutrino Oscillations 16
2.3 Search For Neutrino Oscillations 20
2.4 The CERN Wide Band Neutrino Beam 22
2.5 The SPS Beam 23
2.6 The NOMAD Detector 25
2.6.1 The NOMAD Magnet 27
2.6.2 The Veto 27
2.6.3 The Front Calorimeter 28
2.6.4 The Drift Chambers 28
2.6.5 The Transition Radiation Detector 30
2.6.6 The Trigger 31
2.6.7 The Preshower Detector 32
2.6.8 The Electromagnetic Calorimeter 32

2.6.9 The Hadronic Calorimeter 34
2.6.10 The Muon Detector 35
2.7 Data recording and handling 36
2.7.1 Data acquisition 36
2.7.2 Triggering 38
2.8 The NOMAD Software Environment 40
2.8.1 Beam Simulation 40
2.8.2 Neutrino Event Generation 41
2.8.3 Detector Simulation 41
2.8.4 Event Reconstruction 41

3 The Front Calorimeter 42
3.1 Introduction 42
3.2 Motivation for the construction of the FCAL 42
3.3 Description of the FCAL 45
3.3.1 The Front I 45
3.3.2 FCAL Scintillators 45
3.3.3 FCAL Photomultipliers 48
3.3.4 Readout Electronics 48
3.4 Calibration Procedure 51
3.4.1 Relative Calibration 51
3.4.2 Absolute Calibration 56
3.4.3 Absolute calibration of the FCAL using the Monte Carlo 61
3.4.4 Sources of uncertainty 67
3.4.5 Results of the Calibration 79

4 Neutrino Interactions in the FCAL 80
4.1 Introduction 80
4.2 Muon Identification 81
4.3 ν_μ Charged Current Event Selection 85
4.3.1 Fiducial Volume 85
4.3.2 Selection Criteria 87
4.4 The NOMAD Data and Event Statistics 89
4.5 Reconstruction of ν_μ^{CC} Interaction Kinematics 91
4.5.1 Hadronic and Neutrino Energy Reconstruction 92
4.5.2 Reconstruction of the Kinematic Variables 104

5 Dimuon Events 124
5.1 Introduction 124
5.2 Dimuon Event Identification 124
5.2.1 Categorisation of opposite sign dimuon events 125

5.2.2 Dimuon Selection Efficiency 126
5.3 Dimuon Background 126
5.3.1 The Like Sign Dimuon Events 129
5.3.2 Background Reduction 135
5.4 Dimuon Data Sample 138
5.5 FADE - An Alternative Charm Monte Carlo 145
5.5.1 Detector Acceptance and Smearing 146
5.5.2 The FADE Single Muon Event Generator 147
5.6 The FADE Dimuon Event Generator 148
5.6.1 Charm Fragmentation 148
5.6.2 Transverse Momentum of the D meson 151
5.6.3 Charmed hadron decay 152
5.7 Dimuon Rates and the Charm Threshold 158
5.7.1 Extraction of the Relative Rates 158
5.8 Previous Experiments 160

6 Charm Analysis **165**
6.1 Introduction 165
6.2 Philosophy of the Analysis 165
6.3 Analysis Method 167
6.4 Charm Quark Mass Analysis 169
6.4.1 Systematic Uncertainties 174
6.5 The Strange Quark Content of the Nucleon 175
6.5.1 Systematic Uncertainties 179
6.5.2 Results from previous experiments 180
6.6 The Average Semileptonic Branching Ratio 180
6.7 Future Prospects 182

Conclusion **187**

A Code Versions **189**

Bibliography **190**

List of Figures

1.1 Leading order diagram for deep inelastic lepton-nucleon scattering. 4

1.2 Schematic parton model picture of deep inelastic scattering. (a) The boost to the infinite momentum frame compresses the nucleon into a flat pancake and slows down the partons within the nucleon. The partons are essentially "frozen" during the interaction, allowing the lepton to interact incoherently with one free parton (b). As the scattered lepton recedes, the fragments of the nucleon recombine to form the hadron shower (c). This occurs on a time scale much longer than the initial collision. 9

1.3 Quark-level diagram of charm production in neutrino-nucleon deep inelastic scattering. The primary muon comes from the lepton vertex while the secondary muon comes from the decay of the intermediate charmed hadron. 15

2.1 Limits on neutrino oscillations set by a number of experiments. The curve attributed to NOMAD is described in reference [9]. The areas of phase space to the right of the curves is excluded. 19

2.2 Kinematic configuration of background and signal events in the plane transverse to the neutrino beam axis for leptonic decay channels of the τ^-. 21

2.3 Schematic layout of the WANF beam line pointing out its main elements. (Not drawn to scale). The proton beam enters from the left and strikes the target. The resulting particle beam, comprising mostly π and K mesons, passes throught the magnetic lens system (horn and reflector) and enters the decay tunnel where the mesons decay to yield the final neutrino beam. 22

2.4 The structure of the SPS cycle (Not drawn to scale). 23

2.5 Operating principle of the horn and reflector system. Charged particles of one sign are focussed by a toroidal magnetic field. Particles of the opposite sign are defocussed. 24

2.6 Energy spectra of neutrinos at NOMAD, predicted by NUBEAM[41], the NOMAD beam simulation program. 25
2.7 Top view (top) and side view (bottom) of the NOMAD detector. The co-ordinate system is shown on each plot. 26
2.8 Schematic view of a drift chamber 29
2.9 Top view of the TRD setup 30
2.10 An exploded view of the Preshower 32
2.11 (left) Perspective view of one lead-glass counter and (right) vertical view of a lead-glass module. 33
2.12 Front view of the HCAL 35
2.13 Geometric layout of the muon chambers. The left figure is the view from above showing the interleaved chambers. The right figure is the horizontal view showing the position of module 5. 36
2.14 Hardware layout of the NOMAD Data acquisition system. . . 37

3.1 Neutrino trident production processes. 43
3.2 Neutral heavy lepton sensitivity region in the two dimensional phase space ($M_{\mathcal{N}}$,$|U|^2$). The projected limits using the FCAL is shown[28]. 44
3.3 View of the FCAL from the side. The neutrino beam comes in from the left of the diagram. 46
3.4 View of the FCAL (top) looking along the direction of the neutrino beam and (bottom) from the top. The direction of the neutrino beam is into the page in the top figure and down the page in the bottom figure. 47
3.5 Attenuation behaviour for a typical FCAL scintillator. The scintillator response is shown on a log scale. 49
3.6 Schematic of the FCAL readout system. 50
3.7 Parameters used in the relative calibration of the FCAL. . . . 52
3.8 Typical energy deposition distribution for muons passing through a single FCAL module. The distribution has been fitted with the $\mathcal{L}$ function (described in the text). 54
3.9 The dependence of $< ln(R) >$ on the muon impact point x. The gradient of the fit provides a measurement of the attenuation length and the intercept on the $< ln(R) >$ axis is an estimate of the asymmetry according to Equation 3.15. The outermost bins have been excluded from the fit as they are at the very edge of the FCAL volume. 57
3.10 The efficiency of the FCAL trigger as a function of the deposited energy. 63

3.11 Comparison of the energy deposition distributions for data (points) and Monte Carlo samples (histogram). The relative energy scale is 1.0. 65
3.12 The fit χ^2 as a function of the relative energy scale. The number of degrees of freedom is 19. The plot shows an optimal relative scale of (0.800 ± 0.005). 65
3.13 Comparison of energy deposition distributions for Stack 1. The category of events in each plot is displayed in the upper right corner of that plot and is described in the text. 68
3.14 Comparison of energy deposition distributions for Stack 2. The category of events in each plot is displayed in the upper right corner of that plot and is described in the text. 69
3.15 Comparison of energy deposition distributions for Stack 3. The category of events in each plot is displayed in the upper right corner of that plot and is described in the text. 70
3.16 Comparison of energy deposition distributions for Stack 4. The category of events in each plot is displayed in the upper right corner of that plot and is described in the text. 71
3.17 The top plot shows a scatter plot of the deposited energy in mips as a function of the energy transferred to the hadronic system for Monte Carlo events in sample A, which has been modified for neutral current events. The bottom plot is a profile histogram with a linear fit superimposed. The fit parameters are shown in the top right corner of this plot. 73
3.18 Comparison of the 1995 data with Monte Carlo predictions for ν_μ^{CC} interactions in the drift chamber target. Shown are (left) the visible energy distributions in different radial bins and (right) the radial distributions in the three energy bins. . 74
3.19 The difference between the estimated X and Y positions of the vertex and the point at which the interaction actually occurred in a sample of ν_μ^{CC} Monte Carlo events. Shown are the differences for the muon extrapolation method (left side) and for the center of gravity method (right side) in ν_μ^{CC} interactions. The distributions are normalised to the same number of events. 77
3.20 Comparison of the ν_μ^{CC} data with the Monte Carlo for the estimated position of the event vertex on the X axis (top) and the Y-axis (bottom). The simulated distributions are overlayed as a histogram to the data points.The distributions are normalised to the same number of events. 78

4.1 (a) Muon momentum quality; (b) Bias as a function of the simulated muon momentum. 81
4.2 (a) Muon energy quality including energy loss in the FCAL and coil averaged over all stacks; (b) Bias as a function of the simulated muon energy. 82
4.3 The difference between the simulated angle of the muon with respect to the neutrino direction and the reconstructed angle for events occurring in each stack. Shown are the distributions for Stack 1 (top left), Stack 2 (top right), Stack 3 (bottom left) and Stack 4 (bottom right). 83
4.4 FCAL vertex distributions for ν_μ^{CC} events. The vertices have been calculated using the center of gravity method. The data points are shown overlaid on the Monte Carlo histogram and the distributions are normalised to the same number of events. 86
4.5 Distribution of the stack in which the ν_μ^{CC} interaction occurred. A cut requesting less than 10% of the event energy in stack 1 has been applied. The data points are overlaid on the Monte Carlo histogram and the distributions have been normalised to the same number of events. 86
4.6 Comparison of the reconstructed and simulated values for the hadronic energy of events in Stack 1 (left) and Stack 2 (right). The top plot is a simple comparison. The middle plot shows the quality and the bottom plot shows the bias as a function of the simulated value. 94
4.7 Comparison of the reconstructed and simulated values for the hadronic energy of events in Stack 3 (left) and Stack 4 (right). The top plot is a simple comparison. The middle plot shows the quality and the bottom plot shows the bias as a function of the simulated value. 95
4.8 Hadronic energy bias as a function of the X and Y position of the vertex. The dip in the bias at central values of Y results from energy absorption in the mid FCAL gap. 96
4.9 The simulated width of the FCAL energy response distributions as a function of the square root of the simulated energy of test beam pions, overlaid with a fit to a straight line. 97
4.10 Comparison of the Monte Carlo input and Monte Carlo reconstructed distributions for the neutrino energy of events in Stack 1 (left) and Stack 2 (right). The top plot is a simple comparison. The middle plot shows the quality and the bottom plot shows the bias as a function of the simulated value. . 100

4.11 Comparison of the Monte Carlo input and Monte Carlo reconstructed distributions for the neutrino energy of events in Stack 3 (left) and Stack 4 (right). The top plot is a simple comparison. The middle plot shows the quality and the bottom plot shows the bias as a function of the simulated value. . 101

4.12 Comparison of the data (points) and Monte Carlo (histogram) distributions for the visible hadronic energy E_{had} in events originating in each stack. The data and Monte Carlo distributions have been normalised to equal areas. 102

4.13 Comparison of the data (data) and Monte Carlo (histogram) distributions for the visible energy E_{vis} in events originating in each stack. The data and Monte Carlo distributions have been normalised to equal areas. 103

4.14 Single muon energy spectrum. The top plot is in a linear scale and the bottom plot is in a logarithmic scale on the vertical axis. The data points are overlaid on the Monte Carlo histogram. 105

4.15 (top) Comparison of the inverse momentum distribution in 1995 data and simulation before the alignment correction. (bottom) Same comparison after the correction for the incorrect alignment was applied. The data and simulation distributions have been normalised to equal areas. 105

4.16 Single muon energy spectrum after correction for the SPY data have been applied. The top plot is in a linear scale and the bottom plot is in a logarithmic scale on the vertical axis. The data points are overlaid on the Monte Carlo histogram and the distributions have been normalised to equal areas. 106

4.17 Comparison of reconstructed (points) and simulated (histogram) values of Q^2 for events occurring in Stack 1 (left) and Stack 2 (right). The middle plots show the quality and the bottom plots show the bias as a function of the simulated value. . . . 109

4.18 Comparison of reconstructed (points) and simulated (histogram) values of Q^2 for events occurring in Stack 3 (left) and Stack 4 (right). The middle plots show the quality and the bottom plots show the bias as a function of the simulated value. . . . 110

4.19 Comparison of reconstructed (points) and simulated (histogram) values of x_{Bj} for events occurring in Stack 1 (left) and Stack 2 (right). The middle plots show the quality and the bottom plots show the bias as a function of the simulated value. . . . 111

4.20 Comparison of reconstructed (points) and simulated (histogram) values of x_{Bj} for events occurring in Stack 3 (left) and Stack 4 (right). The middle plots show the quality and the bottom plots show the bias as a function of the simulated value. . . . 112

4.21 Comparison of reconstructed (points) and simulated (histogram) values of W^2 for events occurring in Stack 1 (left) and Stack 2 (right). The middle plots show the quality and the bottom plots show the bias as a function of the simulated value. . . . 113

4.22 Comparison of reconstructed (points) and simulated (histogram) values of W^2 for events occurring in Stack 3 (left) and Stack 4 (right). The middle plots show the quality and the bottom plots show the bias as a function of the simulated value. . . . 114

4.23 Comparison of reconstructed (points) and simulated (histogram) values of y_{Bj} for events occurring in Stack 1 (left) and Stack 2 (right). The middle plots show the quality and the bottom plots show the bias as a function of the simulated value. . . . 115

4.24 Comparison of reconstructed (points) and simulated (histogram) values of y_{Bj} for events occurring in Stack 3 (left) and Stack 4 (right). The middle plots show the quality and the bottom plots show the bias as a function of the simulated value. . . . 116

4.25 Comparison between data (points) and Monte Carlo (histogram) for the reconstruction of the kinematic variable x_{Bj} for events occurring in each stack. The data and Monte Carlo distributions have been normalised to equal areas. 117

4.26 Comparison between data (points) and Monte Carlo (histogram) for the reconstruction of the kinematic variable y_{Bj} for events occurring in each stack. The data and Monte Carlo distributions have been normalised to equal areas. 118

4.27 Comparison between data (points) and Monte Carlo (histogram) for the reconstruction of the kinematic variable Q^2 for events occurring in each stack. The data and Monte Carlo distributions have been normalised to equal areas. 119

4.28 Comparison between data (points) and Monte Carlo (histogram) for the reconstruction of the kinematic variable W^2 for events occurring in each stack. The data and Monte Carlo distributions have been normalised to equal areas. 120

4.29 Hadron-muon relative energy calibration. 123

5.1 (top) Distance between the extrapolated positions of the two muons at the vertex plane for like sign events in the data. (bottom) Distance between the extrapolated positions of the two muons at the vertex plane for like sign events in the simulation. The data exhibits a flat background component due to the overlap beam muons. 133
5.2 Comparison of the shapes of the kinematic distributions of like sign dimuon simulation (points) and data (histogram). Shown are (top left) the energy of the primary muon, (top right) the energy of the secondary muon candidate, (bottom left) the visible hadronic energy and (bottom right) the visible neutrino energy. The data and Monte Carlo have been normalised to equal area. 136
5.3 Comparison of the shapes of the kinematic distributions of like sign dimuon simulation (points) and data (histogram). Shown are (top left) the square of the 4-momentum transfer, (top right) Bjorken x and (bottom left) the Bjorken y distribution. The data and Monte Carlo have normalised to equal area. . . 137
5.4 Example of an opposite sign dimuon event occurring at the end of Stack 2 in the FCAL. The two tracks are the oppositely charged muons in the event. 141
5.5 Comparison of kinematic distributions from opposite sign dimuon simulation (histogram) and data (points) . The data has been corrected for background. Shown are (top left) the energy of the primary muon, (top right) the energy of the secondary muon, (bottom left) the visible hadronic energy distribution and (bottom right) the visible neutrino energy distribution. The data and Monte Carlo have been normalised to the same area. 142
5.6 Comparison of kinematic distributions from opposite sign dimuon simulation (histogram) and data (points). The data has been corrected for background. Shown are (top left) Q^2, (top right) Bjorken x, (bottom left) Bjorken y and (bottom right) z_{vis}. The data and Monte Carlo have been normalised to the same area. 143
5.7 Comparison of the kinematics distributions of dimuon events from the NOMAD Monte Carlo, NEGLIB, and according to the appropriate dimuon production cross section. Shown are the energy of the incoming neutrino (top), Bjorken x (middle) and Bjorken y (bottom). Both calculations used a charm mass of 1.3 GeV/c^2 and identical structure functions. 144

5.8 Comparison of kinematic distributions from the FADE single muon ν_μ^{CC} simulation (histogram) and data (points). The data and the simulation have been normalised to equal areas. Shown are (top left) the energy of the primary muon, (top right) the visible hadronic energy of the event, (middle left) the neutrino energy, (middle right) the momentum transferred to the hadronic system, (bottom left) the Bjorken y distribution and (bottom right) the Bjorken x distribution. 149

5.9 Comparison of kinematic distributions from the FADE opposite sign dimuon simulation (histogram) and data (points). The data has been corrected for background. Shown are (top left) the energy of the primary muon, (top right) the energy of the secondary muon, (bottom left) the visible hadronic energy distribution and (bottom right) the visible neutrino energy distribution. Data and Monte Carlo have been normalised to equal areas. 154

5.10 Comparison of kinematic distributions from the FADE opposite sign dimuon simulation (histogram) and data (points). The data has been corrected for background. Shown are (top left) Q^2, (top right) Bjorken x, (bottom left) Bjorken y and (bottom right) z_{vis}. Data and Monte Carlo have been normalised to equal areas. 155

5.11 Neutrino-induced opposite sign dimuon rates corrected for acceptance and kinematic effects using FADE and assuming a charm mass of 1.3 (GeV/c^2). The NOMAD results are displayed as open circles. Also shown are the CCFR results (closed circles) and CDHS results (crosses). The line is the theoretical ratio of cross sections assuming the slow rescaling mechanism in Leading Order QCD, a charm mass of 1.3 (GeV/c^2), and the validity of the CCFR structure functions. . 161

5.12 Neutrino-induced opposite sign dimuon rates corrected for acceptance and kinematic effects using the standard NOMAD Monte Carlo program, NEGLIB. The program assumes a charm mass of 1.35 (GeV/c^2) and uses the GRV-HO structure functions. The NOMAD results are displayed as open circles. Also shown are the CCFR results (closed circles) and CDHS results (crosses). The line is the theoretical ratio of cross sections assuming the slow rescaling mechanism in Leading Order QCD and a charm mass of 1.35 (GeV/c^2). The GRV-HO structure functions have also been used. 162

6.1 Comparison between two visible neutrino energy spectra for different values of κ and m_c. The top plot was generated with $m_c = 1.5$ (GeV/c^2) and two different values of κ. The bottom plot was generated with $\kappa = 0.37$ and different values for m_c. The shape of the energy spectrum changes substantially for different charm masses. No significant shape difference is observed for different values of κ. 172
6.2 The χ^2 of the charm mass fit as a function of the charm mass. The central value is 1.3 (GeV/c^2) at a χ^2 of 6.1 with 5 degrees of freedom. The statistical error is determined by the points on either side of the central mass value at which the χ^2 is one unit above the minimum. The curve is a fit of a third order polynomial to the histogram and the 68% confidence limits are shown on the charm mass axis. 173
6.3 The χ^2 of the of the fit to the strange content of the nucleon sea as a function of κ. The central value is 0.45 with a χ^2 of 3.3 with 4 degrees of freedom. The statistical error is determined by the points on either side of the central value at which the χ^2 is one unit above the minimum. The curve is a fit of a fourth order polynomial to the histogram and the 68% confidence limits are shown on the κ axis. 178
6.4 The average semileptonic branching ratio as a function of the neutrino energy. The dotted line in each plot is the average semileptonic branching ratio calculated from production rates measured at E531[66]. The points represent the average semileptonic branching ratio measured in NOMAD in energy bins. The errors are statistical only. The solid line in each plot displays the contribution of a particular charmed hadron to the total average semileptonic branching ratio. Shown are (top left) the contribution from D^0 mesons, (top right) the contribution from D^+ mesons, (bottom left) the contribution from Λ_c baryons and (bottom right) the contribution from other mesons (D^-,$\overline{D}^0$,D_s). 183

List of Tables

1.1 Common properties of quarks and leptons. Note that the existence of the τ-neutrino has not been experimentally verified. 2
1.2 Mediators of the fundamental interactions 2

2.1 Monte Carlo predictions for NOMAD (for 2.4×10^{19} p.o.t.) . . 24
2.2 Features of the NOMAD magnet 27
2.3 Individual signals which are used to generate NOMAD triggers. 38

3.1 Specifications of the FCAL scintillators. 48
3.2 Specifications of FCAL photomultipliers. 48
3.3 Average values and RMS of the deposited energy distributions for Data and Monte Carlo samples under different cuts. 72

4.1 Energy thresholds for muons to reach each station of the muon chambers with 50% probability as a function of the stack in which the interaction occurred. 84
4.2 Muon angular differences for events occurring in each stack. The bias decreases the closer to the back face of the FCAL the event occurs. The average spread over all stacks is approximately 9 mrad. 84
4.3 ν_μ charged current event selection efficiency for events beginning in each stack. 88
4.4 Statistics of data sample used in this analysis 90
4.5 Statistics of the Monte Carlo simulation samples used in this analysis 90
4.6 Average percentage of energy loss and E_{had} resolution for events occurring in each stack. 93
4.7 The mean and width of the energy reponse distributions of the FCAL at different simulated hadronic energies. 97
4.8 Average percentage of energy loss and E_ν resolution for events occurring in each stack. 99

4.9 Average values of Monte Carlo simulated and reconstructed kinematic variables in deep inelastic ν_μ^{CC} interactions originating in each Stack. Also shown is the corresponding bias and resolution. 108

4.10 Average and RMS values of reconstructed kinematic variable distributions in data and Monte Carlo. 121

5.1 ν_μ opposite sign dimuon event selection efficiency for simulated events beginning in stacks 1 and 2. 127

5.2 ν_μ opposite sign dimuon event selection efficiency for simulated events beginning in stacks 3 and 4. 128

5.3 Rejection efficiency for beam muon overlap events. 132

5.4 Numbers of positively and negatively charged particles in simulated ν_μ^{CC} events. The fraction of positive to negative mesons is 1.471 ± 0.005. 134

5.5 Ratio of the number of opposite sign background events and like sign events observed in simulated ν_μ^{CC} and $\overline{\nu_\mu}^{CC}$ samples. . 135

5.6 Number of like sign dimuon events normalised to the number of observed ν_μ^{CC} events for data and simulation. The errors are only statistical. 135

5.7 Number of opposite sign dimuon events and opposite sign background events normalised to the number of ν_μ^{CC} events in the simulation within the fiducial volume. The errors are statistical. 138

5.8 The background reduction function $\mathcal{S}$ as a function of the value of the cut on the energy of the secondary muon. This table suggests that the optimal energy cut is at 4.5 GeV. 139

5.9 Number of ν and $\overline{\nu}$-induced events identified using the dimuon selection algorithm as a function of the stack in which the interaction occurred. Shown are the total number of opposite sign events observed, the total number of like sign events, a background estimate and the number of opposite sign events from charm production corrected for background. The background is estimated by scaling the number of like sign events by 1.5 ± 0.3 (see Section 5.3.1) for the neutrino induced dimuons and by 2.0 ± 1.0 for the antineutrino sample. The uncertainty on the number of corrected events contains the statistical error on the raw OSDM and LSDM event numbers combined in quadrature with the error on the background scaling factor. . 139

5.10 Mean and RMS values of the reconstructed kinematic variable distributions for opposite sign dimuons in data and Monte Carlo, together with the χ^2 of the comparison of the shapes of the distributions. 145
5.11 Fit parameters used in the parametrisation of the muon direction smearing. 147
5.12 Experimental determination of the charm quark fragmentation parameter for the Peterson and Collins-Spiller fragmentation functions. 151
5.13 The branching ratio of D meson and Λ_c baryon semileptonic decays relative to the total semileptonic branching fraction. . . 152
5.14 Mean and RMS values of the reconstructed kinematic variable distributions for opposite sign dimuons in data and Monte Carlo, together with the χ^2 of the comparison of the shapes of the distributions. 153
5.15 ν_μ opposite sign dimuon event selection efficiency for events generated by FADE beginning stacks 1 and 2. 156
5.16 ν_μ opposite sign dimuon event selection efficiency for events generated by FADE beginning stacks 1 and 2. 157
5.17 Neutrino induced opposite sign dimuon rates corrected for acceptance and kinematic cuts by a dimuon simulation with a charm mass of 1.3 (GeV/c^2). Columns represent : (1) energy bin, (2) raw single muon data after all cuts, (3) background subtracted dimuon data after all cuts, (4) acceptance correction to the single muon data (5) acceptance correction to the dimuon data and (6) dimuon to single muon ratio. 160
5.18 Summary of data samples from previous neutrino charm production experiments. 164

6.1 The variation of the fitted value of the charm mass for different sources of systematic uncertainty. 176
6.2 Results on m_c from previous experiments. Both the Leading Order and Next-to-Leading Order results are shown for CCFR. 176
6.3 The variation of the fitted value of κ for different sources of systematic uncertainty. 179
6.4 Results on κ from previous experiments. Both the Leading Order and Next-to-Leading Order results are shown for CCFR. 181
6.5 The average semileptonic branching ratio obtained from previous experiments. 182
6.6 The variation of the fitted value of the average semileptonic branching ratio for different sources of systematic uncertainty. 184

A.1 Versions of NOMAD Software used in the 1995 and 1996 data production. Note that the PRS code was merged with the CAL code for the 1996 data production. 189

Chapter 1

Theory

1.1 Introduction

Over the last three decades experimental and theoretical efforts to understand the fundamental constituents of matter have condensed into a theory called the Standard Model. This theory, initially devised by Glashow, Weinberg and Salam [1], includes the unified theory of electroweak interactions and the theory of strong interactions, Quantum Chromodynamics. Many excellent texts describing the Standard Model in detail are available [2, 3, 4] and so only a brief discussion of the structure of the theory will be made here.

The Standard Model presents a rather simple picture of the structure of matter. All fundamental interactions occur between spin-$\frac{1}{2}$ fermions. These are either *leptons*, which do not experience strong interactions, or *quarks*, which are the fundamental constituents of all particles which interact via the strong force (and which are collectively known as *hadrons*). The fermions are grouped into three generations as shown in Table 1.1. Ordinary matter is made up of fermions from the first generation. The second and third generations are essentially higher mass[1] analogues of the first. All the fermions are associated with their respective anti-fermions which have the same mass but opposite quantum numbers.

The fermions interact with each other through the exchange of spin-1 gauge bosons. These are listed in Table 1.2. All fermions interact weakly via the exchange of the massive $W^{\pm}$ and Z^0 particles. Electrically charged

[1] Quark masses cannot be measured directly and must be inferred from their influence on hadron properties. As a result the values of the quark masses depend on how they are defined. The definitions can be broken into two broad classes : "constituent" masses in which the quark masses are determined from hadron mass spectra, and "current" masses where the masses enter as parameters in the the QCD Lagrangian. The values shown in Table 1.1 are current masses.

Quarks			
	Flavour	Electric Charge (e)	Mass (MeV/c^2)
First Generation	Up (u)	+2/3	≈ 4
	Down (d)	-1/3	≈ 7
Second Generation	Charm (c)	+2/3	$\approx 1,500$
	Strange (s)	-1/3	≈ 200
Third Generation	Top (t)	+2/3	$\approx 180,000$
	Bottom (b)	-1/3	$\approx 4,700$
Leptons			
	Flavour	Electric Charge (e)	Mass (MeV/c^2)
First Generation	e-neutrino (ν_e)	0	< 0.007
	Electron (e)	-1	0.511
Second Generation	μ-neutrino (ν_μ)	0	< 0.27
	Muon (μ)	-1	0.105
Third Generation	τ-neutrino (ν_τ)	0	< 31
	Tau (τ)	-1	1777

Table 1.1: Common properties of quarks and leptons. Note that the existence of the τ-neutrino has not been experimentally verified.

Interaction	Relative Strength	Mediator	Range (m)
strong	1	gluon	$\leq 10^{-15}$
electromagnetic	10^{-2}	photon	∞
weak	10^{-5}	Z^0 and $W^\pm$	10^{-18}
gravity	10^{-42}	graviton	∞

Table 1.2: Mediators of the fundamental interactions

fermions may also interact electromagnetically through the exchange of a photon. Finally, quarks interact strongly by exchanging the mediator of the colour force, the gluon. Gravity is assumed to be mediated by the graviton, but the gravitational coupling is negligible at accelerator energies and will not be discussed further.

Although the predictions of the Standard Model have been confirmed in experiment upon experiment, it cannot be the ultimate description of matter and its interactions. A number of questions have yet to be answered. For instance, the apparent redundancy of the three fermion generations is not understood, nor is the pattern of fermion and boson masses (although there is currently the hope that the Higgs mechanism can account for the phenomenon of particle mass, even if it cannot predict the absolute values). Another problem is the small asymmetry observed between the properties of matter and anti-matter, related to CP violation, which the Standard Model can accommodate but cannot explain.

Whatever the problems, there is no doubt that the Standard Model is a major step towards understanding matter. It is hoped that as accelerators reach higher energies and results become more precise, new physics may point the way to understanding some or all of the currently unanswered questions.

1.2 The Description of Neutrino-Nucleon Collisions

Neutrinos make excellent probes of hadronic matter. They are structureless, comparatively easy to generate in accelerators and their electroweak properties are well understood. One of the common methods of studying hadrons at the quark level is by investigating the collisions of neutrinos with protons and neutrons in a fixed target. Before further discussion of such interactions, it is useful to introduce the common variables used to describe deep inelastic scattering events [2]. Figure 1.1 shows the lowest order Feynmann diagram of the neutrino-nucleon scattering process. In the diagram k^μ and l^μ are the four-momenta of the incoming neutrino and outgoing lepton respectively, q^μ is the four-momentum transferred to the hadronic system, P^μ is the 4-momentum of the nucleon, x is Bjorken x (see below) and W^μ is the four momentum of the outgoing hadronic system.

Measurement of these 4-vectors allows the determination of all the kinematic quantities of the $\nu_\mu - \mathrm{N}$ scattering process:

[2] Here and in the following discussion we assume that the event involves a muon neutrino interacting with a nucleon and that the subsequent outgoing lepton is a muon.

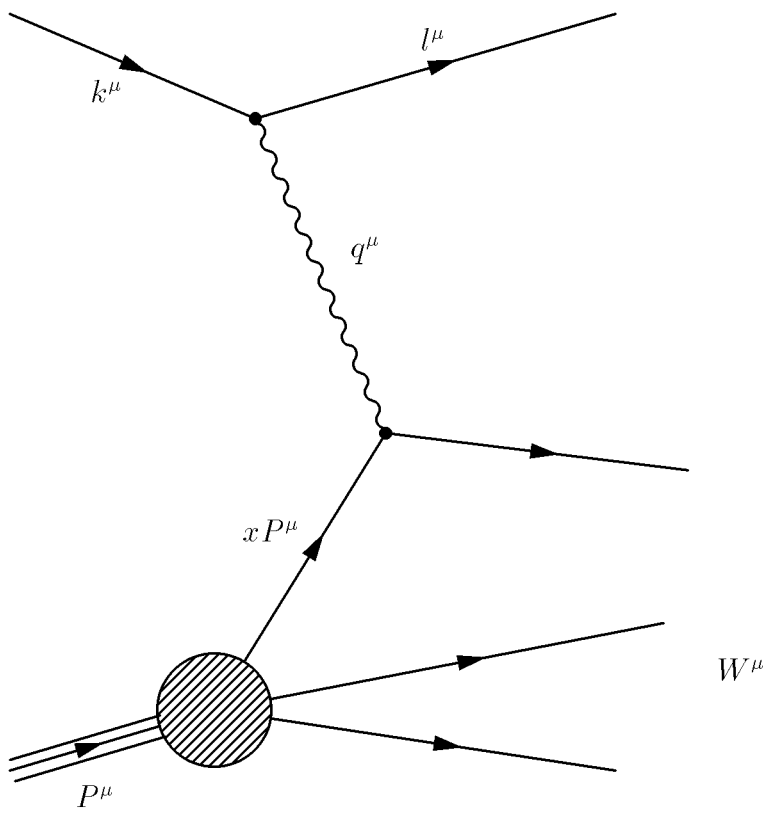

Figure 1.1: Leading order diagram for deep inelastic lepton-nucleon scattering.

- **Square of the centre of mass energy :**

$$s = (k + P)^2 = 2M_N E_\nu + M_N^2 \approx 2M_N E_\nu \tag{1.1}$$

where the nucleon mass has only been retained to first order and the four-momentum dot product has been evaluated in the laboratory frame.

- **Energy transfer to the hadronic system :**

$$\nu = \frac{P \cdot q}{M} = \mathrm{E}_\nu - \mathrm{E}_\mu \quad \text{(in the laboratory frame.)} \tag{1.2}$$

- **Square of the 4-momentum transfer to the hadronic system :**

$$-q^2 = Q^2 = -(k - l)^2 = 2\,(E_l E_\nu - |p_l| E_\nu cos\theta) - m_l^2 \tag{1.3}$$

where E_l is the energy of the outgoing lepton and θ is the scattering angle between the outgoing lepton and the incoming neutrino in the laboratory frame. If the mass of the lepton is neglected then $E_l \approx p_l$ and Equation 1.3 may be expressed in the more common form

$$Q^2 = 4E_\nu E_l sin^2\left(\frac{\theta}{2}\right) \tag{1.4}$$

- **Bjorken scaling variable x_{Bj} :**

$$x_{Bj} = \frac{Q^2}{2P \cdot q} = \frac{Q^2}{2M_N \nu} \tag{1.5}$$

- **Fraction of energy lost by the neutrino (Bjorken y):**

$$y_{Bj} = \frac{P \cdot q}{P \cdot k} = \frac{\nu}{E_\nu} \quad \text{(in the laboratory frame.)} \tag{1.6}$$

- **Square of the invariant mass of the hadronic system :**

$$W^2 = (q + P)^2 = M_N^2 + Q^2(\frac{1}{x_{Bj}} - 1) \tag{1.7}$$

In a frame in which the nucleon 4-momentum is much larger than the typical transverse momenta of its constituent quarks (the "infinite momentum frame" cf. Section 1.4) the scaling variable x_{Bj} represents the fraction of the nucleon momentum carried by the interacting parton. The y_{Bj} variable is related to the scattering angle of the outgoing lepton in the neutrino-parton center-of-mass system.

1.3 The Charged Current Neutrino-Nucleon Interaction

This section outlines the important details of the charged current neutrino-nucleon scattering cross section. A full derivation may be found in Reference [5]. In the following, unless otherwise specified, "natural" units in which

$$h = c = 1 \tag{1.8}$$

are used.

The inclusive, spin averaged, cross section for neutrino-nucleon scattering may be written as

$$\frac{d^2\sigma^{\nu(\overline{\nu})\mathcal{N}}}{d\Omega_\mu dE_\mu} = \frac{G^2}{(2\pi)^2}\left(\frac{M_W^2}{M_W^2+Q^2}\right)^2 \frac{E_\mu}{E_\nu} L_{\mu\nu}W^{\mu\nu} \tag{1.9}$$

where G is the Fermi constant, M_W is the W boson mass, E_ν (E_μ) is the energy of the incident neutrino (final state muon) and $d\Omega_\mu$ is the solid angle element into which the muon scatters. The lepton tensor, $L_{\mu\nu}$, is completely calculable and is given by :

$$L^{\mu\nu} = k^\mu k'^\nu - g^{\mu\nu} k\cdot k' + k'^\mu k^\nu \pm i\epsilon^{\mu\nu\rho\sigma}k_\rho k'_\sigma \tag{1.10}$$

where the contribution from the last term is positive for ν and negative for $\overline{\nu}$ interactions.

The tensor $W^{\mu\nu}$ describes the dynamics of the nucleon-boson interaction. It is not currently possible to calculate the form of this tensor from first principles. Generally, however, $W^{\mu\nu}$ must be a function only of the available 4-vectors P^μ, the 4-momentum of the incoming nucleon, and q^μ, the invariant momentum transfer. The most general expression for $W^{\mu\nu}$ involving tensors constructed from these 4-vectors is :

$$\begin{aligned} W_{\alpha\beta}^{\nu(\overline{\nu})} = &-\left(g_{\alpha\beta} - \frac{q_\alpha q_\beta}{q^2}\right) W_1^{\nu(\overline{\nu})} \\ &+ \frac{1}{M^2}\left(p_\alpha - \frac{pq}{q^2}q_\alpha\right)\left(p_\beta - \frac{pq}{q^2}q_\beta\right) W_2^{\nu(\overline{\nu})} \\ &- \frac{i}{2M^2}\epsilon_{\alpha\beta\rho\sigma}p^\rho q^\sigma W_3^{\nu(\overline{\nu})} + \frac{1}{M^2}q_\alpha q_\beta W_4^{\nu(\overline{\nu})} \\ &+ \frac{1}{M^2}(p_\alpha q_\beta + q_\alpha p_\beta) W_5^{\nu(\overline{\nu})} + \frac{i}{M^2}(p_\alpha q_\beta - q_\alpha p_\beta) W_6^{\nu(\overline{\nu})} \end{aligned} \tag{1.11}$$

W_1 to W_6 are dimensionless functions of the independent Lorentz scalars $p \cdot q$ and $q \cdot q$. When contracted with the leptonic tensor (Equation 1.10) the terms proportional to W_4, W_5 and W_6 in Equation 1.11 become proportional to the mass of the outgoing lepton and are usually discarded. The resulting cross section has the form

$$\frac{d^2\sigma^{\nu(\overline{\nu})\mathcal{N}}}{d\Omega_\mu dE_\mu} = \frac{G^2}{(2\pi)^2}E_\mu^2\left(\frac{M_W^2}{M_W^2+Q^2}\right)^2\left\{cos^2(\frac{\theta}{2})W_2^{\nu(\overline{\nu})} + 2sin^2(\frac{\theta}{2})W_1^{\nu(\overline{\nu})} \pm \frac{(E_\nu+E_\mu)}{m_\mu}sin^2\frac{\theta}{2}W_3^{\nu(\overline{\nu})}\right\} \quad (1.12)$$

where E_μ is the energy of the outgoing muon and θ is the angle of the outgoing muon with respect to the direction of the incoming neutrino in the centre of momentum frame.

It is convenient to express this differential cross-section in terms of the kinematic quantities defined in Equations 1.1-1.6.

$$\frac{d^2\sigma^{\nu(\overline{\nu})\mathcal{N}}}{dxdy} = \frac{G^2ME_\nu}{\pi}\left(\frac{M_W^2}{M_W^2+Q^2}\right)^2\left\{2x\frac{y^2}{2}F_1^{\nu(\overline{\nu})}(x,Q^2) + 2xF_2^{\nu(\overline{\nu})}(x,Q^2)\left(1-y-\frac{Mxy}{2E_\nu}\right) \pm xF_3^{\nu(\overline{\nu})}(x,Q^2)y\left(1-\frac{y}{2}\right)\right\} \quad (1.13)$$

where the structure functions in Equation 1.12 have been replaced by the equivalent, and more commonly used, functions

$$\begin{aligned} W_1 &= F_1 \\ \frac{\nu W_2}{M} &= F_2 \\ \frac{\nu W_3}{M} &= F_3 \end{aligned} \quad (1.14)$$

In principle Equation 1.13 contains twelve structure functions, three for each of the νp, νn, $\overline{\nu}p$ and $\overline{\nu}n$ interactions. This number may be reduced by making assumptions about the structure of the target nucleon.

The basis of the most successful model of nucleon structure devised to date, Quantum Chromodynamics (QCD), is the Quark-Parton Model.

1.4 The Quark-Parton Model

In the Quark-Parton model the incoming lepton scatters, incoherently, off point-like spin-$\frac{1}{2}$ *partons* within the nucleon. This scattering is generally conceptualised in the "infinite momentum" frame in which the nucleon 3-momentum is very large and all masses can be neglected. The scattering process, as seen in this frame, is shown in Figure 1.2. Suppose that in the hadron rest frame the rate at which partons interact with each other is characterised by a time τ. As a result of the boost to the infinite momentum frame, the relative velocity with respect to the laboratory frame of which is close to c, the interaction time becomes $\tau^* = \tau(1 - v^2/c^2)^{-1/2}$, substantially larger than τ. Since the time an incoming lepton takes to cross the nucleon is on the order of the nucleon size, which has undergone Lorentz contraction during the boost and is consequently much smaller than τ^*, the lepton observes the collection of partons as being essentially free. This mechanism allows the structure functions to be expressed as the addition of probabilities of scattering from single free partons without the complication of having to consider parton-parton coherence effects.

After the collision the scattered quark must recombine with the spectator quarks. The basic assumption in the theory of deep inelastic scattering is that the time taken to form the final hadronic system is much longer than the lepton-parton interaction time and can be treated as a process entirely separate from the initial scattering.

This model makes several predictions which are in good agreement with current experimental results. The most important of these are :

- **Scaling:** In 1969 Bjorken[6] used the quark-parton model to predict that the structure functions would be independent of any momentum scale entering into the deep inelastic process. In the limit $Q^2 \longrightarrow \infty$ and $\nu \longrightarrow \infty$ such that x_{Bj} remains finite (known as the Bjorken limit) it was proved that

$$F_i(x, Q^2) \longrightarrow F_i(x) \qquad i = 1, 2, 3 \tag{1.15}$$

  If the quarks in the nucleon were non-interacting, Bjorken scaling would hold over the entire range of Q^2. However, experiment has shown that the structure functions depend, weakly, on Q^2 (known as *scaling violation*). This dependence is characteristic of quark-quark and quark-gluon interactions and is a prime signature of gluon emission.

- **Callan-Gross Relation[2]:** If the neutrino and antineutrino were to scatter completely off spin $\frac{1}{2}$ nucleon components then in the Bjorken

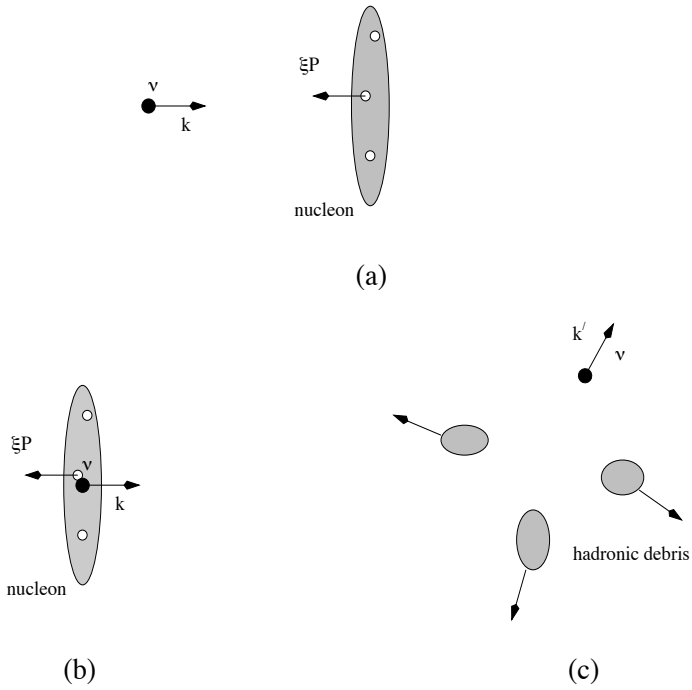

Figure 1.2: Schematic parton model picture of deep inelastic scattering. (a) The boost to the infinite momentum frame compresses the nucleon into a flat pancake and slows down the partons within the nucleon. The partons are essentially "frozen" during the interaction, allowing the lepton to interact incoherently with one free parton (b). As the scattered lepton recedes, the fragments of the nucleon recombine to form the hadron shower (c). This occurs on a time scale much longer than the initial collision.

limit

$$2xF_1(x) = F_2(x) \tag{1.16}$$

This relation is not an exact one and only holds in the approximation of the quark-parton model. In reality this relation is broken by the presence of spin-1 gluons and by higher order non-scaling QCD processes. The exact relationship is conventionally written as

$$2xF_1(x) = F_2(x)\left(\frac{1+Q^2/\nu^2}{1+R}\right) \tag{1.17}$$

where R is defined as the ratio of the longitudinal to transverse W boson absorption cross sections.

For the purposes of the following discussion exact Callan-Gross behaviour is assumed.

In the quark-parton model the quark and antiquark probability densities are defined in terms of the individual quark densities. Denoting the densities of the up, down, strange and charm quarks by $u(x)$, $d(x)$, $s(x)$ and $c(x)$ respectively , the quark and antiquark momentum distributions for neutrino and antineutrino scattering off a proton target are

$$\begin{aligned} xq^{\nu P}(x) &= xd^P(x) + xs^P(x) \\ x\overline{q}^{\nu P}(x) &= x\overline{u}^P(x) + x\overline{c}^P(x) \\ xq^{\overline{\nu} P}(x) &= xu^P(x) + xc^P(x) \\ x\overline{q}^{\overline{\nu} P}(x) &= x\overline{d}^P(x) + x\overline{s}^P(x) \end{aligned} \tag{1.18}$$

where the $\nu(\overline{\nu})$ superscripts refer to the quark or antiquark content seen by a neutrino (antineutrino) probe.

Strong isospin symmetry and the assumption that the sea quark momentum distributions are identical to the sea antiquark momentum distributions suggest that the neutron parton densities may be written in terms of the proton quark densities

$$\begin{aligned} xq^{\nu N}(x) &= xu^P(x) + xs^P(x) \\ x\overline{q}^{\nu N}(x) &= x\overline{d}^P(x) + x\overline{c}^P(x) \\ xq^{\overline{\nu} N}(x) &= xd^P(x) + xc^P(x) \\ x\overline{q}^{\overline{\nu} N}(x) &= x\overline{u}^P(x) + x\overline{s}^P(x) \end{aligned} \tag{1.19}$$

Using the incoherence property of deep inelastic scattering the structure functions may be expressed as linear combinations of the quark densities

$$\begin{aligned} F_2^{P(N)}(x) &= xq^{P(N)}(x) + x\overline{q}^{P(N)}(x) \\ xF_3^{P(N)}(x) &= xq^{P(N)}(x) - x\overline{q}^{P(N)}(x) \end{aligned} \tag{1.20}$$

and so the double differential cross section for neutrino scattering off a proton or neutron target may be written in terms of the quark and antiquark momentum distributions

$$\begin{aligned} \frac{d^2\sigma^{\nu P(N)}}{dxdy} = \frac{G^2 M E_\nu}{\pi}\left(\frac{M_W^2}{M_W^2+Q^2}\right)^2 \Bigg[&\left((1-y)^2 - \frac{Mxy}{2E_\nu}\right) x\overline{q}^{P(N)}(x) \\ &+ \left(1 - \frac{Mxy}{2E_\nu}\right) xq^{P(N)}(x)\Bigg] \end{aligned} \tag{1.21}$$

and for antineutrino scattering

$$\frac{d^2\sigma^{\overline{\nu}P(N)}}{dxdy} = \frac{G^2 M E_\nu}{\pi}\left(\frac{M_W^2}{M_W^2+Q^2}\right)^2\left[\left((1-y)^2 - \frac{Mxy}{2E_\nu}\right)xq^{P(N)}(x) + \left(1-\frac{Mxy}{2E_\nu}\right)x\overline{q}^{P(N)}(x)\right] \quad (1.22)$$

In the case of a target in which the numbers of protons and neutrons are unequal (referred to as a "non-isoscalar" target) the total double differential cross section is taken to be the weighted average of the contributions from the different target types. Specifically, if Z is the number of protons in a target nucleus and N is the number of neutrons, then the total double differential cross section is taken to be

$$\frac{d^2\sigma^{\nu(\overline{\nu})}}{dxdy} = \frac{1}{Z+N}\left(Z\frac{d^2\sigma^{\nu(\overline{\nu})P}}{dxdy} + N\frac{d^2\sigma^{\nu(\overline{\nu})N}}{dxdy}\right) \quad (1.23)$$

In an isoscalar target, Z = N, and Equation 1.23 simplifies to be the average of the differential cross sections from protons and neutrons.

1.5 Charm Quark Production

In the first approximation, charm production by neutrino deep inelastic scattering is a special case of Equation 1.21[3] According to the Standard Model the presence of a charm quark in the final state requires that the struck quark be a d or a s quark. In neutrino interactions this implies that the structure functions take the form (c.f. Equation 1.20)

$$2xF_2^{\nu P} = xF_3^{\nu P} = x(|V_{cd}|^2 d(x) + |V_{cs}|^2 s(x)) \quad (1.24)$$

where the Cabibbo flavour mixing has been made explicit by the inclusion of the Cabibbo-Kobayashi-Maskawa (CKM) matrix elements $|V_{cd}|$ and $|V_{cs}|$. Inserting these structure functions into Equation 1.21 and assuming an isoscalar target, massless charm quarks, the Callan-Gross relationship (Equation 1.16) and neglecting the mass of the proton the double differential cross section for charm production is :

$$\frac{d^2\sigma^{\nu P}}{dxdy} = \frac{G^2 M E_\nu}{2\pi}\left(\frac{M_W^2}{M_W^2+Q^2}\right)^2\left[|V_{cd}|^2(xd(x)+xu(x)) + 2|V_{cs}|^2 xs(x)\right] \quad (1.25)$$

[3]Unless otherwise specified in the following discussion deep inelastic scattering of neutrinos is assumed. The antineutrino case is completely analogous.

If charm quarks were massless this would be the final cross section. However, the correct inclusion of massive quark effects introduces complications into the treatment outlined above. At leading order in QCD, the mechanism used to account for heavy quark effects is referred to as "slow rescaling".

1.5.1 Slow Rescaling in Heavy Quark Production

The slow rescaling mechanism was developed by Georgi and Politzer [7] in order to present a correct account of kinematic effects arising from non-negligible masses in perturbative QCD. Their proposition was that the structure functions do not scale with x_{Bj} but rather with

$$\xi = \frac{Q'^2}{2M_p\nu}\left(\frac{2}{1+\sqrt{(1+Q'^2/\nu^2)}}\right) \tag{1.26}$$

where

$$2Q'^2 = Q^2 + m_F^2 - m_I^2 + \sqrt{\left(Q^4 + 2Q^2(m_F^2+m_I^2) + (m_F^2-m_I^2)^2\right)} \tag{1.27}$$

The struck quark mass is m_I, the produced quark is m_F, the proton mass is M_p and Q^2 and ν have been introduced in Section 1.2. In the case of charm production m_I can be set to zero and so, in the limit that $Q^2 \gg M_p$, Equation 1.26 reduces to

$$\xi = x + \frac{m_F^2}{2M_p\nu} \tag{1.28}$$

A more physically intuitive derivation of the same result may be carried out by imposing the condition that the produced parton be on its mass shell. If the struck quark carries momentum ξP where P is the 4-momentum of the nucleon and interacts with a W boson of momentum q then the mass shell condition implies that

$$(\xi P + q)^2 = m_F^2 \tag{1.29}$$

When Equation 1.29 is expanded one finds that

$$\begin{aligned}\xi &= -\frac{\nu}{M_p}\left(1-\sqrt{\left(1+\frac{Q^2+m_F^2}{\nu^2}\right)}\right)\\ &\approx \frac{Q^2}{2M_p\nu} + \frac{m_F^2}{2M_p\nu}\\ &= x + \frac{m_F^2}{2M_p\nu}\end{aligned} \tag{1.30}$$

and so, in the case of heavy quark production, Equation 1.26 may be seen as arising from 4-momentum conservation at the quark-boson vertex.

Slow rescaling may now be used to introduce the proper treatment of the charm quark mass threshold into the charm production cross section. The procedure mainly consists of replacing x by ξ in the structure functions and parton densities,

$$\begin{aligned} F_2(x,Q^2) &\longrightarrow F_2(\xi,Q^2) \\ xF_3(x,Q^2) &\longrightarrow \frac{x}{\xi}\xi F_3(\xi,Q^2) \end{aligned} \tag{1.31}$$

These are inserted into the charged current cross section to yield

$$\begin{aligned} \frac{d^2\sigma^{\nu(\overline{\nu})\mathcal{N}}}{dxdy} = \frac{G^2 M E_\nu}{\pi}\left(\frac{M_W^2}{M_W^2+Q^2}\right)^2 \Bigg\{ \frac{2x}{2\xi}\frac{y^2}{2} 2\xi F_1^{\nu(\overline{\nu})\mathcal{N}}(\xi,Q^2) + \\ F_2^{\nu(\overline{\nu})\mathcal{N}}(\xi,Q^2)\left(1-y-\frac{Mxy}{2E_\nu}\right) \pm \frac{x}{\xi}\xi F_3^{\nu(\overline{\nu})\mathcal{N}}(\xi,Q^2) y\left(1-\frac{y}{2}\right)\Bigg\} \end{aligned} \tag{1.32}$$

Writing the structure functions as linear combinations of the quark densities as before and changing variables from (x,Q^2) to (ξ,Q^2) allows the charm production cross section to be expressed as

$$\begin{aligned} \frac{d^2\sigma^{\nu\mathcal{N}}}{d\xi dy} = \frac{G^2 M E_\nu \xi}{\pi}\left[\left(u(\xi,Q^2)+d(\xi,Q^2)\right)|V_{cd}|^2 + 2s(\xi,Q^2)|V_{cs}|^2\right] \\ \left(1-y+\frac{xy}{\xi}+\Gamma(1-y-\frac{Mxy}{2E_\nu})-\frac{Mxy}{2E_\nu}\right) \end{aligned} \tag{1.33}$$

for neutrino interactions and

$$\begin{aligned} \frac{d^2\sigma^{\overline{\nu}\mathcal{N}}}{d\xi dy} = \frac{G^2 M E_\nu \xi}{\pi}\left[\left(\overline{u}(\xi,Q^2)+\overline{d}(\xi,Q^2)\right)|V_{cd}|^2 + 2\overline{s}(\xi,Q^2)|V_{cs}|^2\right] \\ \left(1-y+\frac{xy}{\xi}+\Gamma(1-y-\frac{Mxy}{2E_\nu})-\frac{Mxy}{2E_\nu}\right) \end{aligned} \tag{1.34}$$

for antineutrino events.

In Equations 1.33 and 1.34 the variable Γ is introduced to take the exact Callan-Gross relationship into account and is written as (c.f. Equation 1.17)

$$\Gamma = \left(\frac{1+R}{1+\frac{4M^2\xi^2}{Q^2}}\right) - 1 \tag{1.35}$$

Kinematic limits for ξ and y may be derived from the requirement that Q^2 be greater than zero and that the invariant hadronic mass, W^2, be larger

than the square of the sum of the charm mass and the nucleon mass :

$$\begin{aligned} Q^2 &> 0 \\ W^2 &> (m_c + M_N)^2 \end{aligned} \tag{1.36}$$

These limits are

$$\begin{aligned} \frac{m_c^2}{2ME_\nu} &\leq \xi \leq 1 \\ \frac{(m_c + M)^2 - M^2}{2ME_\nu} &\leq y \leq 1 \end{aligned} \tag{1.37}$$

1.6 Opposite Sign Dimuon Production

The double differential cross sections derived in the previous section only describe the production of a charm quark in neutrino-nucleon interactions. In opposite sign dimuon production the charm quark must fragment into a charmed hadron which then decays semileptonically, resulting in two oppositely charged muons in the final state: the *primary* muon which comes from the lepton vertex and the *secondary* muon from the semileptonic decay.

The fragmentation process describes the recombination of the charm quark with an antiquark from the nucleon sea. It is conventionally represented by a fragmentation function, $D(z)$, which specifies the probability that a given charmed hadron will carry a fraction z of the momentum of the initial charm quark. The choice of form of $D(z)$ will be discussed further in Chapter 5. In the quark parton model the fragmentation function is factorised from the double differential cross section for charm quark production. This is not true in higher order QCD theory.

The final double differential cross section for dimuon production at leading order in QCD is

$$\frac{d^2\sigma(\nu\mathcal{N} \to \mu^-\mu^+X)}{d\xi dy} = \frac{d^2\sigma(\nu\mathcal{N} \to c\mu^-)}{d\xi dy} D(z) B_c(c \to \mu^+\nu_\mu X) \tag{1.38}$$

where the factor $B_c(c \to \mu^+\nu_\mu X)$ is the probability that the charmed hadron will undergo a semimuonic decay. The leading order diagram for the dimuon production process is shown in Figure 1.3.

Some conclusions may be drawn from the form of the dimuon double differential cross section

- The CKM matrix element $|V_{cd}|^2$ is much smaller than $|V_{cs}|^2$ ($|V_{cd}|^2 = 0.0484$ as opposed to $|V_{cs}|^2 = 0.9494$). This, coupled with the approximately equal numbers of down and strange quarks in the nucleon sea (at

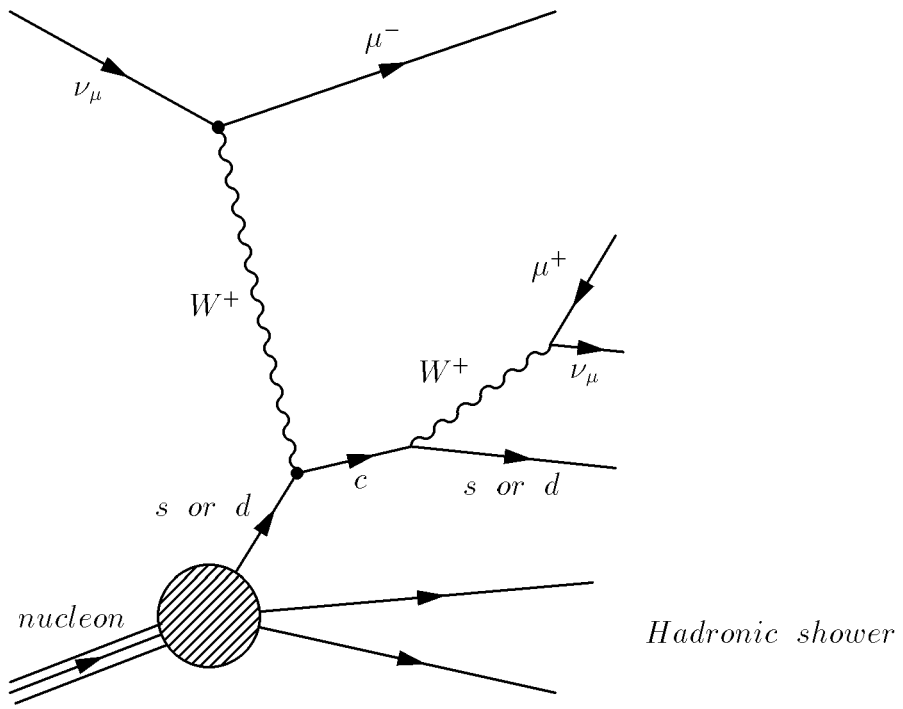

Figure 1.3: Quark-level diagram of charm production in neutrino-nucleon deep inelastic scattering. The primary muon comes from the lepton vertex while the secondary muon comes from the decay of the intermediate charmed hadron.

least up to a factor of two) implies that roughly 90% of the anti-neutrino induced anti-charm dimuon events originate from $\overline{\nu}$ scattering off anti-strange quarks in the sea. The result of this is that the anti-neutrino induced dimuon event x_{Bj} distributions are extremely sensitive to the shape of the strange quark momentum distribution, providing a means for the extraction of the strange quark density.

- The slow rescaling mechanism naturally includes the mass of the charm quark. The x_{Bj}, Q^2 and E_ν distributions should, therefore, be sensitive to this mass.

In recent years attention has become focussed on the formulation of neutrino charm quark production in Next-to-Leading Order (NLO) QCD. Discussion of this work may be found in references [86, 87, 88, 89] but is outside the scope of this thesis.

Chapter 2

The NOMAD experiment

2.1 Introduction

The **NOMAD**[1] (WA96) is an experiment approved in September 1991 to search for $\nu_\mu \to \nu_\tau$ neutrino flavour oscillations in the CERN wideband neutrino beam. NOMAD can also partially explore the parameter space suggested by the LSND collaboration for the $\nu_\mu \to \nu_e$ oscillation channel[8].

2.2 Neutrino Oscillations

The question of whether neutrinos have mass is one of the outstanding problems in particle physics. The Standard Model, in assuming that right handed neutrino components do not exist, implicitly sets the neutrino mass to zero. Nevertheless, most extensions of the Standard Model predict the existence of massive neutrinos[11]. One of the more promising avenues of investigation into neutrino properties is the study of neutrino oscillations.

It is well known that quark flavour eigenstates are not identical to the mass eigenstates, giving rise to the instability of strange hadrons and such phenomena as strangeness oscillations in the $K^0 - \overline{K^0}$ system. The weak eigenstates are related to the mass eigenstates through the unitary Cabibbo-Kobayashi-Maskawa (CKM) matrix. In a similar way, if neutrinos are assumed to be massive and mixed then a neutrino weak eigenstate with flavour $\alpha(\alpha = e, \mu, \tau)$ can be expressed as a linear combination of neutrino fields with definite mass $\nu_i(i = 1, 2, 3)$[12]

$$\nu_\alpha = \sum_i U_{\alpha i}\, \nu^i \tag{2.1}$$

[1] **N**eutrino **O**scillation **MA**gnetic **D**etector

where $U_{\alpha i}$ is a unitary mixing matrix.

If $U_{\alpha i}$ contains non-diagonal elements then a neutrino of a given flavour α at time $t = 0$ may change into another flavour during propagation. It should be noted that the following simplified description of neutrino oscillation theory is only valid when the neutrino is propagating through vacuum.

Using $U_{\alpha i}$ one may write the state of a neutrino of flavour α after a time interval t as

$$|\nu_\alpha(t)\rangle = \sum_i e^{i(\vec{p}_i\cdot\vec{x}-E_i t)} U_{\alpha i} |\nu_i\rangle \tag{2.2}$$

The probability of observing a neutrino of flavour β at time t is then

$$\begin{aligned} P(\nu_\alpha \to \nu_\beta) &= |\langle \nu_\beta | \nu_\alpha(t)\rangle|^2 && (2.3)\\ &= |\sum_i e^{i(\vec{p}_i\cdot\vec{x}-E_i t)} U_{\alpha i} U^\dagger_{i\beta}|^2 && (2.4)\\ &= \sum_i \sum_j U_{\alpha i} U^*_{\beta i} U^*_{\alpha j} U_{\beta j}\ e^{i(\vec{p}_i-\vec{p}_j)\cdot\vec{x}} e^{-i(E_i-E_j)t} && (2.5) \end{aligned}$$

where the fact that $\langle \nu_i | \nu_j \rangle = \delta_{ij}$ has been used.

Relativistic neutrinos have $|\vec{p}| \gg m_i$ and so their energy may be approximated by

$$E_i = \sqrt{p^2 + m_i^2} \approx p + \frac{m_i^2}{2p} \approx p + \frac{m_i^2}{2E} \tag{2.6}$$

where here, and below, natural units in which $c = \hbar = 1$ have been used. With the approximation of Equation 2.6, Equation 2.5 becomes

$$P(\nu_\alpha \to \nu_\beta) = \sum_i \sum_j U_{\alpha i} U^*_{\beta i} U^*_{\alpha j} U_{\beta j}\ e^{-i\frac{\Delta m^2_{ij}}{2E}t} \tag{2.7}$$

where $\Delta m^2_{ij} = m_i^2 - m_j^2$ is the difference between the squares of the mass eigenvalues.

In the case of two-flavour mixing[2] the unitary matrix $U_{\alpha i}$ may be written as

[2]two flavour mixing is an approximation to the more general three flavour mixing scheme. It is, however, mathematically simpler to describe and will be used for the purposes of this discussion.

$$U = U^* = \begin{pmatrix} \cos\theta & \sin\theta \\ -\sin\theta & \cos\theta \end{pmatrix} \tag{2.8}$$

Substituting Equation 2.8 into Equation 2.7 and considering only the real part one can write the expression for $P(\nu_\alpha \to \nu_\beta)$ as

$$P(\nu_\alpha \to \nu_\beta) = \sin^2(2\theta)\ \sin^2\left(\frac{\pi\ L}{L_{osc}}\right) \tag{2.9}$$

where the *oscillation distance* L_{osc} is defined by

$$L_{osc} \equiv \frac{4\pi E}{\Delta m^2_{21}} = \frac{2.48(E/GeV)}{(\Delta m^2_{21}/eV^2)}[m] \tag{2.10}$$

and L is the distance between the neutrino source and the detector. The oscillation distance defines which region of the $\log(\Delta m^2)$-$\log(\sin^2 2\theta)$ plane any particular experiment is capable of searching. Oscillatory behaviour becomes important when

$$L \simeq L_{osc} \tag{2.11}$$

In order to be sensitive to very small Δm^2 an experiment must have L large and E small. Experiments based on detecting oscillations in solar neutrinos are ideal. Such experiments typically have $L \simeq 1 \times 10^{11}$ m and $E \simeq 1$ MeV giving a sensitivity to Δm^2 at the level of approximately 1×10^{-11} $(\mathrm{eV/c})^2$. These type of experiments are referred to as "long baseline" experiments.

Short baseline experiments, with $L \simeq 1$ km and $E \simeq 10$ GeV are sensitive to $\Delta m^2 \simeq 10$ $(\mathrm{eV/c})^2$. These are usually accelerator experiments.

Results from neutrino oscillation experiments are presented in the form of a limit plot. Assuming no oscillation signal the oscillation probability (Equation 2.9) can be used to form confidence regions in the $\log(\Delta m^2)$-$\log(\sin^2 2\theta)$ plane. A typical set of limit curves for accelerator experiments is shown in Figure 2.1. The region to the right of the curves are excluded at the 90% confidence level. The curves for NOMAD[9] and CHORUS[3][10] are shown.

[3]Cern Hybrid Oscillation Research apparatUS. CHORUS is a neutrino oscillation experiment upstream from NOMAD. In order that τ meson decay can be directly observed, the CHORUS tracking detector and target is constructed from plates of nuclear emulsion which has extremely good spatial resolution (see Section 2.3).

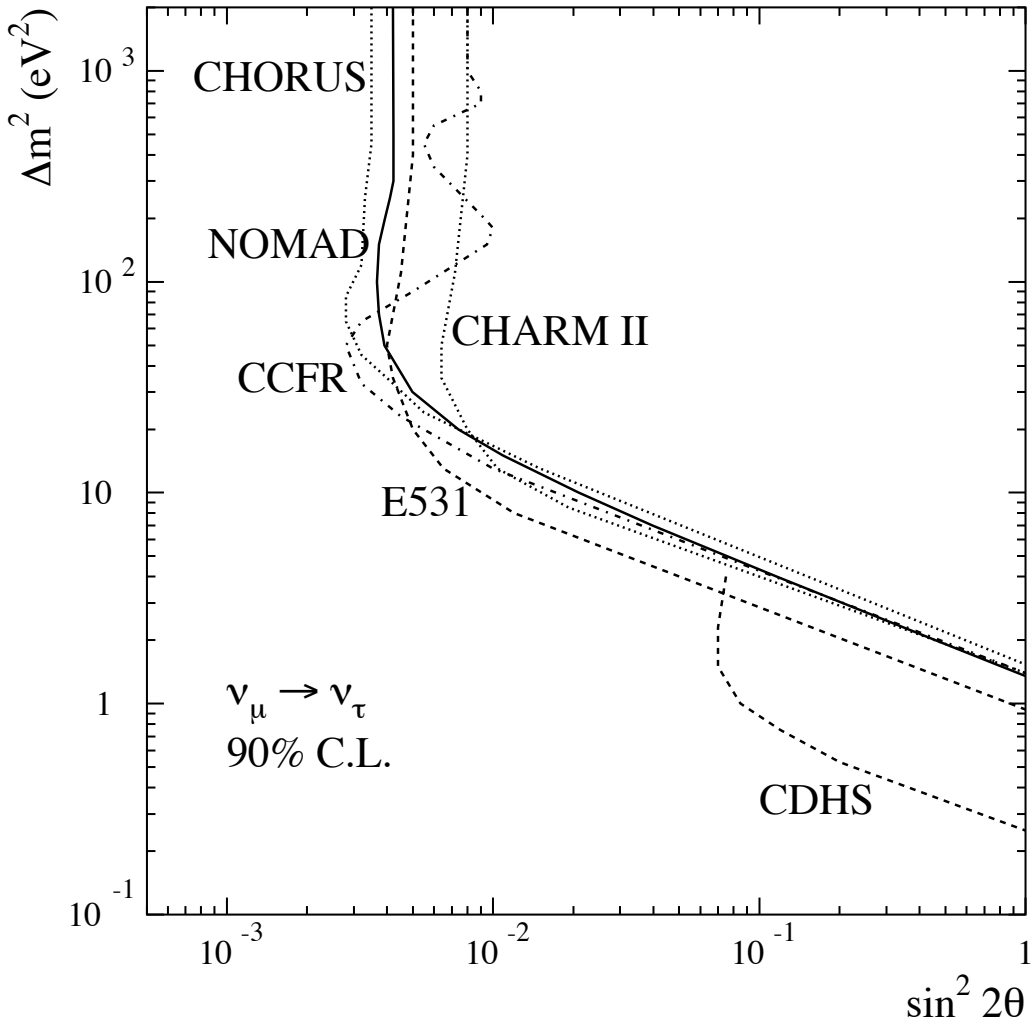

Figure 2.1: Limits on neutrino oscillations set by a number of experiments. The curve attributed to NOMAD is described in reference [9]. The areas of phase space to the right of the curves is excluded.

2.3 Search For Neutrino Oscillations

Assuming that the intrinsic ν_τ content of the neutrino beam is extremely small, the observation of a ν_τ charged current interaction is a sure indicator that flavour oscillation has occurred between the neutrino target and the detector. Such an interaction is tagged by observation of the decay of the resulting primary τ^-. Two approaches for the detection of the τ^- decay are being investigated at CERN.

- **Detection of the τ^- decay vertex**

  The τ^- has a proper decay length of $c\tau = 88.6\,\mu m$. Hence, the decay of the τ^- will take place at vertex separate from the primary production vertex. In the case of the purely leptonic decay $\tau^- \to \mu^- \nu_\tau \overline{\nu_\mu}$ the decay will appear as a kink in the primary lepton track. With a high precision tracking detector this kink and the associated impact parameter of the decay lepton with respect to the primary production vertex may be measured. This approach is being followed by the CHORUS experiment which uses nuclear emulsions as its target and tracking detector. Detectors following this approach require a position resolution much better than the typical decay length. Since the typical decay length of a τ^- is on the order of 1 mm, this requirement precludes the use of this method in NOMAD.

- **Reconstruction of the τ^- decay kinematics**

  The τ^- may also be identified by its decay kinematics. Since any decay will involve an outgoing ν_τ which will not be detected the momentum balance of the observed final state particles will be disturbed. If the directions of the final state particles and the incoming neutrino are known, the missing momentum in a plane transverse to the beam axis may be measured. Cuts on various kinematic variables are used to isolate ν_τ interaction candidates. The NOMAD experiment follows this approach.

The principle of kinematic tagging of τ^- decays is illustrated in Figure 2.2. The missing transverse momentum vector, in principle, can be reconstructed in any event. Two main difficulties arise :

- **Neutral Hadrons :** Photons resulting from π^0 decays are precisely measured by an electromagnetic calorimeter. However other neutral hadrons ($n, K_L^0, \ldots$) may only be detected by a hadronic calorimeter with (usually) a relatively poor energy resolution. Errors in the energy

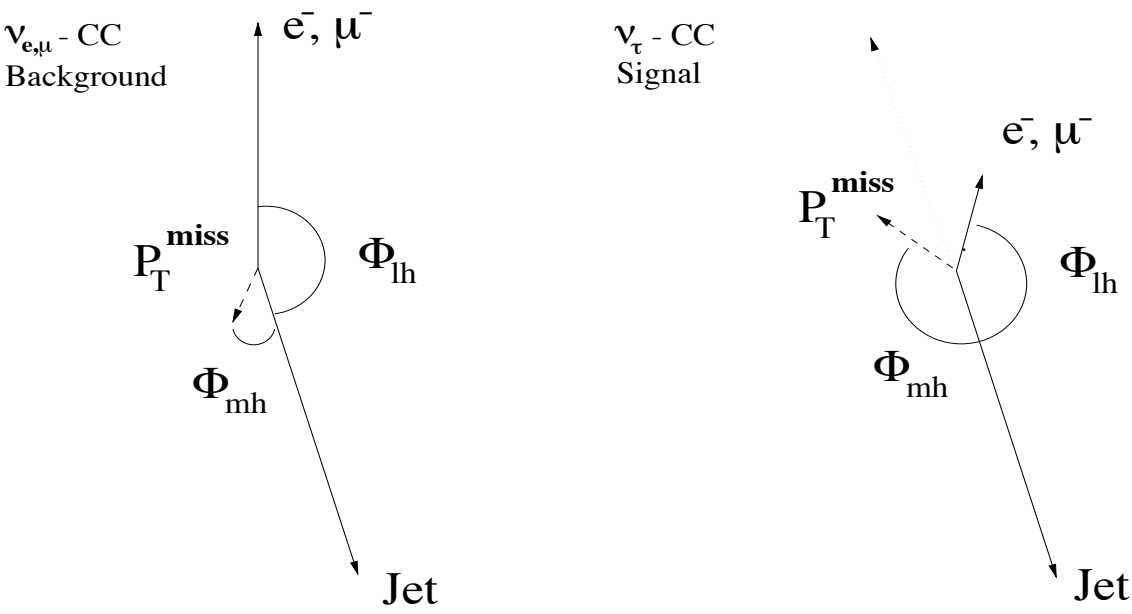

Figure 2.2: Kinematic configuration of background and signal events in the plane transverse to the neutrino beam axis for leptonic decay channels of the τ^-.

measurement and untagged neutral hadrons generate their own missing transverse momentum.

- **Experimental Resolution :** The finite experimental resolution, arising from such effects as tracking inefficiencies, misreconstruction of events with complicated topologies and residual motion of the nucleon (Fermi momentum) introduces an experimental fake $\vec{p}_t^{miss}$.

Two variables may be defined:

- Φ_{lh} : The angle between the momentum vectors of the outgoing lepton and the hadronic jet in the plane transverse to the incoming neutrino direction.

- Φ_{mh} : The angle between the momentum vector of the hadronic jet and the missing momentum $\vec{p}_t^{miss}$ in the plane transverse to the incoming neutrino direction.

A mismeasurement of the direction of the hadronic jet is generally randomly oriented in the transverse plane. In contrast, the $\vec{p}_t^{miss}$ resulting from the non-detection of neutrinos in a τ decay is strongly correlated with the direction of the lepton. This behaviour may be summarised by the distributions of

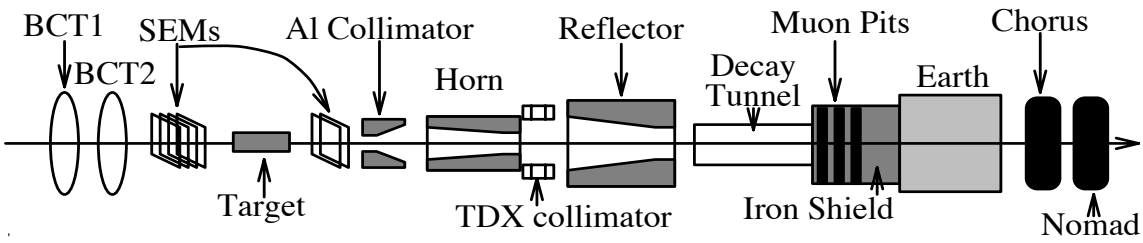

Figure 2.3: Schematic layout of the WANF beam line pointing out its main elements. (Not drawn to scale). The proton beam enters from the left and strikes the target. The resulting particle beam, comprising mostly π and K mesons, passes throught the magnetic lens system (horn and reflector) and enters the decay tunnel where the mesons decay to yield the final neutrino beam.

the angles Φ_{lh} and Φ_{mh}. Φ_{lh} is strongly peaked at 180° in standard charged current interactions of ν_μ or ν_e, whereas this dependence is weakened in ν_τ^{CC} events as a result of the undetected decay neutrinos. The angle Φ_{mh} has a flat distribution in standard charged current events. In the case of ν_τ^{CC} events the τ^- is produced back-to-back with the hadron jet and hence Φ_{mh} is peaked at 180°.

These and other cuts on the topology of the event are used to distinguish the true ν_τ signal from the $\nu_{\mu,e}^{CC}$ and $\nu_{\mu,e}^{NC}$ background.

2.4 The CERN Wide Band Neutrino Beam

High energy neutrino experiments may be divided into several categories depending upon the means by which the neutrinos are generated. Some experiments use naturally produced neutrinos from the sun or from atmospheric showers produced by cosmic ray interactions. Other experiments, such as accelerator or reactor experiments, use artifically produced neutrinos. Neutrinos from accelerators arise as decay products of secondary particles produced by the interaction of protons with some target with good thermo-mechanical properties, such as beryllium.

The CERN Super Proton Synchrotron (SPS) generates a 450 GeV proton beam which is used to produce the neutrino beam used in the West Area Neutrino Facility (WANF).

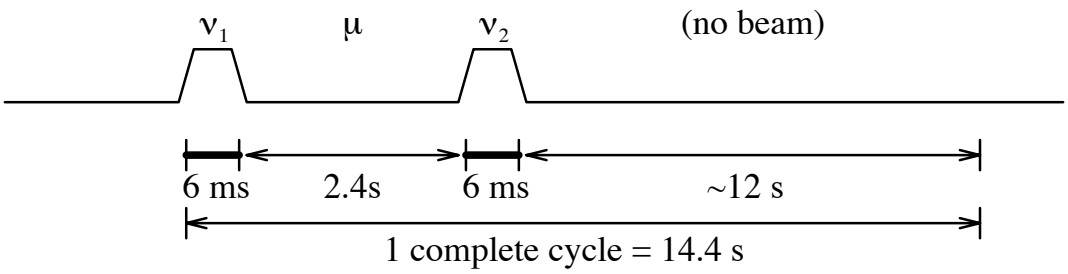

Figure 2.4: The structure of the SPS cycle (Not drawn to scale).

2.5 The SPS Beam

The geometry of the WANF beam line is show in Figure 2.3. The SPS accelerates protons to 450 GeV and extracts the beams for each experiment every 14.4 seconds. The structure of the beam spill on the neutrino targets is outlined in Figure 2.4. Protons are extracted from the SPS in two extraction spills. The first neutrino extraction, ν_1, containing approximately 1.2×10^{13} protons on target (*p.o.t.*), occurs in a 6 ms period following the start of the cycle. This is followed by a 2.4 s period of "flat-top" muons, labelled μ. In this period protons are allocated to other targets and experiments. NOMAD uses the muons which arrive in this period for calibration purposes. Finally $\approx 1.2 \times 10^{13}$ protons are extracted in a further 6 ms period, ν_2, after the flat-top.

The neutrinos are primarily produced by the decay in flight of π and K mesons produced by a beam of 450 GeV protons incident on a beryllium target. The proton beam intensity is measured by two Beam Current Transformers (BCT) and several Secondary Emission Monitors (SEM). These monitor the beam density profile by measuring the emission of secondary electrons from the monitor surface as the beam passes through.

The target consists of a series of eleven collinear beryllium rods separated by 9 mm gaps. Each rod is 10 cm long and has a diameter of 3 mm. The proton beam passes through these rods, generating a shower of secondary π and K mesons. Immediately after the target, the secondary particles pass through a large-angle aluminium collimator and are then focussed by a pair of magnetic lenses, the horn and reflector, located at 20 m and 90 m from the target respectively. These lenses deflect charged particles in a toroidal field produced by two coaxial conductors carrying current of equal magnitude but opposite direction (see Figure 2.5).

Immediately after the focussing elements lies a 290 m long decay tunnel. Within this tunnel the π and K mesons decay via the weak reactions

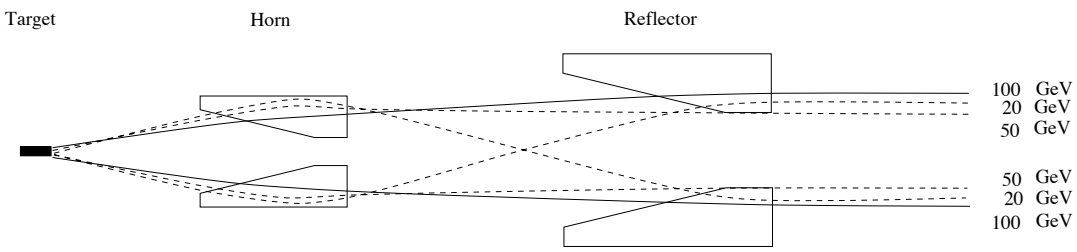

Figure 2.5: Operating principle of the horn and reflector system. Charged particles of one sign are focussed by a toroidal magnetic field. Particles of the opposite sign are defocussed.

$$\begin{aligned} \pi^+ &\longrightarrow \mu^+ + \nu_\mu \\ K^+ &\longrightarrow \mu^+ + \nu_\mu, e^+ + \nu_e \\ K_L^0 &\longrightarrow \mu^+ + \nu_\mu + \pi^-, e^+ + \nu_e + \pi^- \end{aligned}$$

These reactions are the main ones occurring in the decay tunnel. The charge conjugate reactions also occur, giving rise to a $\overline{\nu_\mu}$ component in the beam.

Shielding made of iron and earth directly after the decay tunnel filters out all but neutrinos and some muons. Silicon detectors in several pits within the shielding regions are used for beam monitoring and for absolute flux measurements. The NOMAD (CHORUS) detectors are situated at 835 m (823 m) from the target.

	Average E_ν (GeV)	Relative Abundance	ν CC Events
ν_μ	23.6	1.000	1.15×10^6
$\overline{\nu_\mu}$	22.7	0.070	0.39×10^5
ν_e	37.0	0.010	0.17×10^5
$\overline{\nu_e}$	33.2	0.003	0.22×10^4

Table 2.1: Monte Carlo predictions for NOMAD (for 2.4×10^{19} p.o.t.)

The beam line has been simulated by a detailed GEANT [13] simulation. The predicted neutrino energy spectrum at the NOMAD detector is shown in Figure 2.6 for the different neutrino species. The relative abundances of the various neutrino types and their average energies together with the expected number of charged current interactions are summarized in Table 2.1[14].

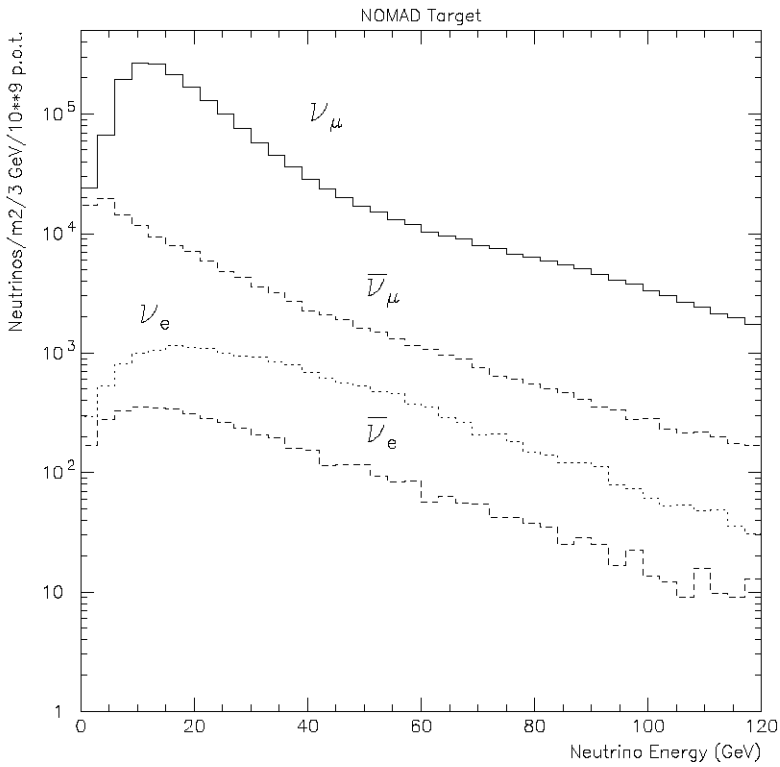

Figure 2.6: Energy spectra of neutrinos at NOMAD, predicted by NUBEAM[41], the NOMAD beam simulation program.

2.6 The NOMAD Detector

The NOMAD detector[15] must accommodate several conflicting design criteria in order to meet the physics goals for which it was constructed. It must provide a large enough target mass so that the estimated number of 1.1×10^6 ν_μ^{CC} events may be achieved whilst keeping the target density small enough so that multiple scattering effects does not degrade the momentum resolution below acceptable limits. It must be able to measure electrons and muons efficiently and achieve a high level of rejection against tracks which mimic these particles.

NOMAD has a target density similar to bubble chambers. The magnetic field is perpendicular to the neutrino beam and has a value of 0.4 T. A schematic view of the detector is shown in Figure 2.7. The various subdetectors are described below and the front calorimeter is described in more detail in chapter 3.

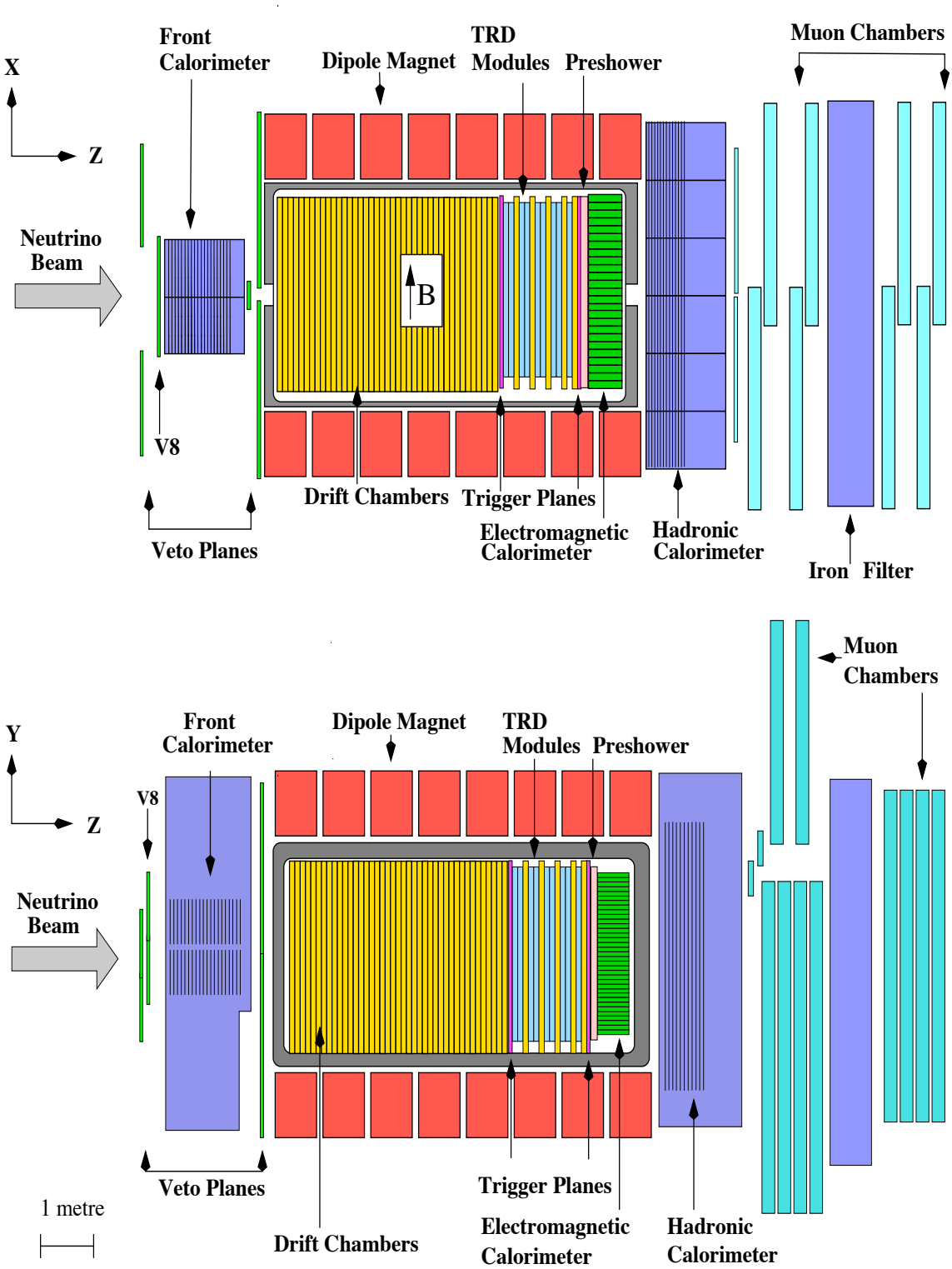

Figure 2.7: Top view (top) and side view (bottom) of the NOMAD detector. The co-ordinate system is shown on each plot.

2.6.1 The NOMAD Magnet

Features of the NOMAD magnet	
Field Type	Dipole
Magnet material	Aluminium
Return yoke material	Iron
Maximum Field	0.7 T
Nominal NOMAD field	0.4 T
Current at 0.4 T	5713 kA
Field homogeneity (centre)	2%
Field homogeneity (edges)	10%

Table 2.2: Features of the NOMAD magnet

The NOMAD detector uses the dipole magnet from the UA1 experiment. The main features of this magnet are shown in Table 2.2[16]. Both of the support pillars have been instrumented as calorimeters. The front pillar has been used to form the front calorimeter (see Section 2.6.3 and Chapter 3) and the back pillar forms the hadronic calorimeter (Section 2.6.9).

2.6.2 The Veto

The beam at NOMAD still contains many charged particles : muons which are not fully absorbed or which have been produced in material near or after the end of the decay tunnel and particles from upstream interactions in CHORUS. In order to prevent constant triggering on these particles the front face of NOMAD has been covered with an arrangement of scintillators. The veto system consists of 59 scintillation counters covering an area of $5 \times 5\text{m}^2$ on the upstream face of the detector. The scintillators have a thickness of 2 cm, a width of 21 cm and a length of either 300 cm or 210 cm. Fifty-six of these counters are read out on both ends by photo-multipliers and the remaining 3 have single-ended read-out. The signals from each scintillator are passed to discriminators and then (bar those from the single ended counters) to mean-timers. The mean-timer modules produce a signal which is independent of the impact position of the particle on the scintillator. The veto signal is constructed from a global OR of the signals from the individual counters. The efficiency of the veto is constantly monitored and is stable at about $96\% - 97\%$.

2.6.3 The Front Calorimeter

The central part of the NOMAD detector is contained within a basket which is suspended from the back and front magnet support pillars. Both these pillars have been instrumented as iron-scintillator calorimeters. The calorimeter constructed from the back support, the Hadronic Calorimeter, is discussed in Section 2.6.9. The front support forms the Front Calorimeter (FCAL).

The FCAL consists of 20 iron plates, between which are inserted scintillators. The scintillator panels are 18.5 cm wide, 0.5 cm thick, and 185 cm long. Groups of five scintillators are ganged together via adiabatic light guides to form a module. Each module is read out on both sides by 3-inch phototubes. Ten such modules are arranged vertically to form a stack. There are four stacks aligned along the beam axis. The instrumented region has a mass of 17.7 t and is about 5 nuclear interaction lengths deep.

Interactions in the FCAL are the subject of this thesis. The FCAL will be discussed more completely in Chapter 3.

2.6.4 The Drift Chambers

The central part of the NOMAD detector comprises the drift chambers. A novel, and important, feature of the drift chamber design is that the chambers provide both the target material and the tracking. This unavoidably entails conflicting requirements. The drift chamber walls should be as massive as possible to ensure a large number of neutrino interactions and as light as possible in order to minimize multiple scattering of the particles in the interaction.

The chambers have a total transverse area of 3×3 m^2. The total number of chambers is 49.

A schematic of a single chamber is shown in Figure 2.8.

Each chamber is constructed from panels made from Aramid fibres in a honeycomb structure. These panels are sandwiched between two layers of Kevlar-epoxy resin which impart mechanical rigidity to the structure as well as providing a low Z, low density target. Four such planes separated by an 8 mm gap filled with an argon (60%) - ethane (40%) gas mixture make up a single chamber.

The gaps in each chamber are instrumented with sense wires at angles of 5, 0 and -5 degrees with respect to the magnetic field direction. This geometry allows stereo-reconstruction of the particle coordinates along the drift direction. The drift field is shaped by aluminised mylar strips glued onto the inner chamber walls. The strips are 2.8 mm wide, 12 μm thick, and are separated by 1.2 mm. The potentials on the strips provide a drift field

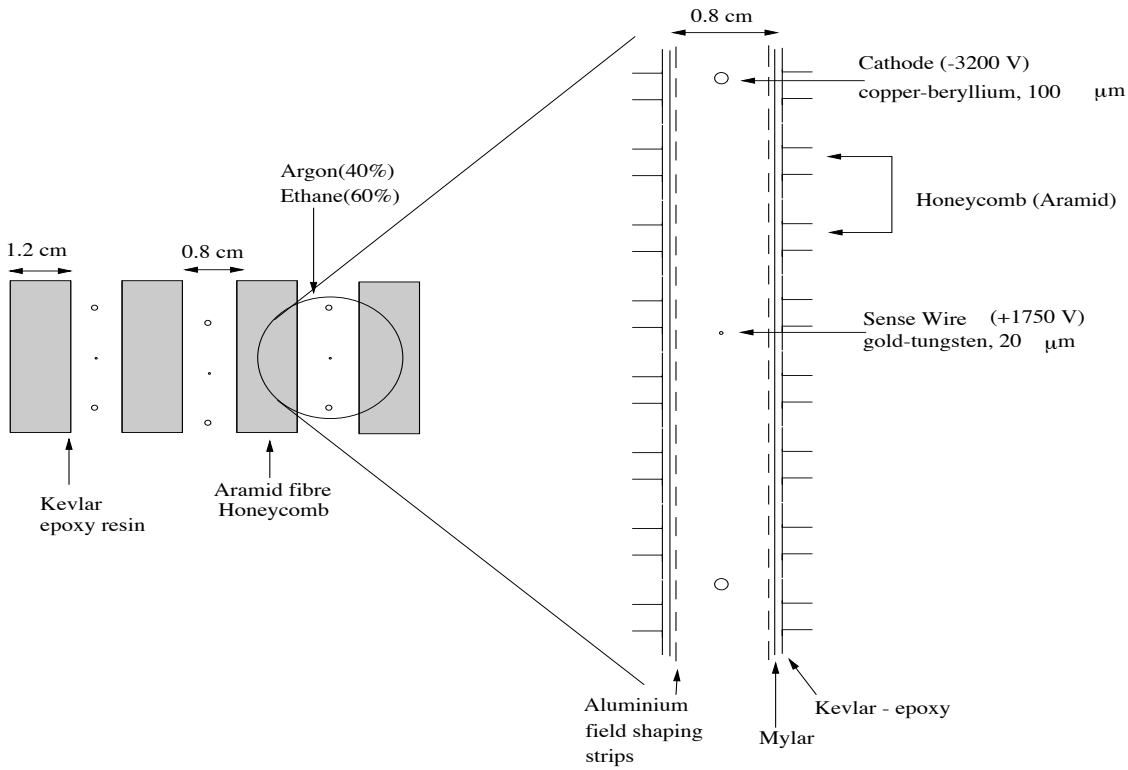

Figure 2.8: Schematic view of a drift chamber

of 1 kV/cm.

Four chambers are grouped into a module. To avoid left-right ambiguities in the reconstruction each pair of consecutive chambers are displaced vertically by 3.2 cm.

The position resolution of the chambers has been studied using a prototype chamber. The resolution parallel to the drift direction has been measured to be 180 μm. The point resolution along the wires is 1.5 mm.

The momentum resolution is a function of the particle momentum and track length. For charged hadrons and muons travelling normal to the measurement planes the resolution may be parametrised as :

$$\frac{\sigma_p}{p} \simeq \frac{0.05}{\sqrt{L}} \oplus \frac{0.007p}{\sqrt{L^5}} \tag{2.12}$$

where the momentum p has units of GeV/c, the track length L has units of m and the symbol $\oplus$ indicates addition in quadrature. The first term represents the contribution to the finite resolution from multiple scattering and the second term comes from the single hit resolution.

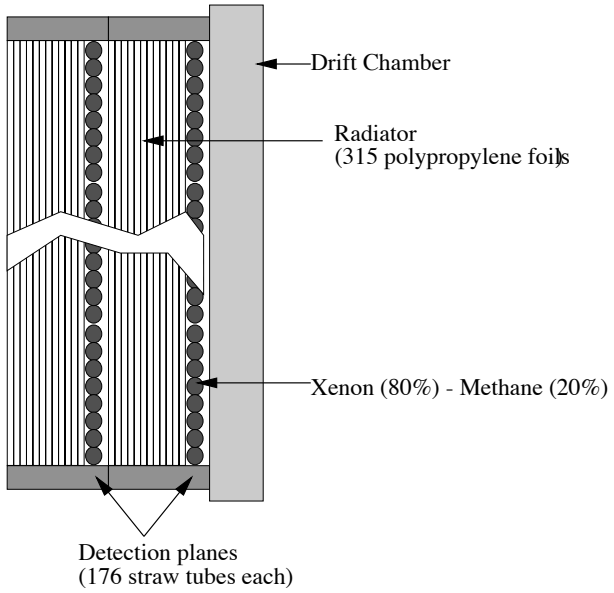

Figure 2.9: Top view of the TRD setup

2.6.5 The Transition Radiation Detector

One of the primary channels for the neutrino oscillation search is the decay of the τ^- to an electron, $\tau^- \to e^- + \overline{\nu_e} + \nu_\tau$. In order to eliminate neutral current background events in which an isolated pion simulates an electron, a pion rejection factor of at least 10^5 is required.

The transition radiation detector (TRD) has been designed to identify electrons with 90% efficiency while providing a pion rejection factor of 10^3 in a momentum range of 1 to 50 GeV/c [17, 15]. In conjunction with the electromagnetic calorimeter and the preshower detector a total rejection factor of 10^5 against pions can be achieved.

Transition radiation (TR) is produced by charged particles crossing boundaries between media of different electron densities [19, 20]. The number of X-ray TR photons produced at an interface is proportional to the Lorentz factor $\gamma = \frac{E}{m}$. The number of photons produced at one boundary crossing is small so a large number of radiators, providing many interfaces, is used.

The TRD has an active area of 2.85×2.85 m^2, making it one of the largest transition radiation detectors ever built. It consists of 9 identical modules, each of which includes a radiator followed by a detection plane. The first 8 TRD modules are grouped into 4 doublets, each separated by a drift chamber to allow track measurements up to the calorimeter.

The design of a TRD module is as follows (Figure 2.9)

- **Radiator foils:** The radiator module contains 315 polypropylene foils. Each foil is 15 μm thick and has an active area of 2.85×2.85 m^2 . The foils are separated by 250 μm wide gaps filled with nitrogen.

- **The detection plane:** A transition radiation detection plane is placed after each foil module. Each plane consists of 176 vertical straw tubes, each 3 metres long , 16 mm in diameter and fed with a 80%-20% xenon-methane mixture. The tubes themselves are constructed from 28 μm thick aluminized mylar. The sense wire of each straw is a gold plated tungsten wire with a diameter of 50 μm.

Calibration and monitoring of the TRD is extensive. The absolute calibration is based on the measurement of energy deposited by 5.89 keV X-rays emitted by ^{55}Fe sources. Tapes soaked in an ^{55}Fe sulphate solution are stretched horizontally across each straw planes allowing for continual monitoring of the tube response at the middle point of the tube. Variations in response along the tube length are measured and corrected for using muons.

2.6.6 The Trigger

Neutrino interactions in NOMAD are selected using two trigger planes. The first plane directly follows the drift chamber volume and the second plane is positioned behind the TRD region. The planes have an active area of 280×286 cm^2 and consist of 32 scintillation counters with single-ended photomultiplier readout. Each scintillator has a thickness of 0.5 cm and a width of 19.9 cm. Twenty-eight of these are installed horizontally and have a length of 124 cm and four, with a length of 130 cm, are installed vertically at the sides of the detector.

The photomultipliers used are the so-called "proximity-mesh" Hamamatsu type R2490. These tubes are relatively insensitive to magnetic fields along the tube axis. Measurements have shown that, at the nominal magnetic field in NOMAD (0.4 T), the loss of signal due to the magnetic field is at most 30%. The photomultiplier signals from each plane are fed to a discriminator and then into a logical OR. A coincidence between the logic signals for each plane is required for a valid trigger.

The average single particle efficiency of the trigger has been determined to be (93.5 ± 0.1%). For those neutrino events in which the charged track multiplicity is at least two, the trigger efficiency increases to more than 99.6%[14].

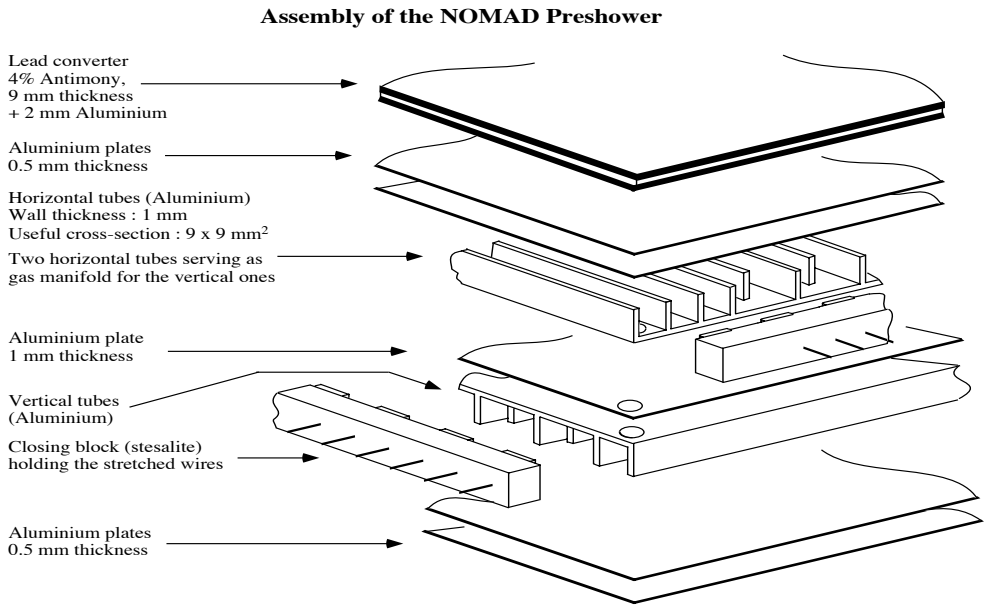

Figure 2.10: An exploded view of the Preshower

2.6.7 The Preshower Detector

The preshower detector (PRS) is positioned directly in front of the electromagnetic calorimeter. Two 9.0 mm thick lead-antimony sheets separated by a 2.0 mm thick aluminium plate serve as a converter, 1.6 radiation lengths deep, which initiates electromagnetic showers from incident electrons and photons. Following this converter are two planes of proportional tubes (286 horizontal and 288 vertical) which have a square cross-section of 9×9 mm^2 and 1 mm thick walls. The tubes have gold-plated tungsten wires and operate in a gas mixture of Ar (80%) - CO_2 (20%) at 1500 V. The signals from the proportional tubes are sent to charge sensitive ADCs via Delaying and Pulse Shaping Amplifiers (DPSA). An exploded view of the preshower is shown in Figure 2.10.

As well as initiating the electromagnetic shower, the preshower may be used in conjunction with the TRD and the electromagnetic calorimeter to enhance the pion rejection factor. The preshower also aids in the resolution of overlapping energy clusters in the electromagnetic calorimeter.

2.6.8 The Electromagnetic Calorimeter

The electromagnetic calorimeter (ECAL) was designed with two main functions in mind :

- To measure the energy, position and direction of electromagnetic showers with high precision.
- To aid, in conjunction with the TRD and the PRS, in the identification of electrons.

The high precision requirements dictate a calorimeter with excellent resolution and a uniform response over a large range of energies. With this in mind the NOMAD collaboration has chosen a calorimeter constructed from lead glass.

The ECAL consists of 875 lead-glass Čerenkov counters. Each block is 19 radiation lengths deep and has a rectangular cross-section of 79×122 mm^2. The blocks are arranged in a matrix of 35×25 counters oriented parallel to the longitudinal (Z) axis of the detector. The light from the counters is collected by four-stage Hamamatsu photomultipliers (phototetrodes) of type R2186.

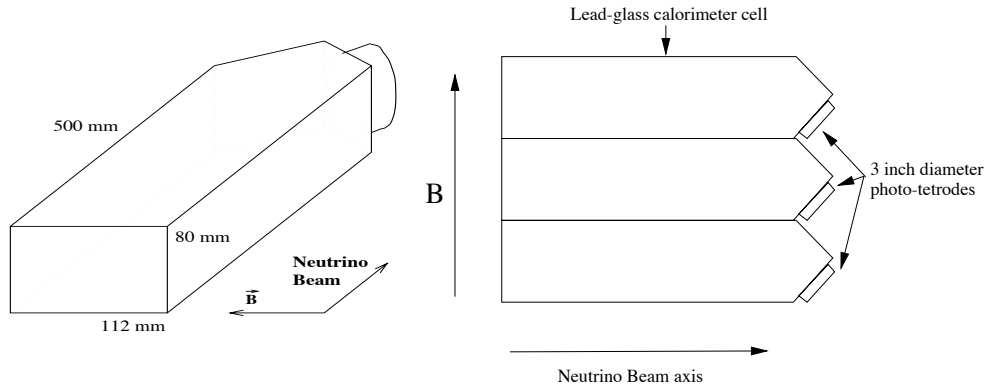

Figure 2.11: (left) Perspective view of one lead-glass counter and (right) vertical view of a lead-glass module.

In order to minimise signal losses due to operations inside the NOMAD magnetic field, the tetrodes are coupled to the lead-glass blocks with their axis at an angle of 45° with respect to the field axis (see Figure 2.11). This geometry reduces the collected signal by 20%. The signal from each phototetrode is amplified and shaped in a low noise electronic chain[24].

A time measurement via a fast signal is provided in order to reject energy depositions that are not correlated with the event trigger and for use of the ECAL as part of a trigger. The time resolution is on the order of a few nanoseconds.

Constant monitoring of the response of each block is carried out using two blue LEDs. The LEDs are driven by current pulses of high stability providing

a constant reference signal[23]. A further check is made by monitoring the response of each block to straight through muons which deposit an almost constant amount of energy in the lead-glass.

Each lead-glass block has been calibrated in a test beam of 10 GeV electrons. Corrections to the calibration for magnetic field effects in NOMAD have been calculated using LED measurements with the field on and off.

The linearity of the ECAL response to electrons of energies between 1.5-80 GeV has been studied. Deviations from linearity are less than 1.5%. The energy resolution of the ECAL for electrons has been measured and is parametrised by

$$\frac{\sigma_E}{E} \simeq \frac{(3.22 \pm 0.07)\%}{\sqrt{E(GeV)}} \oplus (1.04 \pm 0.01)\%$$

where the first term represents the error due to shower fluctuations and the second term describes losses in the detector.

2.6.9 The Hadronic Calorimeter

The hadron calorimeter (HCAL) is an iron-scintillator sampling calorimeter. Like the FCAL it consists of scintillators inserted into gaps in the back part of the magnet support. The function of the HCAL is :

- to detect and measure the energy and position of neutral hadrons
- to act as a consistency check on the momentum measurement of charged hadrons and to aid in distinguishing between muons and charged hadrons.

The iron pillars consist of 23 4.9 mm thick iron plates separated by 1.8 mm of air. The first 12 gaps have been instrumented. The active volume of the HCAL provides an effective depth of 3.1 hadronic interaction lengths. The scintillators are slabs 360 cm long, 18.3 cm wide and 1.5 cm thick. Adiabatic light guides are glued to the ends of each scintillator which serve to channel the scintillation light into 5 cm photomultiplier tubes at either end of the calorimeter module (Figure 2.12). In order to accommodate the basket support elements three horizontal gaps have been left uninstrumented and several small notches have been cut into two of the central modules.

The signal from each phototube is split in two. One signal is sent to a charge-integrating ADC and the other is sent to a TDC. The ADC signals are used for energy and position measurements while the TDC signals are used to time the event. The horizontal position measurement in each module is determined by signal-sharing between phototubes at either end of a module.

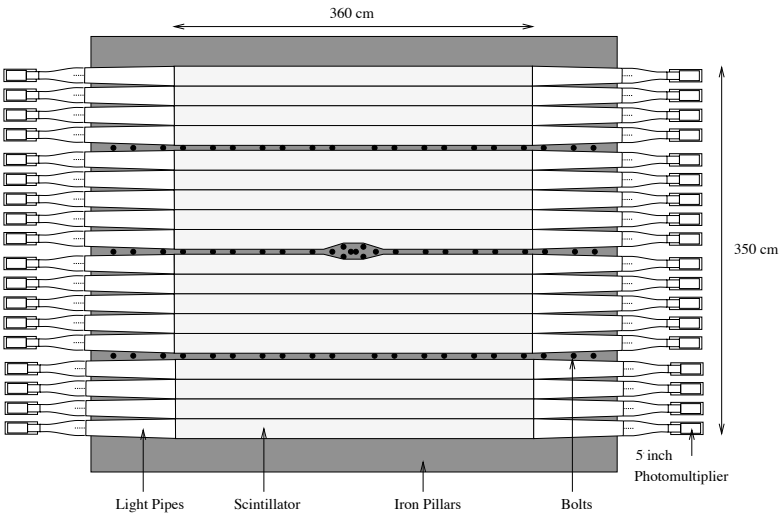

Figure 2.12: Front view of the HCAL

Typical horizontal position resolutions of 20 cm have been measured using the difference between the position predicted by the HCAL and the extrapolated impact position of the muon in single muon events. Vertical positions are determined from the pattern of energy sharing between modules.

The energy resolution of the HCAL is approximately $120\%/\sqrt{E(GeV)}$.

2.6.10 The Muon Detector

The muon detector consists of 10 drift chambers as shown in Figure 2.7, each with an active area of 375×555 cm. The chambers consist of 48 vertical and 78 horizontal drift cells which are 14.9 cm wide and 4.4 cm deep providing for reconstruction of both the x and y co-ordinate of through-going particles. Each cell has a single 50 μm stainless steel wire in the centre. Field shaping cathodes at the sides of each cell ensure a constant drift velocity of 52 $\mu m/ns$ over the width of the tube. The drift cells are positioned in two layers and each layer is displaced by half a cell in order to help resolve left-right ambiguities. The chambers are grouped into two stations. Station 1 has three modules and is in front of an 80 cm thick iron wall that acts as a hadron absorber. Station 2 has two modules and is positioned behind the wall. Each module is constructed from two chambers. Modules 1 and 2, and modules 3 and 4 are interleaved. Module 5 is positioned above Modules 1 and 2. The geometry is displayed in Figure 2.13. The position resolution is about 430 μm for a track crossing at 0°. The average hit efficiency is 92.5% where the dominant source of the inefficiency is due to dead areas between

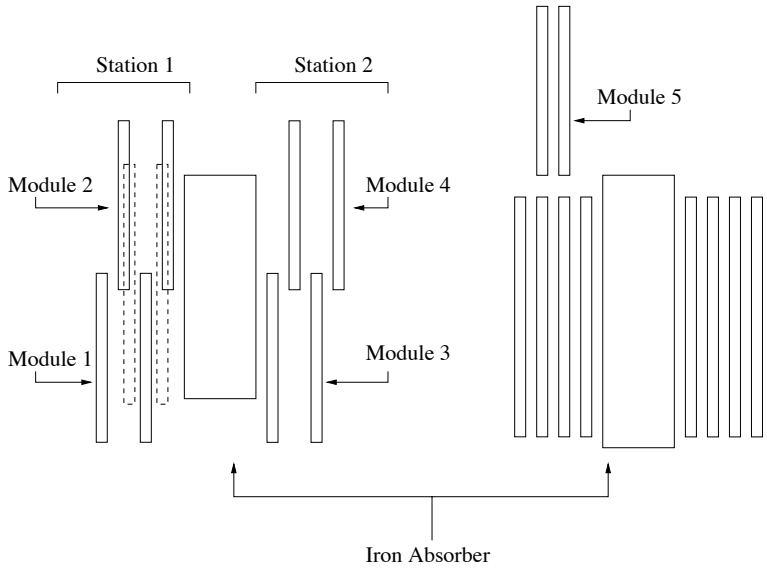

Figure 2.13: Geometric layout of the muon chambers. The left figure is the view from above showing the interleaved chambers. The right figure is the horizontal view showing the position of module 5.

the tubes. A small gap between the muon chambers in station 1 was closed by the addition of two scintillators in late 1995.

2.7 Data recording and handling

2.7.1 Data acquisition

Analog signals from each of the subdetectors are digitised in FASTBUS modules. Three types of modules are used, depending on the specific needs of each subdetector : 12-bit charge-integrating ADCs, 12-bit peak-sensing ADCs and 16-bit TDCs. The ADCs were designed at CERN and have 64 channels with a 256 event memory. The TDCs are Lecroy 1876 Model 100 and have 96 channels, a 64 channel buffer and a time resolution of 1 ns.

Readout of the front-end electronics is handled by 5 VME-based boards (FIC 8234) with Motorola 68040 processors. These boards control block transfer of data, check data integrity and format the data into subevents. These subevents are then transferred to the event builder, another VME processor, which assembles the subdetector data into complete event structures and writes them to one of two 9 GB disks. Several times a day the data stored on these disks is automatically transferred to the CERN tape

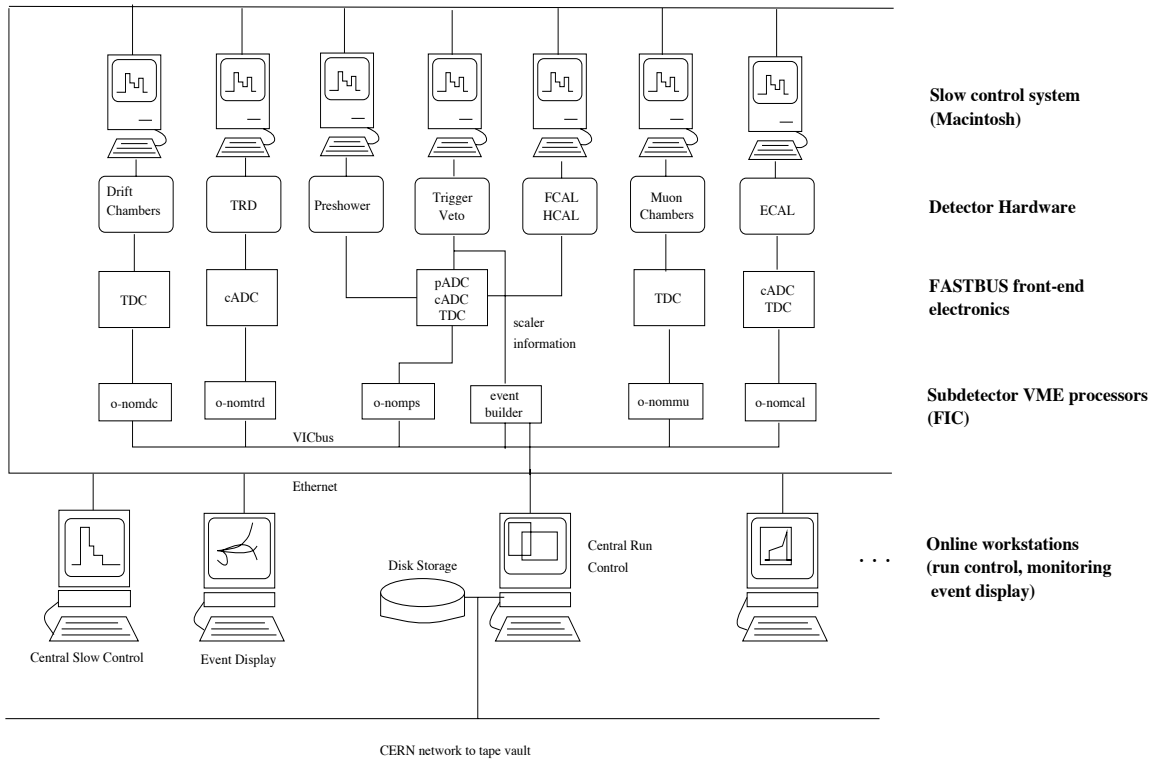

Figure 2.14: Hardware layout of the NOMAD Data acquisition system.

vault for storage on tape. A schematic of the NOMAD DAQ is presented in Figure 2.14.

The data acquisition software is based around a CERN designed package called CASCADE. Each FIC is assigned a process referred to as a *stage*. The associated software handles scheduling and provides event access tools for each FIC.

Monitoring programs for each of the nine subdetectors, as well as for the event builder and scalers, generate summary histograms over the length of a run. These are used to check data integrity and quality. An online reconstruction program processes the muons received during the SPS muon flat-top for calibration and monitoring purposes.

The performance of the various detectors is monitored by the slow control system. This is a set of Apple Macintosh computers running the graphical language LabVIEW [22]. These computers monitor all high and low voltages, gas systems and temperatures in the experiment and pass the information to a SUN workstation which generates alarms when required. Alarms are recorded on disk for later offline use.

2.7.2 Triggering

The NOMAD event selection system must be able to take a range of triggers formed from different parts of the detector and from both the neutrino and muon gates. In order to adequately control this the trigger has been implemented in a VME based module called MOTRINO (MOdular TRIgger for NOmad). This module is capable of the following tasks :

- Generation of the time signals to synchronise data taking with the SPS machine cycle.
- Handling the generation of trigger signals from up to eight input signals. There is one module devoted to producing different triggers in the neutrino spills and one which generates trigger signals in the muon gate for calibration purposes.
- Distribution of the trigger signals to the different FICs.
- Storage of the trigger time information relative to the start time of the SPS cycle.
- Determination of the live time of each of the triggers.
- Application of artificial dead-times to high rate triggers (such as the flat top muon events).

Trigger Signal Components	
$\mathbf{T_1}$	First trigger plane signal
$\mathbf{T_2}$	Second trigger plane signal
$\mathbf{V_8}$	Signal from a subset of the veto planes attached to the FCAL
FCAL	FCAL signal
FCAL′	Signal from FCAL at a lower discriminator threshold
ECAL	Electromagnetic calorimeter
V	Veto signal

Table 2.3: Individual signals which are used to generate NOMAD triggers.

The following triggers are implemented in NOMAD during the neutrino gates. The trigger signal components are described in Table 2.3. :

- $\overline{\mathbf{V}} \times \mathbf{T_1} \times \mathbf{T_2}$: This is the primary neutrino interaction trigger. In order to fulfill the trigger conditions one charged particle must cross both the trigger planes and there must be no signal from the veto planes. The rate of this trigger is approximately $5.0/10^{13}$ p.o.t.. Of these only about 0.5 triggers are actual neutrino interactions. The rest are cosmic ray interactions (~ 1), non-vetoed muons (~ 1.5) and interactions in the magnet coil and flux returns (~ 2.0).

- $\overline{\mathbf{V_8}} \times \mathbf{FCAL}$: This trigger is designed to study deep inelastic neutrino interactions in the FCAL. Through-going muons are suppressed by the signal $\overline{V_8}$. The rate of this trigger is $\sim 6.5/10^{13}$ p.o.t. with very little noise. The fraction of the data-taking cycle during which data may be taken with this trigger (the "livetime") is $(90 \pm 3)\%$.

- $\overline{\mathbf{V_8}} \times \mathbf{FCAL'} \times \mathbf{T_1} \times \mathbf{T_2}$: Quasielastic neutrino scattering events provide a relative flux measurement of the neutrino beam as a function of neutrino energy. The muon from these interactions in required via the trigger subset of $T_1 \times T_2$. The rate of this trigger is $\sim 1.0/10^{13}$ p.o.t. and the livetime is $(90 \pm 3)\%$.

- $\overline{\mathbf{T_1} \times \mathbf{T_2}} \times \mathbf{ECAL}, \overline{\mathbf{V_8}} \times \mathbf{ECAL}$: The ECAL is also used as a target. Physics topics such as $\nu_\mu \to \nu_e$ oscillations may be addressed using this trigger. Beam muons are vetoed by $T_1 \times T_2$ or by V_8 in anticoincidence with the ECAL signal[4].

- **RANDOM** : A random trigger had been set up to study detector occupancy and to estimate the probability of event overlaps. This trigger records detector activity 22 μs after a given SPS cycle.

Various triggers are also set up in the muon spill. These are :

- $\mathbf{V} \times \mathbf{T_1} \times \mathbf{T_2}$: This trigger tags flat-top muons. It is the basic trigger used for drift chamber alignment and subdetector calibration with minimum ionizing particles.

- $\mathbf{V_8} \times \mathbf{T_2}$: With this trigger the efficiency of T_1 may be measured.

- $\mathbf{V_8} \times \mathbf{T_1}$: This trigger aids in the measurement of the efficiency of T_2.

[4]At the beginning of the 1995 datataking period and during 1996 the $\overline{T_1 \times T_2}$ signal was used. For the largest part of the 1995 dataking period, however, the $\overline{V}$ signal was used.

- $\mathbf{V_8 \times T_1 \times T_2 \times FCAL'}$: The muons in the muon spill enter the detector at an angle of several degrees to the normal of the upstream face of NOMAD. Some parts of NOMAD are not mapped by this beam. This trigger was implemented to enhance the sample of muons crossing these regions and to provide muons for the calibration of the FCAL.

- $\mathbf{V \times T_1 \times T_2 \times ECAL}$: This trigger combination is used to study electrons in NOMAD. Electrons from delta rays are used to calibrate the TRD and to provide a clean sample for the study of electron behaviour in NOMAD.

In total 60 muon triggers are taken in every muon spill. Of these, 20 are written to tape.

2.8 The NOMAD Software Environment

The analysis of data from high energy physics experiments relies heavily on the simulation of physics processes using Monte Carlo methods. Such simulations are often the only method of estimating the efficiencies of event selection algorithms and the effect on event distributions of detector acceptances. In the NOMAD software the simulation of neutrino interactions proceeds along the following lines :

1. the simulation of the neutrino beam.

2. the generation of neutrino interactions.

3. the simulation of the detector response to these interactions.

2.8.1 Beam Simulation

The geometry of the WANF neutrino beam line has been described in Section 2.4. A full Monte Carlo simulation of this beam line and the processes leading to the generation of neutrinos has been implemented in NUBEAM, the NOMAD neutrino beam simulation. Within NUBEAM the proton-beryllium collisions and subsequent hadronic interactions are simulated using the FLUKA package[40] and the subsequent transport of the secondary particle down the beamline is carried out using the GEANT[42] package.

2.8.2 Neutrino Event Generation

The generation of neutrino interactions in NOMAD is handled by the NOMAD Event Generator LIBrary (NEGLIB)[43]. This is a set of packages which handle the various stages of event generation, from the hard scattering at the quark level to the fragmentation of the partons in the hadronic shower. The kinematics of deep inelastic neutrino-nucleon scattering is simulated by the LEPTO 6.1[44] package. This code is based on leading order electroweak cross sections with options for higher order processes such as boson-gluon fusion. The fragmentation of produced partons into hadrons is performed by the JETSET[45] package. NOMAD uses only the leading order options with the default parton distribution set of GRV-HO[55] in the PDFLIB package[46].

In the case of ν_τ^{CC} interactions, τ decays are simulated using the KORALZ[47] package containing the tau decay code TAUOLA[48].

2.8.3 Detector Simulation

The final stage in the generation of Monte Carlo neutrino interactions is the simulation of the detector response to the particles in the event. The NOMAD detector simulation is based on GEANT[42]. GENOM[49] (GEant NOMad library) contains a detailed description of NOMAD geometry and is used to track particles through the detector and to record the response of each subdetector to these particles. Events that have been passed though GENOM are then reconstructed in the same way as the data.

2.8.4 Event Reconstruction

The reconstruction of Monte Carlo and data events proceeds in two stages. The first stage, Phase 1, performs the reconstruction of raw data from each subdetector using the general reconstruction program RECON[50]. The second step, Phase 2, combines the information from the various detectors in order to identify the particles involved in the interaction. The output from Phase 2 is stored in a compressed DST[51] (Date Summary Tape) format for use in later analyses. A list of the versions for each subdetector reconstruction code used in this analysis can be found in Appendix A.

Chapter 3

The Front Calorimeter

3.1 Introduction

In Chapter 2 the Front Calorimeter [28] of the NOMAD experiment was introduced. This chapter expands on that introduction. The motivation for the construction of the Front Calorimeter (FCAL) is outlined followed by a description of the physical components of the FCAL. Methods for energy and vertex reconstruction are then discussed, with particular emphasis on the energy calibration.

3.2 Motivation for the construction of the FCAL

NOMAD was designed to search for evidence of neutrino flavour oscillations. The detector may, however, also be used to investigate other topics of interest in neutrino physics. As mentioned in Chapter 2 the upstream part of the NOMAD support structure has been instrumented to form an iron-scintillator sampling calorimeter. The heavy target and high neutrino flux available from the WANF permits several physics processes to be studied :

- **Opposite-Sign Dimuons** The cleanest signal of charm production is the emission of two oppositely charged muons in neutrino charged-current interactions. This process has been already discussed in Chapter 1 and will be considered further in Chapter 5.

- **Like-sign Dimuons**

  Events with two muons of the same electric charge are expected to arise from π^-/K^-decay or from processes involving $\bar{c}$ quark production. It is conceivable that such events may also indicate an intrinsic charm component in the nucleon wave function.

The CCFR collaboration has studied these events, finding a small excess of events [26]. The expected number of these events in FCAL is approximately 2000, an order of magnitude larger than has been obtained to date.

- **Trident production**

  The trident production process is shown in Figure 3.1. A neutrino elastically scatters off the electric field of a nucleus. The resulting W or Z^0 decays to the muonic channel and the decay products are brought onto the mass-shell by the exchange of a virtual photon with the nucleon field. The interference between the two processes leads to a reduction of the overall cross section by approximately 40%. Observation of this process is a direct test of the validity of the Standard Model.

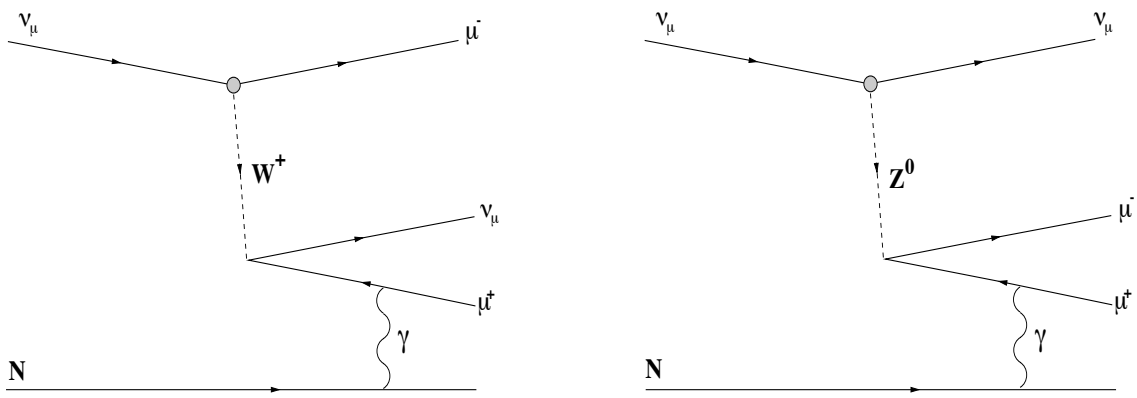

Figure 3.1: Neutrino trident production processes.

Trident events were first observed by the Charm II collaboration[27], and then by the CCFR collaboration[25] who reported the observation of destructive interference between the charged current and neutral current processes. NOMAD has the capacity to increase the available event sample size by an order of magnitude.

- **Neutral Heavy Lepton Search**

  The existence of neutral heavy leptons coupling with standard model neutrinos are predicted in many extensions of the Standard Model. The production rate of such particles is determined by their mass, $M_{\mathcal{N}}$, and the strength of their coupling to the light neutrinos, $|U|^2$. A search for decays of neutral particles in the NOMAD detector which are correlated with neutrino interactions in the FCAL would yield a sensitivity in the parameter space ($M_{\mathcal{N}}$,$|U|^2$) which has not been experimentally investigated, as shown in Figure 3.2[28]

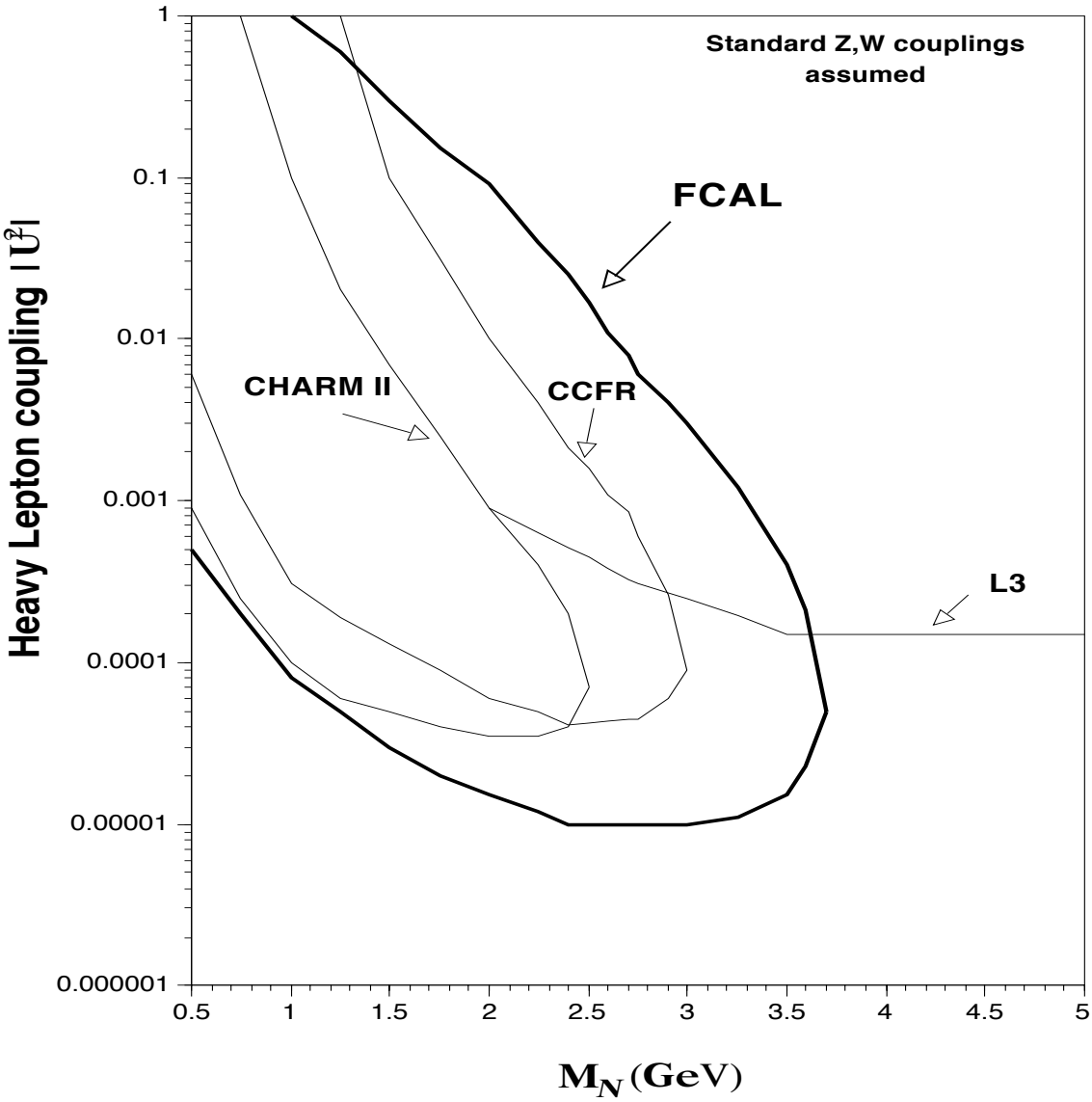

Figure 3.2: Neutral heavy lepton sensitivity region in the two dimensional phase space ($M_{\mathcal{N}}$,$|U|^2$). The projected limits using the FCAL is shown[28].

3.3 Description of the FCAL

3.3.1 The Front I

The FCAL occupies the central region of the front part of the NOMAD magnet support pillar (the "front I"). The I consists of 23 iron plates, each having a thickness of 4.9 cm. Each plate is separated from its neighbour by a 1.8 cm wide air gap.

The first 20 gaps (as measured from the most upstream plate) are instrumented with slabs of plastic scintillator. The last three gaps and a 4.4 cm wide strip at the centre of the FCAL are not instrumented as they are occupied by structural elements of the I. The mass of the total instrumented region of the FCAL is 17.7 t.

The FCAL is divided into four "stacks" aligned along the beam direction. Each stack is composed of ten horizontal modules placed on top of one another as shown in Figure 3.3. To ensure optimal light collection efficiency each module is formed from five adjacent scintillators which are grouped together onto a single photomultiplier by means of antlered light guides. Top and front views of the FCAL geometry are shown in Figure 3.4.

The stacks are numbered from 1 to 4 starting at the most upstream stack. The modules within each stack are numbered from 0 to 9 beginning at the bottom module. Each photomultiplier is labelled, within the module, by 1 (Left) and 2 (Right) if looking from the direction of the beam. Any module has a unique label based on the formula:

$$\text{Module} = 100 \times \text{Stack} + 10 \times (\text{Module number within the stack}) \tag{3.1}$$

3.3.2 FCAL Scintillators

The FCAL uses plastic scintillators of type NE102A. The scintillator specifications are presented in Table 3.1.

The attenuation length of each scintillator was measured using an ultraviolet light source and three pin diode detectors. Details of this procedure can be found in [29]. Figure 3.5 shows the response of one scintillator at different positions along the slab [28]. Superimposed on this plot is a fit of the data to an exponential curve. The good fit justifies the assumption of exponential light attenuation.

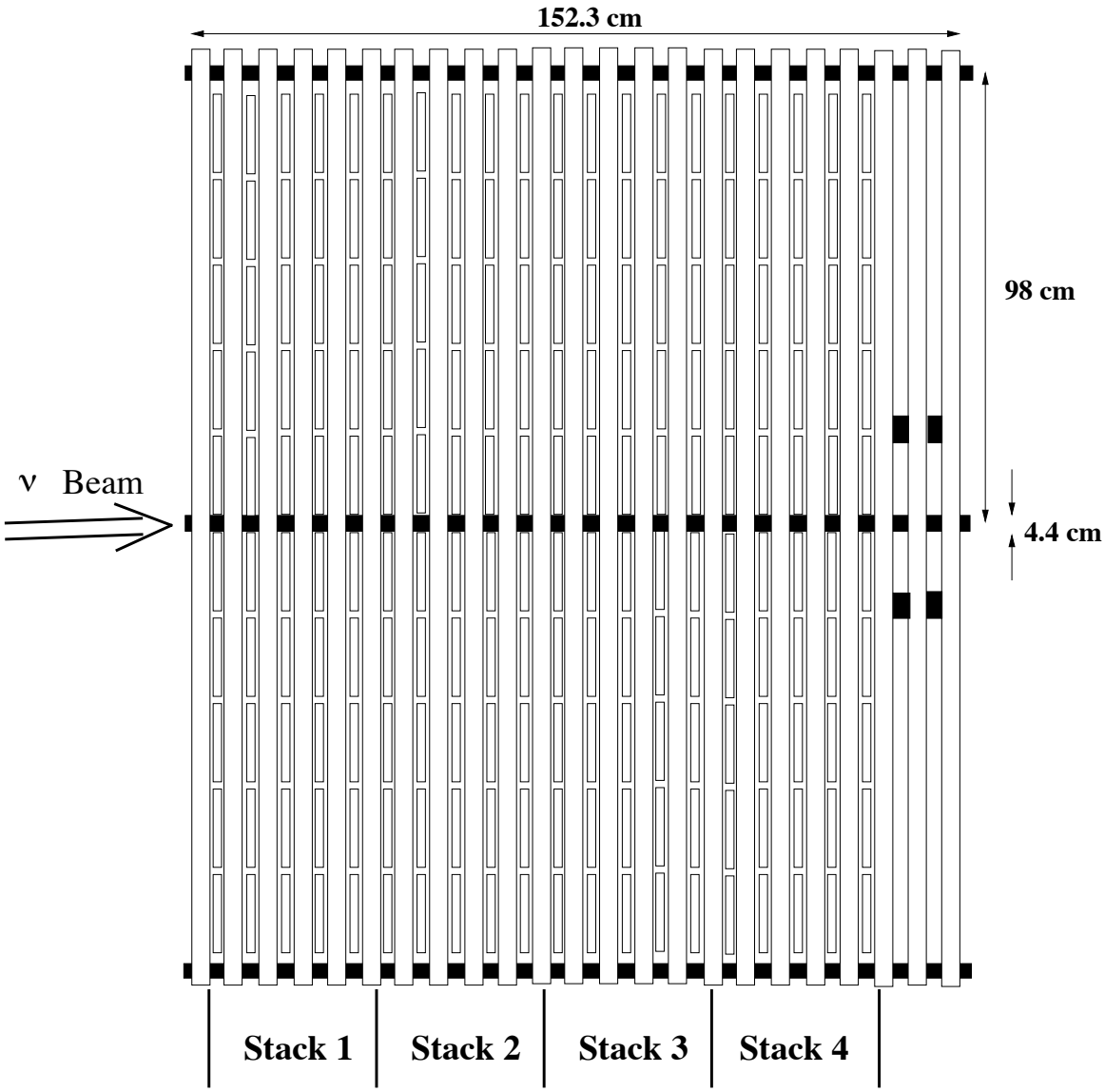

Figure 3.3: View of the FCAL from the side. The neutrino beam comes in from the left of the diagram.

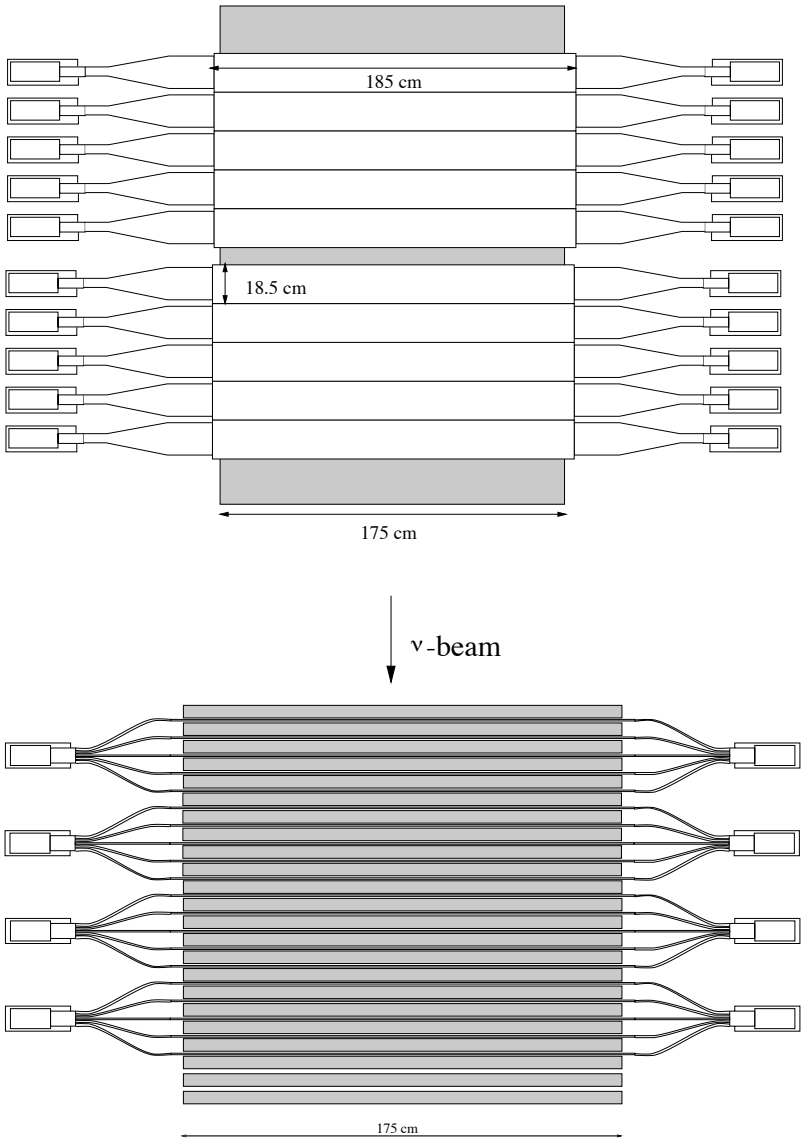

Figure 3.4: View of the FCAL (top) looking along the direction of the neutrino beam and (bottom) from the top. The direction of the neutrino beam is into the page in the top figure and down the page in the bottom figure.

Type of scintillator	NE102A
Length of scintillator	175 cm
Width of scintillator	18.5 cm
Thickness of scintillator	0.6 cm
Wavelength of maximum emission	423 nm
Density	1.032 gcm^{-3}
Refractive Index	1.580
Attenuation Length	$\simeq$ 150 cm

Table 3.1: Specifications of the FCAL scintillators.

Type of Photomultiplier	SRC GT75B01
Diameter of Phototube	7.6 cm (3 inches)
Diameter of Photocathode	6.6 cm (2.6 inches)
Cathode material	semi-tranparent Cs-K-Sb
Wavelength of max. response	(400 ± 50) nm
Quantum Efficiency	22%
Number of Dynode stages	10
Maximum Supply Voltage	2.25 kV
Current Amplification at 1.5 kV DC	4.5×10^5

Table 3.2: Specifications of FCAL photomultipliers.

3.3.3 FCAL Photomultipliers

Each module is read out on both sides by 3 inch SRC GT75B01 photomultipliers. Table 3.2 shows the specifications of the photomultiplier tubes. In order to lessen the effect of attenuation in the scintillators a yellow Kodak-Wratten 2E gelatine filter was glued to each photomultiplier. The function of the filter was to shift the wavelength of maximum response closer to that of the photodiodes used to measure the attenuation lengths of the scintillators. The absolute gain of each photomultiplier was determined by studying the pulse height spectra for different input supply voltages.

3.3.4 Readout Electronics

The schematics of the readout electronics are shown in Figure 3.6. Signals from the photomultipliers are amplified and divided into three different channels by custom-designed active pulse splitters. The pulse splitters are described in detail in [29].

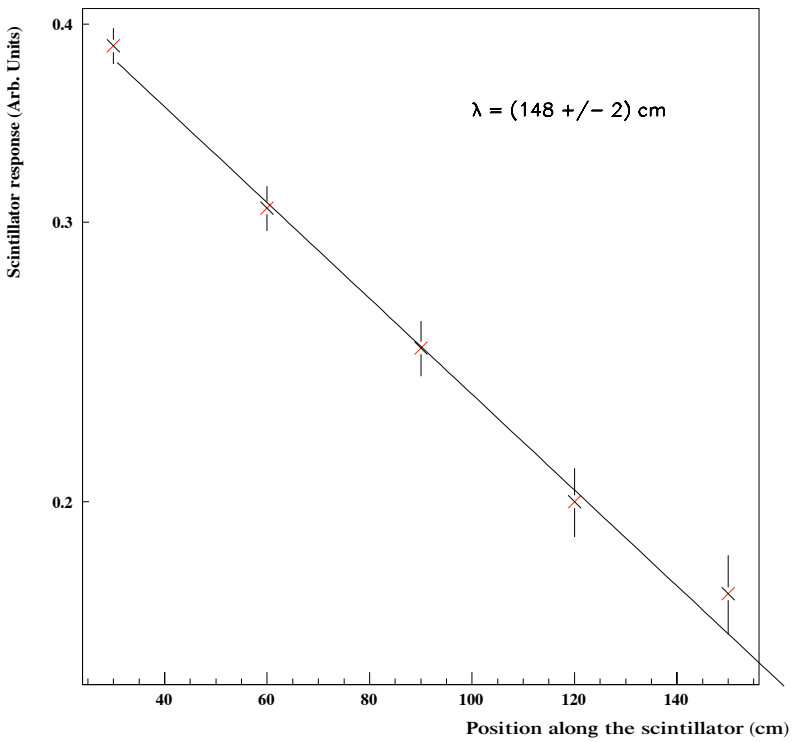

Figure 3.5: Attenuation behaviour for a typical FCAL scintillator. The scintillator response is shown on a log scale.

- **Energy measurement**

  The first channel is used for energy measurement. The signals from this channel, labelled "Delay out" in Figure 3.6, are delayed by passive analog delay lines of type SECRE DPI S14 in order to be in time with the main NOMAD trigger, which arrives 400 ns after the interaction has occurred. The delay lines conserve the total charge of the pulse but distort the pulse shape. This is not a problem as only the integrated charge is required for energy measurements. The signals are recorded by charge-integrating ADCs with 100 ns gate width and 12 bit dynamic range.

- **Time measurement**

  The second channel, labelled "Out" is used for time measurements. This channel is discriminated by standard LeCroy CAMAC Type 4413 discriminators with a low threshold of 15 mV. The discriminated signal is sent to TDC modules (LeCroy type 1876 Model 100).

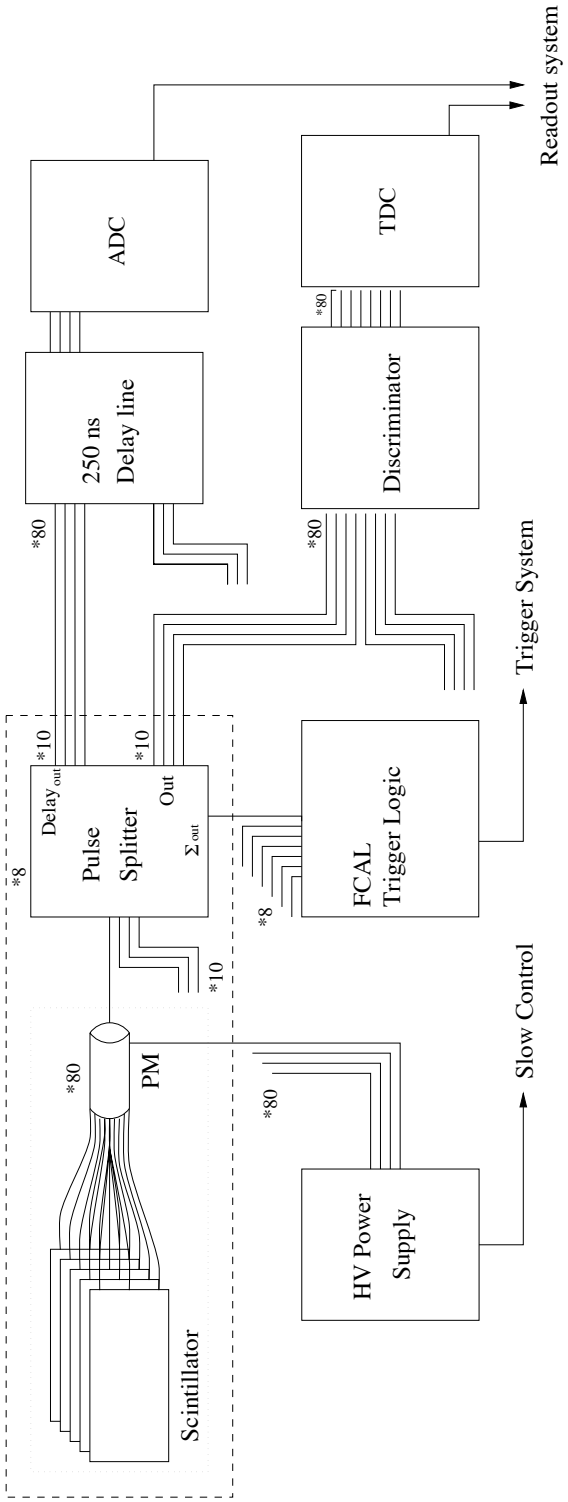

Figure 3.6: Schematic of the FCAL readout system.

- **Trigger Formation**

  The final channel, "Σ Out", is used to form the FCAL trigger. The signals from the photomultipliers in each stack and on each side are summed to form two signals per stack; one from the left hand photomultipliers, F_i^L, and one from the right hand photomultipliers, F_i^R, for stack i. A linear fan-in sums these signals to form one analog output F_i for each stack. The F_i are then discriminated at two different thresholds, corresponding to the two triggers FCAL and FCAL'. The FCAL part of the trigger signals themselves are formed from a logical OR of the four signals :

$$FCAL := (F_1 \vee F_2 \vee F_3 \vee F_4) \tag{3.2}$$

In order to resolve highly energetic hadronic showers as well as minimum ionising particles (hereafter referred to as "mips") a compromise in the gain of the ADCs was reached. Monte Carlo simulations of neutrino interactions in the FCAL showed that less than 1% of the modules see a deposited energy of greater than 70 mips. Assuming a hadronic energy equivalent of 0.5 GeV/mip the corresponding mip equivalent was chosed to be $\simeq$ 50 ADC counts.

3.4 Calibration Procedure

The FCAL is an intrinsic part of the structural elements of the NOMAD detector. Since there was no possibility of establishing a direct calibration using a test beam of known energy, a more complicated procedure had to be applied.

When charged particles pass through the FCAL they interact with molecules in the plastic scintillators, depositing a minimum ionizing energy which, to first order, does not depend on particle type or energy. Two quantities are needed, then, to measure the energy of a hadronic shower. The first is the amount of energy deposited by mips in each module in ADC counts. This measures the response of each module to the deposition of the same amount of energy. The second is the factor which converts energy measured in units of mips to units of GeV.

The results from Reference [29] have been used extensively in this section.

3.4.1 Relative Calibration

The first step in the calibration of the FCAL is to measure the relative response of each module to a constant energy deposition. An FCAL module

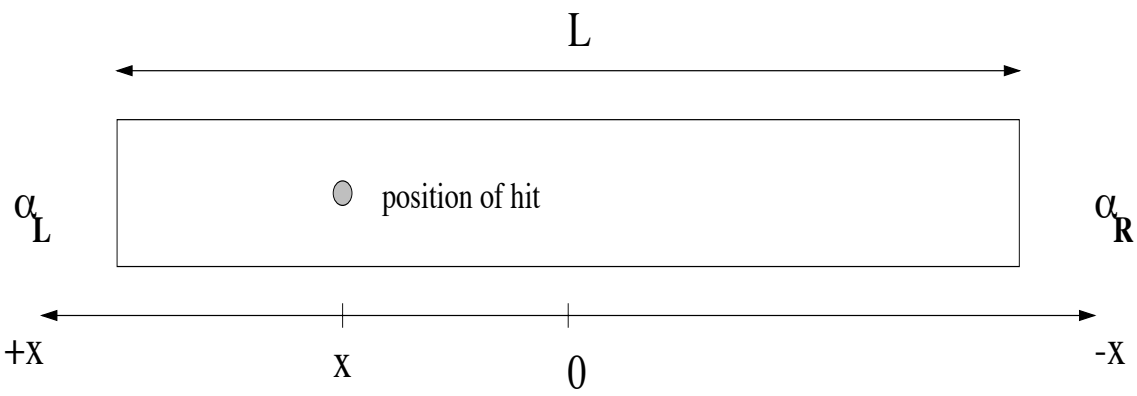

Figure 3.7: Parameters used in the relative calibration of the FCAL.

may be described by the attenuation length λ and the gains of the photomultipliers at each end of the module, α_L and α_R.

Suppose a particle deposits an energy E (GeV) in a module at a distance x (cm) from the center of a counter of length L (cm) (see Figure 3.7). Assuming an exponential light absorption in the scintillator, the number of ADC counts measured at each end of the module may be written as :

$$ADC_{Left} = \alpha_{Left} \cdot E \cdot exp\left(-\frac{L/2 - x}{\lambda}\right) \tag{3.3}$$

$$ADC_{Right} = \alpha_{Right} \cdot E \cdot exp\left(-\frac{L/2 + x}{\lambda}\right) \tag{3.4}$$

Defining the constants (for each pair of photomultipliers in a module[1]):

$$\alpha := \sqrt{\alpha_{Left} \cdot \alpha_{Right}} \cdot exp\left(-\frac{L}{2}\right) \tag{3.5}$$

$$\beta := \frac{\alpha_{Left}}{\alpha_{Right}} \tag{3.6}$$

it is useful to calculate the quantities

$$M := \sqrt{ADC_{Left} \cdot ADC_{Right}} = \alpha E \tag{3.7}$$

$$R := \frac{ADC_{Left}}{ADC_{Right}} = \beta exp\left(\frac{2x}{\lambda}\right) \tag{3.8}$$

[1]The scintillators in each module were chosen so that their attenuation lengths were similar. They are not identical, so that the left and right response factors, α_{Left} and α_{Right}, can in principle be different for each scintillator. The measured response factor is an average over the individual scintillator response.

The quantity M is independent of the position at which the particle hit the module and is the geometric mean of the pulse heights from the left and right photomultiplier at the end of each module. R is independent of the energy deposited in the module (although saturation of the ADCs will affect this quantity. This is discussed further in Section 3.4.4). Inverting these relations yields :

$$E = \frac{M}{\alpha} \tag{3.9}$$

$$x = \frac{\lambda}{2} exp\left(\frac{R}{\beta}\right) \tag{3.10}$$

Hence, if the energy deposited by the particles is constant (e.g. a mip equivalent) then it is possible to measure α (the gain) and, knowing the attenuation length, β (the asymmetry) of each module.

Measurement of the module gain

Highly energetic muons are a reasonable approximation to minimum ionising particles. Since the amount of energy deposited in the FCAL by these muons is relatively independent of the muon momentum, the study of these particles provides a direct measurement of the gain, α, for each module.

As described in Section 2.7.1 NOMAD collects events in the muon gate at the rate of $\simeq 20$ muons per SPS cycle. Those muons satisfying the trigger requirements of $V \times T_1 \times T_2$ or $V_8 \times T_1 \times T_2$ are used to calibrate the modules. Muon tracks are reconstructed in the drift chambers and the muon chambers using the NOMAD reconstruction program RECON [33]. The drift chamber tracks are extrapolated forward into the muon chambers. Only tracks which geometrically match muon chamber tracks, in both position and angle, are used for the calibration. These muons are then extrapolated back to the mid-stack position of the modules under investigation.

A typical distribution of the energy deposition is shown in Figure 3.8. The energy deposition profile is composed mainly of a Landau distribution with additional contributions from noise, muon bremsstrahlung and photoelectron smearing. One mip was defined to be the mode of the distribution of energy deposited in a module. In order to measure this parameter, the experimental distribution was fitted with a function, $\mathcal{L}$, which was a combination of :

1. a Landau function $\psi(X)$ which describes the energy deposition in a noise free environment.

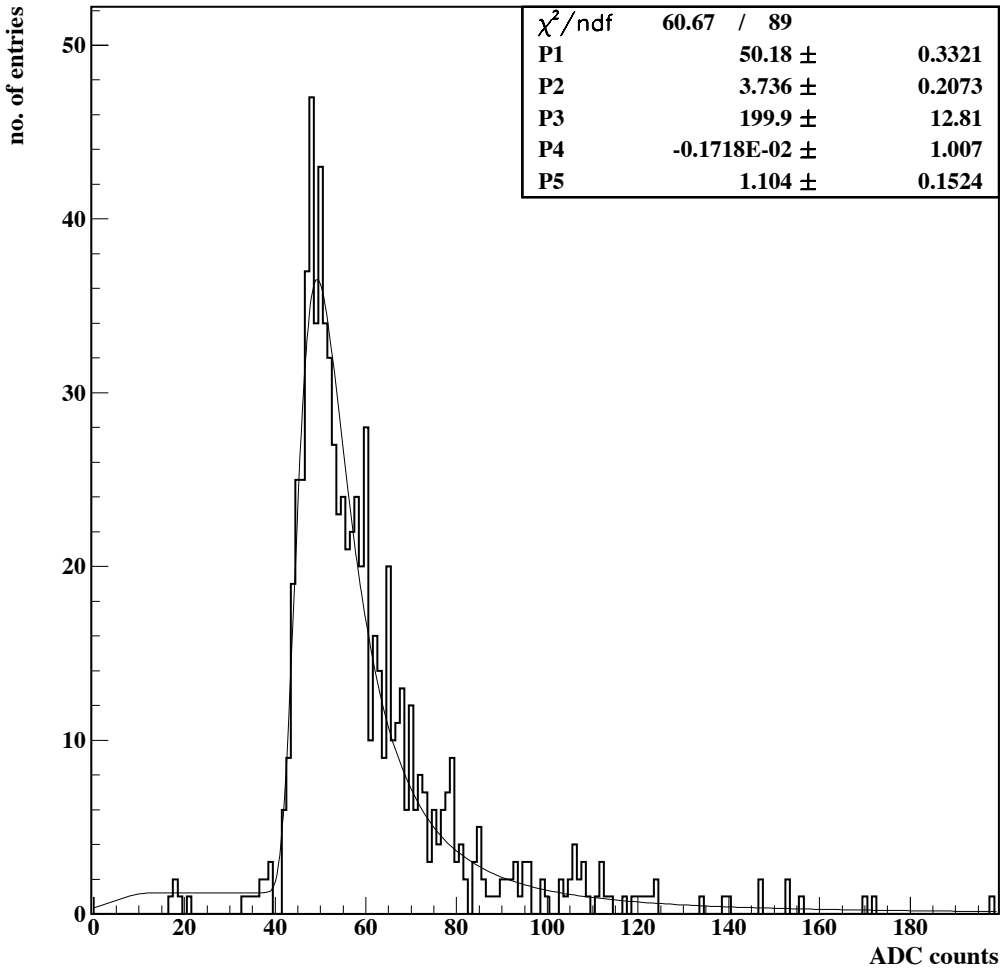

Figure 3.8: Typical energy deposition distribution for muons passing through a single FCAL module. The distribution has been fitted with the $\mathcal{L}$ function (described in the text).

2. a Gaussian distribution $\Phi(X)$ with width σ_g which describes the smearing due to noise processes such as fluctuations in the number of photoelectrons reaching the anode of the photomultiplier and

3. a background distribution $B(X)$

$\mathcal{L}$ is defined by :

$$\mathcal{L}(y) \;:=\; B\left(\frac{y}{p}\right) + h\int_{-3}^{3}\Phi(z)\,\psi\left(\frac{z+y-p}{\sigma_l}\right)dz \tag{3.11}$$

where the parameters are defined below.

The smearing function $\Phi(y)$ is defined by

$$\Phi(y) \;:=\; \frac{1}{\sigma_g\sqrt{2\pi}}exp\left(\frac{-y^2}{2\sigma_g^2}\right) \tag{3.12}$$

and the Landau distribution by[30]

$$\psi(y) \;:=\; \frac{1}{\pi}\int_0^{\infty} exp\left(-uln(u) - yu\right) sin(\pi u)du \tag{3.13}$$

In these equations the variable y represents the energy deposited in units of ADC counts.

The background distribution $B(y)$ is an empirically determined function which describes the low energy part of the distribution. The Landau distribution has essentially no low energy tail so any events which deposit a very low energy would distort the fit. The inclusion of the background function improves the stability of the fit in this low energy region. The function is defined by

$$B\left(\frac{y}{p}\right) := \begin{cases} b^2\cdot exp(-\frac{((y/p)-0.25)^2}{2\cdot(0.16)^2}) & y < 0.25 \\ b^2 & 0.25 \leq y < 0.75 \\ b^2\cdot exp(-\frac{((y/p)-1.39)^2}{2\cdot(0.16)^2}) & 0.75 \leq y < 1.39 \\ 0 & \text{otherwise} \end{cases} \tag{3.14}$$

The function $\mathcal{L}$ contains five free parameters. These are

- **p** : The position (in ADC counts) of the most probable energy deposition.

- **h** : Normalisation factor of the distribution.

- σ_l : The width of the Landau distribution in ADC counts.

- σ_g : The standard deviation of the Gaussian $\Phi(y)$ in units of ADC counts.
- **b** : The background parameter describing the normalisation of the background distribution.

If the parameter p is measured in units of ADC counts then the gain, α, is equivalent to p.

Measurement of the counter asymmetry and attenuation length

In order to obtain the asymmetry, β, of a module the impact point of the muon must be known. This may be ascertained using backward extrapolation of the muon track in the drift chambers to the module under study. Taking the average of many muons at the same position x allows the measurement of both β and λ through the relation

$$< ln(R) >=< ln(\beta) > +2 \cdot \frac{x}{\lambda} \tag{3.15}$$

where R is defined by Equation 3.8. A straight line fit to a plot of $< ln(R) >$ as a function of x yields both an estimate of β and λ (see Figure 3.9).

A list of all the relevant parameters derived from the 1995 data may be found in Reference [53].

3.4.2 Absolute Calibration

Having obtained the relative calibration, all the modules measure energy in units of the mip. The second step in calibrating the FCAL is to measure the GeV equivalent of a mip. Having obtained this calibration constant, the hadronic energy deposited in the FCAL is calculated using

$$E_{had} = \kappa \cdot \left(\sum_{i=1}^{4} \sum_{j=0}^{9} M_{ij}/\alpha_{ij} - \sum_{i=1}^{N_\mu} E_{if}^0 \right) \tag{3.16}$$

The first term is a double sum which runs over all modules in each stack. M_{ij} are the recorded energies in ADC counts deposited in module j of stack i, α_{ij} are the module gains defined in the previous section and κ is the absolute calibration constant. The second term runs over the number of muons in the event. In this sum E_f^0 is the mean amount of energy deposited in the FCAL by a muon. A muon will, on average, deposit one mip of energy per stack. If

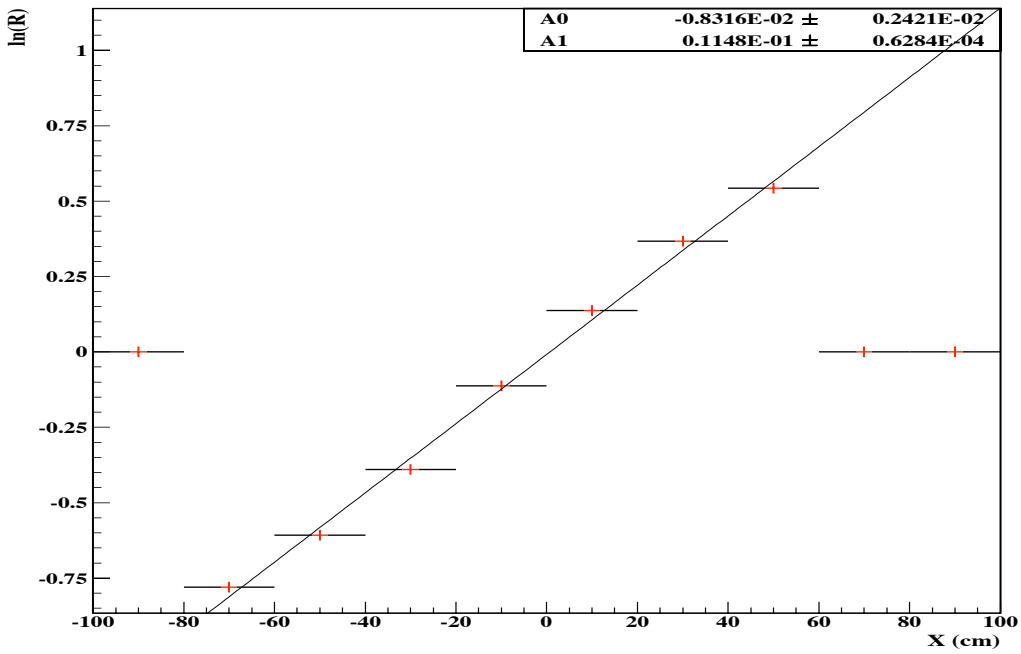

Figure 3.9: The dependence of $< ln(R) >$ on the muon impact point x. The gradient of the fit provides a measurement of the attenuation length and the intercept on the $< ln(R) >$ axis is an estimate of the asymmetry according to Equation 3.15. The outermost bins have been excluded from the fit as they are at the very edge of the FCAL volume.

the event is assumed to occur at the mid plane of the first stack hit, f, then the mean amount of energy deposition may be expressed as

$$E_f^0 = (4 - f + 0.5) \ \ [\text{mip}] \tag{3.17}$$

There are a number of ways to obtain the absolute energy scale. Here three are considered : a test beam calibration, a calibration utilising the kinematic properties of deep inelastic neutrino-nucleon scattering and a calibration using the GEANT based Monte Carlo, GENOM.

Method 1 : Test Beam Calibration

The usual method of calibrating a hadronic calorimeter is by studying its response to a test beam of monoenergetic hadrons. However, since the I containing the FCAL is an integral part of the detector support structure and the FCAL was instrumented *in situ* this option was not available.

Method 2 : Kinematic Calibration

For an inclusive deep inelastic neutrino nucleon scattering reaction $\nu_\mu N \longrightarrow \mu^- X$ with any hadronic final state X, the Bjorken y variable, y_{Bj}, is defined by (see Equation 1.6)

$$y_{Bj} = \frac{p \cdot q}{p \cdot k} \tag{3.18}$$

where p^μ is the four-momentum of the nucleon, k^μ is the four-momentum of the incoming neutrino and q^μ is the four-momentum of the exchanged boson. In the laboratory frame, this variable may be written as

$$y_{Bj} = \frac{\nu}{E_\nu} \tag{3.19}$$

where ν is the energy transferred to the hadronic system and E_ν is the energy of the incoming neutrino. In this frame Bjorken y measures the fraction of neutrino energy transferred to the hadronic system.

Neglecting the mass of the target nucleon, y_{Bj} may be expressed as

$$y_{Bj} = \frac{E_{had}}{E_{had} + E_\mu} \tag{3.20}$$

The muon momentum can be measured with high precision in the NOMAD drift chambers and hadronic energies are measured in the FCAL.

If there is a mismeasurement of the hadronic energy by a constant factor, so that :

$$E_h' = (1 + c) \cdot E_{had} \tag{3.21}$$

then the resulting *measured* distribution of y_{Bj} will be distorted by a calculable amount. In fact

$$y_{Bj}' = \frac{1 + c}{1 + \epsilon + \frac{E_\mu}{E_{had}}} = y_{Bj}\frac{1 + c}{1 + \epsilon y_{Bj}} \tag{3.22}$$

The cross section dependence on y' is

$$\frac{d\sigma}{dy'} = \frac{d\sigma}{dy}\frac{dy}{dy'} = \frac{d\sigma}{dy} \cdot \frac{(1 + cy)^2}{1 + \epsilon} \tag{3.23}$$

Hence, by comparing the shape of the y_{Bj} distribution to either a perfectly calibrated Monte Carlo y_{Bj} distribution or to a previously measured experimental distribution of y_{Bj} which has been corrected for acceptance and smearing effects , the constant ϵ may be measured. The calibration procedure would follow the prescription :

1. Starting with the Monte Carlo derive a constant relating deposited energy in mips to the energy transfer ν.
2. Assume this constant is correct for data.
3. Produce the y_{Bj}' distribution using events which have been identified as charged current interactions (e.g. by the presence of a muon track pointing back to the module in which the interaction occurred).
4. Taking into account the detector acceptance and the effects of event selection algorithms, compare this experimental distribution with the reference y-distribution.
5. Calculate the miscalibration factor, ϵ, using Equation 3.23.
6. Iterate until the miscalibration factor is stable.

The result of this procedure is a constant that relates the deposited energy in units of mips to the energy transfer, ν in GeV. An intrinsic part of this procedure is that energy "leakage" (where energy has escaped from the FCAL, either in a form invisible to the calorimeter (neutrinos, for example), or as tracks appearing the drift chambers) is not taken into account. By weighting the y_{Bj} distribution one can effectively take the leakage into account in the calibration constant.

Method 3 : Calibration by Monte Carlo

The other method which may be used to calibrate the FCAL is, perhaps, somewhat more conventional and relies heavily on the correctness of the detector simulation. The procedure essentially imitates the measurements of a test beam, although the real beam is substituted by the detector Monte Carlo simulation.

The calibration proceeds as follows :

1. Charged current neutrino events in which the hadronic showers are contained completely within the FCAL are selected.

2. The distributions of energy deposition (in units of mips) in the data and Monte Carlo for these events are compared.

3. The relative energy scale between the data and the Monte Carlo is established by changing this scale in data until the shape of the deposited mip distributions match.

4. The absolute energy scale is established in the Monte Carlo. The absolute energy scale in the data may be obtained by multiplying this by the relative scale found in the previous step.

5. As a check, this calibration constant is applied to other event configurations. If the constant that is obtained is the true energy scale and if the Monte Carlo describes the formation of the hadronic jet and the detector response correctly then deposited energy distributions for any event configuration should look the same in data and Monte Carlo.

Discussion of the optimal calibration procedure

The motivation for Method 2 was that it would not only provide a mip to GeV calibration constant but also take energy leakage into account. In principle, by reweighting the y_{Bj} distribution one can include energy losses, which distort the distribution, into the calibration constant. A consequence of this is that the constant becomes a function of the vertex position. In practice Method 2, if used in this manner, contains a number of problems. First and foremost, the calibration procedure must be carried out in many small subvolumes of the main FCAL volume. This requires a prohibitively large number of events since each subvolume must have enough events to form its own y_{Bj} distribution with small statistical errors.

Secondly, the procedure calculates a calibration constant which is an *average* over an ensemble of events. In any given y_{Bj} bin one can have a collection

of different event configurations ranging from events in which the energy is completely contained to events which leak much of their energy or in which the energy appears in a form invisible to the calorimeter, such as neutrinos or neutrons. Hence by reweighting the y_{Bj} distribution one is averaging over the entire ensemble in each bin. This factor, although valid at the distribution level, tends to be incorrect on an event-by-event basis and is, furthermore, very sensitive to the specific region of phase space used in the calibration procedure. Fiducial cuts, which sample a specific region of the beam, and event recognition algorithms, which sample specific kinematic regions, would have to be the same in all analyses using the calibration constant derived using Method 2. Moreover, this constant would not be applicable in any study of *exclusive* hadronic channels in which the leakage characteristics could potentially be very different from the inclusive sample with which the calibration was performed (e.g. an analysis of dimuons where a second muon in the jet is required). An exclusive process emphasises a particular region of phase space and would have a different average calibration constant.

It is clear that Method 2 cannot be used to correct for leakage as well as for different analyses. However, if the procedure is applied to totally contained events it may be used to measure the absolute hadronic energy scale of the FCAL. However, at this point, Methods 2 and 3 are equivalent. Each relies on the correct simulation of ν_μ^{CC} interactions; Method 2 for the acceptance function that must be applied to the observed y_{Bj} distribution and Method 3 for the spectrum of energy deposition, and the outcome of both methods is a single calibration constant that converts deposited energy in mips to deposited energy in GeV. The dimuon analysis performed in Chapter 5 includes events in which energy has leaked out of the FCAL. Since the outcome of Method 2 is highly dependent on both the leakage properties of the events and the event cuts used in the calibration , the mip to GeV energy calibration was carried out using Method 3. The shape of the observed y_{Bj} distribution is used in Chapter 4 as a check on the results of the calibration procedure.

3.4.3 Absolute calibration of the FCAL using the Monte Carlo

The first step in the absolute calibration using Method 3 is to define the cuts which will be used to select events in one local region of phase space. The event selection criteria require knowledge of the vertex position. This is estimated by extrapolating the muon generated at the leptonic vertex in ν_μ^{CC} events back to mid-plane of the first stack in which the deposited energy

is above a threshold of 0.5 mip. This procedure will be discussed more completely in Section 3.4.4. For now it is assumed that the vertex position is known with reasonable accuracy.

The cuts used in the analysis were:

- **Charged Current Interaction:** There must have been one and only one negatively charged track in the drift chambers which geometrically matched, both in position and angle, with a track in the muon chambers.

- **ADC saturation:** The response of the FCAL to hadronic showers has been modelled in the GENOM detector simulation introduced in Chapter 2. The ADCs have an infinite dynamic range in the Monte Carlo but can saturate in the data. Since this saturation is highly dependent on the relative calibration discussed above (the scintillator response may change over time but the ADC length remains constant) the saturation is performed at the level of the analysis. Given the energy deposition and the approximate longitudinal position of a hit in a module one can, using Equation 3.10, calculate the ADC values for that module. Then, using the relative energy scale between data and Monte Carlo and assuming a saturation level in the data, each of the modules in a Monte Carlo event can be saturated. In this study the saturation level in the data is measured to be approximately 70 mip.

- **Trigger threshold:** The FCAL will not register the presence of an event below an energy threshold defined by a discriminator level in the data acquisition system. As already mentioned in Section 3.3.4 signals in the FCAL are discriminated at two different levels, corresponding to two separate trigger components, FCAL and FCAL′. Any event which satisifies the criteria for an FCAL trigger (defined by the larger discrimination threshold) automatically satisfies the conditions for the FCAL′ trigger (but not vice versa). The trigger efficiency for FCAL can be measured by comparing events which pass the the conditions for both triggers with those which only satisfy the FCAL trigger criteria. Figure 3.10 shows the turn on curve for the FCAL trigger as a function of deposited energy in units of mips. The threshold corresponds to a deposited energy of 4.0 mips and the efficiency is essentially 1.0 above an energy deposition of 5.0 mips.

  In order that the calibration not be sensitive to the exact shape of the trigger threshold only events above threshold were considered. In

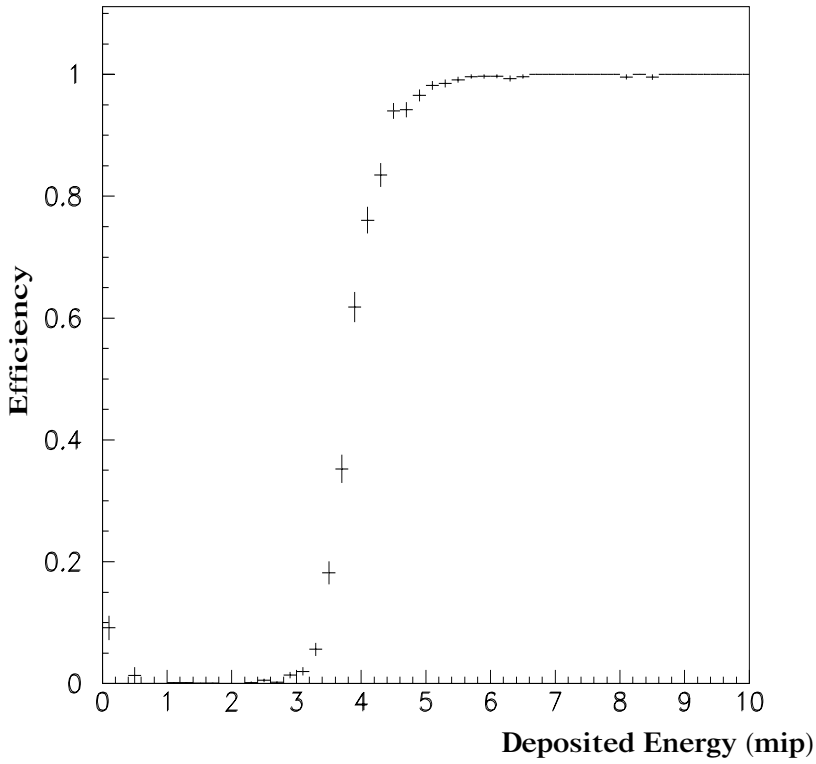

Figure 3.10: The efficiency of the FCAL trigger as a function of the deposited energy.

practice this imposed the condition :

$$\text{Total deposited energy} > 5 \text{ mip} \tag{3.24}$$

- **Transverse Leakage:** The transverse dimensions of a hadronic shower are relatively independent of the shower energy [34] and scale roughly with the nuclear interaction length, λ_I. On average 95% of the hadronic energy is laterally contained within a radius of 1 λ_I. To minimise lateral leakage the vertex was required to be at least one λ_I away from the boundaries of the FCAL. Energy is also unaccounted for if it is absorbed in the uninstrumented region at the center of each stack. To correct for this the interaction was required to have occurred at least one module width away from this area. One nuclear interaction length in iron is 16.8 cm so the fiducial cuts were :

$$|X_{vertex}| < 70.0 \text{ cm}, \quad 20.0 \text{ cm} < |Y_{vertex}| < 70.0 \text{ cm} \tag{3.25}$$

- **Longitudinal Leakage:** Longitudinal energy leakage is a major concern in a calorimeter as short as the FCAL. To deal with this the fourth stack was used as a veto. The fraction of energy deposited in stack 4 was required to be less than 10% of the total deposited energy. In order to take account of the muon in the charged current interaction one mip was subtracted from the total sum of deposited mips for each full stack crossed and 0.5 mips for the first stack hit. Defining M_i to be the number of mips deposited in stack i and F to be the first stack hit, the appropriate cut is

$$\frac{M_4 - 1.0}{(\sum_{i=F}^{4}(M_i - 1.0)) + 0.5} < 0.1 \tag{3.26}$$

These cuts, although rather strict, limit the events to be used in the calibration to a small region of phase space. Figure 3.11 shows the distribution of deposited energy in units of mips for Monte Carlo and data assuming a relative energy scale of 1.0. The distributions have been normalised to the same area and obviously have different shapes. The Monte Carlo overestimates the number of events with low energy deposition indicating that the absolute energy scale in the data is less than that in the Monte Carlo. Changing the relative energy scale allows the χ^2 of the comparison of the energy deposition in the simulation and data to be mapped.

Figure 3.12 shows the χ^2 curve with 19 degrees of freedom as a function of the relative energy scale. Using this curve the optimal relative energy scale was measured to be :

$$\frac{\kappa_{MC}}{\kappa_{Data}} = (0.800 \pm 0.005) \tag{3.27}$$

where the uncertainty was determined from the relative scales at which the χ^2 was one unit above the minimum. This error is only approximate as it is expected that systematic errors will contribute a larger uncertainty.

This scale, in and of itself, is not very useful. It merely reflects the difference between the data and the Monte Carlo for one particular set of fiducial cuts. In order that it may be used as part of the calibration procedure, the scale must be the same for a number of different cuts and hadronic shower development profiles.

A set of standard cuts have been defined. These cuts sample events with different shower developments and which sample different areas of the beam. The cuts for each event sample are :

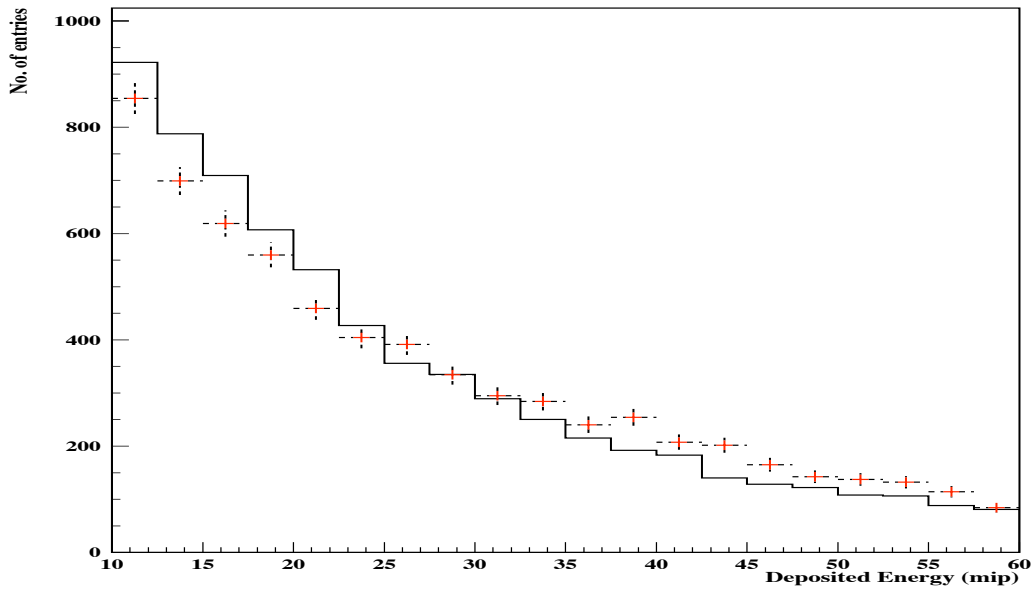

Figure 3.11: Comparison of the energy deposition distributions for data (points) and Monte Carlo samples (histogram). The relative energy scale is 1.0.

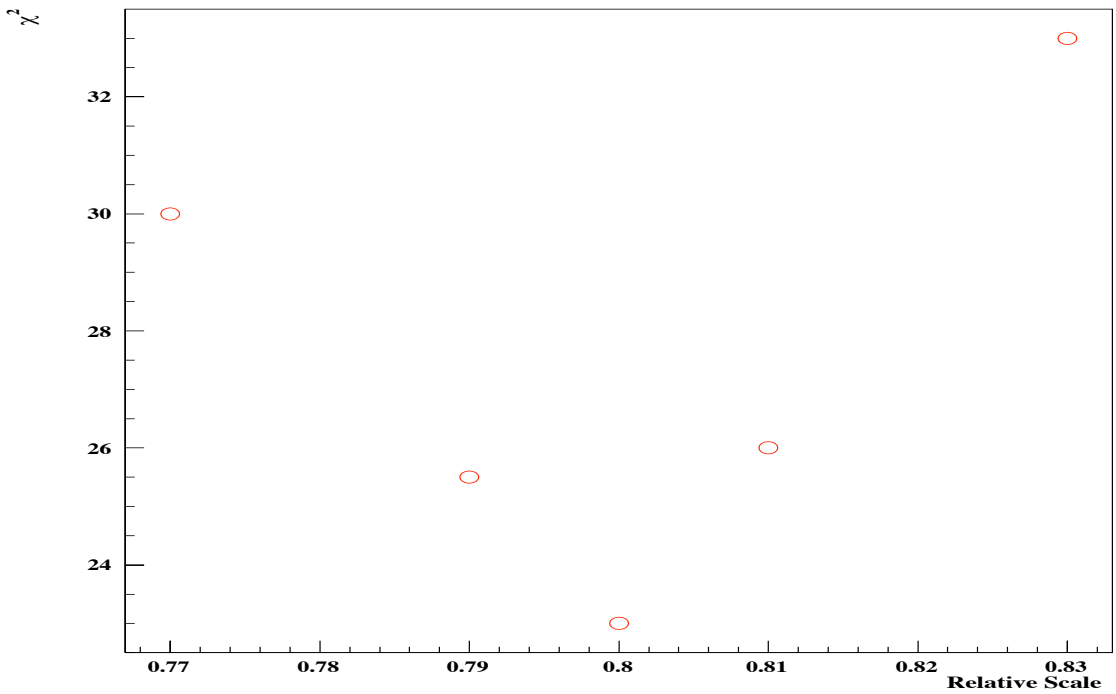

Figure 3.12: The fit χ^2 as a function of the relative energy scale. The number of degrees of freedom is 19. The plot shows an optimal relative scale of (0.800 ± 0.005).

- **Sample A :** This category contains only fully contained events.

  $|X_{vertex}| < 70$ cm

  20 cm $< |Y_{vertex}| < 70$ cm

  One track in the drift chamber.

  $\frac{M_4 - 1.0}{(\sum_{i=F}^{4}(M_i - 1.0)) + 0.5} < 0.1$

- **Sample B :** This allows events in the central, uninstrumented region and restricts showers from Stack 1 and Stack 2 events to be less than two stacks long.

  $|X_{vertex}| < 70$ cm

  $|Y_{vertex}| < 70$ cm

  One track in the drift chamber.

  $\frac{M_3 - 1.0}{(\sum_{i=F}^{4}(M_i - 1.0)) + 0.5} < 0.1$

  $\frac{M_4 - 1.0}{(\sum_{i=F}^{4}(M_i - 1.0)) + 0.5} < 0.1$

- **Sample C :** The events in this sample are restricted from leaking energy from the face of the FCAL closest to the main NOMAD detector, but are permitted to lose energy from the sides of the FCAL.

  One track in the drift chamber.

  $\frac{M_4 - 1.0}{(\sum_{i=F}^{4}(M_i - 1.0)) + 0.5} < 0.1$

- **Sample D :** All events are allowed, except those on the very edge of the calorimeter.

  $|X_{vertex}| < 70$ cm

  $|Y_{vertex}| < 70$ cm

- **Sample E :** Only events in the core of the neutrino beam are accepted.

  $|X_{vertex}| < 40$ cm

  $|Y_{vertex}| < 40$ cm

Figures 3.13,3.14,3.15 and 3.16 display a comparison of the distribution of energy deposition for the different samples outlined above for ν_μ^{CC} interactions occurring in each stack. The means and RMS deviations for data and Monte Carlo are summarised in Table 3.3. Some of the cuts above cannot be

applied to all stacks. For instance, events in Samples A and C and originating in Stack 4 would have very low energy showers. Such events would not satisfy the conditions of the FCAL trigger. In these cases the requirement that the energy deposition in Stack 4 be less than 10% of the total hadronic energy was omitted. Sample B requires events with short hadronic showers. It is impossible for events originating in Stacks 3 and 4 to satisfy the conditions for this category, and this sample has been omitted for Stack 2 events due to poor statistics.

The most obvious feature of these distributions is that the comparisons worsen as one moves further towards the most downstream face of the FCAL. This is an indication that, as the interactions occur closer to the back face of the FCAL, the energy leakage becomes more pronounced. Both the means and RMS deviations are systematically higher in the Monte Carlo implying that the saturation of the ADCs in the Monte Carlo is different in the data. This may be a consequence of using a single saturation level of 70 mip rather than a level which is module specific. However, only the very high energy part of the tails of the distributions are affected. In general, the distributions for the different event configurations agree well, imparting confidence that the relative energy scale used is the true scale that relates the actual energy deposition in the data to that in the Monte Carlo.

The final step in the calibration of the FCAL is to calculate the absolute energy scale in the Monte Carlo. Figure 3.17 shows the distribution of the energy transfer, $\nu(GeV)$, as a function of the sum of deposited energy in mips, for Monte Carlo neutral current events. Since there is no muon from the leptonic vertex in neutral current events, tight energy containment cuts may be applied. The selected events must have been fully contained within the FCAL. In practice this means that there should have been no charged tracks in the drift chamber and no energy deposited in the fourth stack.

The energy conversion factor for the Monte Carlo is :

$$1[\mathrm{GeV}] = (2.366 \pm 0.001)[\mathrm{mip}] \tag{3.28}$$

and using the relative scale between data and Monte Carlo (see Section 3.4.2), the absolute calibration for events in the data is

$$1[\mathrm{GeV}] = (2.95 \pm 0.02)[\mathrm{mip}] \tag{3.29}$$

3.4.4 Sources of uncertainty

Three possible sources of uncertainty can be identified in this procedure.

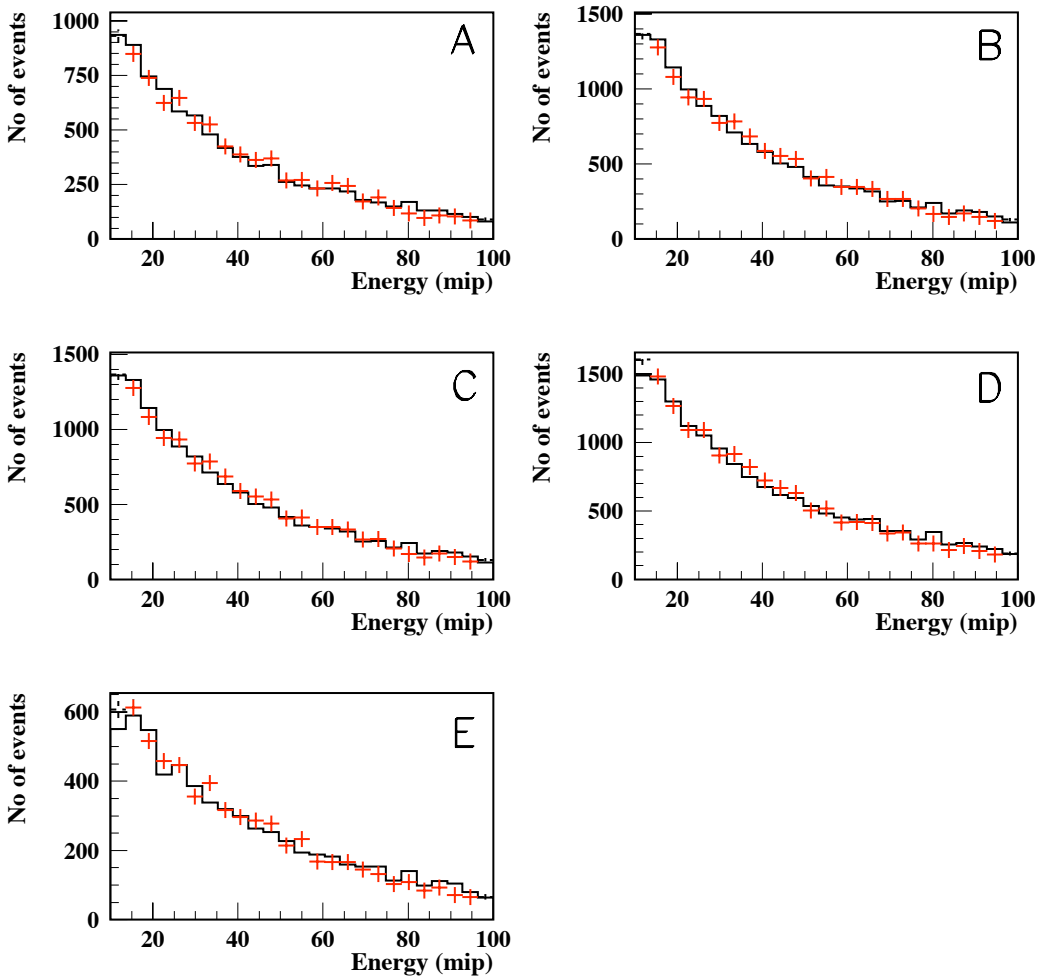

Figure 3.13: Comparison of energy deposition distributions for Stack 1. The category of events in each plot is displayed in the upper right corner of that plot and is described in the text.

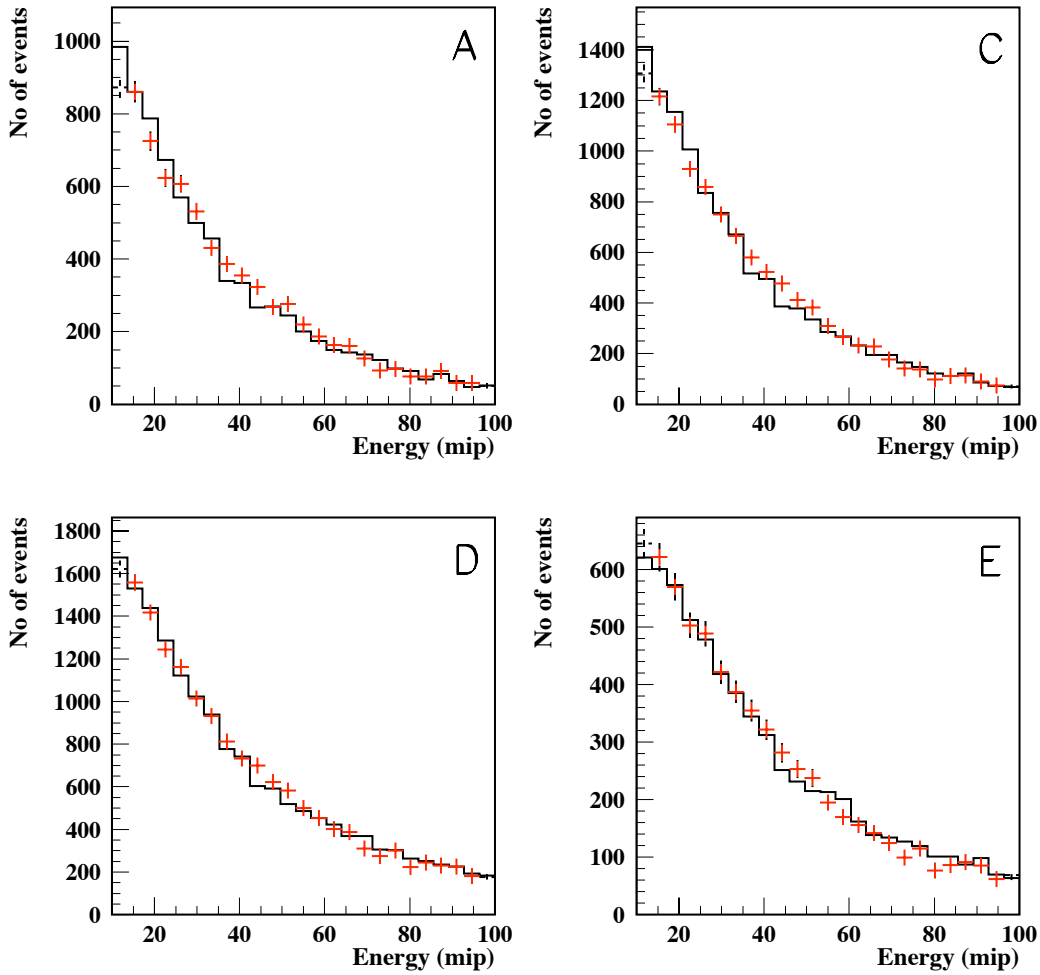

Figure 3.14: Comparison of energy deposition distributions for Stack 2. The category of events in each plot is displayed in the upper right corner of that plot and is described in the text.

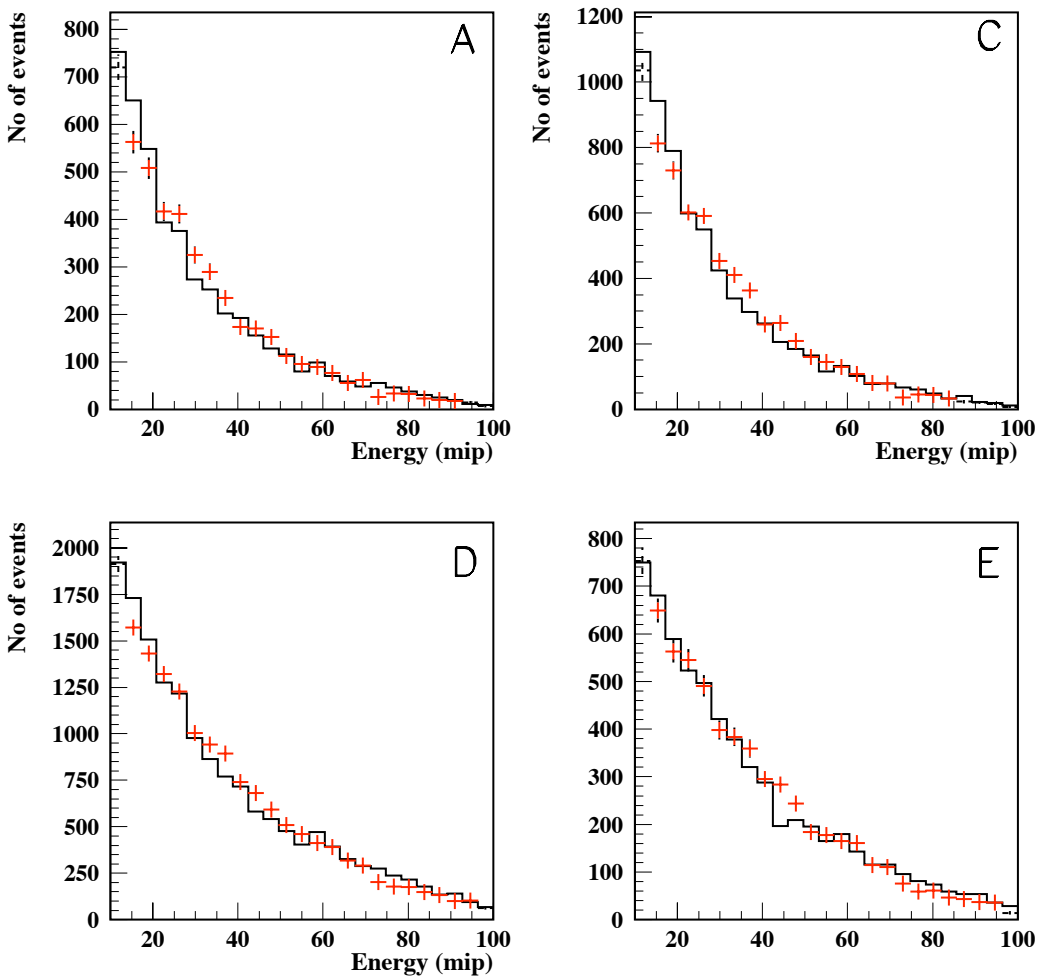

Figure 3.15: Comparison of energy deposition distributions for Stack 3. The category of events in each plot is displayed in the upper right corner of that plot and is described in the text.

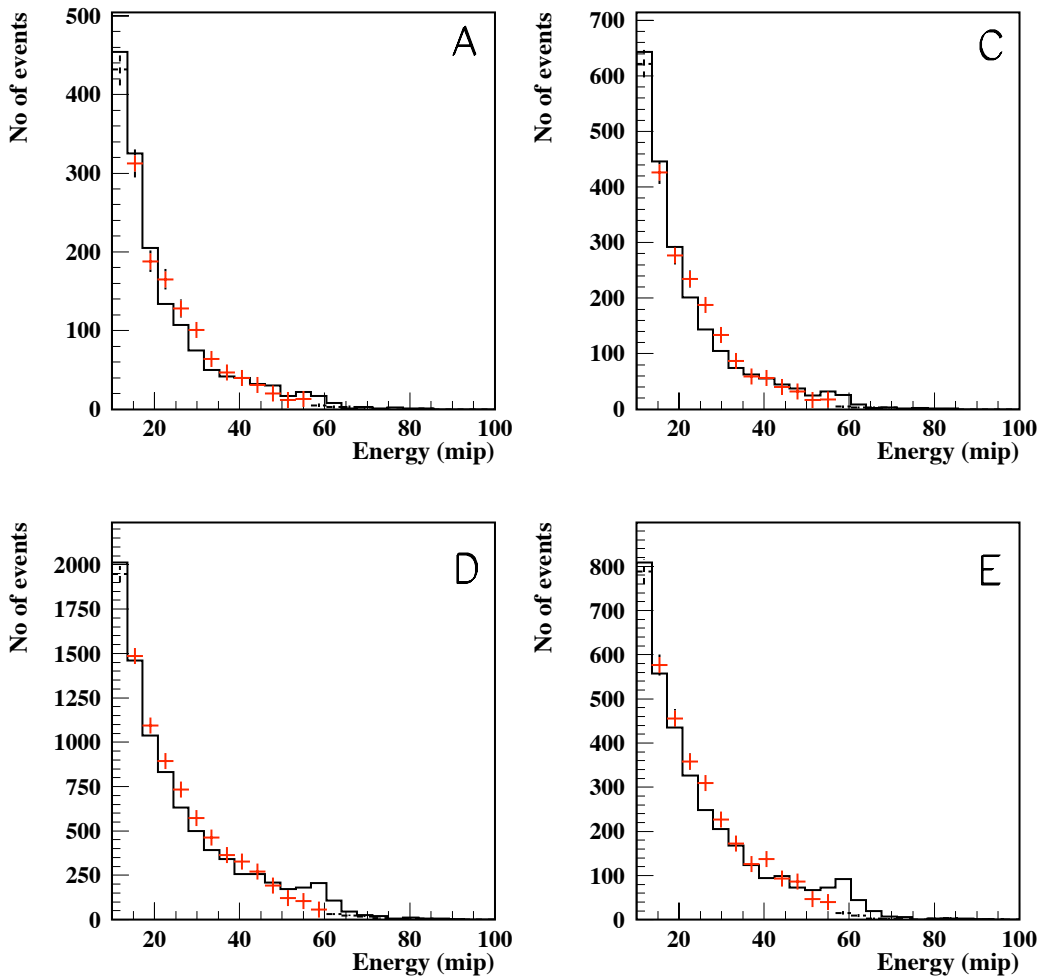

Figure 3.16: Comparison of energy deposition distributions for Stack 4. The category of events in each plot is displayed in the upper right corner of that plot and is described in the text.

Stack 1				
	ν_μ^{CC} *Data*		ν_μ^{CC} *MonteCarlo*	
Sample	Mean (mip)	RMS (mip)	Mean (mip)	RMS (mip)
A	37.9	22.4	38.1	23.0
B	37.7	22.3	37.9	22.9
C	37.4	22.3	37.5	22.2
D	38.9	23.0	40.0	23.7
E	38.7	22.6	40.2	23.5

Stack 2				
	ν_μ^{CC} *Data*		ν_μ^{CC} *MonteCarlo*	
Sample	Mean (mip)	RMS (mip)	Mean (mip)	RMS (mip)
A	35.0	21.0	34.3	21.0
C	34.7	20.7	34.2	20.9
D	38.2	22.7	38.4	23.0
E	37.6	22.2	38.3	22.6

Stack 3				
	ν_μ^{CC} *Data*		ν_μ^{CC} *MonteCarlo*	
Sample	Mean (mip)	RMS (mip)	Mean (mip)	RMS (mip)
A	30.2	17.9	30.1	18.6
C	30.0	17.5	29.6	18.2
D	34.9	20.4	35.2	21.2
E	34.2	19.7	34.7	20.8

Stack 4				
	ν_μ^{CC} *Data*		ν_μ^{CC} *MonteCarlo*	
Sample	Mean (mip)	RMS (mip)	Mean (mip)	RMS (mip)
A	21.4	10.6	21.8	12.2
C	21.2	10.5	21.7	12.0
D	23.9	12.3	25.2	14.4
E	23.4	11.8	25.0	14.3

Table 3.3: Average values and RMS of the deposited energy distributions for Data and Monte Carlo samples under different cuts.

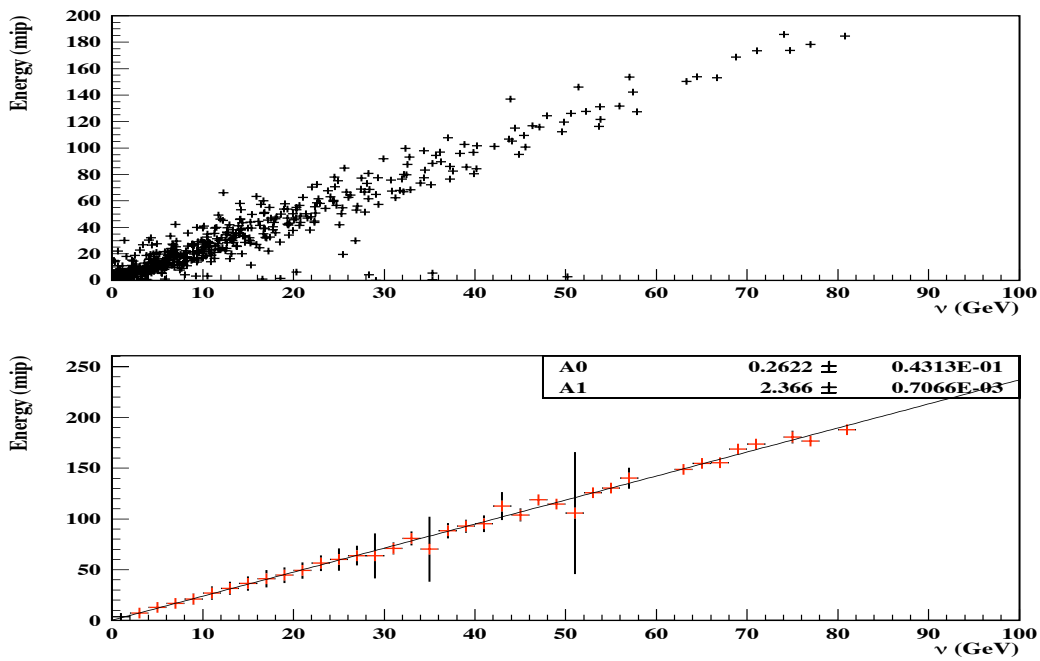

Figure 3.17: The top plot shows a scatter plot of the deposited energy in mips as a function of the energy transferred to the hadronic system for Monte Carlo events in sample A, which has been modified for neutral current events. The bottom plot is a profile histogram with a linear fit superimposed. The fit parameters are shown in the top right corner of this plot.

Beam profile

The calibration procedure described above relies heavily on the ability to sample the same regions of phase space in both the data and the Monte Carlo. If the neutrino beam profile in the Monte Carlo differs markedly from that in the data, this will not be true. In this case event samples resulting from different fiducial cuts, for example, will have different average neutrino energies. Interactions within these regions will therefore occur with different cross sections and will result in different kinematics.

Figure 3.18 compares the visible energy distributions and the distribution of the radial position of vertices as measured in data with that predicted by the NUBEAM package in the drift chamber target region [14]. The qualitative agreement is rather good in all bins, although there appears to be an excess of events in the data for the energy region 35 GeV $< E_\nu <$ 55

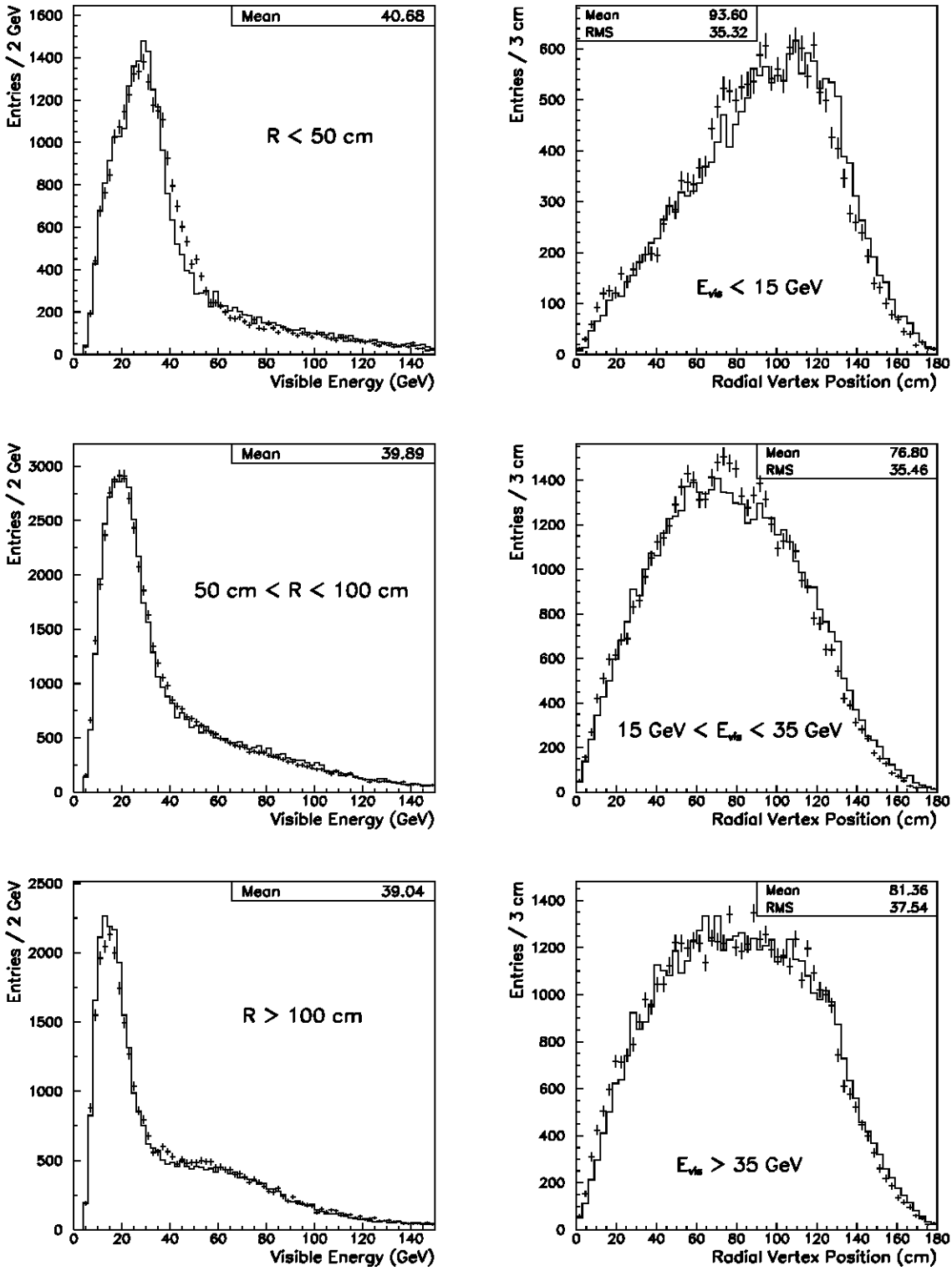

Figure 3.18: Comparison of the 1995 data with Monte Carlo predictions for ν_μ^{CC} interactions in the drift chamber target. Shown are (left) the visible energy distributions in different radial bins and (right) the radial distributions in the three energy bins.

GeV at radii of less than 50 cm. It is known [35] that the distribution of transverse momenta of particles produced in the p - Be interactions is incorrectly simulated in FLUKA (cf. Section 2.8). This is thought to cause the observed excess of events and has been confirmed by the first results of the SPY collaboration [36].

The beam profile appears to be reasonably well described by NUBEAM. It is known, however, that the shape of the ν_μ flux is better estimated when using the 1995 version of FLUKA, than when using FLUKA92, the version which is, by default, interfaced to GEANT, to model the p-Be interaction. In order that these different effects can be studied, weighting tables to and from the different beam prescriptions have been produced [39]. An estimate of the uncertainty due to a non-optimal beam profile on the calibration may be made by weighting the Monte Carlo neutrino events generated with a given energy E_ν at a given position in the FCAL by the relative difference in the flux predictions. That is, each event is assigned a weight defined by :

$$weight(E_\nu, R) := \frac{\Phi^{FLUKA95}(E_\nu, R)}{\Phi^{FLUKA92}(E_\nu, R)} \tag{3.30}$$

where R is the radial distance of the interaction point from the center of the beam in the NOMAD frame of reference.

The calibration is relatively insensitive to fine differences in the beam profile. The calibration scale that resulted from using the weighted Monte Carlo events was

$$\frac{\kappa_{MC}}{\kappa_{Data}} = (0.78 \pm 0.02) \tag{3.31}$$

which differs from the result derived above by approximately 3%. To be conservative the uncertainty in the calibration due to an incorrect beam description was taken to be 5%.

Determination of the Event Vertex in the FCAL

Linked with the question of the beam profile is the issue of determination of the event vertex. Again, if the determinations in the Monte Carlo and the data are inconsistent then the same fiducial cuts will sample different sections of the total cross-section.

The longitudinal (Z) position of the vertex cannot be precisely determined, as the longitudinal information available from the FCAL is very coarse. The procedure taken here is that the Z position of the vertex is taken as the center plane of the first stack with energy above 0.5 mips. Neutrinos interact uniformly in Z. The variance of a uniform distribution on an

interval of width W is

$$\sigma^2 = \frac{W^2}{12} \tag{3.32}$$

so the error in the determination of longitudinal position of the vertex in a stack is just $1/\sqrt{12}$ times the width of the stack, or

$$\sigma_z = 9.7 \text{ cm} \tag{3.33}$$

The transverse position of the vertex may be ascertained in two ways :

- **Muon extrapolation**

  Applicable only to processes in which a muon is generated at the event vertex (such as ν_μ^{CC} deep inelastic or quasielastic processes), this method involves the extrapolation of the muon track coordinates in the drift chamber back to the Z position of the vertex.

- **Estimation using the Centre of Gravity**

  The position of the vertex may also be estimated using the hadronic shower. Section 3.4.1 has shown that it is possible to estimate the mean position of the energy deposition in a single module using only the energy information in that module. The event vertex in the XY-plane can be estimated by combining the position estimates in the first stack hit. The center of gravity co-ordinates are calculated using

$$x_{FCAL} = \frac{\sum_{i=0}^{9} E_i \cdot x_i}{\sum_{i=0}^{9} E_i}, \quad y_{FCAL} = \frac{\sum_{i=0}^{9} E_i \cdot y_i}{\sum_{i=0}^{9} E_i} \tag{3.34}$$

  where E_i is the energy of the hit and $x_i(y_i)$ is the X(Y) position of the hit in the i-th module.

The difference between the estimated vertex positions and the interaction points for a sample of Monte Carlo ν_μ^{CC} events are shown in Figure 3.19. In general, the difference is larger for the centre of gravity vertexing method. In particular the distribution in Y for this method is very broad. The reason for this is that there is no information about where, on the Y axis, a hit occurred in a module. The Y position of the hit is arbitrarily chosen to be at the centre of the module.

The method of muon extrapolation appears to estimate the vertex with better precision than the centre of gravity method. It also has the added

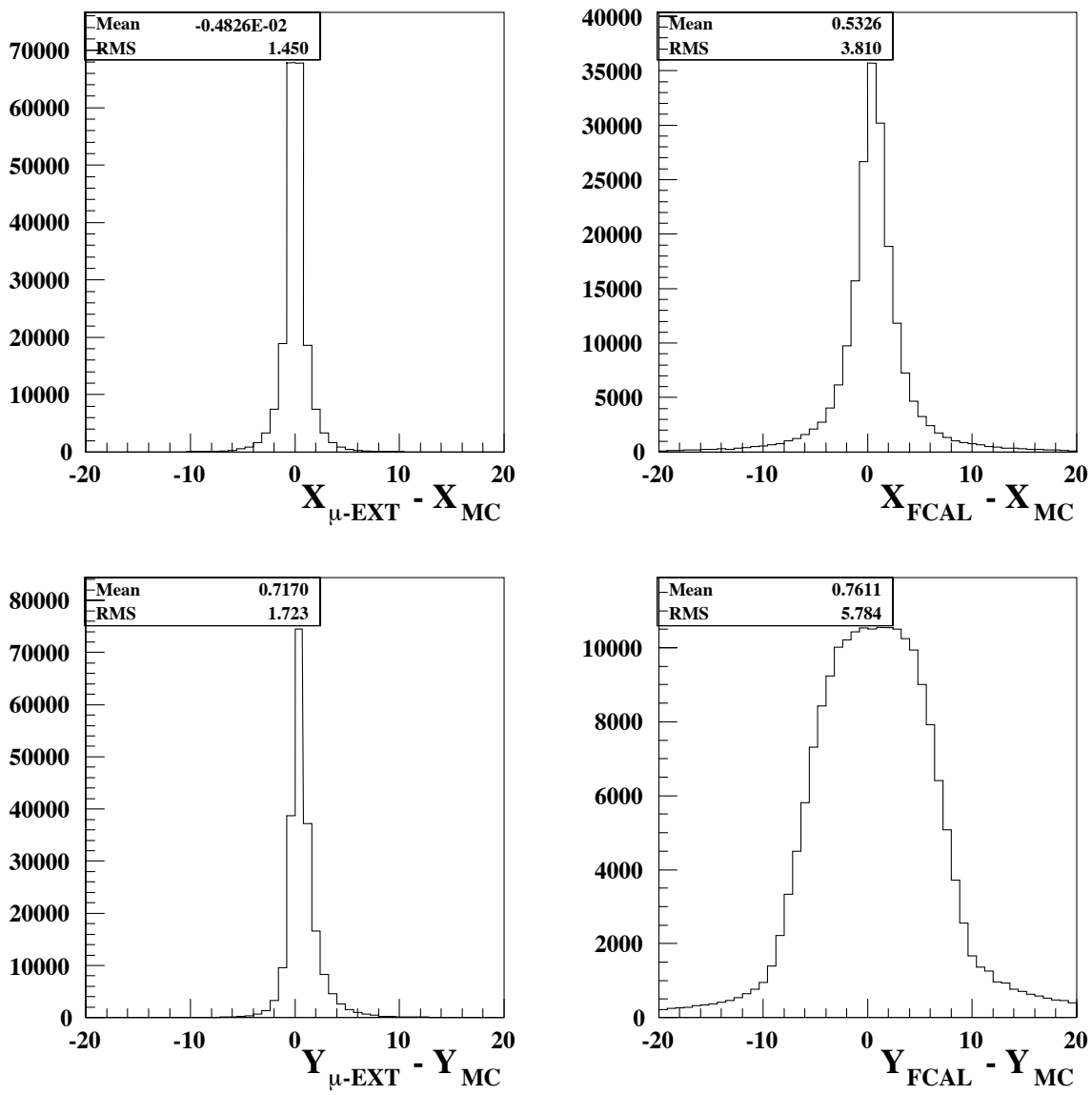

Figure 3.19: The difference between the estimated X and Y positions of the vertex and the point at which the interaction actually occurred in a sample of ν_μ^{CC} Monte Carlo events. Shown are the differences for the muon extrapolation method (left side) and for the center of gravity method (right side) in ν_μ^{CC} interactions. The distributions are normalised to the same number of events.

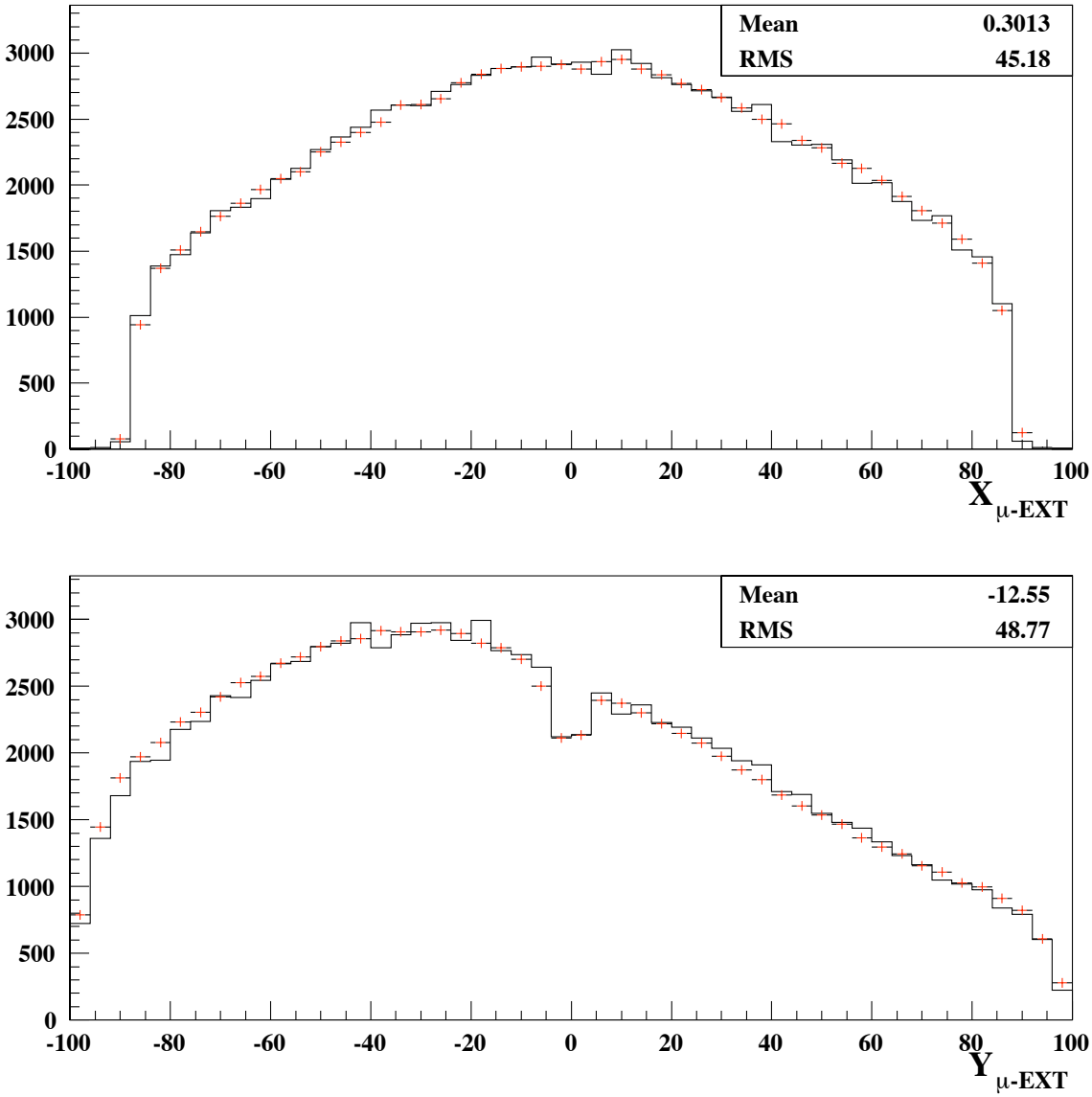

Figure 3.20: Comparison of the ν_μ^{CC} data with the Monte Carlo for the estimated position of the event vertex on the X axis (top) and the Y-axis (bottom). The simulated distributions are overlayed as a histogram to the data points.The distributions are normalised to the same number of events.

advantage that it is independent of experimental effects that bias the energy measurement, such as ADC saturation or non-linearities in the response across the scintillator.

The distribution of vertex positions in the Monte Carlo and the data using the muon extrapolation method are compared in Figure 3.20. The agreement is good in both X and Y positions. The loss of events at Y $\approx$ 0 cm is a consequence of the uninstrumented region at the centre of each stack. Events which deposit little hadronic energy in these regions have a smaller probability of satisfying the *FCAL* trigger conditions.

Since the data and Monte Carlo vertex distributions agree well, the resolution calculated from the Monte Carlo may be assumed to be approximately correct. The vertex criteria in the calibration procedure were varied around their nominal position by 5 cm and the calibration procedure was reapplied. No difference in the final calibration constant was found. The error due to the vertexing procedure is considered to be negligible when compared to the other sources of uncertainty.

Simulation of Hadronic Processes

The final contribution to the error in the calibration constant arises from inaccuracies in the simulation of the hadronic processes in the Monte Carlo. GENOM uses the FLUKA92 package. A comparison of different hadronic packages has been made in relation to the ATLAS experiment [38]. They conclude that in the few GeV range (hadronic energies of less than 5 GeV) the description exhibits a number of problems. In the high energy range FLUKA92 agrees with data to an accuracy of approximately 8%. The error due to calibrating the FCAL using the Monte Carlo is therefore taken to be 8%.

3.4.5 Results of the Calibration

Taking into account the systematic effects discussed above, the energy calibration constants for neutrino interactions occuring in the FCAL were found to be :

$$1[\mathrm{GeV}] = (2.366 \pm 0.001(stat))[\mathrm{mip}] \tag{3.35}$$

for the Monte Carlo events and

$$1[\mathrm{GeV}] = (2.95 \pm 0.02(stat) \pm 0.27(sys))[\mathrm{mip}] \tag{3.36}$$

for data.

Chapter 4

Neutrino Interactions in the FCAL

4.1 Introduction

An analysis of any process using the FCAL requires an understanding of the resolution effects of the detector. Such an understanding may be achieved through the study of inclusive ν_μ^{CC} interactions in which the input variables are well known. This chapter begins with a discussion of muon identification which is followed by a discussion of the techniques for identifying ν_μ^{CC} interactions. Finally a comparison of simulated and experimental data is performed.

Before continuing it is necessary to define the *quality* distribution of a variable.

Definition

The quality of reconstruction of any variable, X, may be defined as

$$Q(X) := \frac{X^{Monte\ Carlo\ Simulated} - X^{Monte\ Carlo\ Reconstructed}}{X^{Monte\ Carlo\ Simulated}} \tag{4.1}$$

where $X^{Monte\ Carlo\ Simulated}$ represents the value of the variable X before detector smearing and reconstruction has been applied to the event and $X^{Monte\ Carlo\ Reconstructed}$ is the value of X after the event has been passed through the detector simulation and reconstruction algorithms. In this chapter, unless otherwise stated, the term "quality" is synonymous with "quality of reconstruction" and refers to the definition 4.1. The "resolution" and "bias" of a variable are defined to be the width and mean of the quality distribution respectively.

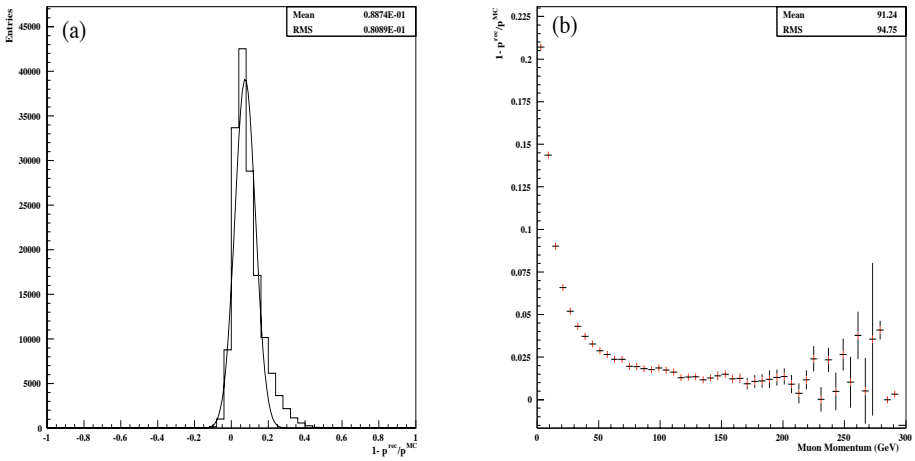

Figure 4.1: (a) Muon momentum quality; (b) Bias as a function of the simulated muon momentum.

4.2 Muon Identification

The primary means of muon identification is the penetrating power of a candidate particle. A candidate muon must pass through at least 8 interaction lengths (see Section 2.6.10) to reach the first muon station and at least 13 interaction lengths to reach the second[1]. The criteria for a track in the drift chambers, but which originated in the FCAL, to be considered to have been caused by a muon are

- the track can be extrapolated to the muon chambers. Particles which are outside the geometric acceptance of the muon chambers, or which rangeout in the detector material can fail this criterion.
- the estimated position of the track, when extrapolated to the muon chambers, matches the location of a track in the muon chambers to within 40 - 50 cm.
- the track points back to the FCAL volume and has its first hit at Z less than 50 cm. This is to ensure that the particle is correlated with the event which fired the FCAL trigger.

Figure 4.1(a) shows the quality of the muon momentum measurement. There is a systematic underestimation of the muon momentum which arises from muon energy loss in the iron and the coil. Figure 4.1(b) shows the muon

[1]This is for events occurring in Stack 4. Muons from interactions in Stack 1 must traverse approximately 13 interaction lengths to reach station 1 and 18 to reach station 2.

momentum bias as a function of the Monte Carlo momentum of the muon. Above a momentum of 40 GeV/c the bias is constant at approximately 2.0%. The effect of energy loss becomes more significant below 40 GeV/c.

Of greater interest is the muon energy, which enters into the calculation of most of the kinematic variables. This is defined by

$$E_\mu = \sqrt{p_\mu^2 + m_\mu^2} + E_{loss} \tag{4.2}$$

where m_μ is the mass of the muon. The muon momentum, p_μ, is measured in the drift chambers, taking energy loss in the main detector into account and E_{loss} accounts for energy loss in the FCAL itself before the muon enters the drift chamber volume. E_{loss} is a constant energy offset which is a function of the stack in which the interaction occurred. The mean muon energy loss in passing through each stack is 0.35 GeV [52] and there is a mean energy loss of 0.25 GeV in the coil. Figure 4.2(a) shows the muon energy quality after correction for energy loss in the FCAL and coil and Figure 4.2(b) shows the bias as a function of the muon energy.

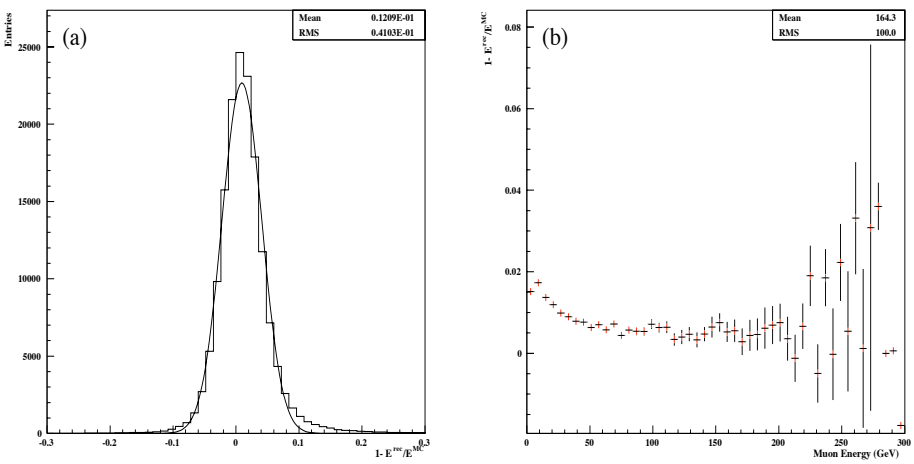

Figure 4.2: (a) Muon energy quality including energy loss in the FCAL and coil averaged over all stacks; (b) Bias as a function of the simulated muon energy.

A tail at large positive energy qualities can still be seen, indicating the presence of events which undergo catastrophic energy loss. A constant energy correction does not account for the energy loss of these types of events well. However the muon energy can generally be measured with a precision of better than 4% over two orders of magnitude.

The energy thresholds to reach the muon chambers with 50% probability are shown in Table 4.1. Detection of a muon implies an energy cut of at least 2.5 GeV.

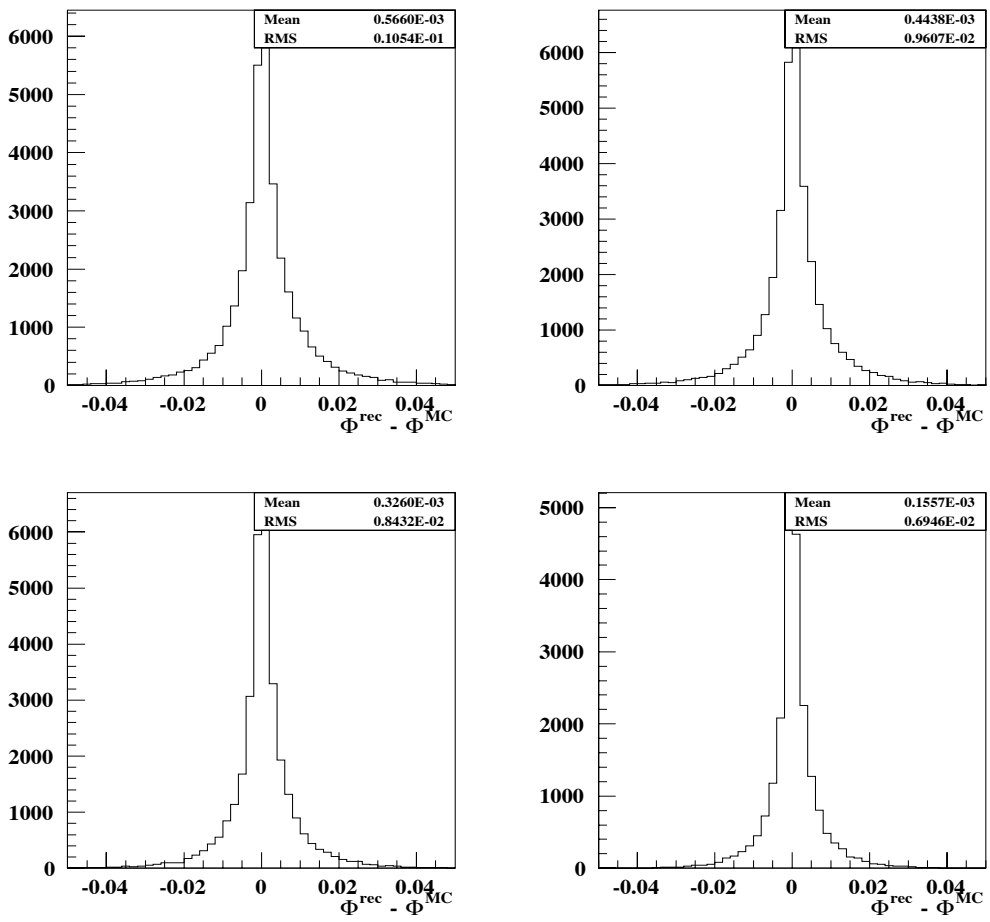

Figure 4.3: The difference between the simulated angle of the muon with respect to the neutrino direction and the reconstructed angle for events occurring in each stack. Shown are the distributions for Stack 1 (top left), Stack 2 (top right), Stack 3 (bottom left) and Stack 4 (bottom right).

Stack	Station 1 (GeV)	Station 2 (GeV)
1	3.80 ± 0.03	5.11 ± 0.05
2	3.50 ± 0.04	4.69 ± 0.05
3	3.24 ± 0.03	4.42 ± 0.05
4	2.61 ± 0.03	4.17 ± 0.05

Table 4.1: Energy thresholds for muons to reach each station of the muon chambers with 50% probability as a function of the stack in which the interaction occurred.

The precision with which the angle of the muon at the event vertex can be measured is limited by multiple scattering in the iron and the coil. Figure 4.3 shows the difference between the simulated angle between the muon and the neutrino direction and the reconstructed angle for events occurring in each stack. As expected the closer to the drift chambers the event occurs, the better is the reconstruction of the angle. The bias and spread for events occurring in each stack are summarised in Table 4.2.

Stack	Bias (mrad)	Width (mrad)
1	0.59	10.5
2	0.44	9.6
3	0.33	8.4
4	0.16	6.9

Table 4.2: Muon angular differences for events occurring in each stack. The bias decreases the closer to the back face of the FCAL the event occurs. The average spread over all stacks is approximately 9 mrad.

In addition to the muon identification criteria described above, several muon quality cuts are used in this analysis. These were

1. **Matching distance:** The transverse (X-Y plane) distance between the extrapolated drift chamber track and the muon chamber track was less than 40 cm in station 1 and less than 50 cm in station 2.

2. **FCAL association:** The matched drift chamber track must have pointed back to the FCAL sensitive volume and started less than 30 cm into the drift chamber volume.

3. **Muon energy:** A minimum muon energy cut of 3.0 GeV was applied to reduce the background from π^-/K^- decays and hadron "punchthrough"

from particles created either in the FCAL or in coil interactions.

4.3 ν_μ Charged Current Event Selection

4.3.1 Fiducial Volume

The choice of the appropriate fiducial area for FCAL analyses is driven almost entirely by energy resolution considerations. This will be discussed in Section 4.5.1. Unless otherwise specified, the fiducial volume used in this analysis is bounded by

$$|X| \leq 70 \text{ cm} \;\; ; \;\; |Y| \leq 70 \text{ cm} \;\; ; \;\; -200 \text{ cm} \leq Z \leq -90 \text{ cm} \qquad (4.3)$$

The vertex co-ordinates are calculated using the centre of gravity method (explained in Section 3.4.4) which, although not ideal, does not presuppose the existence of a muon in any particular interaction.

Figure 4.4 shows the vertex distributions for ν_μ^{CC} interactions using this centre of gravity method. The qualitative agreement in the X position of the vertex is good, although the Monte Carlo appears to underestimate the number of events at the edges of the FCAL. The most probable reason for this is that there are interactions in the lightguides and support structure of the FCAL which are not included in the simulation. This would enhance the number of events with vertices at the edge of the FCAL. The vertex distribution in Y also shows reasonable agreement. The spikes at the centre of the modules indicate events which only fire one module in the first stack hit. In this case the vertex is assumed to have occurred at the center of the relevant module. The Monte Carlo appears to overestimate the number of these events. In the case of events with an identified muon, the vertex is estimated from the extrapolated position of the muon at the first stack hit. The results of this algorithm has been shown to agree well with data in Section 3.4.4 and hence the small discrepancies observed in the vertex distributions using the centre of gravity method are not that important.

The distribution of the first stack hit contains two interesting features. The trigger threshold, described in Section 3.4.2, has been applied to the Monte Carlo. The good agreement in the number of events occurring in Stack 4 gives confidence that this threshold is being applied at the correct level. The overestimate of the number of events in Stack 1 by the Monte Carlo can be explained by the phenomenon of self-vetoing in which events occurring close to the front of the FCAL backsplash into the veto plane covering the face of the FCAL. The trigger conditions for FCAL interactions specify that there be no signal in this veto plane, so this type of event would

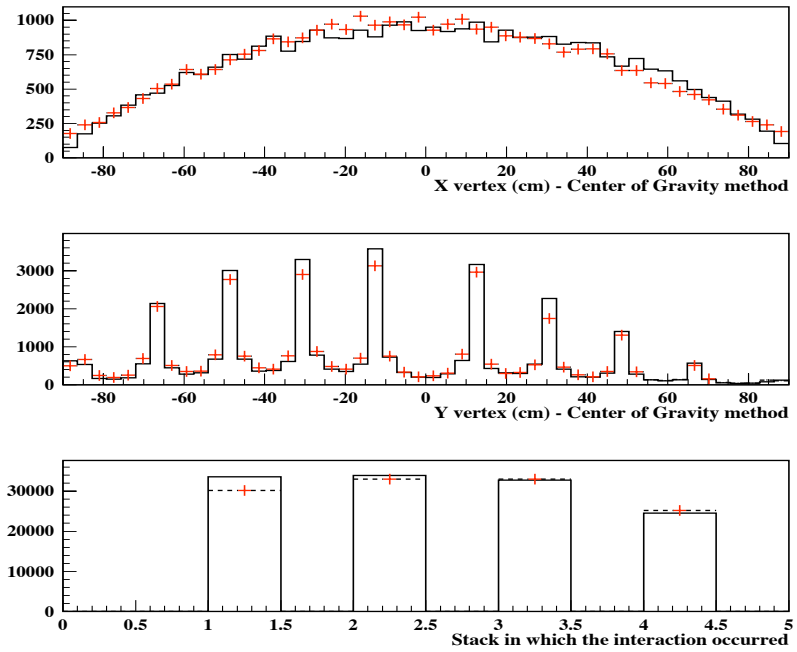

Figure 4.4: FCAL vertex distributions for ν_μ^{CC} events. The vertices have been calculated using the center of gravity method. The data points are shown overlaid on the Monte Carlo histogram and the distributions are normalised to the same number of events.

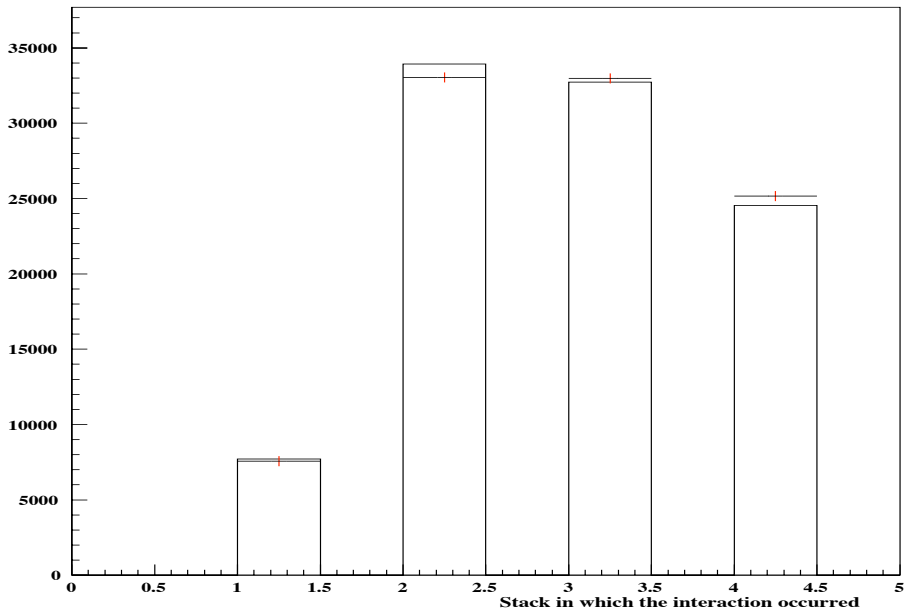

Figure 4.5: Distribution of the stack in which the ν_μ^{CC} interaction occurred. A cut requesting less than 10% of the event energy in stack 1 has been applied. The data points are overlaid on the Monte Carlo histogram and the distributions have been normalised to the same number of events.

not satisfy the trigger conditions. The degree of belief in this hypothesis increases when the distribution of Stack 1 events in which less than 10% of the total hadronic shower energy is deposited in Stack 1 is plotted. Such events most likely occur close to the end of the first stack and the level of backsplash is expected to be small. This distribution is shown in Figure 4.5 and the agreement between Monte Carlo and data is reasonable.

4.3.2 Selection Criteria

An event was assumed to be a ν_μ charged current event if it satisfied the following criteria :

- **Trigger Condition :** The FCAL trigger must have fired. The trigger efficiency has been discussed in Section 3.4.2. The trigger threshold occurs at approximately 4.0 mips in the data. Using the Monte Carlo-data relative energy scale obtained in Chapter 3 this corresponds to a threshold in the Monte Carlo of 3.2 mip.

- **Presence of a muon :** A track passing the muon identification cuts described above must exist.

- **Association with an FCAL event :** The backward extrapolation of the muon track must lie within 30 cm of the event vertex determined using the centre of gravity vertexing algoritm.

The event was considered to be induced by a ν_μ if the charge of the muon candidate in the event was negative, otherwise it was considered to be a $\overline{\nu_\mu}$ interaction.

Selection Efficiency

The efficiency of these cuts has been calculated using a sample of ν_μ^{CC} Monte Carlo events. Table 4.3 presents the number of events which pass each cut, the relative efficiency of each cut and the total efficiency breakdown. Note that the fiducial area cuts have been applied at the beginning of the analysis. The efficiencies quoted refer to events within the fiducial area.

The average selection efficiency for ν_μ charged current events, in the fiducial area described above, is $(66.5 \pm 0.4)\%$ where the uncertainty is only statistical. The calculation of this efficiency included Stack 4 events, which, as Table 4.3 shows, differ markedly from events occurring in Stacks 1 to 3. If Stack 4 events are neglected, the average efficiency rises to $(70.0 \pm 2.0)\%$. The reason for the difference is that many events in Stack 4 do not deposit

Stack 1			
Cut	Number of events	Efficiency	Relative Efficiency
Fiducial Volume	46245	100.0%	100%
Trigger threshold	43508	94.0 %	94.0 %
$N_\mu > 0$	33486	72.4 %	77.0 %
Vertex association	32711	70.7 %	97.7 %
$E_\mu > 3$	32711	70.7 %	100 %
Stack 2			
Cut	Number of events	Efficiency	Relative Efficiency
Fiducial Volume	45767	100.0 %	100%
Trigger threshold	42565	93.0%	93.0%
$N_\mu > 0$	33023	72.2%	77.6%
Vertex association	32317	70.6%	97.9%
$E_\mu > 3$	32317	70.6%	100%
Stack 3			
Cut	Number of events	Efficiency	Relative Efficiency
Fiducial Volume	44762	100%	100%
Trigger threshold	41239	92.1%	92.1%
$N_\mu > 0$	31692	70.8%	76.8%
Vertex association	31168	69.6%	98.3%
$E_\mu > 3$	31159	69.6%	99.9%
Stack 4			
Cut	Number of events	Efficiency	Relative Efficiency
Fiducial Volume	42617	100%	100%
Trigger threshold	32464	76.1%	76.1%
$N_\mu > 0$	23374	54.8%	72.0%
Vertex association	23238	54.5%	99.4%
$E_\mu > 3$	23137	54.2%	99.6%
Global efficiencies (averaged over all stacks)			
Cut	Number of events	Efficiency	Relative Efficiency
Fiducial Volume	179391	100%	100%
Trigger threshold	159776	89.0%	89.0%
$N_\mu > 0$	121575	67.7%	76.0%
Vertex association	119434	66.6%	98.2%
$E_\mu > 3$	119324	66.5%	99.9%

Table 4.3: ν_μ charged current event selection efficiency for events beginning in each stack.

enough energy to satisfy the FCAL trigger conditions. In the other stacks the major contribution to the loss of efficiency is the acceptance of the muon chambers for the primary muon.

Background Estimate

The background for ν_μ charged current events consists of :

- Decay in flight of π^- or K^- in ν_μ^{NC} interactions.
- Hadron punchthrough in ν_μ^{NC} events
- Decay in flight of π^- or K^- in ν_μ^{CC} and $\overline{\nu}_\mu^{CC}$ interactions where the primary muon is lost.
- Hadron punchthrough in ν_μ^{CC} or $\overline{\nu}_\mu^{CC}$ events in which the primary muon is lost.

Other sources, such as cosmic ray muons which fake a primary muon track in time with an FCAL interaction and which are not vetoed by the veto planes and beam muons leaking through the veto planes, contribute a neglible amount to the background in the ν_μ^{CC} sample.

In general, muons from meson decay are indistinguishable from the primary muon in charged current interactions. The only means of discriminating between the decay background and the signal is by measuring the angle the decay muon makes with the parent meson. This is impossible for decays within the FCAL volume and, as the kink angle is generally small, meson decays in the drift chamber volume are usually not resolvable. The contamination is, however, small. The relative contribution to the ν_μ^{CC} event sample from π^-/K^- decay and hadron punchthrough in ν_μ^{NC} and $\overline{\nu}_\mu^{CC}$ interactions was estimated from simulation to be less than 0.05% of the total ν_μ^{CC} sample.

The contribution from hadron punchthrough in ν_μ^{CC} , averaged over all stacks, is $(0.11 \pm 0.05)\%$.

4.4 The NOMAD Data and Event Statistics

The NOMAD experiment was originally scheduled to start taking data in 1994. The FCAL, however, was only instrumented in mid 1995 in which there were several distinct data taking periods. These were :

- **4 module data :** Between May 18th and June 24th 1995 only four drift chamber modules were installed in the target region of the detector.

Data Statistics			
Sample	source	Initial Statistics (filtered for at least one muon)	After fid. cuts
Data	11-module 1995	718,058	489,318
	1996	4,902,776	3,076,792

Table 4.4: Statistics of data sample used in this analysis

Monte Carlo Statistics				
Sample	source	Initial Statistics	After fid. cuts	Identified muon
	ν_μ^{CC}	288,012	179,391	138,532
Monte Carlo	ν_μ^{NC}	57,945	35,428	74
	ν_μ induced charm	85,226	54,803	43,789
	$\overline{\nu_\mu}^{CC}$	72,144	37,141	33,231

Table 4.5: Statistics of the Monte Carlo simulation samples used in this analysis

During this period 2.8×10^{18} p.o.t. were delivered to the neutrino target.

- **8 module data :** In the period July 5th to August 15th 1995 a total of 8 drift chamber modules were present in the target region of the detector. The integrated intensity delivered by the SPS in this period was 3.3×10^{18} p.o.t.

- **11 module data :** After August 22nd 1995 the drift chamber target consisted of the full 11 modules. At the end of the run on October 11th, a total intensity of 3.0×10^{18} p.o.t. was delivered to the neutrino target in this period.

During 1996 all drift chambers were fully functional. At the end of the 1996 run the SPS had delivered an integrated intensity for the year of 1.5×10^{19} p.o.t.

Table 4.4 summarizes the available statistics in the data sample used in this analysis and Table 4.5 does the same for the Monte Carlo samples. Only 11 module data is used from the 1995 data set. The reconstruction of the 8 module data was not considered to be reliable. The entire 1996 data set was included.

Note that for reasons of storage space the data used here has been filtered for events containing at least one muon. The reference fiducial volume is

$$|X| \leq 70 \text{ cm} \;\; ; \;\; |Y| \leq 70 \text{ cm} \;\; ; \;\; -200 \text{ cm} \leq Z \leq -90 \text{ cm} \qquad (4.4)$$

4.5 Reconstruction of ν_μ^{CC} Interaction Kinematics

Most analyses in high energy physics are carried out in terms of variables which uniquely define an interaction. These variables have already been described in Chapter 1 and so only a brief summary will be included here. Referring to Figure 1.1 each of the particles in the interaction has an associated 4-momentum. The 4-momenta of the incoming neutrino and outgoing lepton are denoted k^μ and l^μ respectively, q^μ is the four-momentum transferred to the hadronic system and P^μ is the 4-momentum of the nucleon.

The kinematic variables which may be determined by a measurement of these 4-vectors are :

- the square of the centre of mass energy, s.
- the energy transfer to the hadronic system, ν.
- the square of the 4-momentum transfer to the hadronic system, Q^2.
- the square of the invariant mass of the hadronic system, W^2.
- the Bjorken scaling variable, x_{Bj}.
- the fraction of energy lost by the neutrino (Bjorken y) y_{Bj}.

The kinematically allowed regions of phase space correspond to $Q^2 > 0$ and $W > M_N$. However structure functions are, in general, only defined above a certain threshold. In the case of the GRV-HO[55] structure functions used to generate the Monte Carlo sample used in this analysis there is an implicit cut of $Q^2 > 0.3$ $(\text{GeV/c})^2$. In Section 3.4.4 it was pointed out that the simulation of hadronic showers below 5 GeV has been seen to be unreliable. In this analysis only events with visible hadronic energy greater than this value are considered. Therefore the two explicit cuts which have been applied are

$$Q^2 > 0.3 \;\; (\text{GeV/c})^2 \;\; , \;\; E_{had} > 5 \text{ GeV} \qquad (4.5)$$

4.5.1 Hadronic and Neutrino Energy Reconstruction

The visible hadronic energy, E_{had}, is a reasonable estimator of the energy transfer ν. The algorithm used to construct this estimator is reasonably simple.

1. Take the visible energy deposited in the FCAL using the algorithm developed in Chapter 3.

2. Add in the energy of the tracks leaking from the coil, assigning the mass of a pion to those which have not been identified as a muon. Tracks arising from secondary interactions in the drift chamber region are neglected.

The energy of the leakage tracks is a second order contribution to the total energy and as such no attempt is made to add in the contribution from neutral hadrons measured in the HCAL or from unassociated clusters in the ECAL. It is assumed that most of the event energy is absorbed in the FCAL volume. This is a safe assumption in the case of stacks 1,2 and, to a somewhat lesser extent, 3. However, much of the energy will have leaked in events occurring in Stack 4. It is not expected that Stack 4 events will provide reliable energy measurements.

Hadronic Energy Resolution

Figures 4.6 and 4.7 show the comparison of Monte Carlo input and reconstructed hadronic energy. The average amount of energy loss and the resolution of E_{had} is summarised in Table 4.6. As expected, the energy measurement for events occurring in Stacks 1 and 2 are reasonably accurate. Only a small amount of the energy is lost, usually in the form of neutral particles. 11% of the energy is lost in events originating in Stack 3, a consequence of the event occurring closer to the back face of the FCAL. In Stack 4 a substantial amount of the energy is lost. The resolutions measured here are comparable to those measured in neutrino events in the drift chamber target[14].

The hadronic energy bias as a function of the X and Y positions of the vertex is shown in Figure 4.8. The plots contain events from all stacks. The vertical lines mark the bounds of the fiducial area. The uninstrumented gap at the center of the FCAL imposes a dramatic degradation on the hadronic energy resolution. Omitting this region from the fiducial volume has the unfortunate consequence of omitting events from the core of the neutrino beam and hence a large fraction (approximately 30%) of the available statistics. It was decided that this region would be included in the fiducial

Stack	Average amount of energy loss (%)	E_{had} resolution (%)
1	1.7	30.0
2	2.8	30.0
3	11.1	31.6
4	34.8	34.1

Table 4.6: Average percentage of energy loss and E_{had} resolution for events occurring in each stack.

volume but the different energy resolution in this region must be considered in later analyses.

Intrinsic Energy Resolution of the FCAL

The intrinsic energy resolution of a calorimeter is usually presented in the form

$$\frac{\sigma(E)}{E} = \frac{R}{\sqrt{E(GeV)}} \tag{4.6}$$

where R is detector dependent and defines the precision to which a given energy can be measured in the presence of shower fluctuations. This number is often used as a figure of merit to judge the capabilities of different calorimeters. The energy resolution for the FCAL cannot be measured without a test beam, just as a standard calibration procedure could not be applied, but an idea of the intrinsic resolution may be obtained by studying Monte Carlo interactions. The purpose of this section is to provide some feeling for, but not a precise measurement of, the capabilities of the detector.

The intrinsic resolution will depend upon the stack in which the event occurred. As usual, it is expected that the resolution derived from events originating in Stacks 1 to 3 will be credible. The resolution will be determined from events occurring within the first three stacks and in the standard fiducial area.

Samples of pions at different energies were generated using the test beam facility of GENOM and the response of the FCAL at each energy was observed. The mean and standard deviation of a gaussian fit to the FCAL response is displayed in Table 4.7. The RMS deviation from the mean is also shown to indicate the deviation of the response from gaussian behaviour.

A plot of the standard deviation, σ, of these distributions as a function of $\sqrt{E}$ is presented in Figure 4.9. According to the straight line fit in Figure

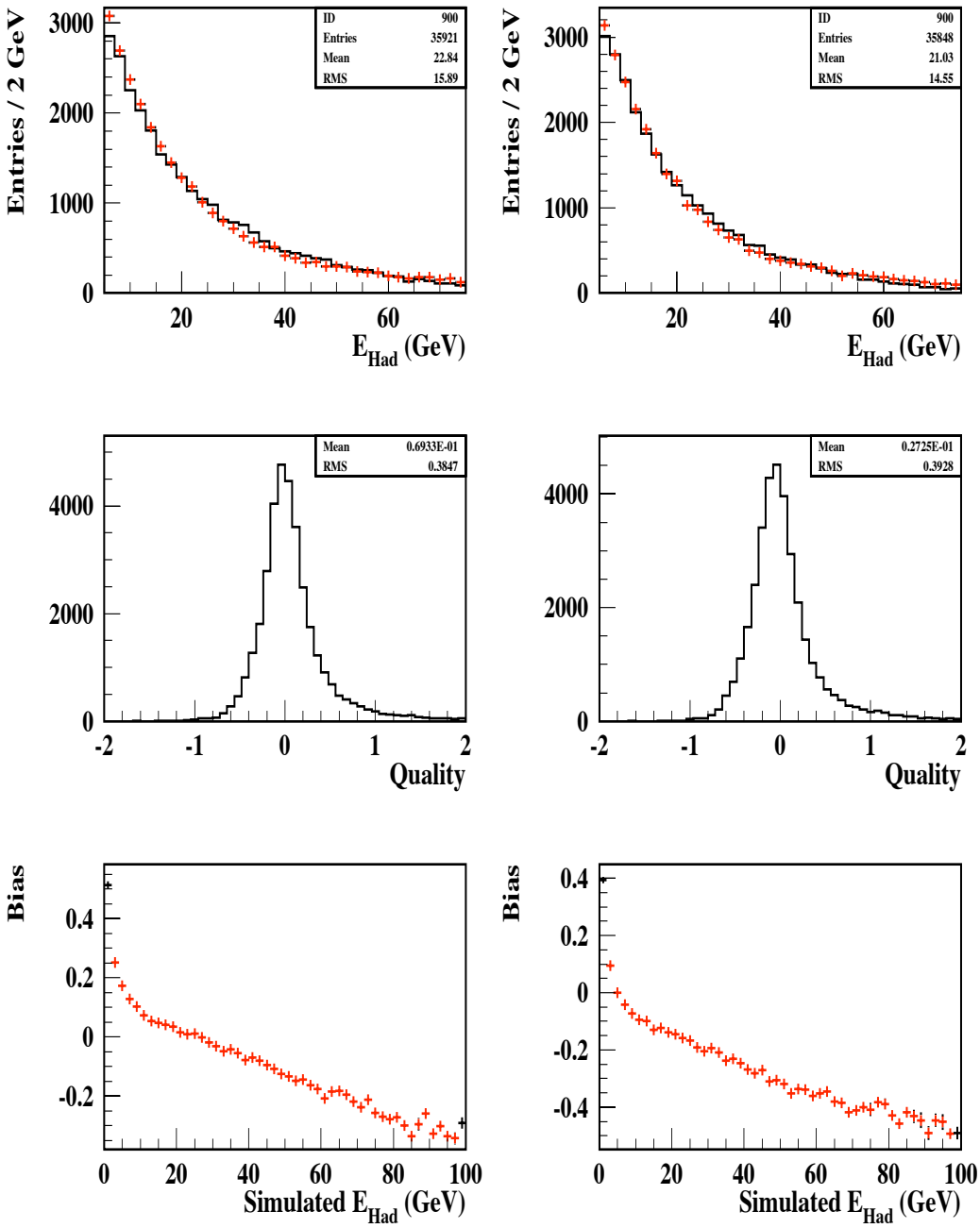

Figure 4.6: Comparison of the reconstructed and simulated values for the hadronic energy of events in Stack 1 (left) and Stack 2 (right). The top plot is a simple comparison. The middle plot shows the quality and the bottom plot shows the bias as a function of the simulated value.

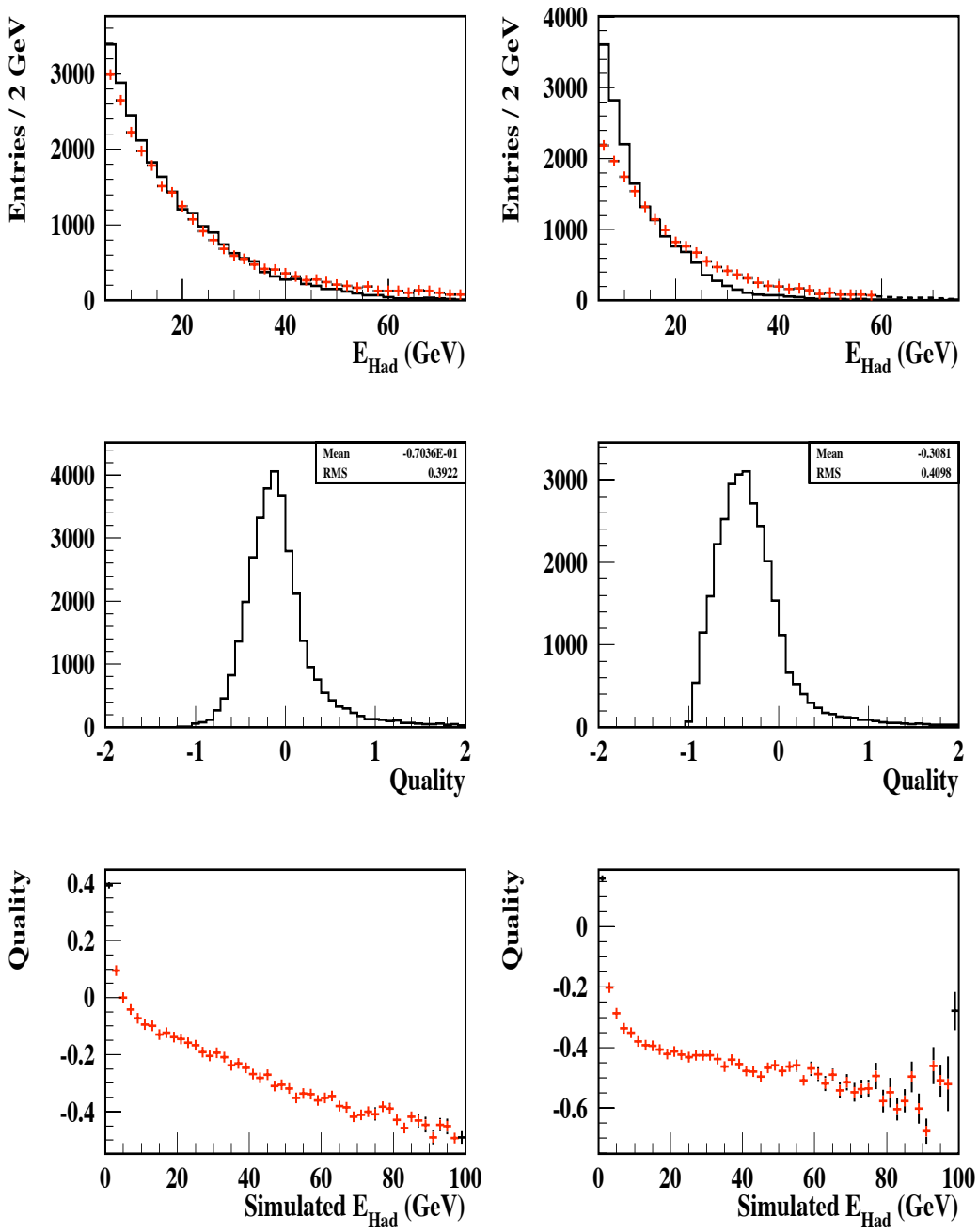

Figure 4.7: Comparison of the reconstructed and simulated values for the hadronic energy of events in Stack 3 (left) and Stack 4 (right). The top plot is a simple comparison. The middle plot shows the quality and the bottom plot shows the bias as a function of the simulated value.

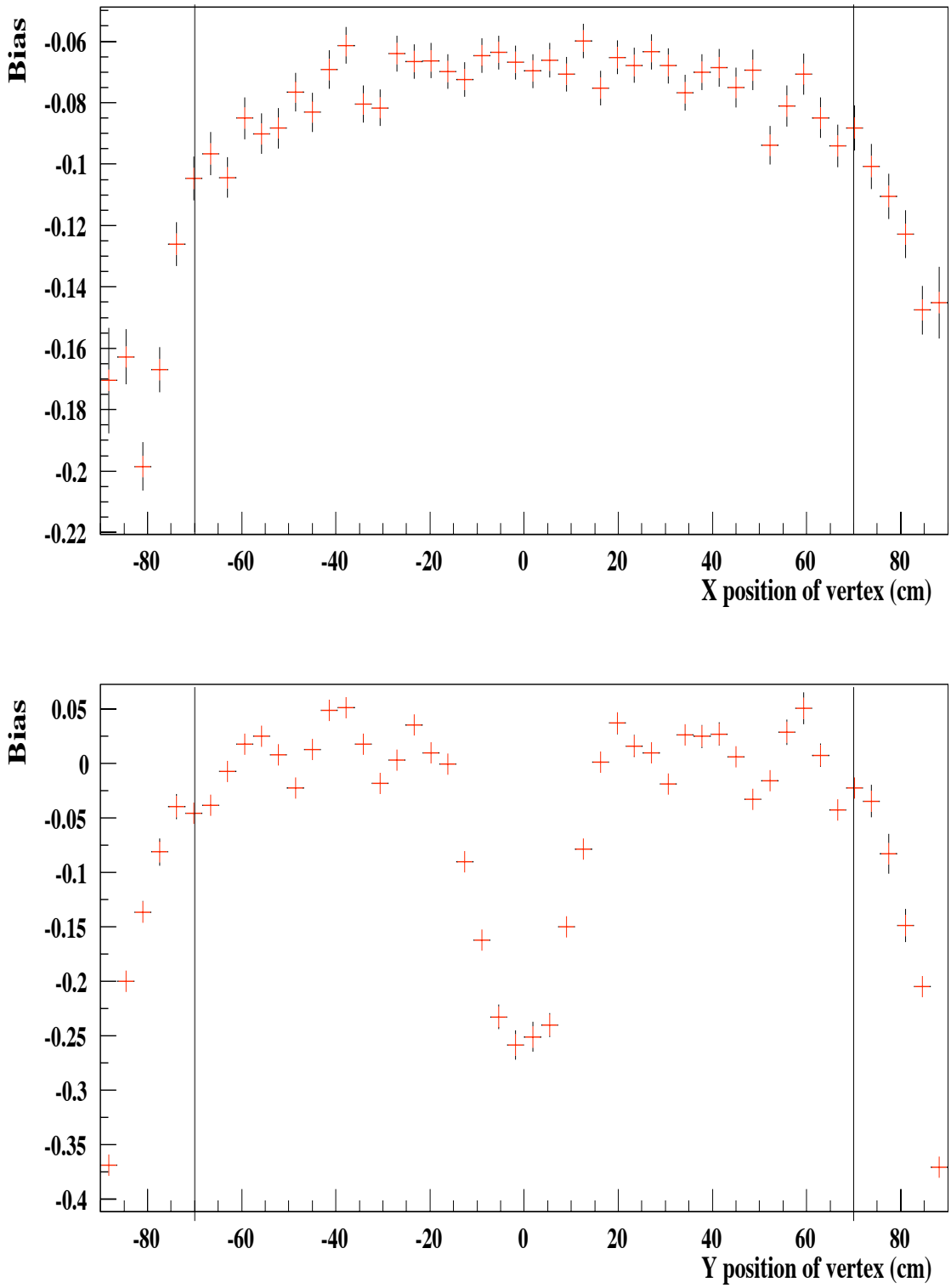

Figure 4.8: Hadronic energy bias as a function of the X and Y position of the vertex. The dip in the bias at central values of Y results from energy absorption in the mid FCAL gap.

Hadronic Energy (GeV)	Mean (GeV)	Standard Deviation (GeV)	RMS (GeV)
1.0	1.41 ± 0.01	1.02 ± 0.03	1.56
4.0	4.03 ± 0.01	1.59 ± 0.03	2.04
10.0	9.85 ± 0.03	2.67 ± 0.05	2.87
15.0	14.7 ± 0.05	3.47 ± 0.05	3.91
20.0	18.98 ± 0.07	4.14 ± 0.07	4.49
25.0	23.8 ± 0.1	4.6 ± 0.1	4.87
30.0	28.4 ± 0.1	5.4 ± 0.1	5.6
40.0	37.6 ± 0.1	5.9 ± 0.1	6.4
50.0	47.3 ± 0.3	6.9 ± 0.2	8.0
60.0	56.3 ± 0.4	7.6 ± 0.3	8.6

Table 4.7: The mean and width of the energy reponse distributions of the FCAL at different simulated hadronic energies.

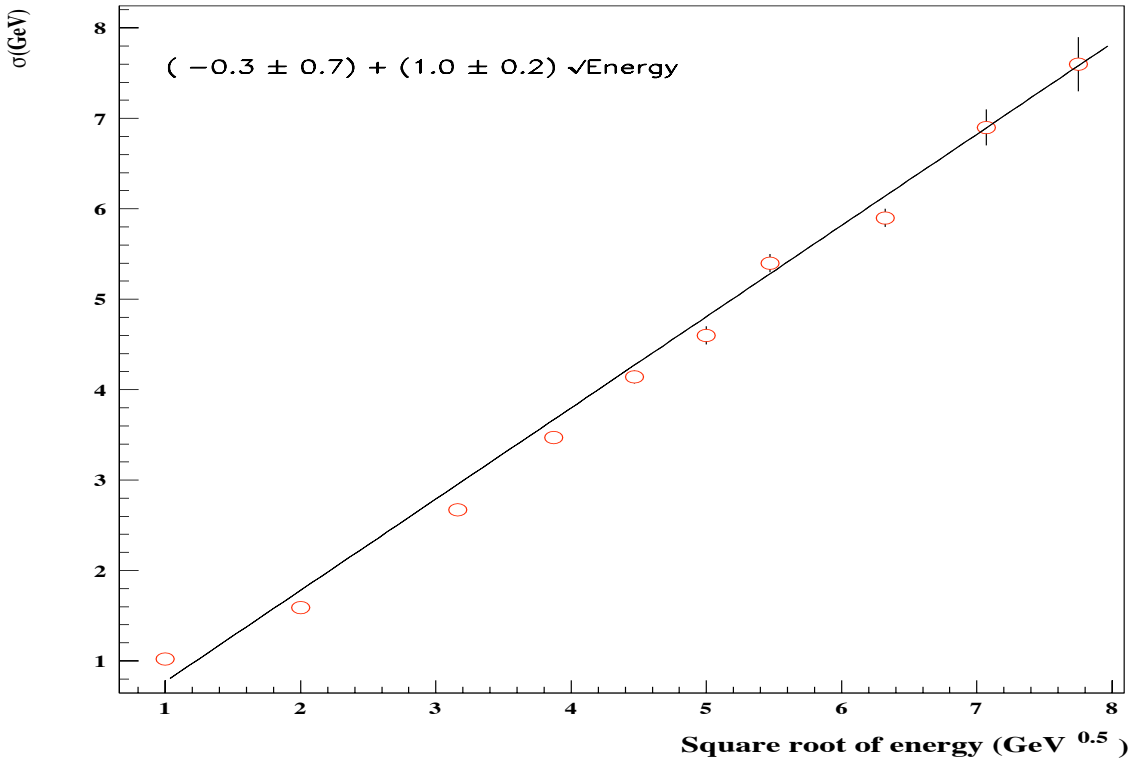

Figure 4.9: The simulated width of the FCAL energy response distributions as a function of the square root of the simulated energy of test beam pions, overlaid with a fit to a straight line.

4.9 the intrinsic energy resolution of the FCAL is

$$\frac{\sigma(E)}{E} = \frac{100.0\%}{\sqrt{E(GeV)}} \tag{4.7}$$

This value should be regarded as (a) an approximation to the true intrinsic energy resolution and (b) a lower limit. The reason for this is that Equation 4.6 is correct only for compensating calorimeters. That is, calorimeters which display the same response to the purely hadronic part of an hadronic shower as to the purely electromagnetic part (induced mainly by π^0 particles in the shower). Since the energy dissipation processes are different for these two components of the shower it is not surprising that the calorimeter response is dependent upon the particular component. The compensation property is described in terms of the ratio

$$\frac{e}{\pi} = \frac{\frac{e}{mip}}{< f_{em} > \frac{\pi^0}{mip} + < f_h > \frac{h}{mip}} \tag{4.8}$$

where $\frac{e}{mip}$ is the visible part of the electron energy with respect to a mip, $< f_{em} >$ is the average electromagnetic part of the pion energy, $\frac{\pi^0}{mip}$ is the visible part of the π^0 energy component with respect to a mip, $< f_h >$ is the average hadronic part of the pion energy and $\frac{h}{mip}$ is the visible part of the hadronic energy component with respect to a mip. In terms of this ratio the intrinsic energy resolution is defined as

$$\frac{\sigma(E)}{E} = \frac{R}{\sqrt{E}} + B(\frac{e}{\pi} - 1) \tag{4.9}$$

where B is a detector dependent parameter that usually must be ascertained from the experiment. Non-compensating calorimeters in general have $\frac{e}{\pi} > 1$. Since the FCAL is non-compensating the resolution presented above is the theoretical best that can be expected. None of the studies in this thesis explicitly use the energy resolution in this form.

The RMS values in Table 4.7 are consistently higher than standard deviation indicating a wider response at all energies. A more realistic estimate of the intrinsic resolution can be made by substituting the RMS values for the standard deviations. Repeating the fit yields an intrinsic energy resolution of

$$\frac{\sigma(E)}{E} = \frac{104.0\%}{\sqrt{E(GeV)}} \tag{4.10}$$

Stack	Average amount of energy loss (%)	E_ν resolution (%)
1	1.5	13.4
2	3.3	14.0
3	6.6	14.8
4	14.9	17.5

Table 4.8: Average percentage of energy loss and E_ν resolution for events occurring in each stack.

which is probably more realistic. The resolution is somewhat better than that measured in the HCAL (which has a resolution of approximately $120\%/\sqrt{E(GeV)}$). This is to be expected as the instrumented region of the HCAL is only half as deep as that in the FCAL and so the shower fluctuations are much larger.

Neutrino Energy Resolution

The visible neutrino energy, E_{vis}^{ν} is simply the sum of the hadronic energy and the energy of the primary muon and is a good approximation to the actual neutrino energy. The quality of the reconstruction of the neutrino energy is shown in Figures 4.10 and Figures 4.11. The average amount of energy loss and the resolution in E_ν is shown in Table 4.8

The distributions for E_ν show the same qualitative features as those for E_{had}. The energy resolution is approximately 14.0% in all stacks except Stack 4. This is twice as good as the resolutions for E_{had} due to the (usually) well-reconstructed muon.

Comparison of Data and Monte Carlo

Figures 4.12 and 4.13 show the distributions for the reconstructed visible hadronic and neutrino energies in the 1995 11 module data and the simulation. The distributions agree well. The discrepancy between data and Monte Carlo in the neutrino energy spectrum measured in the drift chamber region (see Section 3.4.4) is not apparent in these distributions. This is most probably due to the relatively poor energy resolution of the FCAL. The measured FCAL response to a 40 GeV shower, for example, is expected to fluctuate between 34 GeV and 46 GeV in 68% of the events. This behaviour smears out fine details.

The muon energy spectrum is shown on a linear scale (top) and logarithmic scale (bottom) in Figure 4.14. The distribution has a longer tail in the data than in the Monte Carlo. In part, this is due to a problem with

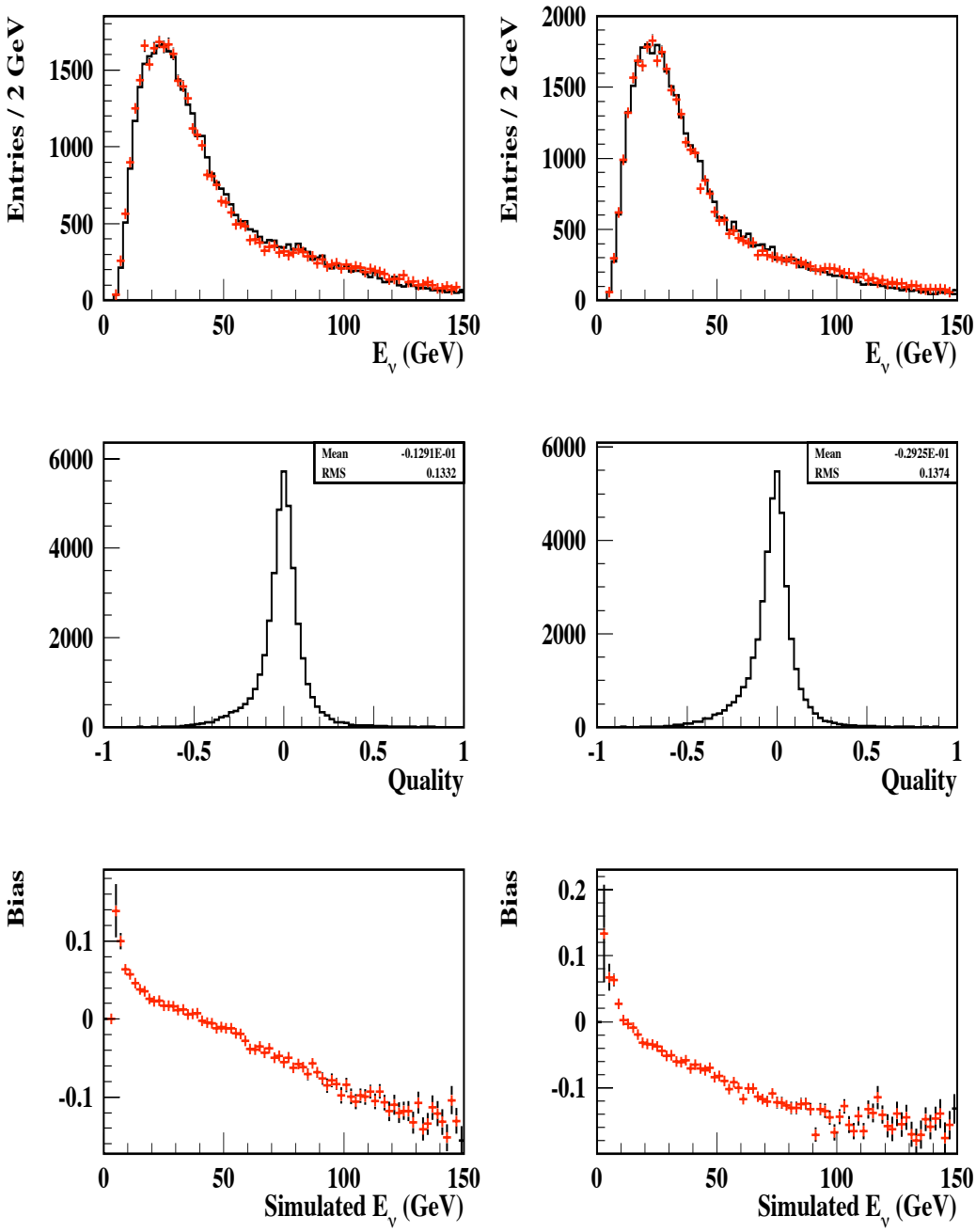

Figure 4.10: Comparison of the Monte Carlo input and Monte Carlo reconstructed distributions for the neutrino energy of events in Stack 1 (left) and Stack 2 (right). The top plot is a simple comparison. The middle plot shows the quality and the bottom plot shows the bias as a function of the simulated value.

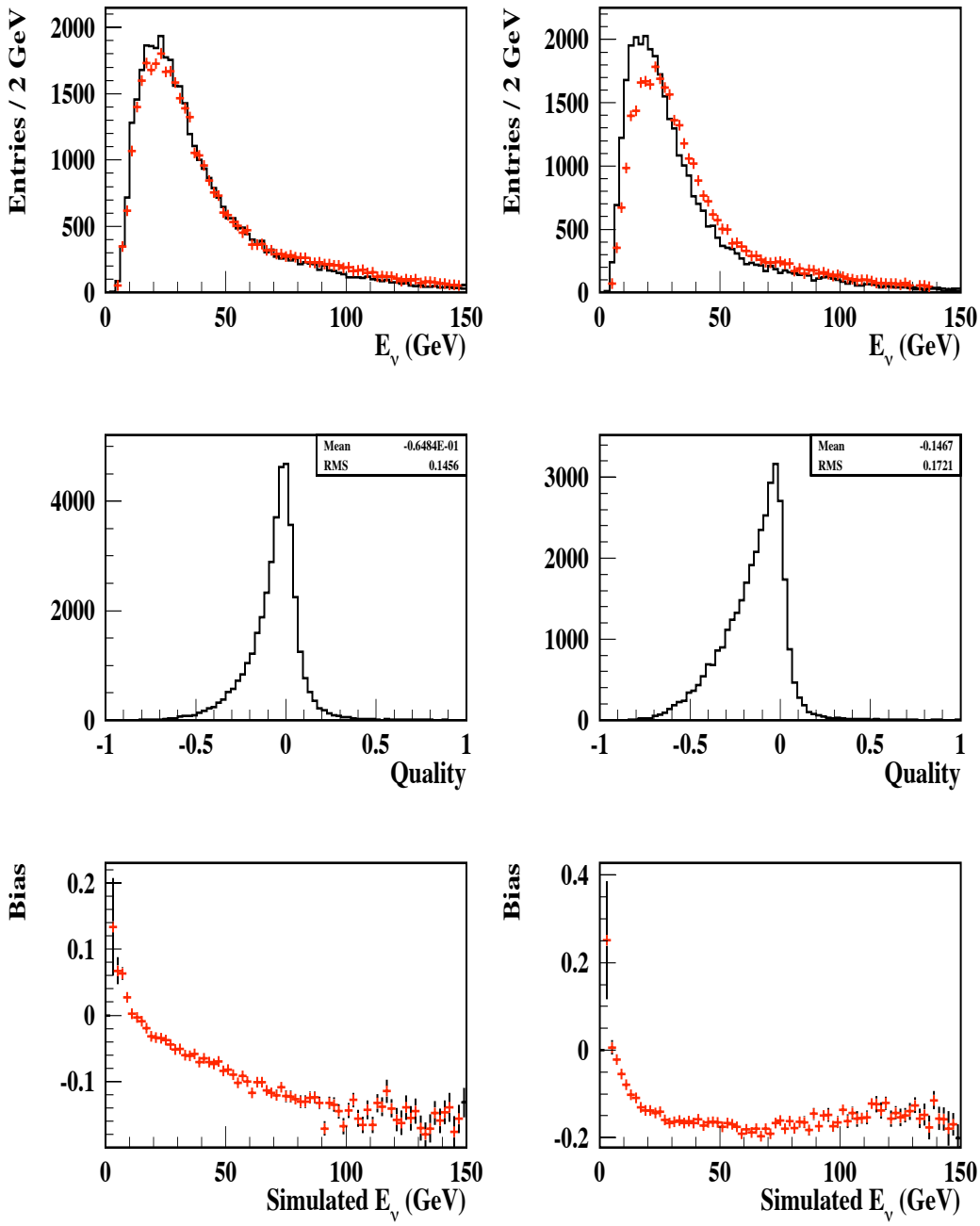

Figure 4.11: Comparison of the Monte Carlo input and Monte Carlo reconstructed distributions for the neutrino energy of events in Stack 3 (left) and Stack 4 (right). The top plot is a simple comparison. The middle plot shows the quality and the bottom plot shows the bias as a function of the simulated value.

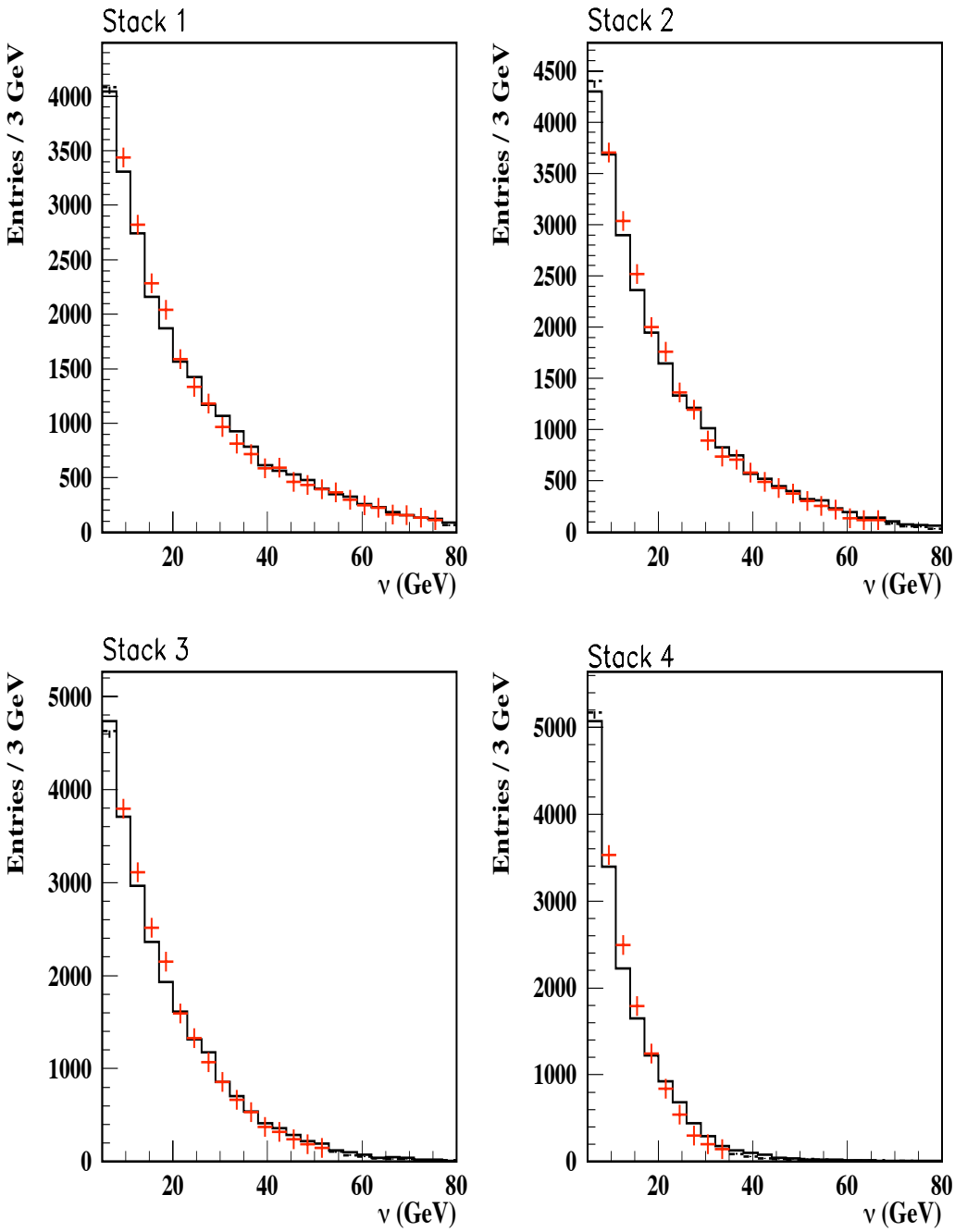

Figure 4.12: Comparison of the data (points) and Monte Carlo (histogram) distributions for the visible hadronic energy E_{had} in events originating in each stack. The data and Monte Carlo distributions have been normalised to equal areas.

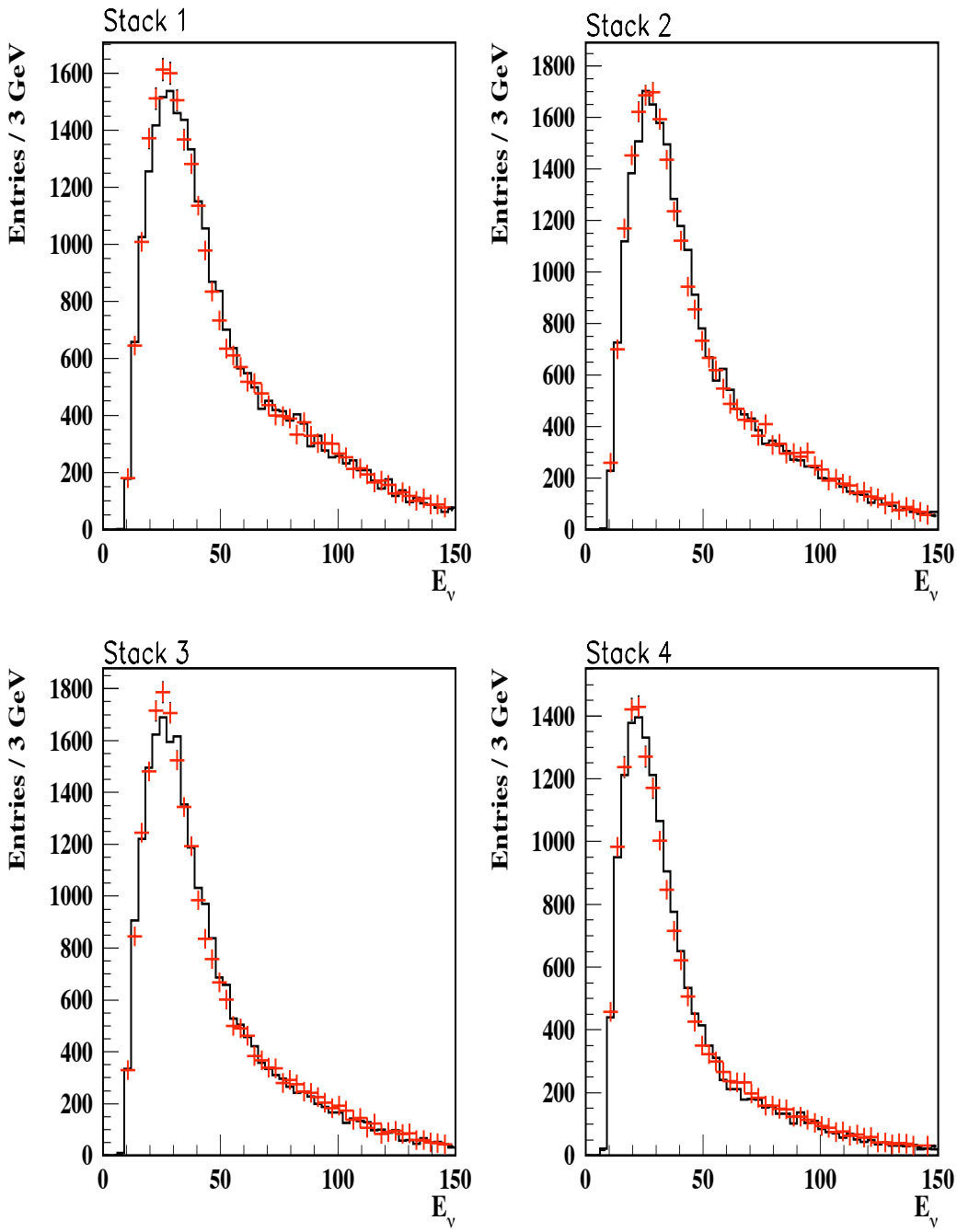

Figure 4.13: Comparison of the data (data) and Monte Carlo (histogram) distributions for the visible energy E_{vis} in events originating in each stack. The data and Monte Carlo distributions have been normalised to equal areas.

the alignment of the drift chambers in part of the 1995 run. The effect is most clearly observed in the distribution of $\frac{1}{p}$ in Figure 4.15 (top plot). A constant offset in the inverse momentum is symptomatic of an alignment problem. In order to take care of this, a constant $\frac{1}{500(GeV/c)}$ was added to the inverse momentum in the data, resulting in the distribution in Figure 4.15 (bottom plot). Even with this correction, however, there is a difference in the shape of the tail of the distributions. There are two possible reasons for this: the first is that the structure functions used in the calculation of the cross section do not exactly describe the NOMAD data and the second is that the Monte Carlo beam profile does not model the real beam.

The neutrino beam consists predominantly of ν_μ which arise from the decay of π^+ and K^+ mesons in the beam. Neutrinos with energies less than 60 GeV come mainly from π^+ decay, whereas those possessing an energy above 60 GeV originate from K^+ decays. The shape of the ν_μ energy spectrum, and hence the shape of the primary muon energy spectrum, is therefore dependent upon the ratio of pions to kaons produced in the debris of the proton-beryllium interaction. The SPY collaboration has measured this ratio over a secondary meson momentum range from 7 GeV/c to 135 GeV/c [37]. Using their results, weighting tables were constructed in the same format as those introduced in Section 3.4.4 and applied to the simulated events. Figure 4.16 shows the primary muon energy spectra, in both linear and logarithmic scale, after the weighting process was applied. There has been a small, but significant, change in the shape of the tail and the chi-square of the comparison between the simulation and the data has improved from 274.2 for 49 degrees of freedom to 153.8 for 49 degrees of freedom. As the chi-square measures show, however, the simulation still does not describe the data exactly. The use of structure functions which do not describe the data exactly is the most probable cause of this residual discrepancy. This will be touched upon in Chapter 5 but for now it should be noted that the remaining difference is small and has little effect on the kinematic distributions to be studied in the next section.

4.5.2 Reconstruction of the Kinematic Variables

Section 4.5 has shown that all the kinematic variables of interest can be formed from the neutrino energy and the outgoing muon momentum and direction. In this section the simulated kinematic variables, the reconstructed simulated kinematic variables, and experimental kinematic variables are compared.

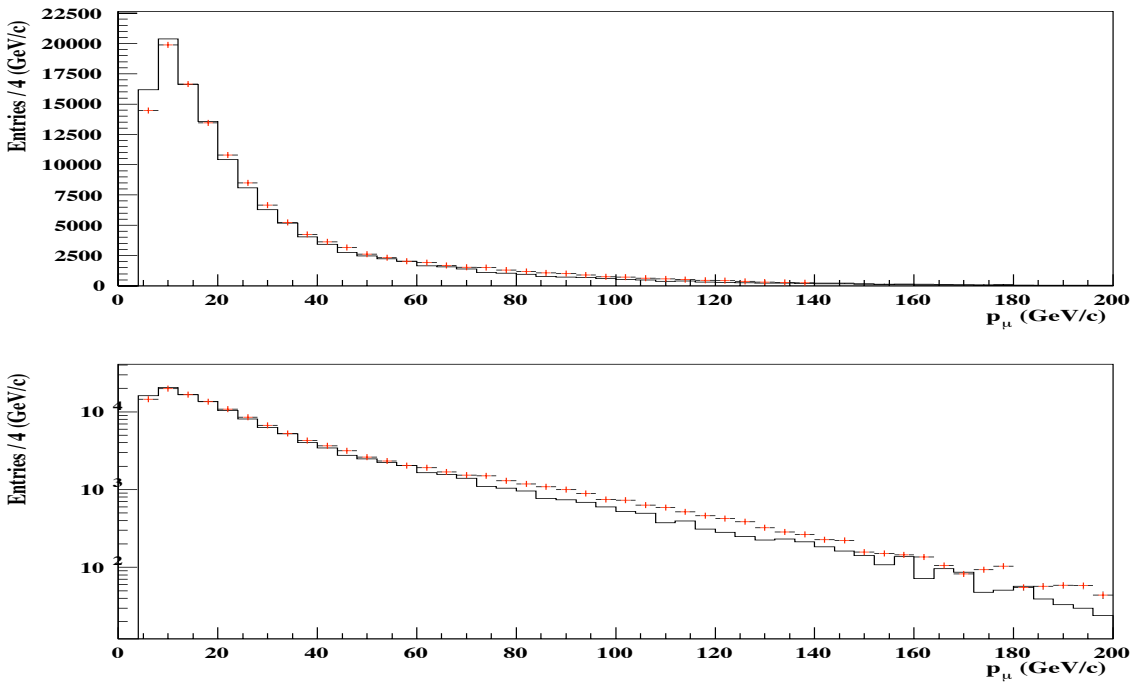

Figure 4.14: Single muon energy spectrum. The top plot is in a linear scale and the bottom plot is in a logarithmic scale on the vertical axis. The data points are overlaid on the Monte Carlo histogram.

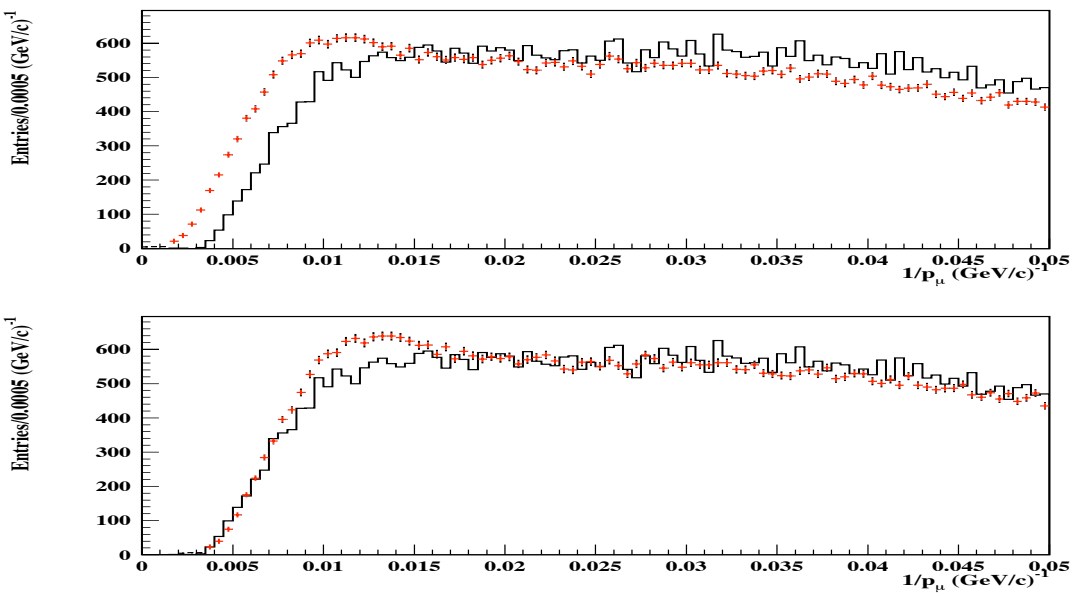

Figure 4.15: (top) Comparison of the inverse momentum distribution in 1995 data and simulation before the alignment correction. (bottom) Same comparison after the correction for the incorrect alignment was applied. The data and simulation distributions have been normalised to equal areas.

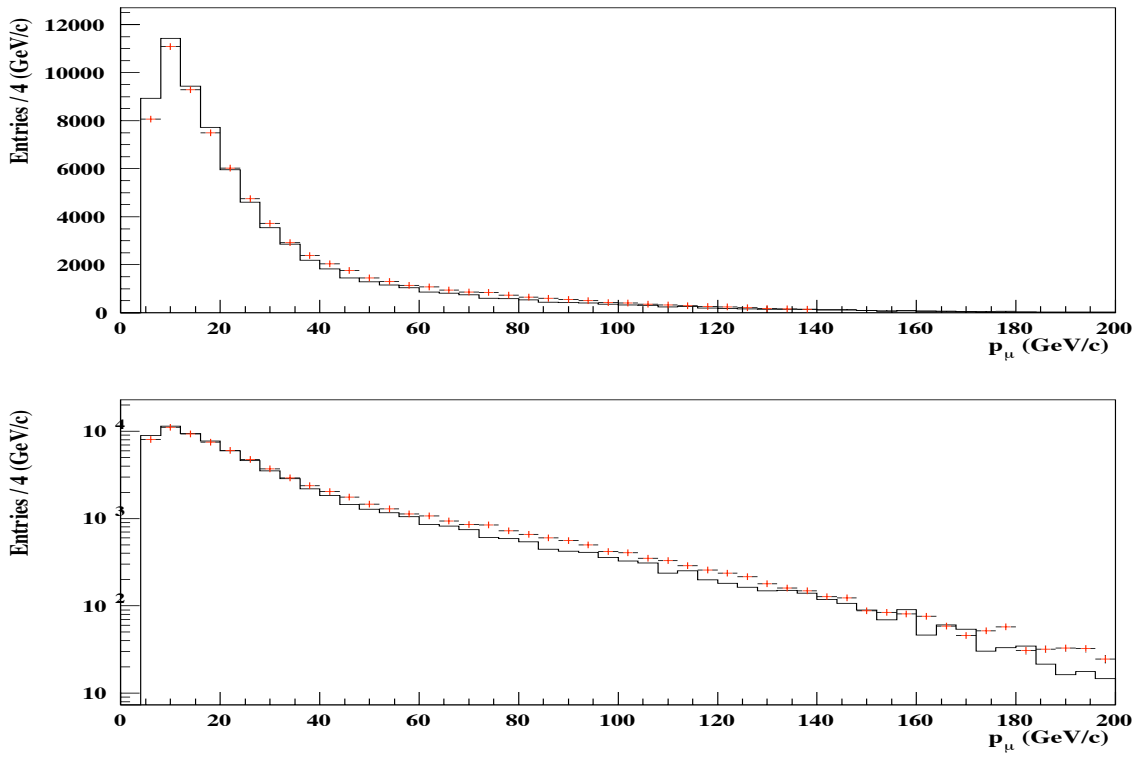

Figure 4.16: Single muon energy spectrum after correction for the SPY data have been applied. The top plot is in a linear scale and the bottom plot is in a logarithmic scale on the vertical axis. The data points are overlaid on the Monte Carlo histogram and the distributions have been normalised to equal areas.

Resolution of the Kinematic Variables

Figures 4.17, 4.18 and Figures 4.19, 4.20 show the distributions of the momentum transfer Q^2 and the Bjorken variable x_{Bj} respectively. The Q^2 reconstruction agrees well with the simulated distribution. The agreement in the x_{Bj} distribution is much worse. This is largely due to the x_{Bj} dependence on $\frac{1}{\nu}$ (Equation 1.5). Since ν tends to be overestimated the average value of reconstructed x_{Bj} is too small. The bias in the Q^2 quality becomes larger with increasing momentum transfer, mostly due to the saturation effect in the measurement of E_{had}. As a result of the ratio, Q^2/ν, the x_{Bj} quality shows little dependence on x_{Bj}.

The distributions for Bjorken y and the invariant mass of the hadronic system W^2 are shown in Figures 4.23, 4.24 and Figures 4.21, 4.22. The agreement between simulated and reconstructed variables displays a familiar pattern : Stack 1 and 2 distributions agree reasonably well, Stack 3 distributions show some obvious discrepancies which can be ascribed to energy leakage and saturation and Stack 4 distributions do not agree well at all. The magnitude of the bias in W^2 increases linearly as a function of the simulated value. Since W^2 is calculated from Q^2 (Equation 1.7) the same behaviour in the quality should be expected. The means and RMS deviations from the mean of the Monte Carlo input and Monte Carlo reconstructed distributions are summarised in Table 4.9 for each kinematic variable, as are the corresponding resolution and bias.

Comparison of Data and Monte Carlo

The reconstructed Monte Carlo distributions are compared to the corresponding experimental distributions in Figures 4.25,4.26, 4.27 and 4.28. The means and RMS deviations from the mean for the experimental and Monte Carlo reconstructed distributions are presented in Table 4.10. In general the distributions show good agreement. There is a slight systematic overestimate in the y_{Bj} distribution at high values of y_{Bj}. This is most probably due to a slightly different level of saturation in the data than in the Monte Carlo. The agreement in Q^2, W^2 and x_{Bj} is good.

Stack 1						
	ν_μ^{CC} Monte Carlo		ν_μ^{CC} MC Reconstructed			
quantity	Mean	RMS	Mean	RMS	Bias	Resolution
$Q^2(GeV/c)^2$	9.5	9.7	9.4	9.5	-3.5%	24.9%
$W^2(GeV/c^2)^2$	32.9	22.5	30.1	22.2	-15.1%	38.9%
x_{Bj}	0.22	0.15	0.25	0.19	18.1%	50.6%
y_{Bj}	0.48	0.22	0.47	0.21	1.4%	17.7%
Stack 2						
	ν_μ^{CC} Monte Carlo		ν_μ^{CC} MC Reconstructed			
quantity	Mean	RMS	Mean	RMS	Bias	Resolution
$Q^2(GeV/c)^2$	9.1	9.4	8.9	9.1	-5.3%	23.5%
$W^2(GeV/c^2)^2$	31.8	22.1	28.2	22.1	-19.0%	37.3%
x_{Bj}	0.22	0.15	0.25	0.19	21.0%	49.5%
y_{Bj}	0.48	0.22	0.46	0.21	0.9%	18.2%
Stack 3						
	ν_μ^{CC} Monte Carlo		ν_μ^{CC} MC Reconstructed			
quantity	Mean	RMS	Mean	RMS	Bias	Resolution
$Q^2(GeV/c)^2$	8.9	9.2	8.5	8.5	-9.2%	21.8%
$W^2(GeV/c^2)^2$	31.2	21.4	24.4	18.2	-29.1%	35.6%
x_{Bj}	0.22	0.15	0.28	0.20	28.0%	51.7%
y_{Bj}	0.48	0.22	0.45	0.21	-0.6%	18.2%
Stack 4						
	ν_μ^{CC} Monte Carlo		ν_μ^{CC} MC Reconstructed			
quantity	Mean	RMS	Mean	RMS	Bias	Resolution
$Q^2(GeV/c)^2$	8.1	8.2	7.6	7.5	-18.7%	21.0%
$W^2(GeV/c^2)^2$	28.7	19.8	17.5	13.4	-48.0%	34.2%
x_{Bj}	0.22	0.15	0.31	0.22	46.7%	64.0%
y_{Bj}	0.47	0.21	0.40	0.21	-18.9%	21.0%

Table 4.9: Average values of Monte Carlo simulated and reconstructed kinematic variables in deep inelastic ν_μ^{CC} interactions originating in each Stack. Also shown is the corresponding bias and resolution.

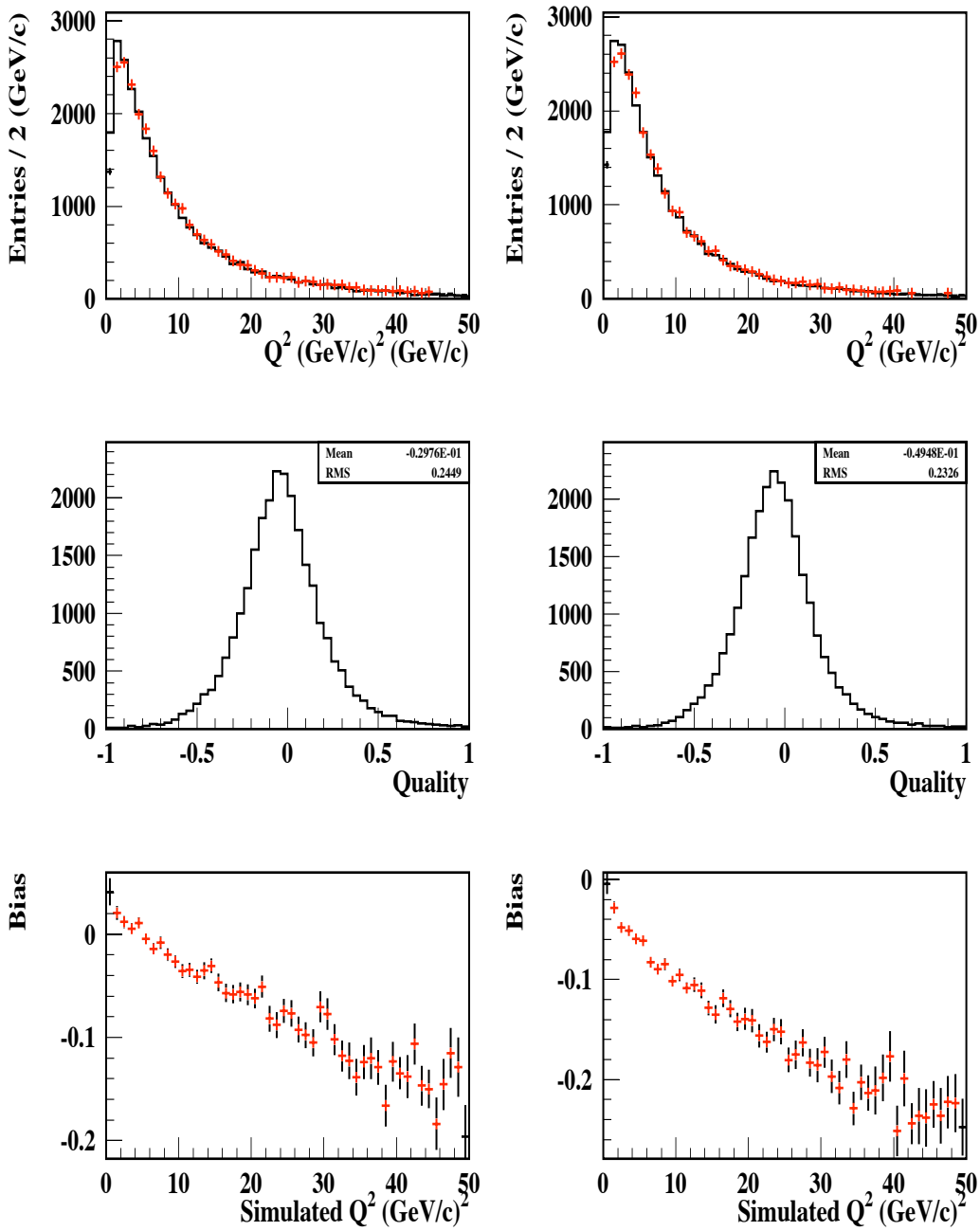

Figure 4.17: Comparison of reconstructed (points) and simulated (histogram) values of Q^2 for events occurring in Stack 1 (left) and Stack 2 (right). The middle plots show the quality and the bottom plots show the bias as a function of the simulated value.

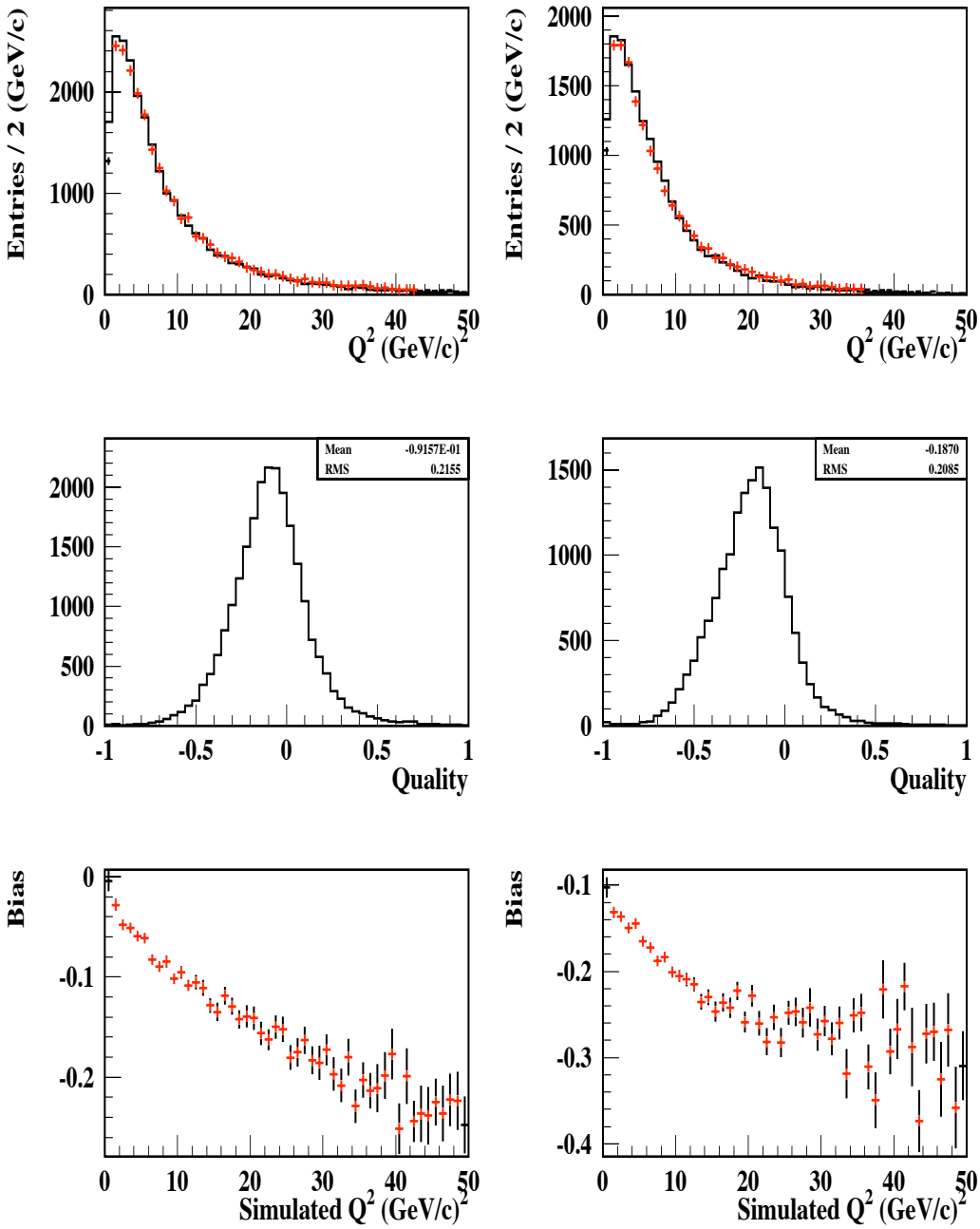

Figure 4.18: Comparison of reconstructed (points) and simulated (histogram) values of Q^2 for events occurring in Stack 3 (left) and Stack 4 (right). The middle plots show the quality and the bottom plots show the bias as a function of the simulated value.

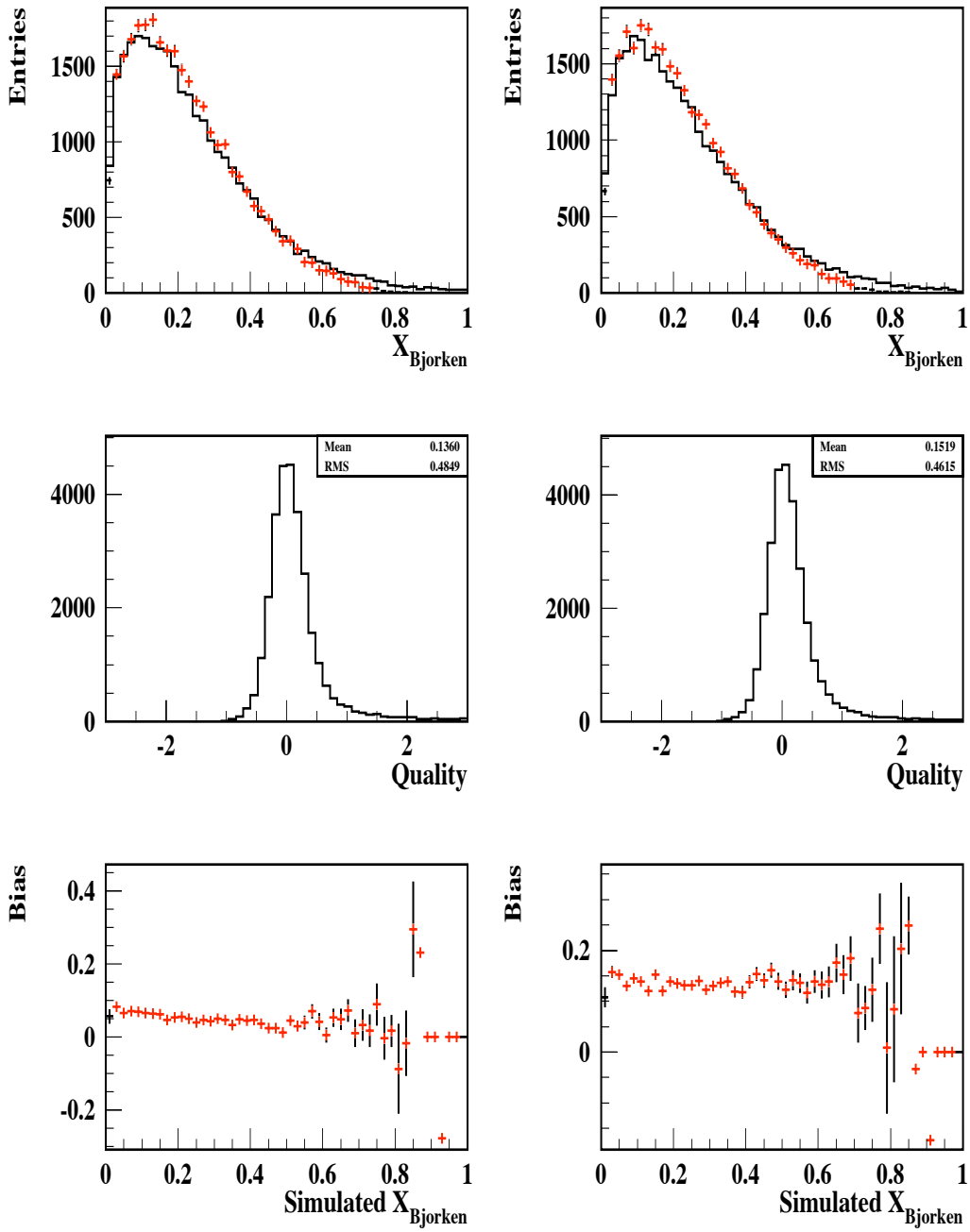

Figure 4.19: Comparison of reconstructed (points) and simulated (histogram) values of x_{Bj} for events occurring in Stack 1 (left) and Stack 2 (right). The middle plots show the quality and the bottom plots show the bias as a function of the simulated value.

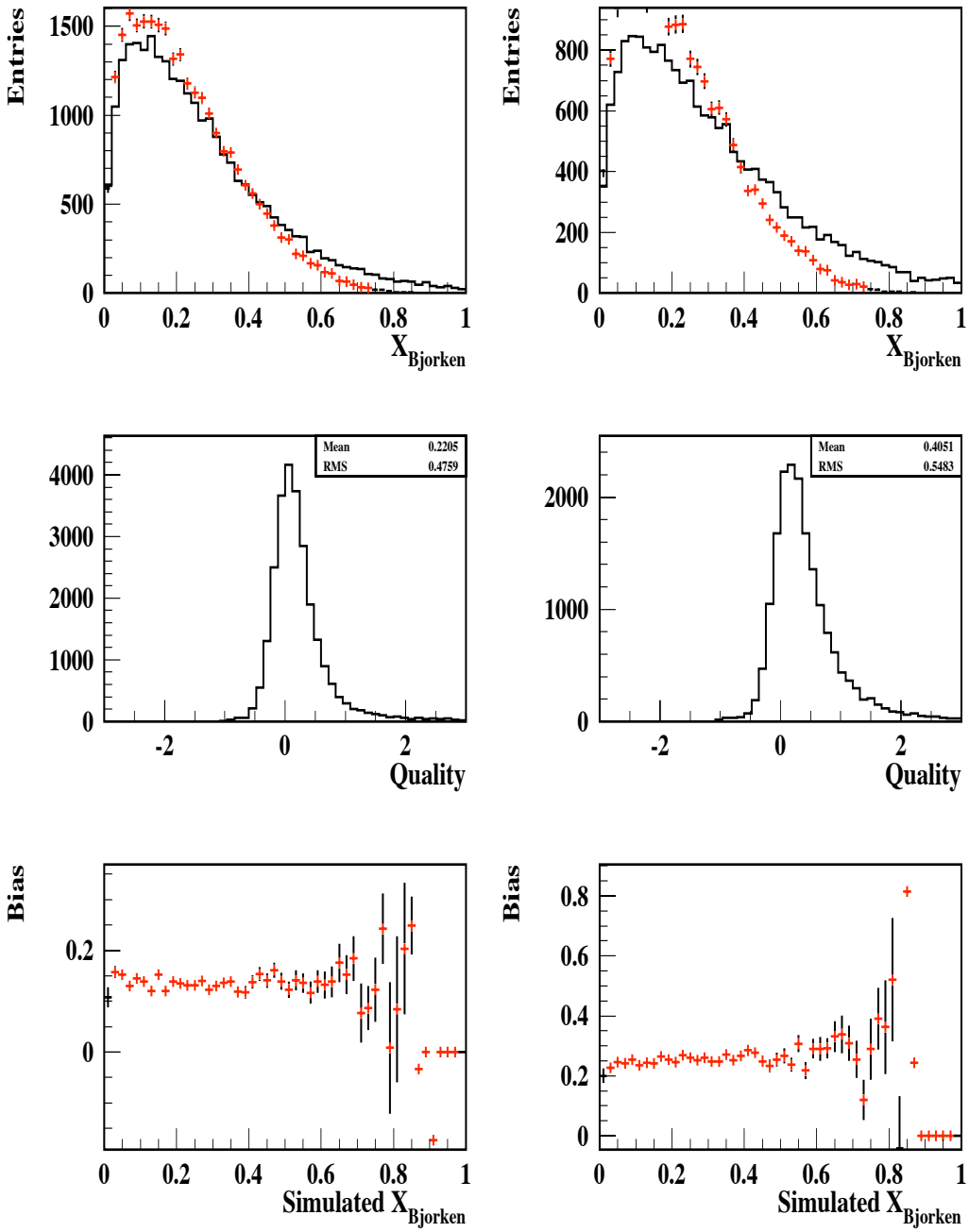

Figure 4.20: Comparison of reconstructed (points) and simulated (histogram) values of x_{Bj} for events occurring in Stack 3 (left) and Stack 4 (right). The middle plots show the quality and the bottom plots show the bias as a function of the simulated value.

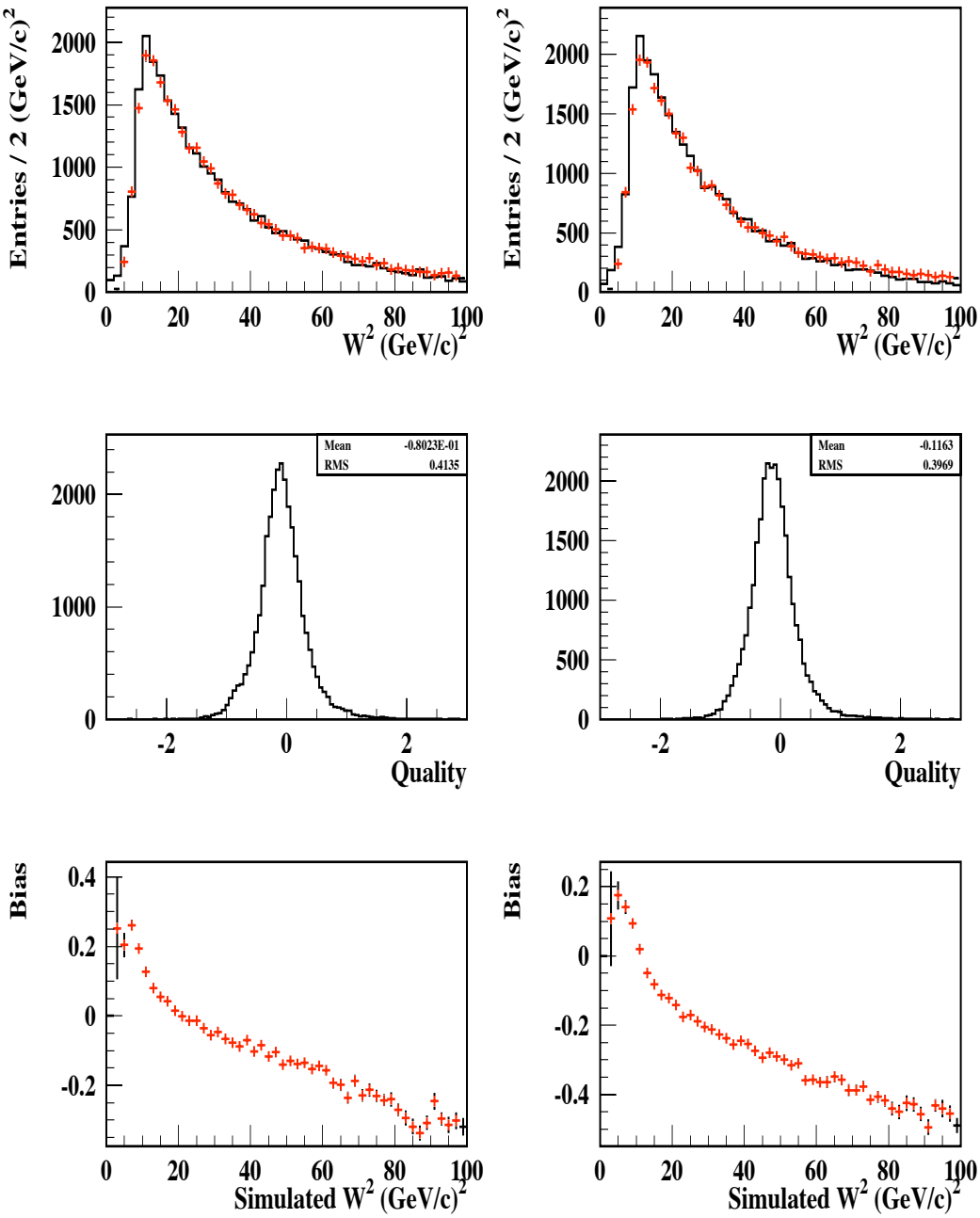

Figure 4.21: Comparison of reconstructed (points) and simulated (histogram) values of W^2 for events occurring in Stack 1 (left) and Stack 2 (right). The middle plots show the quality and the bottom plots show the bias as a function of the simulated value.

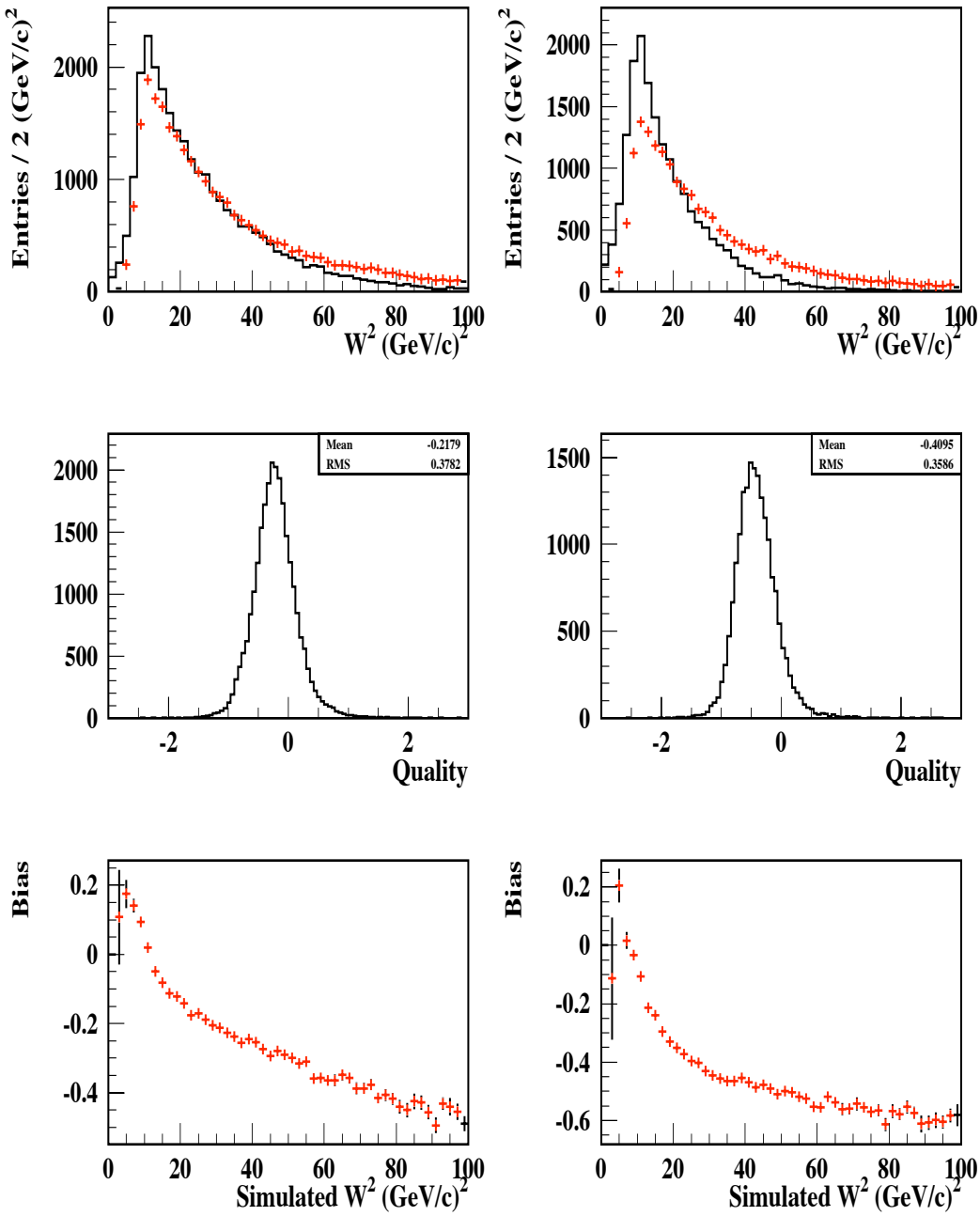

Figure 4.22: Comparison of reconstructed (points) and simulated (histogram) values of W^2 for events occurring in Stack 3 (left) and Stack 4 (right). The middle plots show the quality and the bottom plots show the bias as a function of the simulated value.

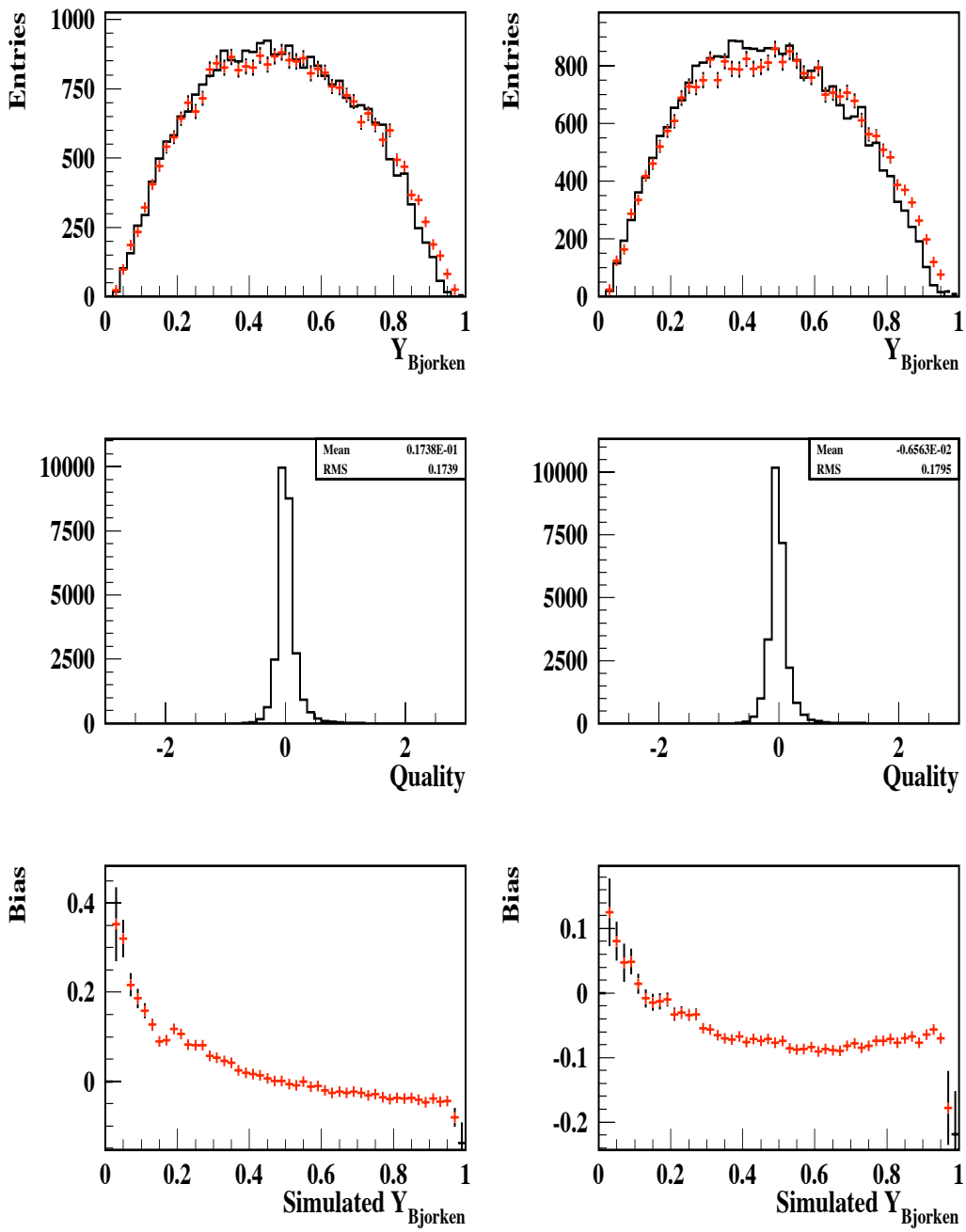

Figure 4.23: Comparison of reconstructed (points) and simulated (histogram) values of y_{Bj} for events occurring in Stack 1 (left) and Stack 2 (right). The middle plots show the quality and the bottom plots show the bias as a function of the simulated value.

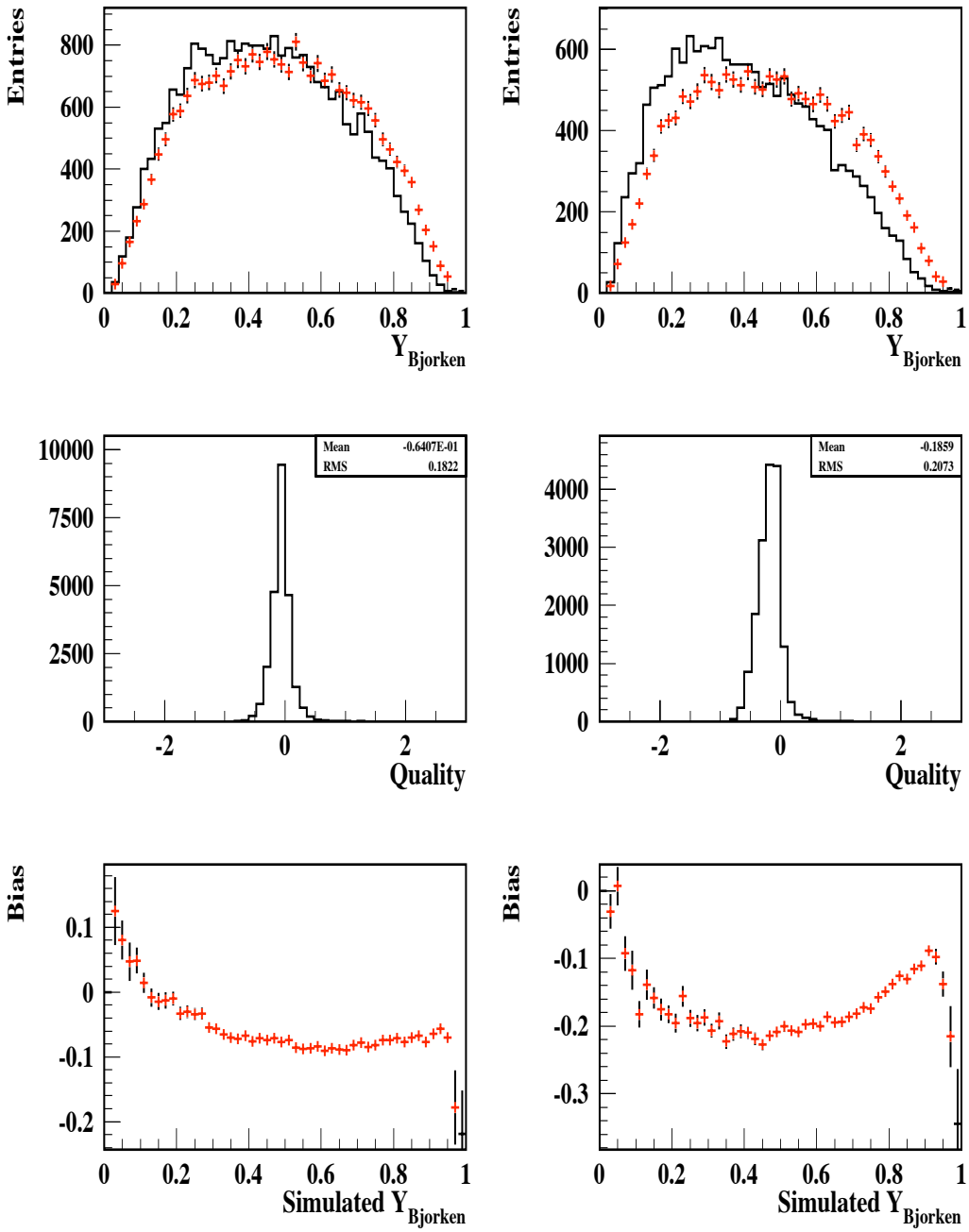

Figure 4.24: Comparison of reconstructed (points) and simulated (histogram) values of y_{Bj} for events occurring in Stack 3 (left) and Stack 4 (right). The middle plots show the quality and the bottom plots show the bias as a function of the simulated value.

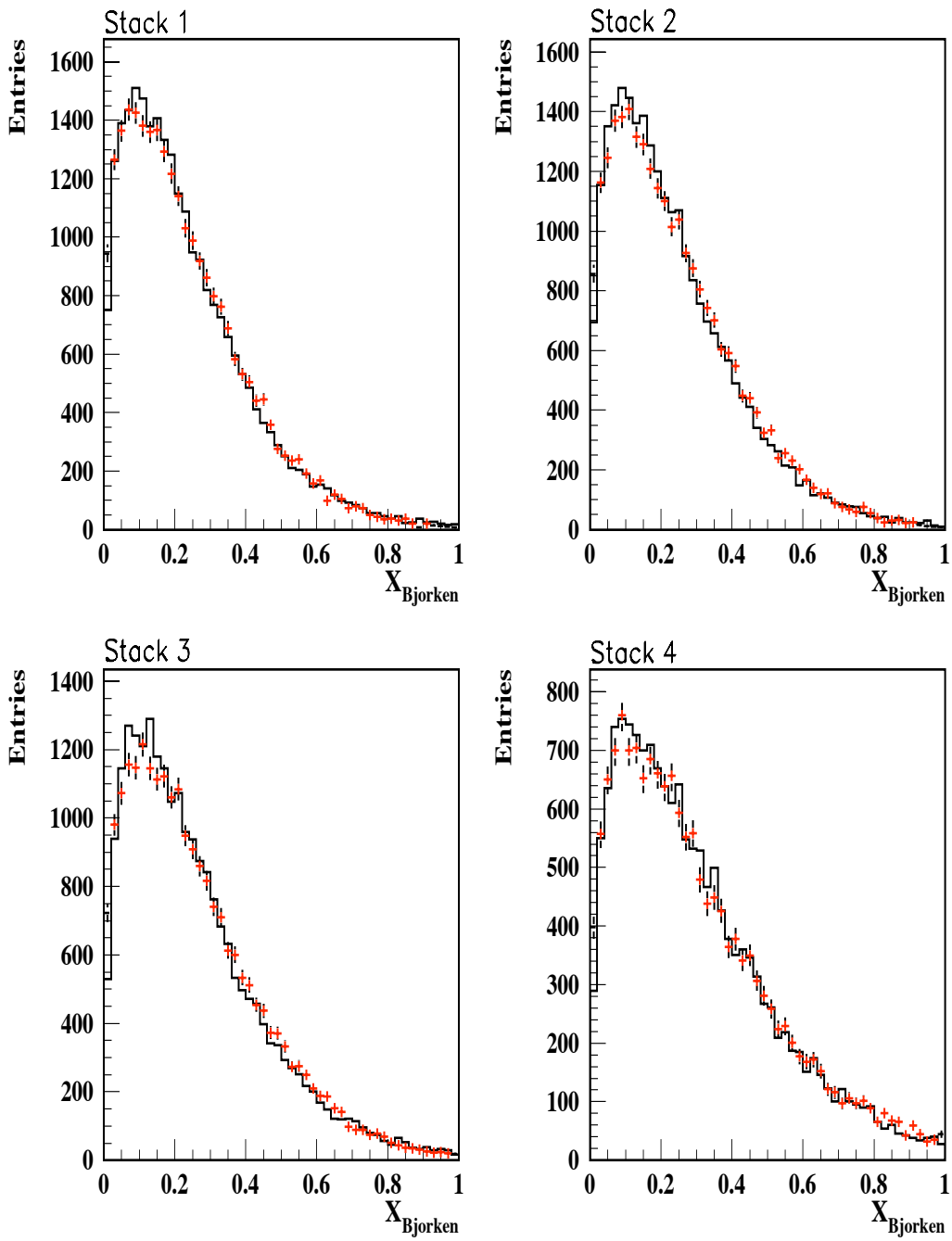

Figure 4.25: Comparison between data (points) and Monte Carlo (histogram) for the reconstruction of the kinematic variable x_{Bj} for events occurring in each stack. The data and Monte Carlo distributions have been normalised to equal areas.

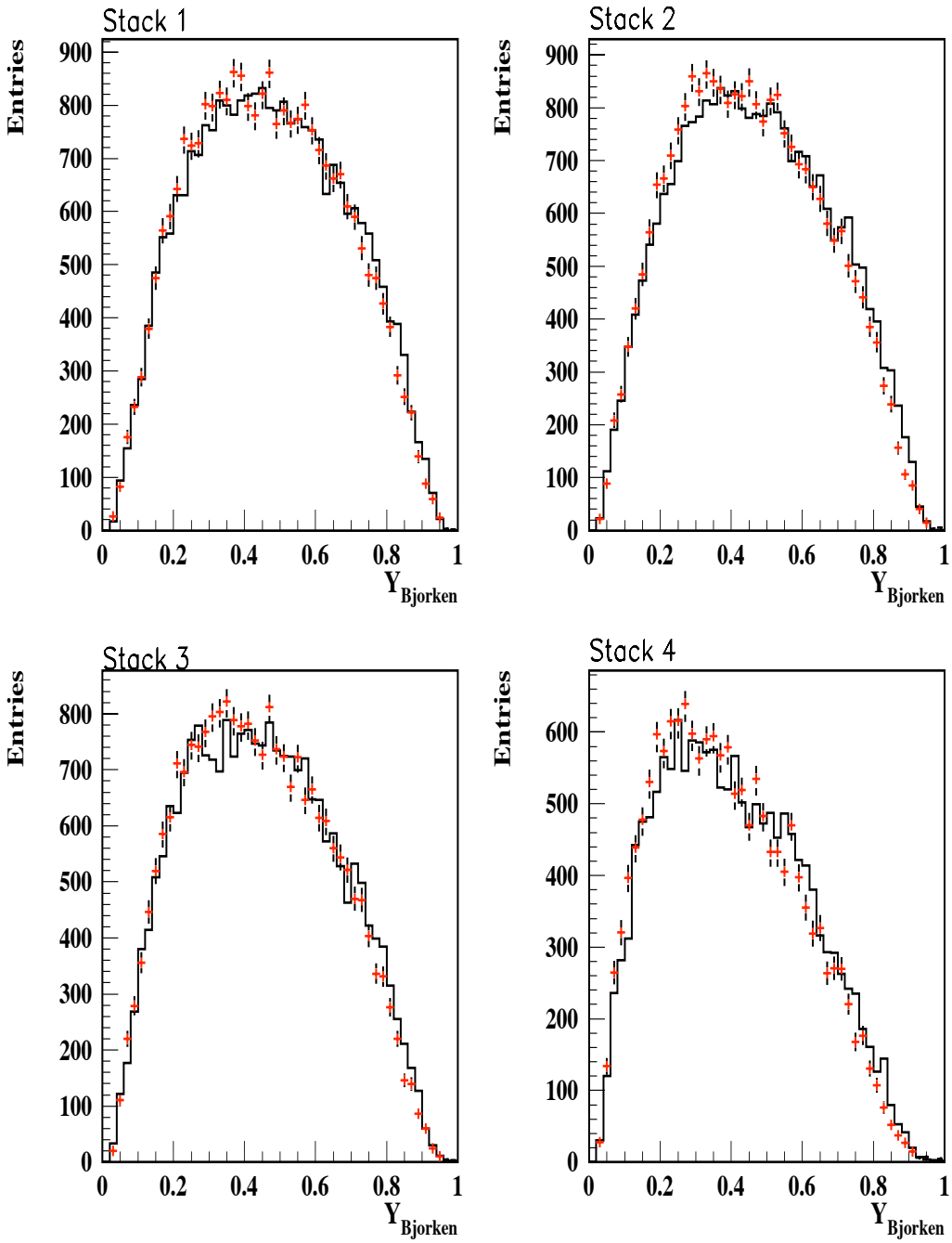

Figure 4.26: Comparison between data (points) and Monte Carlo (histogram) for the reconstruction of the kinematic variable y_{Bj} for events occurring in each stack. The data and Monte Carlo distributions have been normalised to equal areas.

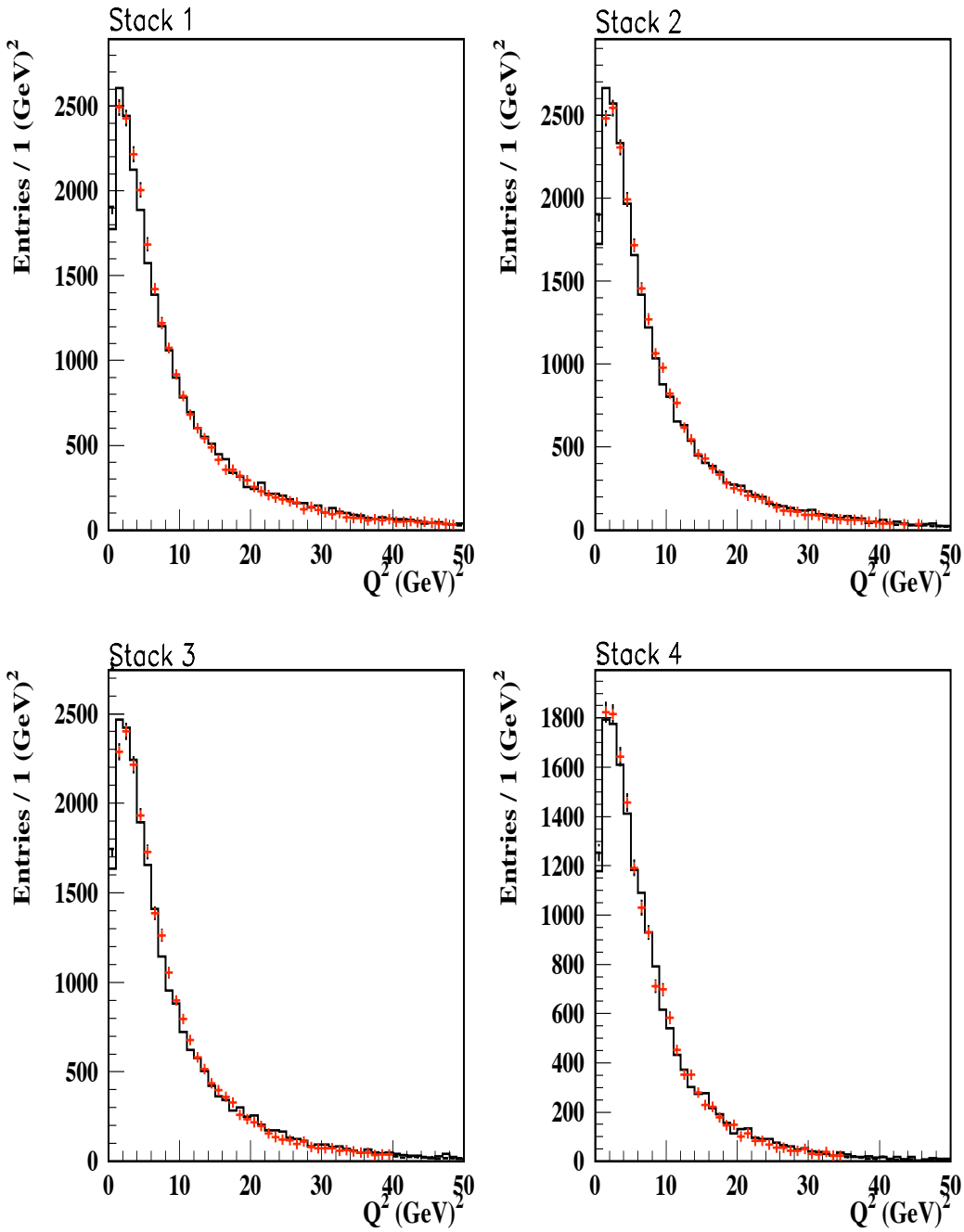

Figure 4.27: Comparison between data (points) and Monte Carlo (histogram) for the reconstruction of the kinematic variable Q^2 for events occurring in each stack. The data and Monte Carlo distributions have been normalised to equal areas.

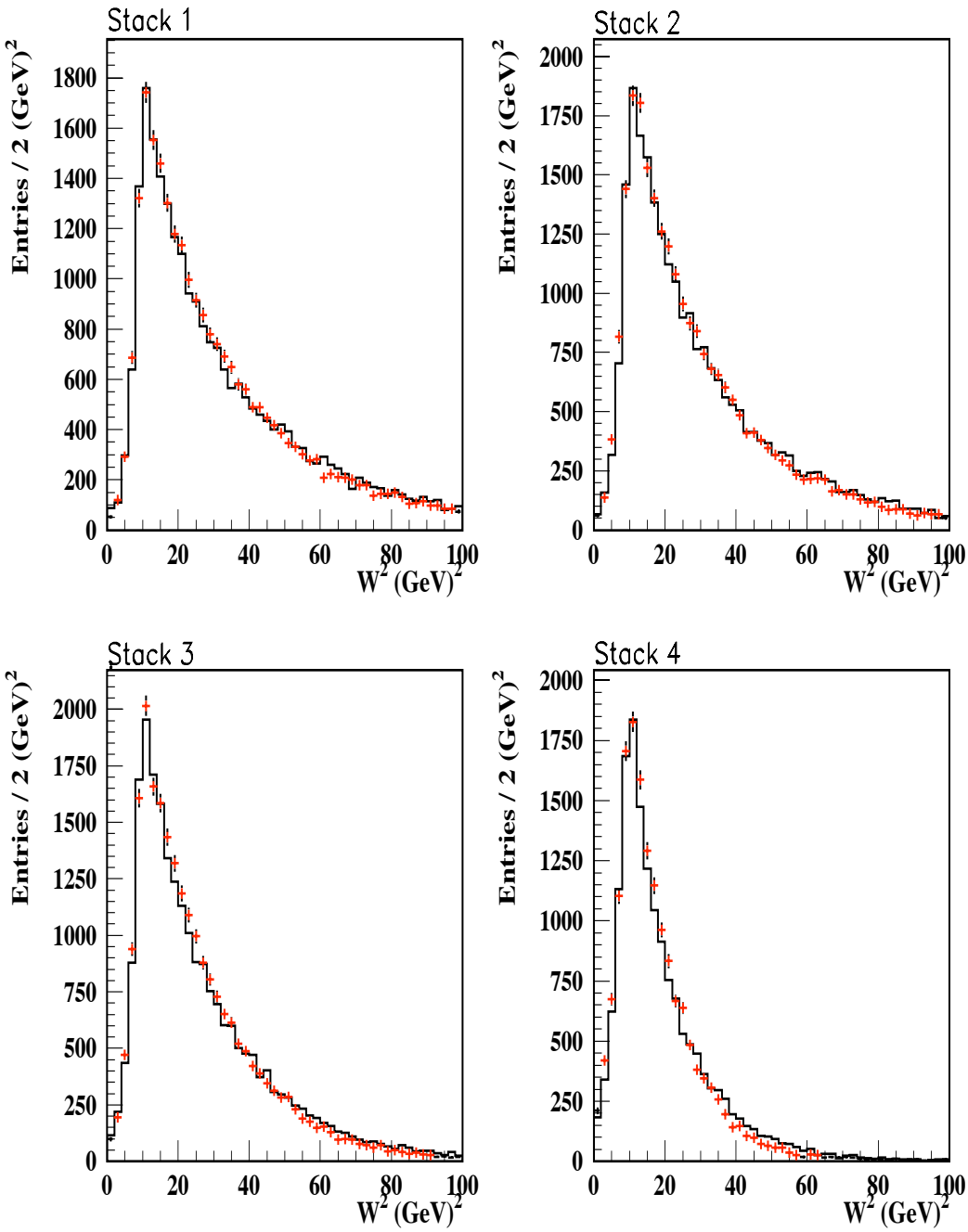

Figure 4.28: Comparison between data (points) and Monte Carlo (histogram) for the reconstruction of the kinematic variable W^2 for events occurring in each stack. The data and Monte Carlo distributions have been normalised to equal areas.

Stack 1				
	ν_μ^{CC} Data		ν_μ^{CC} Monte Carlo	
quantity	Mean	RMS	Mean	RMS
$Q^2(GeV/c)^2$	10.5	12.1	11.2	13.1
$W^2(GeV/c^2)^2$	30.3	22.0	30.3	22.2
x_{Bj}	0.25	0.19	0.26	0.19
y_{Bj}	0.47	0.21	0.48	0.21
Stack 2				
	ν_μ^{CC} Data		ν_μ^{CC} Monte Carlo	
quantity	Mean	RMS	Mean	RMS
$Q^2(GeV/c)^2$	9.7	10.9	10.2	11.9
$W^2(GeV/c^2)^2$	28.1	20.6	28.2	20.9
x_{Bj}	0.26	0.19	0.26	0.19
y_{Bj}	0.46	0.21	0.47	0.21
Stack 3				
	ν_μ^{CC} Data		ν_μ^{CC} Monte Carlo	
quantity	Mean	RMS	Mean	RMS
$Q^2(GeV/c)^2$	8.9	9.6	9.4	10.7
$W^2(GeV/c^2)^2$	24.4	17.6	24.5	18.2
x_{Bj}	0.28	0.20	0.28	0.20
y_{Bj}	0.44	0.20	0.45	0.20
Stack 4				
	ν_μ^{CC} Data		ν_μ^{CC} Monte Carlo	
quantity	Mean	RMS	Mean	RMS
$Q^2(GeV/c)^2$	7.6	7.8	8.1	8.9
$W^2(GeV/c^2)^2$	16.9	12.5	17.6	13.4
x_{Bj}	0.31	0.23	0.32	0.22
y_{Bj}	0.39	0.19	0.40	0.20

Table 4.10: Average and RMS values of reconstructed kinematic variable distributions in data and Monte Carlo.

A cross check of the calibration carried out in Chapter 3 may be made by using a variant on the concept that a miscalibration in the measurement of the hadronic energy distorts the y-distribution. If the ratio of the mean visible neutrino energy in the data, $< E_{vis} >^{DATA}$, and the mean visible neutrino energy in the Monte Carlo, $< E_{vis} >^{MC}$, is plotted as a function of visible Bjorken y, the appearance of a non-zero slope in the plot is an indication of a difference in the relative calibration of E_{had} and E_{μ}. To be more specific, a miscalibration means that the measured hadron and muon energies differ from the true values : $E_{\mu}^{DATA} = \alpha E_{\mu}$ and $E_{had}^{DATA} = \beta E_{had}$. Since the Monte Carlo is perfectly calibrated

$$\begin{aligned} \frac{E_{\nu}^{DATA}}{E_{\nu}^{MC}} &= \frac{E_{had}^{DATA} + E_{\mu}^{DATA}}{E_{had}^{MC} + E_{\mu}^{MC}} \\ &= \frac{\alpha E_{\mu} + \beta E_{had}}{E_{\mu} + E_{had}} \\ &= \frac{\alpha(E_{\mu} + E_{had}) + (\beta - \alpha)E_{had}}{E_{\mu} + E_{had}} \end{aligned} \tag{4.11}$$

Expressed in terms of the visible Bjorken y, Equation 4.11 becomes

$$\frac{E_{\nu}^{DATA}}{E_{\nu}^{MC}} = \alpha + (\beta - \alpha)y_{vis} \tag{4.12}$$

Hence any small miscalibration of the muon energy will appear as a global offset in the plot. A non-zero slope does not, in itself, indicate the presence of a miscalibration in the hadronic energy, since the slope is affected by both the hadronic and muonic energy scales. Knowledge of the offset, however, allows a measurement of β from the slope to be carried out.

Figure 4.29 shows $\frac{E_{\nu}^{DATA}}{E_{\nu}^{MC}}$ as a function of y_{vis}. The fit shows that the miscalibration of the muon energy is present at the level of about 2%, which is consistent with the resolution in the muon energy discussed in Section 4.2. The line has zero slope which indicates that the hadronic energy scales in data and the simulation differ by only 2%. However the error on the slope from the straight line fit is also 2% so it is conceivable that both energy scales are calibrated correctly. It is reasonable to conclude that the hadronic energy scale in the data is correct, or at the very least any differences are rendered unobservable by the poor energy resolution of the FCAL.

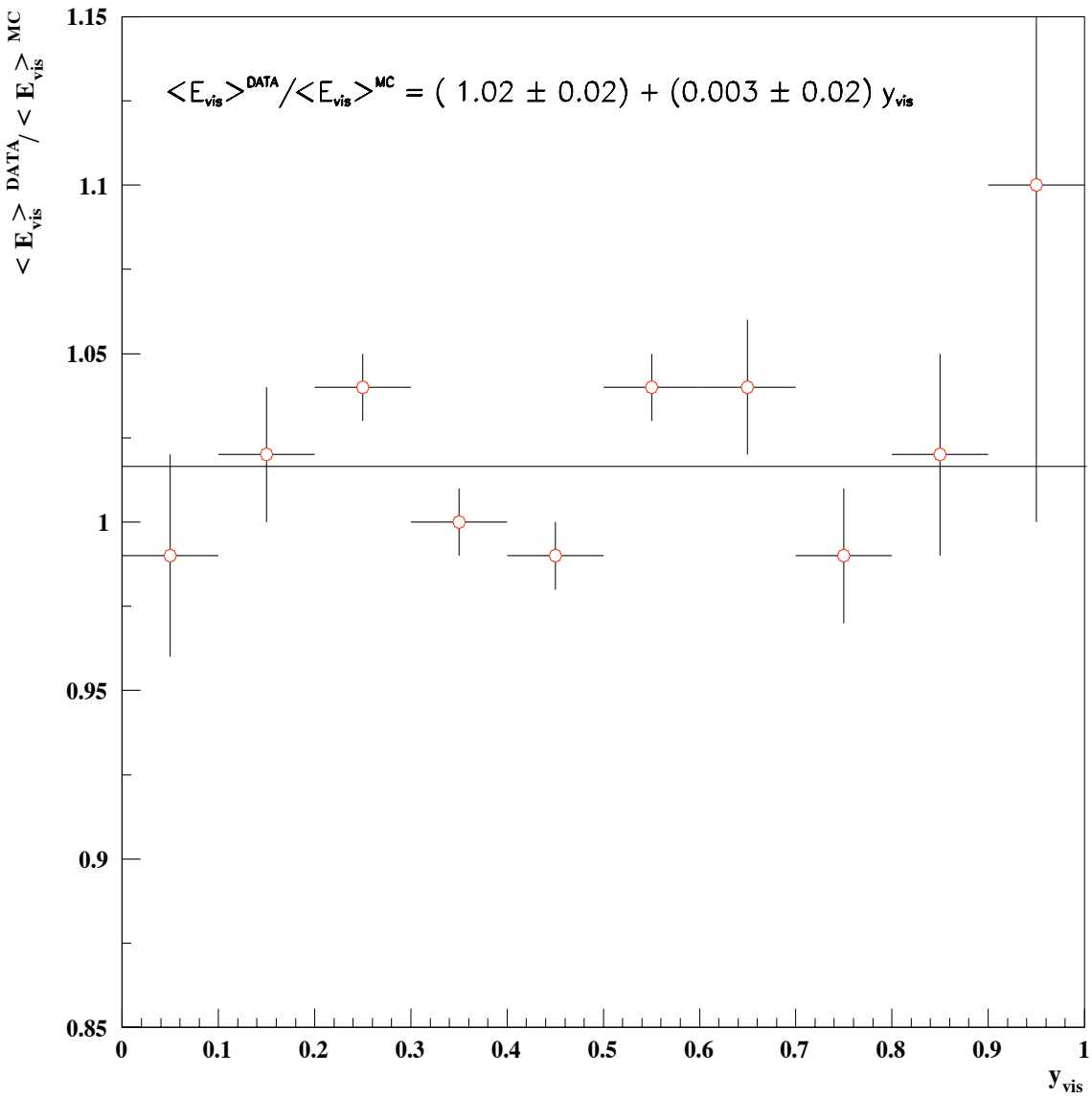

Figure 4.29: Hadron-muon relative energy calibration.

Chapter 5

Dimuon Events

5.1 Introduction

The FCAL was designed to study, amongst other processes, the production of charm quarks in deep inelastic neutrino scattering events. The cleanest signature of such production is the formation of opposite sign dimuon events. The theoretical background describing these events has been discussed in Chapter 1.

The first part of this chapter describes the selection criteria used in the dimuon search, followed by a discussion of the background arising from the decay of pions and kaons in the hadronic system. The question of whether the standard NOMAD Monte Carlo adequately describes charm production is then investigated and an alternative Monte Carlo proposed.

5.2 Dimuon Event Identification

The dimuon event selection algorithm is an extension of that introduced for the recognition of ν_μ^{CC} events in Chapter 4. Listing these for the sake of convenience

- **Trigger Condition :** The FCAL trigger must have fired.
- **Presence of a muon :** A track passing the muon identification cuts described in Chapter 4 must exist.
- **Association with an FCAL event :** The backward extrapolation of the muon track must be within the FCAL fiducial area and lie within 20 cm of the FCAL vertex estimated using the centre of gravity method (see Section 3.4.4).

Events with two muons associated to the primary vertex are dimuon events. The charges of the muons may be either different, in which case the event is referred to as an Opposite Sign Dimuon event (OSDM), or the same and the event is a Like Sign Dimuon event (LSDM). In addition to the charged current event selection criteria listed above, an event is considered to be a dimuon, either OSDM or LSDM, if the following criteria hold :

- **Presence of a second muon :** A second track passing the muon identification cuts exists.
- **Spatial correlation :** The distance between the positions of the muons (extrapolated to the midplane of the first stack hit) is less than 20 cm.
- **Temporal Correlation :** The difference between the times of the first hit of the muon tracks must be less than 5 ns.
- **Muon energy :** Both muons must have an energy greater than 4.5 GeV. The motivation for this value will be discussed in Section 5.3.2.

The correlation and energy cuts are imposed primarily to reduce background and will be discussed to a greater extent below.

5.2.1 Categorisation of opposite sign dimuon events

Charm quarks are produced in neutrino interactions and anticharm quarks in antineutrino interactions. The neutrino and antineutrino production processes are somewhat different since charm from antineutrinos is produced completely from interactions with sea quarks whereas charm from neutrinos can be produced from valence d quarks as well. It is, therefore, important to determine whether a particular dimuon was ν_μ or $\overline{\nu_\mu}$ induced. This is accomplished by measuring the charge of the muon from the leptonic vertex : events in which the primary[1] muon is a μ^- are ν_μ induced whereas those with a primary μ^+ are produced by an incident antineutrino. It is worth noting that since the antineutrino flux in the CERN wide band beam is at the level of 7% of the neutrino flux (see Section 2.4) and the integrated cross section for antineutrino induced opposite sign dimuon production is about 60 % of the neutrino integrated cross section, the expected number of $\overline{\nu_\mu}$ induced dimuon events is only of the order of 4% of those induced by neutrinos.

The algorithm used to determine into which category a dimuon event falls is straightforward. The primary muon is taken to be the one with the

[1] In this context the term "primary" refers to the muon produced at the leptonic vertex.

highest transverse momentum with respect to the beam direction. Monte Carlo studies show that the efficiency of this procedure in choosing the correct primary muon is (95 ± 1) %, where the error is statistical. Combined with the expected ratio of antineutrino to neutrino induced dimuon events, this efficiency implies an extremely pure final neutrino induced dimuon sample.

5.2.2 Dimuon Selection Efficiency

The selection efficiency for opposite sign dimuon events may be estimated from a Monte Carlo simulation. A sample of opposite sign dimuon events was generated using the NOMAD Monte Carlo and passed through the detector simulation and reconstruction chain. The number of events remaining after each cut is presented in Tables 5.1 and 5.2 below, along with the total selection efficiency and the relative efficiency for each cut. All efficiencies are calculated with respect to the standard fiducial area

$$|X_{vertex}| < 70 \text{ cm}, \quad |Y_{vertex}| < 70 \text{ cm} \tag{5.1}$$

As with the ν_μ^{CC} sample the factor that leads to the greatest loss of efficiency is the geometric acceptance of the muon chambers for muons. The loss of efficiency is much greater for the secondary muon due to its low momentum and consequently smaller radius of curvature in the NOMAD drift chamber volume. The characteristics of Stack 4, as expected, show significant deviation from the other stacks and this re-emphasises the requirement to remove Stack 4 events from the data sample used in the final analysis.

5.3 Dimuon Background

The background to the opposite sign dimuon process consists of

1. Muonic decay in flight of pions and kaons in the hadronic jet of ν_μ^{CC} events.

2. Hadrons which punch through to the muon chambers, thereby mimicking muons, in ν_μ^{CC} events.

Beyond a certain point the dimuon background is essentially irreducible from the point of view of kinematic cuts. Muonic decays within the FCAL are undetectible due to the lack of any high precision tracking within the calorimeter and, as mentioned in Section 4.3.2, the kink angle of the π/K decay is, in general, too small to be accurately determined with the drift

Stack 1			
Cut	Number of events	Efficiency	Relative Efficiency
	20142		
Fiducial Area	13809	100 %	100 %
Trigger Threshold	13651	98.8 %	98.8 %
$N_\mu > 0$	11054	80.0 %	81.0 %
Vertex Association	10356	75.0 %	93.7 %
$E_1^\mu > 4.5$ GeV	10018	72.5 %	96.7 %
$N_\mu = 2$	2452	17.7 %	24.4 %
$E_2^\mu > 4.5$ GeV	2038	14.7 %	83.1 %
Spatial Correlation	1946	14.0 %	95.5 %
Temporal Correlation	1898	13.7 %	97.5 %
Identification Algorithm	1860	13.4 %	98.0 %
Stack 2			
Cut	Number of events	Efficiency	Relative Efficiency
	20660		
Fiducial Area	13719	100 %	100 %
Trigger Threshold	13526	98.8 %	98.8 %
$N_\mu > 0$	11136	81.1 %	82.3 %
Vertex Association	10441	76.1 %	93.8 %
$E_1^\mu > 4.5$ GeV	9970	72.7 %	95.4 %
$N_\mu = 2$	2566	18.7 %	25.7 %
$E_2^\mu > 4.5$ GeV	1970	14.4 %	76.8 %
Spatial Correlation	1894	13.8 %	96.1 %
Temporal Correlation	1856	13.5 %	98.1 %
Identification Algorithm	1818	13.3 %	98.0 %

Table 5.1: ν_μ opposite sign dimuon event selection efficiency for simulated events beginning in stacks 1 and 2.

Stack 3			
Cut	Number of events	Efficiency	Relative Efficiency
	20611		
Fiducial Area	13606	100 %	100 %
Trigger Threshold	13270	97.5 %	97.5 %
$N_\mu > 0$	10828	79.5 %	81.6 %
Vertex Association	10125	74.4 %	93.5 %
$E_1^\mu > 4.5$ GeV	9490	69.7 %	93.7 %
$N_\mu = 2$	2693	19.8 %	28.3 %
$E_2^\mu > 4.5$ GeV	1904	14.0 %	70.7 %
Spatial Correlation	1854	13.6 %	97.3 %
Temporal Correlation	1796	13.2 %	96.9 %
Identification Algorithm	1756	12.9 %	97.8 %
Stack 4			
Cut	Number of events	Efficiency	Relative Efficiency
	19971		
Fiducial Area	12949	100 %	100 %
Trigger Threshold	10252	79.1 %	79.1 %
$N_\mu > 0$	8006	61.8 %	78.1 %
Vertex Association	7542	58.2 %	94.2 %
$E_1^\mu > 4.5$ GeV	6936	53.6 %	91.2 %
$N_\mu = 2$	2076	16.0 %	29.9 %
$E_2^\mu > 4.5$ GeV	1303	10.0 %	62.7 %
Spatial Correlation	1271	9.8 %	97.5 %
Temporal Correlation	1241	9.6 %	97.7 %
Identification Algorithm	1218	9.4 %	98.2 %

Table 5.2: ν_μ opposite sign dimuon event selection efficiency for simulated events beginning in stacks 3 and 4.

chambers. Background can be rejected via a cut on the energy of the secondary muon candidate, since the momentum spectrum of the mesons in the jet or from interactions in the magnet coil is softer than that of secondary muons in OSDM production. Beyond this the background must be subtracted statistically.

The amount of background can be estimated by studying dimuon events in which both of the muons have identical electric charge. The dominant source of these events is the decay and punchthrough of pions and kaons in the hadron shower, assuming that no non-standard physics process exists that can produce a prompt like sign signal. Searches for like sign events arising from processes other than meson decay have not yet presented evidence for their existence[57, 58, 59]. These searches have allowed a limit to be placed on size of the production cross section with respect to the single muon ν_μ^{CC} cross section[85] of

$$\frac{\sigma(\nu_\mu + \mathcal{N} \to \mu^- + \mu^- + anything)}{\sigma(\nu_\mu + \mathcal{N} \to \mu^- + anything)} < 5.4 \times 10^{-5} \text{ at 95 \% confidence} \tag{5.2}$$

at the average neutrino energy of 24.4 GeV of the SPS beam. Given this relative cross section it is expected that there are less than 18 events in the entire data set after cuts. A source of prompt like sign events will not be considered further and it will be assumed that all like sign events arise from secondary meson decays and hadron punchthrough.

The same physics processes give rise to both the like sign and opposite sign background events and so a reasonable estimate of this background may be made by predicting the properties of the opposite sign dimuon background based on those of the like sign event sample.

5.3.1 The Like Sign Dimuon Events

Events with two muons with the same charge arise from four main sources :

- the muonic decay of primary mesons produced at the event vertex in the FCAL,
- the muonic decay of secondary mesons produced within the hadronic shower,
- hadrons which reach the muon chambers and simulate the properties of a muon and
- events in which there is an overlap of a ν_μ^{CC} interaction in the FCAL with a muon in the beam.

Other sources of background are

- **Overlap of two neutrino events :** These accidental coincidences are expected to be eliminated by the space and time correlation cuts. The effect of these cuts are described below in the context of beam muon overlap events. The same arguments and conclusions apply to the overlap of neutrino events.

- **Two muon event in neutral current interactions:** The probability of observing a like sign event in which both muons are produced from π/K decay or hadron punchthrough in neutral current events may be estimated using a neutral current Monte Carlo sample. Zero events remained in a sample of 57,945 neutral current events after the dimuon selection algorithm was applied. If the number of events that pass the cuts is treated as following a Poisson distribution then, given an observed number of zero events, the probablility of the true mean of the Poisson distribution being less than 3 events is 95 %. A 95 % C.L. upper bound on the probability of observing a like sign event from a neutral current interaction is 0.00005 (i.e. $3/57,945$). Using the observed number of ν_μ^{CC} events and the cross section ratio[2]

$$\frac{\sigma(\nu_\mu + \mathcal{N} \rightarrow \nu_\mu + anything)}{\sigma(\nu_\mu + \mathcal{N} \rightarrow \mu^- + anything)} = 0.25 \tag{5.3}$$

  less than 40 events are expected in the like sign sample. This is less than 2% of the like sign sample.

The FCAL was instrumented and calibrated without the use of a pion test beam and so there was no possibility of measuring the muon production rates by hadrons. Given this, it was deemed necessary to combine the first three background contributions into one component, the π/K background, and estimate the overall background rate using Monte Carlo methods.

The background subtraction algorithm, for any distribution $\mathcal{A}$ under study, proceeds as follows :

1. Estimate the size of the beam overlap background in the like sign sample.

2. Subtracting this overlap background, estimate the number of π/K like sign events.

3. Using the Monte Carlo, calculate the ratio, $\mathcal{R}$, of the number of observed opposite sign background events to the number of observed like sign events. This scale need not be the same for neutrino and antineutrino induced events.

4. Form the same distribution for the like sign events in the data, $\mathcal{A}_{DATA}^{LSDM}$.

5. Scale $\mathcal{A}_{DATA}^{LSDM}$ in each bin by $\mathcal{R}$.

6. Subtract the reweighted distribution $\mathcal{A}_{DATA}^{LSDM}$ from $\mathcal{A}$.

This prescription implicitly assumes that the simulation describes the like sign events and opposite sign background events adequately. It will be shown below that this is the case.

The following discussion is concerned, unless otherwise specified, with the background estimate for the neutrino induced dimuon sample. The same arguments apply for the antineutrino induced sample except that the signs of the muons are reversed. For example, the like sign sample in neutrino interactions is composed of two muons with negative electric charge, whereas the two muons have positive charge in antineutrino interactions.

Beam Background

A potentially dangerous contaminant of the like sign sample are overlap muons. Despite the extensive shielding in the beam line, some muons from interactions close to NOMAD arrive with the beam. The veto subdetector is not 100 % efficient, allowing 2 - 3 % of these beam muons into the FCAL. If there is a coincidental overlap in time and space of a beam muon with a charged current neutrino interaction then the event will be accepted as a valid like sign dimuon. The danger of these events is that their inclusion in the like sign sample overestimates the number of $\mu^-\mu^-$ events leading, as discussed above, to an overestimate of the opposite sign background.

Figure 5.1 compares the distribution of the distance between the extrapolated positions of the two muons at the vertex plane in like sign events. The top plot is the distribution from data whereas the bottom plot is from the simulation. Whilst the simulated distribution is a steep function, falling essentially to zero at a radius of $\simeq$ 20 cm, the data distribution exhibits an additional flat background caused by the overlapping muons. Since these muons are uncorrelated with the neutrino interaction, both in time and space, it is expected that most will be removed by the correlation cuts. The overlap rejection efficiency cannot be estimated using Monte Carlo methods as these muons are a combination of muons associated with the neutrino beam and those produced in neutrino interactions in all the material upstream of NOMAD, consisting of the CHORUS detector and other structures housing smaller neutrino experiments along the beam line. Interactions in this material are almost impossible to adequately simulate. However, an estimate may be obtained from the study of events which are obvious overlaps. Like

Cut	Number of events	Rejection Efficiency
	3965	0.0 %
$E_1^\mu > 4.5$	3965	0.0 %
$E_2^\mu > 4.5$	3806	4.0 %
Spatial Correlation	116	96.9 %
Temporal Correlation	13	99.7 %

Table 5.3: Rejection efficiency for beam muon overlap events.

sign events in which the two muons have a radial separation of more than 50 cm result from the overlap of beam muon with a single muon ν_μ^{CC} event. These events were scanned and the parameters, spatial position, time and momenta, of the beam muon in the event were recorded. The beam muons were then merged with an independent sample of single muon events taken from the data to form a simulation of the overlap background. Using this procedure, a sample of 3965 beam muons was gathered and merged with ν_μ^{CC} interactions. Table 5.3 shows the number of events remaining after the dimuon selection algorithm was applied.

Treating the number of events which pass the cuts as being Poisson distributed, a 95 % upper bound for the observed number of 13 events is 20 events[54]. That is, if the number of events that pass the cuts follows a Poisson distribution with a mean of 13 then the probability of observing less than 20 events actually passing the cuts is 95 %. This implies that there is 95% probability of the rejection efficiency being greater than 99.5% ($1 - \frac{20}{2965}$). The beam background is essentially eliminated from the like sign sample by the correlation criteria.

π/K Background

The opposite sign background is not fully described by the like sign sample. In a region in which only valence quarks interact ($x_{Bj} > 0.2$), a ν_μ^{CC} interaction is a scatter of the neutrino off a d-quark. Assuming no charm production, the u-quark which is produced may combine either with a $\overline{d}$-quark, producing a π^+, or a $\overline{u}$-quark producing a neutral meson such as π^0 or ρ^0 and an associated π^+. The remainder of the jet must be either neutral, if the neutrino interacts with a neutron, or possess a single positive charge when the scatter is from a proton. Hence, in ν_μ^{CC} interactions more positively charged particles must be produced than negatively charged particles. Table 5.4 shows the fraction of positive and negatively charged pions and kaons with respect to the total number of pions and kaons produced in simu-

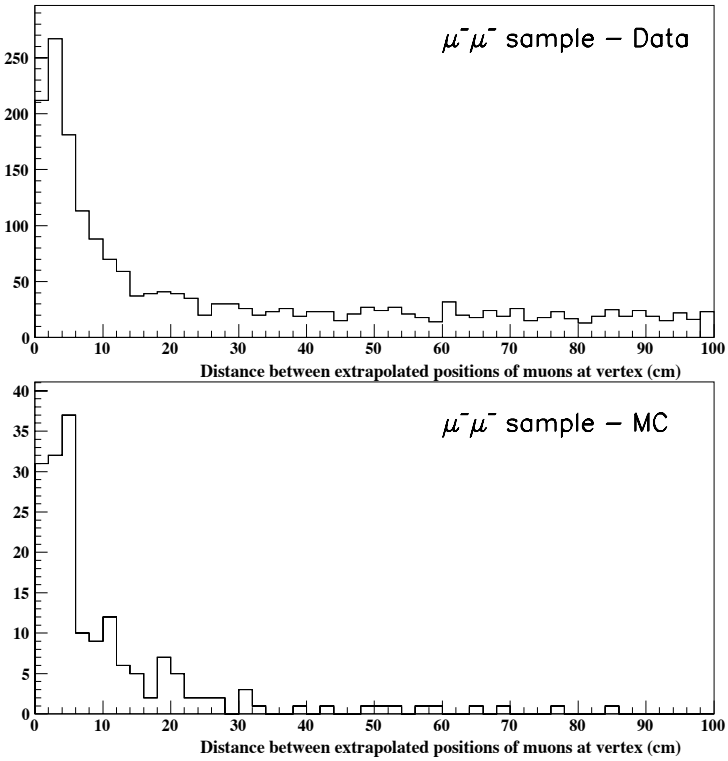

Figure 5.1: (top) Distance between the extrapolated positions of the two muons at the vertex plane for like sign events in the data. (bottom) Distance between the extrapolated positions of the two muons at the vertex plane for like sign events in the simulation. The data exhibits a flat background component due to the overlap beam muons.

Particle	Positive Charge	Negative Charge
π	259302	187054
K	38791	25534
total	298093	202588

Table 5.4: Numbers of positively and negatively charged particles in simulated ν_μ^{CC} events. The fraction of positive to negative mesons is 1.471 ± 0.005.

lated ν_μ^{CC} interactions. The table shows that the number of positive mesons produced is greater than the number of negative mesons by a factor of 1.47.

The scaling factor required is not the ratio of positive to negative *generated* mesons in neutrino interactions, however, but rather the ratio of *observed* opposite sign background to like sign events. That is, the ratio of generated events folded in with the acceptance for the two charge components. The ratio is shown in Table 5.5, for both the neutrino and antineutrino charged current simulations, and both are consistent with the number predicted from the leading charge arguments above. It should be noted that the background itself is a rare process. Starting from the total sample of 288,000 ν_μ^{CC} events, only 61 background events survive the cuts. Making the background scale estimate more precise is, therefore, difficult as the only means available is to generate at least a factor of four more ν_μ^{CC} simulation than is currently available. The generation of an event sample of the required magnitude would call for at least four months processing at a dedicated computing centre. Such an effort could not be realised.

A complication arises when the origin of the positive and negative mesons is considered. Since the positive meson is more likely to be produced as the leading meson in ν_μ^{CC} interactions, the momentum spectrum for this component is expected to be harder than that of the negative meson component. Hence, to be strictly accurate the scaling ratio, $\mathcal{R}$, should be a function of the secondary particle momentum (whether that particle be a true muon or a punchthrough hadron). However, with the amount of ν_μ^{CC} simulation available, splitting the Monte Carlo background into momentum bins would have introduced a larger than acceptable statistical error on the ratio in each bin. The background estimate was made using the total ratio.

Comparison of Like Sign Data and Simulation

In order for the background subtraction prescription outlined above to be valid it is important for the simulation to describe the like sign data satisfactorily. Figure 5.2 and Figure 5.3 show a comparison of the distributions

	ν_μ^{CC}	$\overline{\nu_\mu}^{CC}$
Initial number of events	288,000	72,144
Number of opposite sign background events	(61 ± 8)	(10 ± 3)
Number of like sign events	(40 ± 6)	(5 ± 2)
ratio	(1.5 ± 0.3)	(2 ± 1)

Table 5.5: Ratio of the number of opposite sign background events and like sign events observed in simulated ν_μ^{CC} and $\overline{\nu_\mu}^{CC}$ samples.

	Data		Simulation	
	CC	Like Sign	CC	Like Sign
	3,062,747	834	148,153	40
ratio	$(2.7 \pm 0.1) \times 10^{-4}$		$(2.7 \pm 0.4) \times 10^{-4}$	

Table 5.6: Number of like sign dimuon events normalised to the number of observed ν_μ^{CC} events for data and simulation. The errors are only statistical.

of like sign events in data and simulation. Although the statistics in both the data and the Monte Carlo sample are low the simulation reproduces the shape of each of the kinematic distributions reasonably well.

The final item to consider is the number of like sign dimuon events observed normalised to the number of single muon ν_μ^{CC} events. These numbers are shown in Table 5.6 for events in the data and the simulation which pass all the cuts described above. The number of ν_μ^{CC} events shown for the simulation are the number that survive the charged current event selection cuts. The total sample contained 288,000 events. The relative rates agree well.

Since both the shapes of the kinematic distributions and the relative rates of the like sign events in the data are adequately described by the simulation, there is justification for assuming that the opposite sign background component is also well described by the Monte Carlo.

5.3.2 Background Reduction

As pointed out previously, the energy distribution of the secondary muon in charm production is harder than the energy distribution of muons from meson decay. This provides a useful means with which to cut some of the dimuon background. The optimal cut on the secondary muon momentum

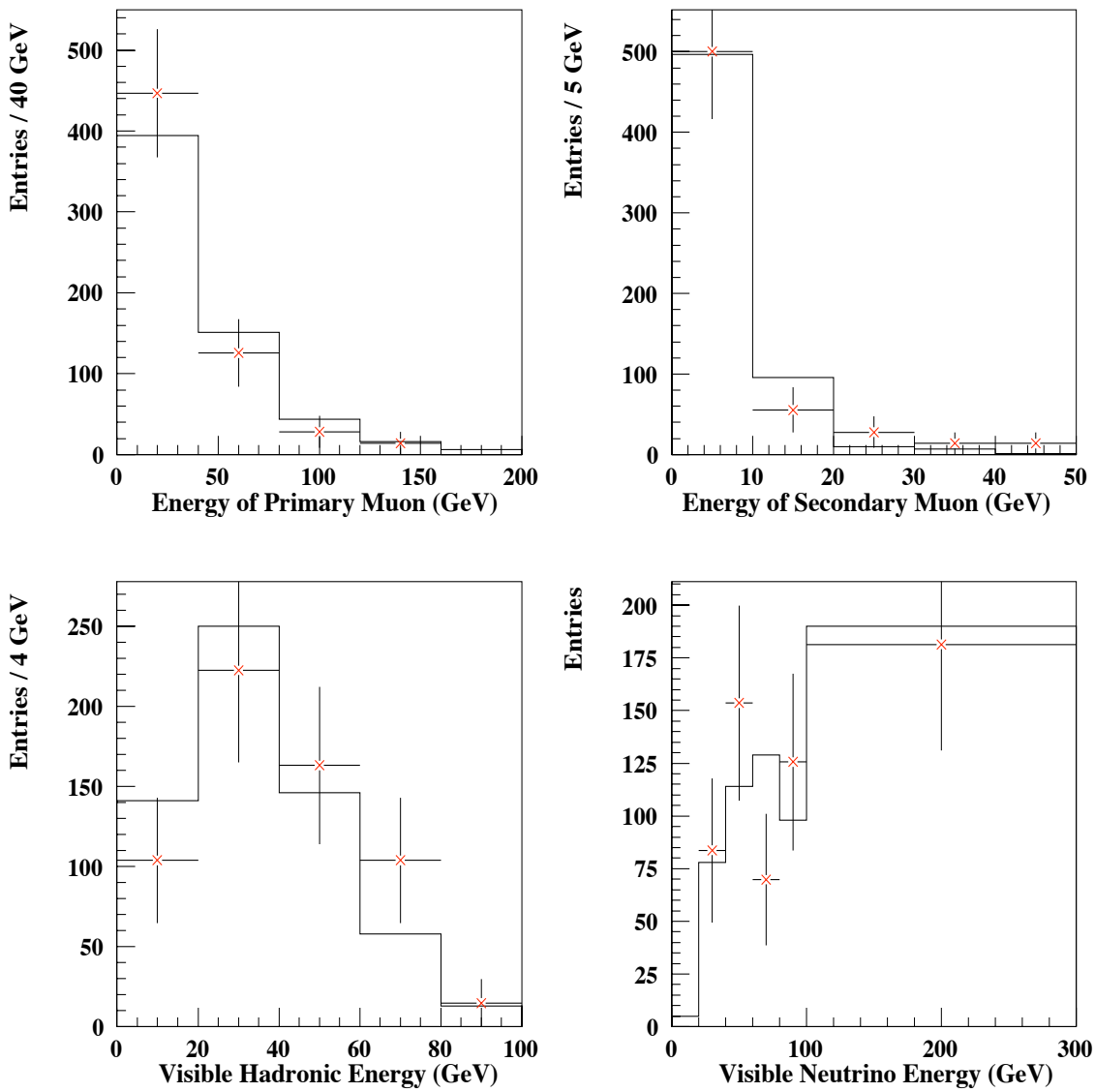

Figure 5.2: Comparison of the shapes of the kinematic distributions of like sign dimuon simulation (points) and data (histogram). Shown are (top left) the energy of the primary muon, (top right) the energy of the secondary muon candidate, (bottom left) the visible hadronic energy and (bottom right) the visible neutrino energy. The data and Monte Carlo have been normalised to equal area.

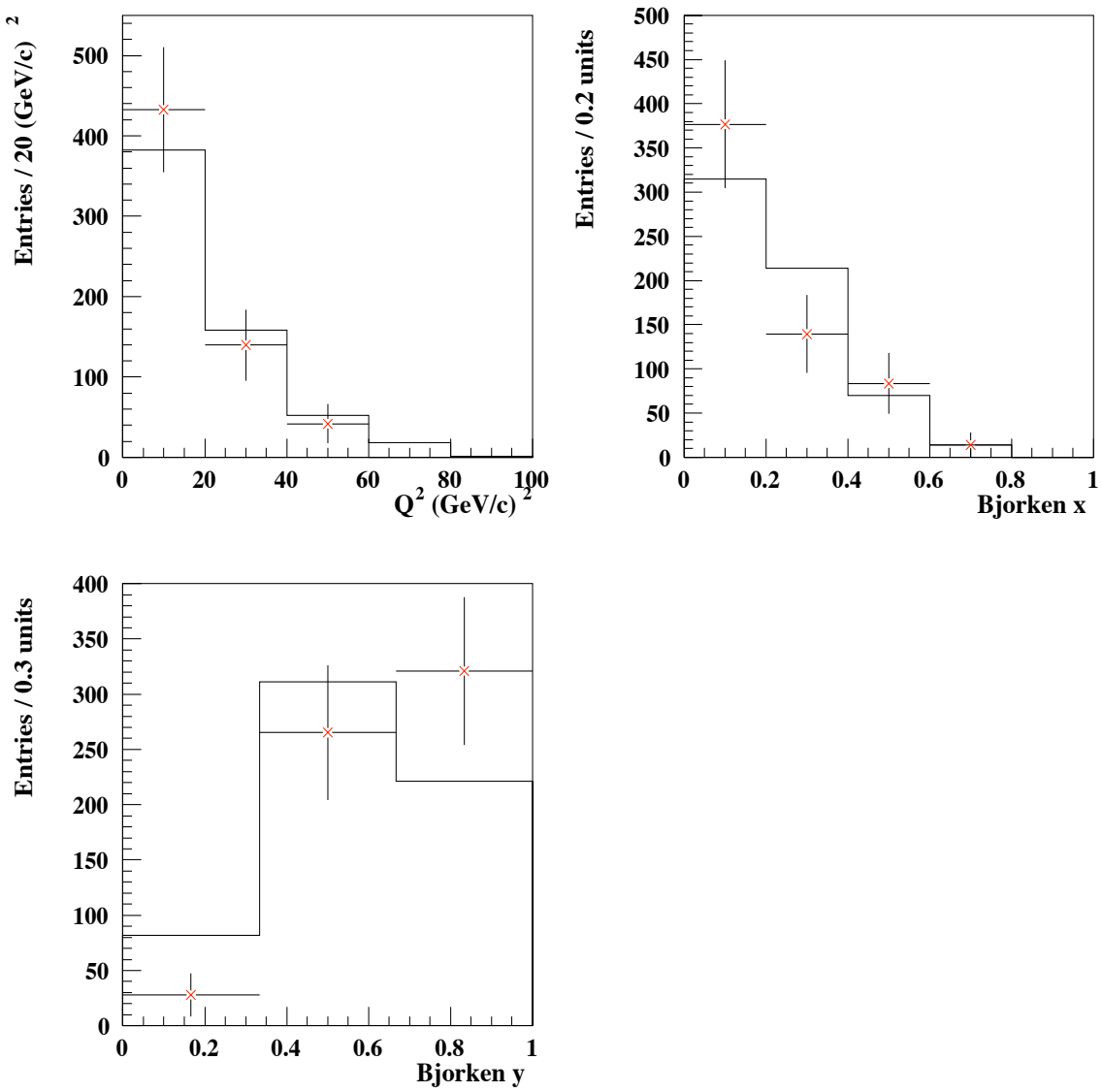

Figure 5.3: Comparison of the shapes of the kinematic distributions of like sign dimuon simulation (points) and data (histogram). Shown are (top left) the square of the 4-momentum transfer, (top right) Bjorken x and (bottom left) the Bjorken y distribution. The data and Monte Carlo have normalised to equal area.

	CC	OSDM	OSDM Background
	93215	209	117
ratio		$(2.24 \pm 0.15) \times 10^{-3}$	$(1.26 \pm 0.11) \times 10^{-3}$

Table 5.7: Number of opposite sign dimuon events and opposite sign background events normalised to the number of ν_μ^{CC} events in the simulation within the fiducial volume. The errors are statistical.

may be found by maximising the function

$$\mathcal{S}(E_{cut}) = \frac{\epsilon_{OSDM}(E_{cut})R_{OSDM} + (1 - \epsilon_{BACK}(E_{cut}))R_{BACK}}{R_{OSDM} + R_{BACK}} \tag{5.4}$$

where $\epsilon_{OSDM}(E_{cut})$ is the selection efficiency of dimuons and is a function of the value of the cut on the energy of the secondary muon, $(1 - \epsilon_{BACK}(E_{cut}))$ is the efficiency for rejecting background events from a ν_μ^{CC} Monte Carlo sample, and R_{OSDM} and R_{BACK} are the production rates of opposite sign dimuon and opposite sign dimuon background events with respect to the number of single muon ν_μ^{CC} interactions produced. The rates of dimuon and dimuon background production are shown in Table 5.7 (i.e. $R_{OSDM} = (2.25 \pm 0.15) \times 10^{-3}$ and $R_{BACK} = (1.26 \pm 0.11) \times 10^{-3}$) and the evolution of $\mathcal{S}$ with successive energy cuts is presented in Table 5.8. In this table the dimuon recognition algorithm has been applied to all samples, with the exception of the secondary muon energy cut, which is being varied. The results suggest that the optimal procedure would be to exclude events which have a secondary muon energy less than 4.5 GeV. The table suggests that the optimal energy cut is at 4.5 GeV.

A similar method based on minimization of the precision of the signal was also investigated. The optimal cut was found to be at the same value as above.

5.4 Dimuon Data Sample

The number of dimuon event candidates, both like sign and opposite sign, which passed the dimuon selection criteria are outlined in the Table 5.9 along with an estimate of the background.

The number of events after correction for the (0.95 ± 0.01) identification probability (cf Section 5.2.1) are (3116 ± 251) for the neutrino induced dimuons and (112 ± 36) for the antineutrino induced dimuons. Approximately

	Charm MC		Background MC		$\mathcal{S}$
E_{cut} (GeV)	Number	Efficiency	Number	Rejection Efficiency	
1.0	8090	100 %	96	0.0 %	64.0
2.0	8090	100 %	96	0.0 %	64.0
3.0	8086	99.9 %	94	2.0 %	64.8
3.5	7927	97.9 %	88	8.3 %	65.4
4.0	7506	92.7 %	78	18.8 %	66.1
4.5	6899	85.3 %	63	34.4 %	67.0
5.0	6266	77.5 %	53	44.8 %	65.8
5.5	5628	69.6 %	44	54.1 %	62.9
6.0	5070	62.7 %	33	65.6 %	59.6
7.0	4198	51.9 %	29	69.8 %	56.8

Table 5.8: The background reduction function $\mathcal{S}$ as a function of the value of the cut on the energy of the secondary muon. This table suggests that the optimal energy cut is at 4.5 GeV.

	OSDM		Like Sign		Background		Corrected OSDM	
Stack	ν_μ	$\overline{\nu_\mu}$	ν_μ	$\overline{\nu_\mu}$	ν_μ	$\overline{\nu_\mu}$	ν_μ	$\overline{\nu_\mu}$
1	1040	72	194	4	291	8	749 ± 87	64 ± 10
2	1284	86	269	9	404	18	880 ± 113	68 ± 11
3	1306	100	324	10	486	20	820 ± 132	80 ± 16
Stacks 1-3	3630	258	787	23	1181	46	2449 ± 194	212 ± 22
4	1006	59	326	4	489	8	517 ± 135	51 ± 10
Total	4636	317	1113	27	1670	54	2966 ± 236	263 ± 24

Table 5.9: Number of ν and $\overline{\nu}$-induced events identified using the dimuon selection algorithm as a function of the stack in which the interaction occurred. Shown are the total number of opposite sign events observed, the total number of like sign events, a background estimate and the number of opposite sign events from charm production corrected for background. The background is estimated by scaling the number of like sign events by 1.5 ± 0.3 (see Section 5.3.1) for the neutrino induced dimuons and by 2.0 ± 1.0 for the antineutrino sample. The uncertainty on the number of corrected events contains the statistical error on the raw OSDM and LSDM event numbers combined in quadrature with the error on the background scaling factor.

half of the antineutrino sample arises from contamination by misidentification in the neutrino sample. As discussed above, the ratio of the number of dimuons produced from antineutrinos to those produced by neutrinos is 4%, implying that there should be on the order of 124 opposite sign dimuons produced from antineutrino interactions. This number is consistent with the number of misidentification corrected antineutrino induced events of (112 ± 36). A display of a dimuon event in NOMAD is shown in Figure 5.4.

The kinematic distributions of dimuons in the data and simulation are compared in Figures 5.5 - 5.6. The means and RMS deviations from the mean for the experimental and reconstructed Monte Carlo samples are summarised in Table 5.10. The variables shown are

- E_1^μ : The energy of the primary muon.
- E_2^μ : The energy of the secondary muon.
- E_{vis}^{had} : The visible hadronic energy including the energy of the secondary muon.
- E_{vis}^{ν} : The visible neutrino energy. This is the sum of E_1^μ and E_{vis}^{had}.
- Q_{vis}^2 : The squared magnitude of the momentum transferred to the hadronic system. This was defined in Equation 1.3.
- x_{Bj} : Bjorken x (see Equation 1.5).
- y_{Bj} : Bjorken y (see Equation 1.6).
- z_{vis} : The fraction of the hadronic energy carried by the secondary muon. This is defined to be

$$z_{vis} = \frac{E_2^\mu}{E_{vis}^{had} + E_2^\mu} \tag{5.5}$$

The distributions from the Monte Carlo do not agree well with those from data. The energy of the secondary muon is significantly softer in the simulation than in the data. The average Q^2 and the average x_{Bj} are much smaller in the data as are the RMS deviations from their respective means. The comparison suggests that charm simulation used in the standard Monte Carlo is not producing the kinematics appropriate to dimuon production from charm. Figure 5.7 compares the distributions of the neutrino energy, E_ν, x_{Bj}, and the energy transferred to the hadronic system, ν, in the NEGLIB simulation and according to the cross section in Equation 1.38. In both

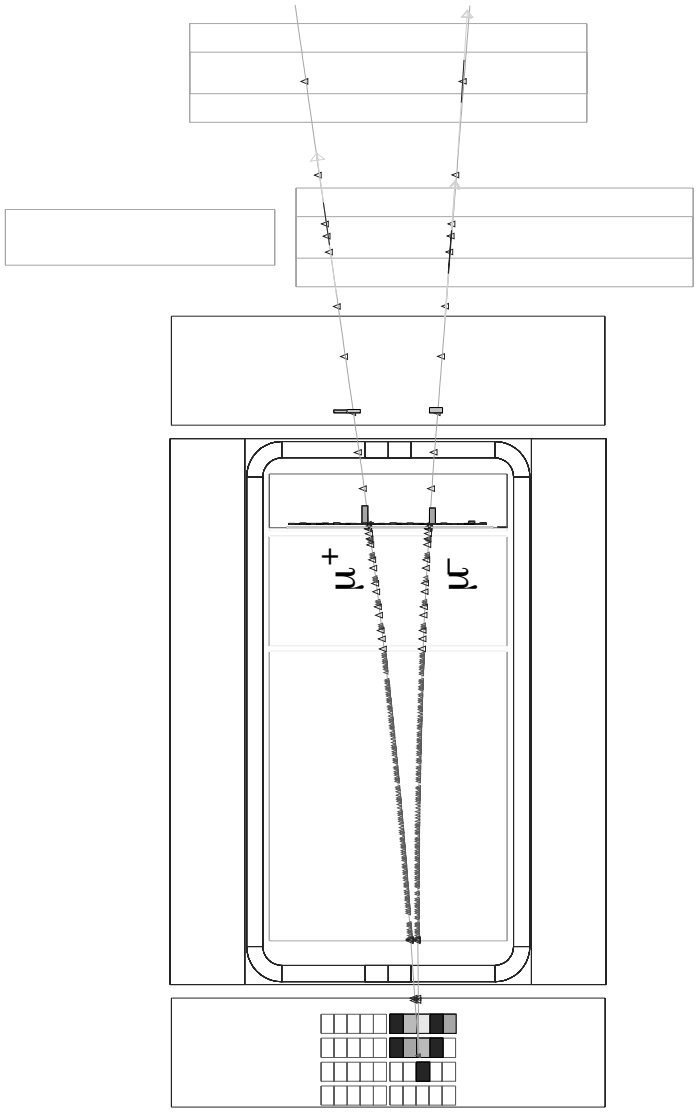

Figure 5.4: Example of an opposite sign dimuon event occurring at the end of Stack 2 in the FCAL. The two tracks are the oppositely charged muons in the event.

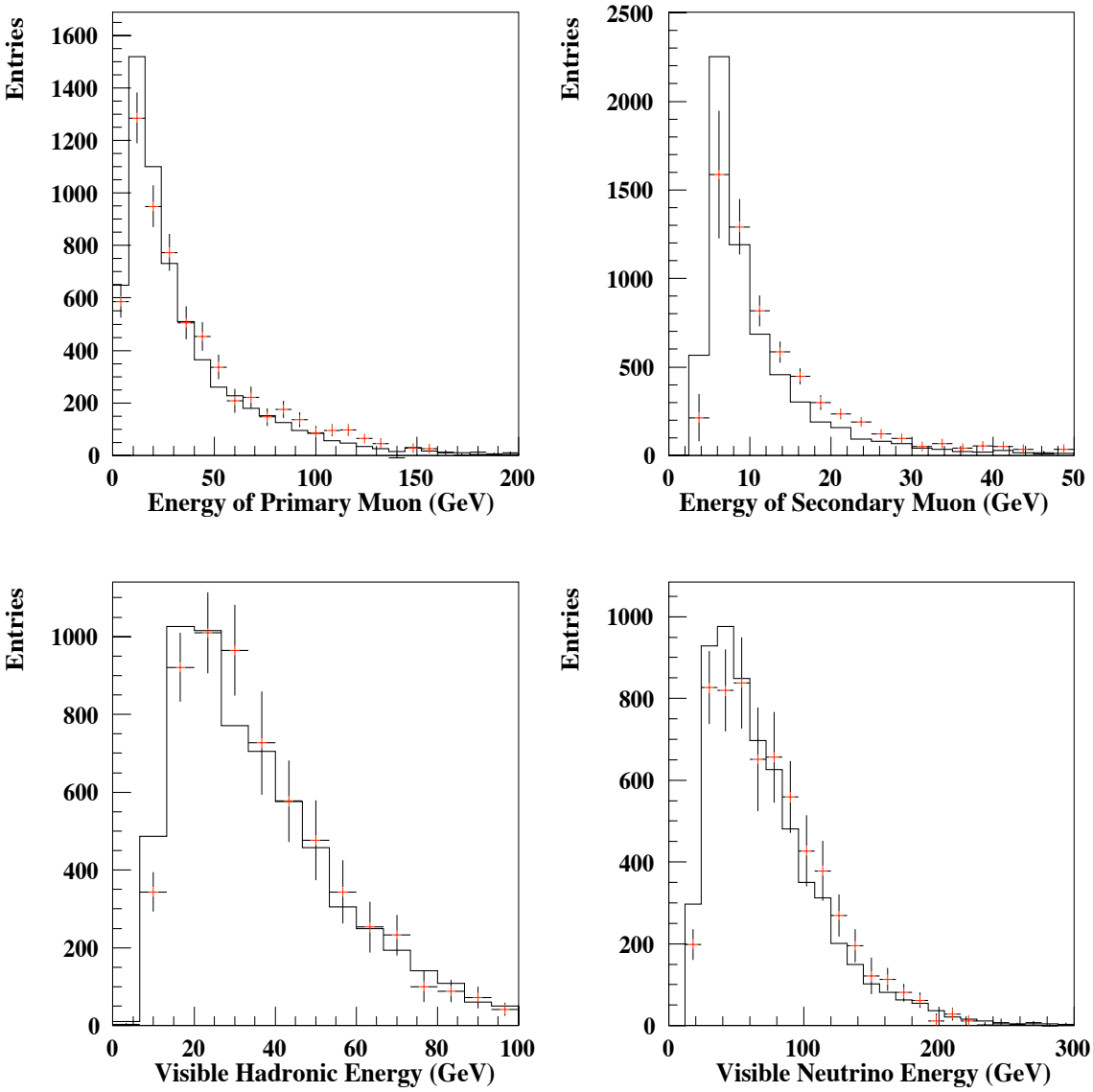

Figure 5.5: Comparison of kinematic distributions from opposite sign dimuon simulation (histogram) and data (points) . The data has been corrected for background. Shown are (top left) the energy of the primary muon, (top right) the energy of the secondary muon, (bottom left) the visible hadronic energy distribution and (bottom right) the visible neutrino energy distribution. The data and Monte Carlo have been normalised to the same area.

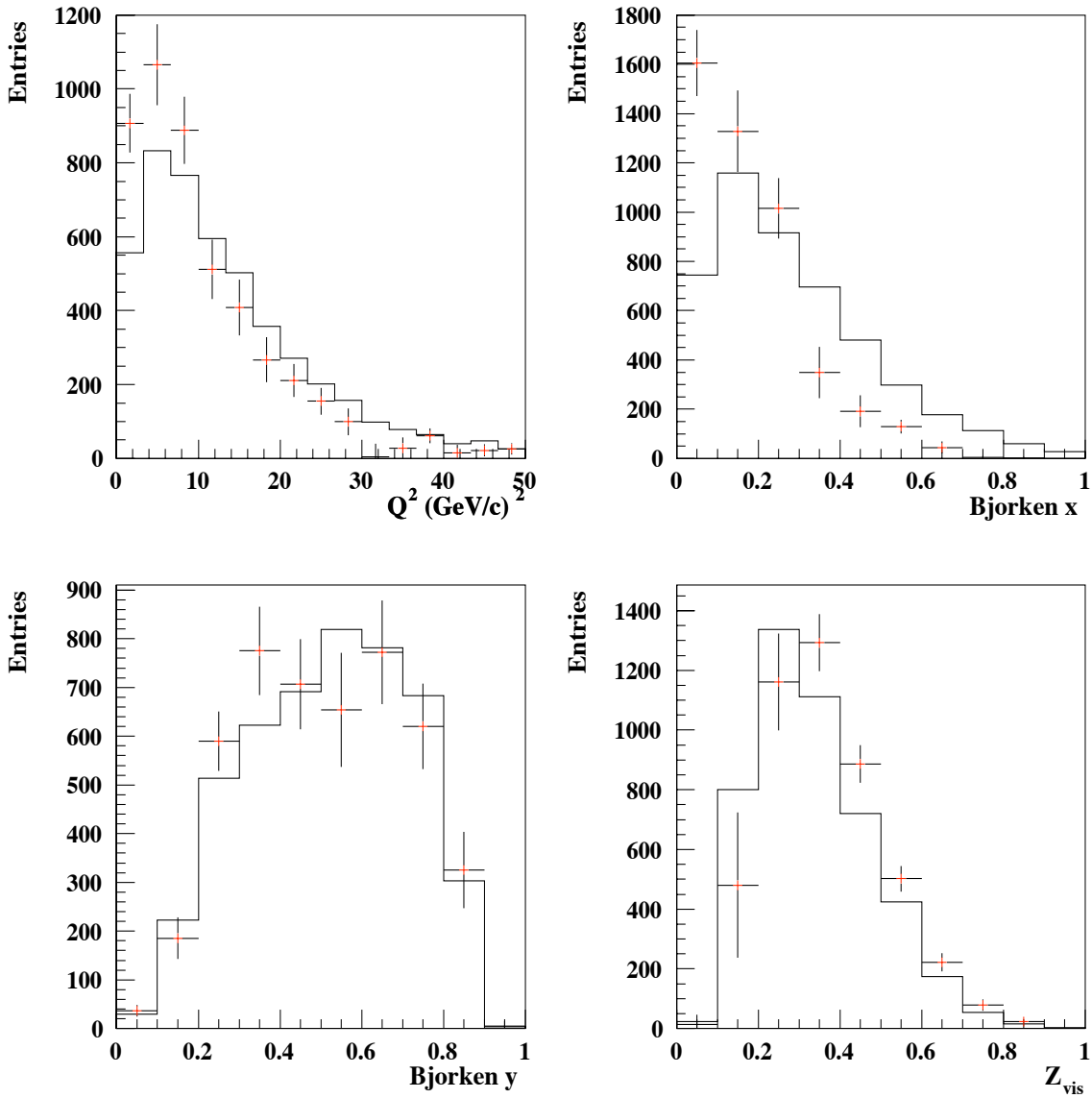

Figure 5.6: Comparison of kinematic distributions from opposite sign dimuon simulation (histogram) and data (points). The data has been corrected for background. Shown are (top left) Q^2, (top right) Bjorken x, (bottom left) Bjorken y and (bottom right) z_{vis}. The data and Monte Carlo have been normalised to the same area.

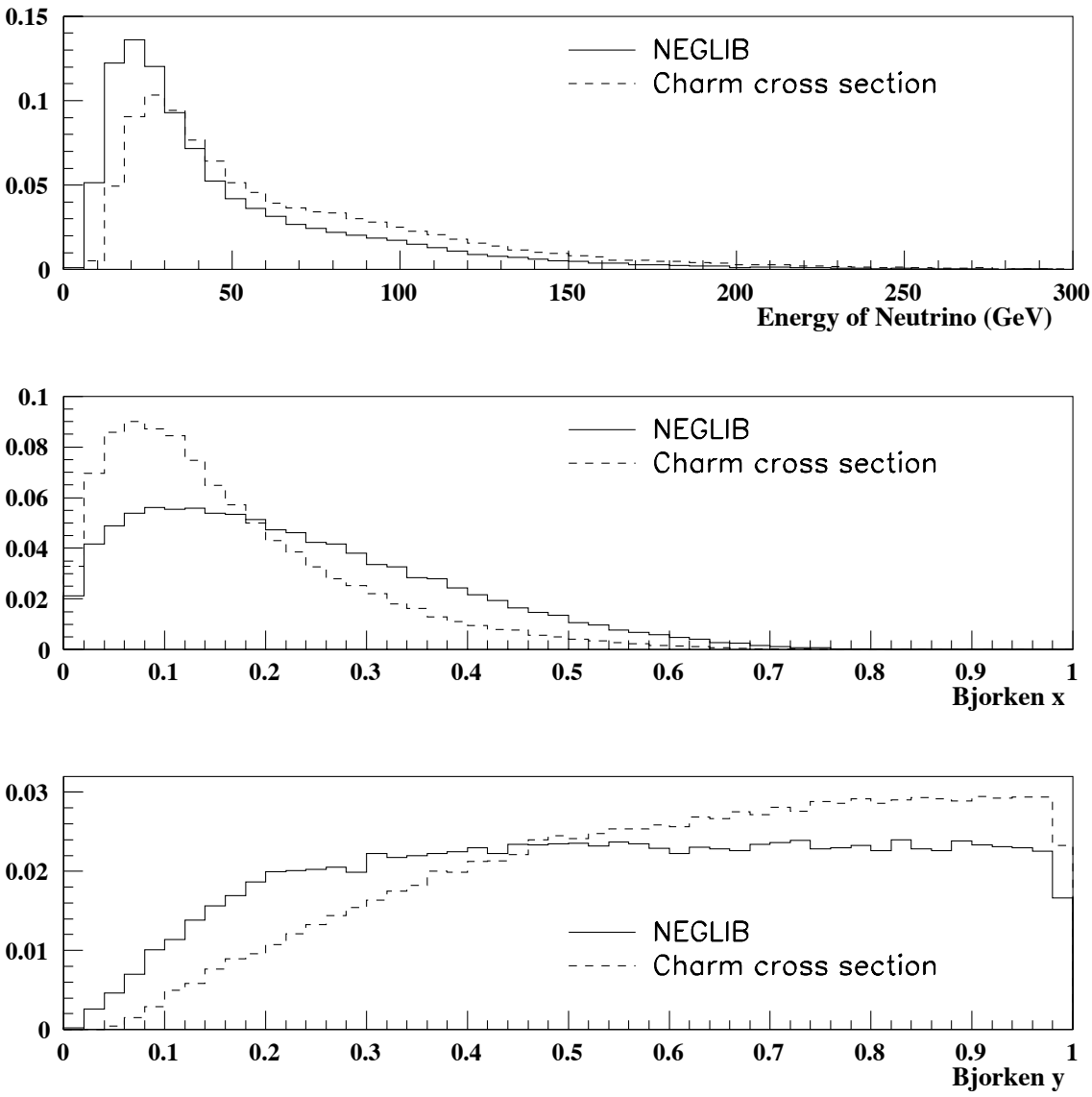

Figure 5.7: Comparison of the kinematics distributions of dimuon events from the NOMAD Monte Carlo, NEGLIB, and according to the appropriate dimuon production cross section. Shown are the energy of the incoming neutrino (top), Bjorken x (middle) and Bjorken y (bottom). Both calculations used a charm mass of 1.3 GeV/c^2 and identical structure functions.

quantity	OSDM Data		OSDM Monte Carlo		χ^2/dof of fit
	Mean	RMS	Mean	RMS	
E_1^μ (GeV)	38.7	34.2	33.9	30.9	35/24
E_2^μ (GeV)	13.3	8.6	10.5	7.1	127/19
E_{vis}^{had} (GeV)	36.1	18.9	35.9	19.8	15/14
E_{vis}^{ν} (GeV)	76.1	41.9	71.3	41.6	25/24
Q_{vis}^2 $(GeV/c)^2$	11.2	9.6	15.6	11.5	46/14
x_{Bj}	0.19	0.14	0.28	0.19	234/9
y_{Bj}	0.54	0.21	0.56	0.20	11/9
z_{vis}	0.36	0.15	0.32	0.15	39/9

Table 5.10: Mean and RMS values of the reconstructed kinematic variable distributions for opposite sign dimuons in data and Monte Carlo, together with the χ^2 of the comparison of the shapes of the distributions.

calculations the value of the charm mass was 1.3 GeV/c^2 and the structure functions used were GRV-HO[55].

As Figure 5.7 shows, the standard NOMAD Monte Carlo does not describe the dimuon production process. The Bjorken y distribution is far less skewed to high values, indicating that the charm mass threshold is not being taken into account properly. The difference in the Bjorken x distributions show that slow rescaling (in which the structure functions are dependent on the slow rescaling variable ξ rather than Bjorken x (see Section 1.5.1)) is not being applied. Inspection of the event generator shows that this is indeed the case : slow rescaling is not implemented and charm mass threshold effects are introduced via a somewhat ad hoc "fast rescaling" procedure in which the invariant mass of the hadronic system is required to be large enough to accommodate a heavy quark. Although this introduces an approximation to the charm mass threshold, in the light of the discussion in Chapter 1, it is clearly an inadequate description.

5.5 FADE - An Alternative Charm Monte Carlo

The problems attendant to the standard NOMAD Monte Carlo description of charm production were resolved using an alternative Monte Carlo which was specifically constructed to simulate opposite sign dimuon events in the FCAL. FADE (Fcal Analysis of Dimuon Events) simulates the kinematics of both

single muon charged current events and opposite sign dimuon events. It then smears the observable variables using smearing and acceptance tables derived from the standard NOMAD Monte Carlo. This allows a large event sample to be generated in a much shorter time than would be the case if each event was passed through the GENOM/RECON chain. The standard NOMAD Monte Carlo chain is used for the estimate of the π/K background as this requires extensive simulation of the hadronic system and its interaction with the detector elements.

5.5.1 Detector Acceptance and Smearing

A detector is not a perfect instrument. Misalignments, errors in the energy measurement, due both to shower fluctuations and error in the energy calibration, tracking errors at high momentum, geometric acceptances; all these (and more) serve to distort the input event variable distributions. It is the function of a detector simulation to model such effects so that corrections may be determined. The simulation used in FADE is straight-forward and relies on the main NOMAD Monte Carlo.

Muon Acceptance and Smearing

GENOM was used in test beam mode to determine the muon geometric acceptance. A sample of 100,000 muons was generated in the centre of each stack of the FCAL with energies between 0 and 300 GeV and with an angular range sufficient to cover the solid angle subtended by the muon chambers at the FCAL. Since the particles follow a curved trajectory in the magnetic field, the acceptance is a function of both angle and momentum.

The direction and energy of the muons were smeared using the results of the muon identification study in Section 4.2. The "measured" energy of the muon was then obtained by smearing the simulated energy by a gaussian with a 1% offset in the resolution and a 3% standard deviation (see Figure 4.2).

The muon direction was smeared by giving the muon a small angular offset with respect to its initial direction of motion. The size of the offset was calculated by comparing the direction of the generated and measured muon momentum vectors in the muon Monte Carlo sample for each stack and fitting a function to the angular deviation distribution. The fit function was

$$f(\theta) = A_1\, \theta\, exp(A_2\, \theta + A_3\, \theta^2) \tag{5.6}$$

Stack	A_1	A_2	A_3
1	9.56	-18.22	9.76
2	10.27	-18.71	9.44
3	12.47	-20.68	11.43
4	15.90	-23.33	13.82

Table 5.11: Fit parameters used in the parametrisation of the muon direction smearing.

where θ is the angle through which the muon track had deviated from the initial direction in radians. The fit parameters for each stack are shown in Table 5.11.

In practice, the muon acceptance is relatively insensitive to the multiple scattering effects within the FCAL. At an energy of 5.0 GeV, which is just above the muon energy threshold, a muon traversing the entire length of FCAL would scatter through a mean angle of approximately 25 mrad. This would result in a shift of the impact position of the muon in the muon chambers by only 15 cm.

Hadronic Energy Smearing

The hadronic energy is smeared in a similar way. Tables were produced relating measured to input hadronic energy for interactions in different parts and different stacks of the FCAL. The central region, near and across the mid-stack gap, is handled by a separate table to take the large difference in energy resolution in this area into account. The tables allow one not only to take the mean measured energy into account, but also the shower fluctuations.

5.5.2 The FADE Single Muon Event Generator

The single muon ν_μ^{CC} events provide an excellent means to test the acceptance and smearing description in the Monte Carlo. A sample of 100,000 ν_μ^{CC} events were generated in FADE and the acceptance and smearing algorithms were applied. The events were generated using the cross section in Equation 1.23. The FCAL target is not isoscalar, containing a 5.67% excess of neutrons, and so the isoscalar corrected cross section was used. The parton densities were those measured by the CCFR experiment [73]. These were found to fit the shape of the data distributions somewhat better than the GRV-HO parton densities. The visible Q^2 of the selected event sample was required to be

greater than 1.0 $(\mathrm{GeV/c})^2$ as the parton densities are not defined below this region. The ν_μ^{CC} selection algorithm used in Section 4.3 was used along with the requirement that the measured hadronic energy be above 5 GeV and the measured muon energy be above 4 GeV. Figure 5.8 shows distributions of various kinematic variables, comparing the ν_μ^{CC} FADE simulation with the single muon data.

The distributions are in relatively good agreement, implying that the acceptance and smearing algorithm used describes the data well. There is a small underestimate of the number of events in the Monte Carlo at low hadronic energy indicating that the smearing at these energies may not be optimal. In general, however, due to the charm mass threshold, dimuon events will occur with large hadronic energies so this problem is expected to be minimised.

5.6 The FADE Dimuon Event Generator

The first step in the generation of opposite sign dimuon events is to choose an event topology based on the cross section in Equation 1.38. Once a valid event is generated, the charm quark is fragmented into a charmed hadron according to a fragmentation function measured using charmed hadron production data in e^+e^- collider experiments[68]. The resulting meson is assigned a component of momentum transverse to the original direction of the charmed quark using empirical data gathered at E531 at Fermilab [66] and is then required to decay semileptonically as described below. As in the single muon case, acceptance functions are applied to the secondary muon, and the visible hadronic energy is smeared. Kinematic variables are then reconstructed using the smeared energies and directions of the hadronic system and the muons.

5.6.1 Charm Fragmentation

Bare quarks are not observed in nature. Hence, there must be some mechanism whereby the quark produced at the hadronic vertex combines with other quarks to form the jet of hadrons seen in the detector. This process of "fragmentation" cannot be described in the scenario of perturbative QCD. However there are a number of non-perturbative models available which describe the basic features.

All fragmentation models define a fragmentation parameter, z. The exact definition tends to depend on the experiment; however, previous experiments on the production of charm in neutrino interactions [62, 63] have defined z

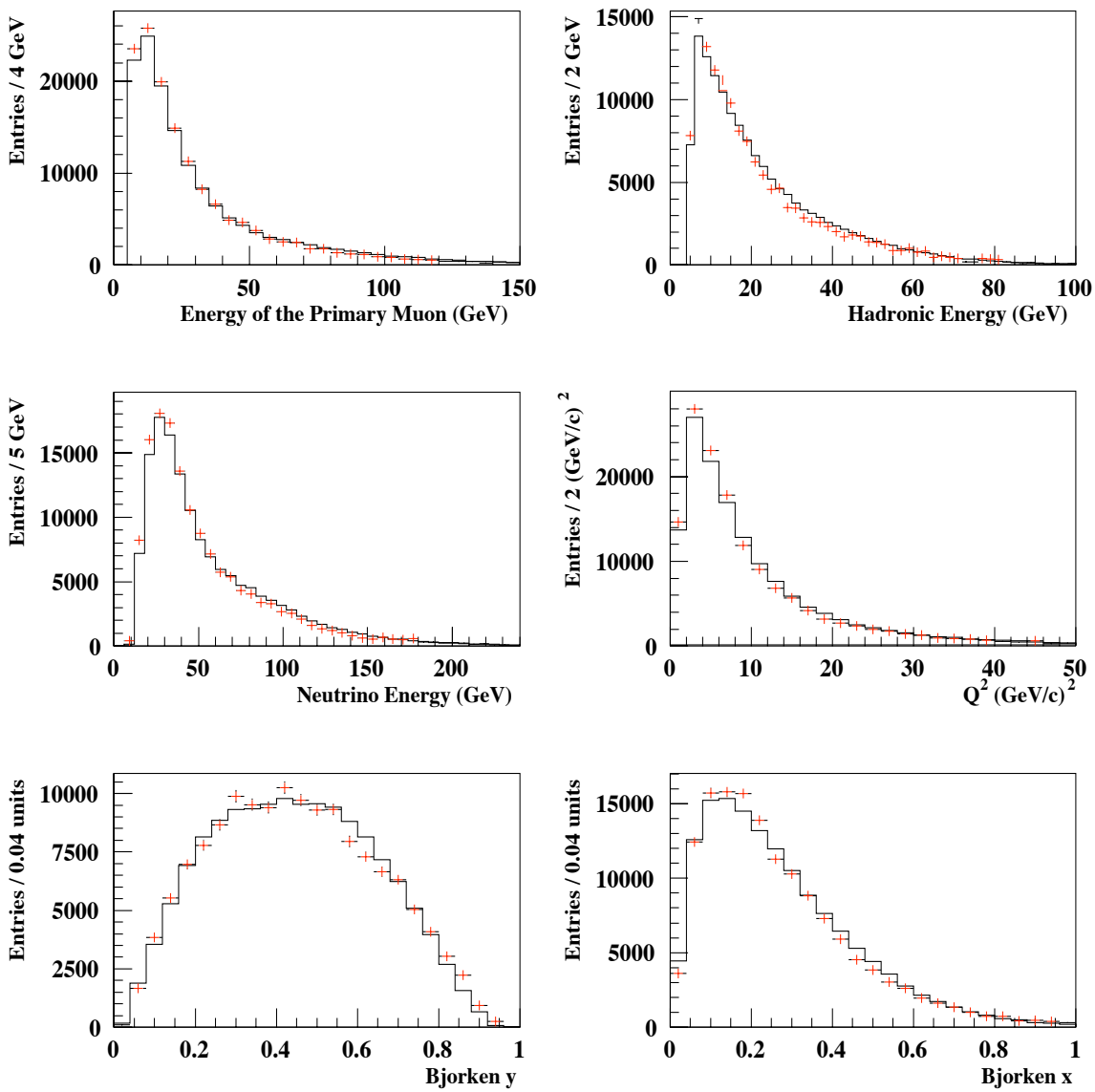

Figure 5.8: Comparison of kinematic distributions from the FADE single muon ν_μ^{CC} simulation (histogram) and data (points). The data and the simulation have been normalised to equal areas. Shown are (top left) the energy of the primary muon, (top right) the visible hadronic energy of the event, (middle left) the neutrino energy, (middle right) the momentum transferred to the hadronic system, (bottom left) the Bjorken y distribution and (bottom right) the Bjorken x distribution.

to be

$$z = \frac{p_M}{p_M^{max}} \tag{5.7}$$

where p_M is the momentum of the hadron, M, and p_M^{max} is the maximum momentum which the kinematics will allow the hadron to carry. For purposes of comparison, this definition will be used in this thesis as well.

In order to use the results of the e^+e^- collider experiments it is necessary that the fragmentation be carried out in the W-boson-nucleon centre of mass frame. In analogy with the CLEO experiment[68], the maximum possible momentum is defined to be

$$p_M^{max} = \sqrt{E_{beam}^2 - m^2} \tag{5.8}$$

where m is the mass of the hadron. In the boson-nucleon centre of mass frame

$$2\ E_{beam} = W \tag{5.9}$$

with W being the invariant mass of the hadronic system, and so

$$p_M^{max} = \sqrt{\left(\frac{W}{2}\right)^2 - m^2} \tag{5.10}$$

The hadron is assigned a fraction z of this momentum.

As alluded to in Chapter 1 the z distribution of the charmed hadron is generally parametrised by a fragmentation function, $D(z)$. There are a number of possible choices for the form of this function, but two specific parametrisations are most often used.

- **Peterson Function :** The Peterson function is defined to be

$$D(z) = \frac{N}{z}\left(1 - \frac{1}{z} - \frac{\epsilon_P}{1-z}\right)^{-2} \tag{5.11}$$

- **Collins-Spiller Function :**

$$D(z) = N\left(\frac{1-z}{z} + \frac{\epsilon_C\,(2-z)}{1-z}\right)(1+z)^2\left(1 - \frac{1}{z} - \frac{\epsilon_C}{1-z}\right)^{-2} \tag{5.12}$$

where ϵ_P and ϵ_C are free parameters, and N is a normalisation factor that ensures that the integral of $D(z)$ is unity.

Experiment	ϵ parameter	
	Peterson	Collins-Spiller
CLEO [68]	0.16 ± 0.01	0.6 ± 0.1
ARGUS [69]	0.19 ± 0.03	
CCFR [63]	0.22 ± 0.05	0.8 ± 0.2

Table 5.12: Experimental determination of the charm quark fragmentation parameter for the Peterson and Collins-Spiller fragmentation functions.

The value of the fragmentation parameter, ϵ, has been measured in both e^+e^- collider experiments and neutrino fixed target experiments. Table 5.12 presents a compilation of the values of the fragmentation parameter, for both the Peterson and the Collins-Spiller functions, derived from various experiments. The CLEO experiment found that the Peterson function did not adequately describe their data, finding a fit χ^2 of 40.0 for 10 degrees of freedom. The Collins-Spiller function, on the other hand, fits the data well with a χ^2 of 6.3 for 10 degrees of freedom. The CCFR determination of the Collins-Spiller fragmentation parameter is larger than that from CLEO, perhaps due to nuclear and reinteraction effects that are not present in the e^+e^- experiments, but is still consistent within the errors. This analysis uses the Collins-Spiller fragmentation function with the fragmentation parameter defined by a weighted average of the CCFR and CLEO results : $\epsilon = (0.64 \pm 0.09)$.

The species of charmed hadrons produced in neutrino interactions was measured by E531 [67]. Above a visible neutrino energy of 30 GeV, the production fractions were $60\pm6\%$ D^0, $26\pm6\%$ D^+, $7\pm5\%$ D_s^+ and $7\pm4\%$ Λ_c^+. However, because the Λ_c is produced at low energies, the secondary muon from Λ_c decays has a correspondingly lower energy than those from D meson decays. The acceptance for these muons is small and most will escape the detector. This, together with the low semileptonic branching ration of the Λ_c, 4.5 ± 1.7 %, means that the dimuon sample may be assumed to be composed solely of D mesons. Monte Carlo studies support this conclusion, showing that the Λ_c contributes to the final event sample at about the level of 5%.

5.6.2 Transverse Momentum of the D meson

During fragmentation, the meson acquires a momentum component transverse to the original direction of the charm quark. The Monte Carlo chooses

$D^{\pm}$ Branching Ratio	
$\nu\ \mu\ \pi$	0.03
$\nu\ \mu\ K$	0.67
$\nu\ \mu\ K^*$	0.30
D^0 Branching Ratio	
$\nu\ \mu\ \pi$	0.08
$\nu\ \mu\ K$	0.67
$\nu\ \mu\ K^*$	0.25
Λ_c Branching Ratio	
$\Lambda\ \nu\ \mu$	1.00

Table 5.13: The branching ratio of D meson and Λ_c baryon semileptonic decays relative to the total semileptonic branching fraction.

a transverse momentum from a spectrum of the form

$$\frac{dN}{dp_T^2} = N_0 e^{-\beta\, p_T^2} \tag{5.13}$$

where N_0 is a normalisation constant. The parameter β was measured to be $\beta = 1.1 \pm 0.3$ by the LEBC EHS collaboration [70].

5.6.3 Charmed hadron decay

Having generated the charmed meson, the final step is to perform the semileptonic decay. The branching ratios of the different semileptonic decay modes of the D meson and the Λ_c baryon are listed in Table 5.13[82].

The D meson is decayed using a spin-1 vector matrix element in the case of the K^* decay mode and a spin-0 pseudoscalar matrix element for the other decays [72]. As in Jetset[45], the decay of the Λ_c baryon is carried out using a V-A matrix element to distribute the decay products. This takes the form

$$|\mathcal{M}|^2 = (p_{\Lambda_c} p_\mu)(p_\nu p_\Lambda) \tag{5.14}$$

where p_i, $i \in \{\Lambda_c, \mu, \nu, \Lambda\}$, are the four momenta of the particles in the decay. The decay is carried out in the centre-of-mass frame of the meson, randomly oriented and then boosted into the laboratory frame.

A comparison of the dimuon distributions obtained from the data and the FADE Monte Carlo are shown in Figures 5.9 and 5.10 and the standard comparisons of means and root mean square deviations from the mean are

quantity	FADE Data		FADE Monte Carlo		χ^2/dof of fit
	Mean	RMS	Mean	RMS	
E_1^μ (GeV)	38.8	34.7	35.5	32.1	23/24
E_2^μ (GeV)	10.1	5.0	9.5	4.7	25/19
E_{vis}^{had} (GeV)	36.8	19.1	39.2	19.8	15/14
E_{vis}^{ν} (GeV)	77.4	42.9	80.8	46.0	25/24
Q_{vis}^2 $(GeV/c)^2$	13.2	10.9	12.8	10.7	12/14
x_{Bj}	0.19	0.14	0.19	0.16	12/9
y_{Bj}	0.51	0.21	0.53	0.21	10/9
z_{vis}	0.36	0.14	0.32	0.16	15/9

Table 5.14: Mean and RMS values of the reconstructed kinematic variable distributions for opposite sign dimuons in data and Monte Carlo, together with the χ^2 of the comparison of the shapes of the distributions.

shown in Table 5.14. The Monte Carlo sample was generated with a fragmentation parameter of 0.64, a charm mass of 1.3 (GeV/c^2) and using the CCFR structure functions.

In all cases the comparison of the simulation and data distributions has improved. In particular, a dramatic improvement has been made in the x_{Bj} and Q^2 distributions, indicating that the correct dependence on the cross section has been implemented.

As a different Monte Carlo program is being used to simulate the dimuon data than was used to arrive at estimates of the selection efficiencies in Section 5.2.1 it makes sense to consider how the efficiency may have changed. The same cuts as in the previous study were applied to the FADE dimuon sample. Tables 5.15 and 5.16 show the cumulative and relative efficiencies as a function of the cuts. Since FADE does not track particles through the detector it was impossible to apply the timing cut. However, this cut affects the dimuon selection efficiency at a level of less than a percent and has a negligible effect on the event distributions of true dimuons.

The efficiencies calculated from the NEGLIB and FADE Monte Carlo differ by about 2 %. The main contribution to the increase in the efficiency is that more events pass the cut on the secondary muon energy in the FADE sample, indicating that the secondary muon has a slightly harder energy distribution in FADE than in NEGLIB. This can be easily understood by noting that the energy threshold induced by charm mass effects in FADE is higher than in NEGLIB. The D meson tends to a higher mean energy which will, in turn, translate into a higher mean energy for the decay muon.

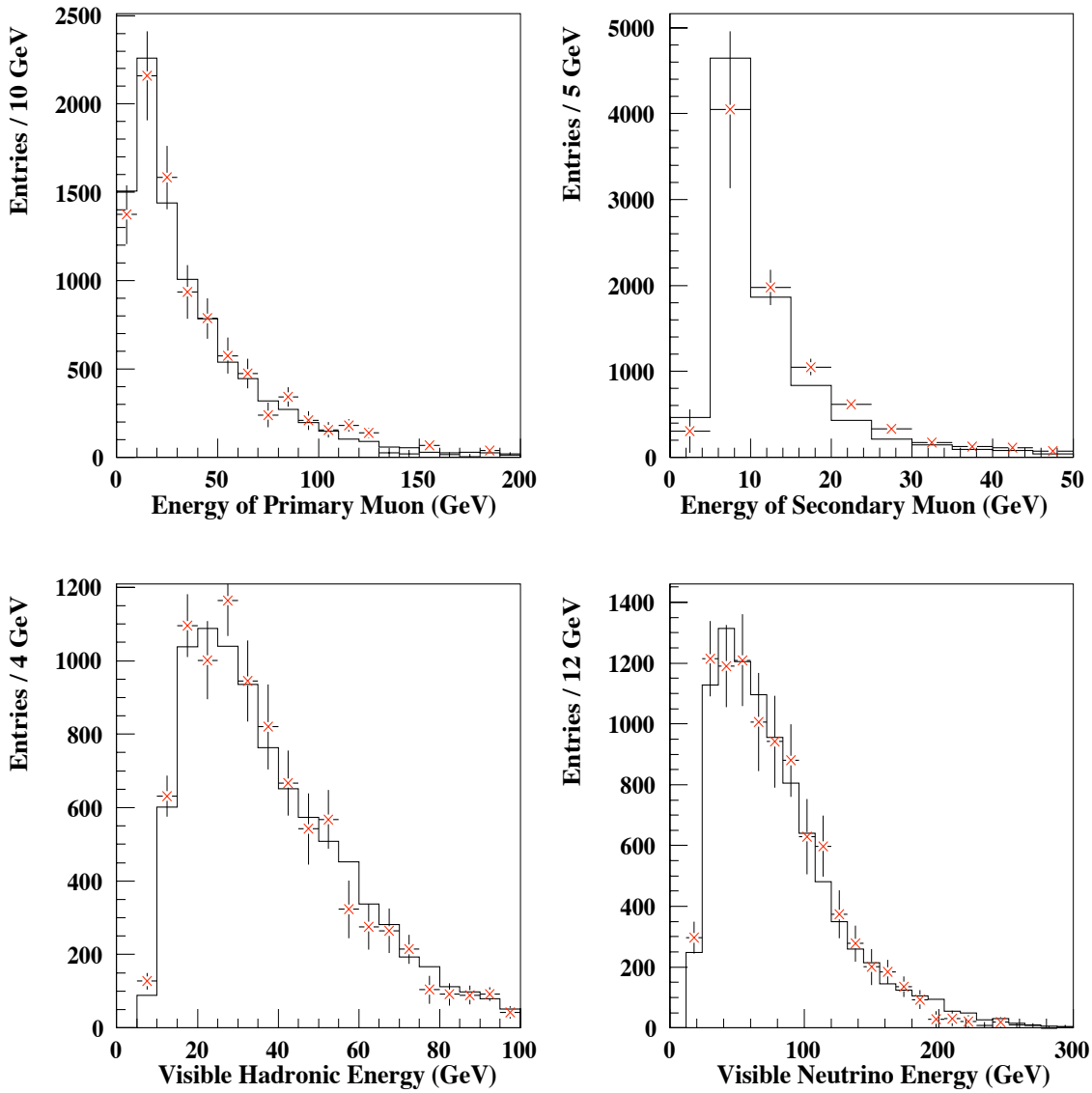

Figure 5.9: Comparison of kinematic distributions from the FADE opposite sign dimuon simulation (histogram) and data (points). The data has been corrected for background. Shown are (top left) the energy of the primary muon, (top right) the energy of the secondary muon, (bottom left) the visible hadronic energy distribution and (bottom right) the visible neutrino energy distribution. Data and Monte Carlo have been normalised to equal areas.

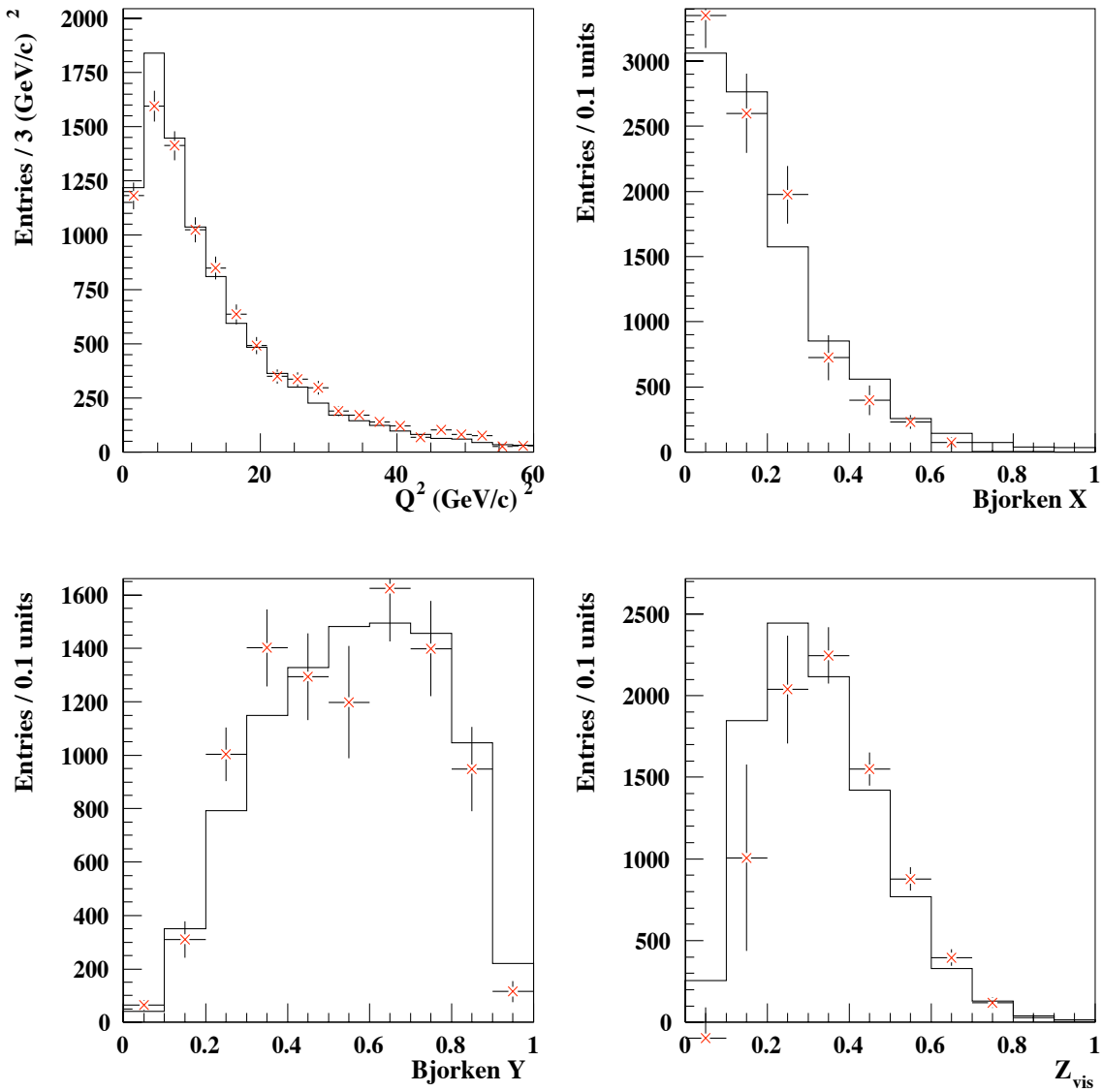

Figure 5.10: Comparison of kinematic distributions from the FADE opposite sign dimuon simulation (histogram) and data (points). The data has been corrected for background. Shown are (top left) Q^2, (top right) Bjorken x, (bottom left) Bjorken y and (bottom right) z_{vis}. Data and Monte Carlo have been normalised to equal areas.

Stack 1			
Cut	Number of events	Efficiency	Relative Efficiency
	25167		
Fiducial Area	17288	100 %	100 %
Trigger Threshold	17263	99.8%	99.8%
$N_\mu > 0$	12946	75.8%	75.0%
Vertex Association	12279	71.0%	94.8%
$E_1^\mu > 4.5$ GeV	11713	67.7%	95.4%
$N_\mu = 2$	2814	16.3%	24.0%
$E_2^\mu > 4.5$ GeV	2754	15.9%	97.8%
Spatial Correlation	2602	15.0%	94.5%
Identification Algorithm	2391	13.8%	91.9%
Stack 2			
Cut	Number of events	Efficiency	Relative Efficiency
	26560		
Fiducial Area	18125	100 %	100 %
Trigger Threshold	18070	99.7%	99.7%
$N_\mu > 0$	13943	76.9%	77.1%
Vertex Association	13316	73.4%	95.5%
$E_1^\mu > 4.5$ GeV	12616	69.6%	94.7%
$N_\mu = 2$	3195	17.6%	25.3%
$E_2^\mu > 4.5$ GeV	3066	16.9%	95.9%
Spatial Correlation	2914	16.0%	95.0%
Identification Algorithm	2719	15.0%	93.3%

Table 5.15: ν_μ opposite sign dimuon event selection efficiency for events generated by FADE beginning stacks 1 and 2.

Stack 3			
Cut	Number of events	Efficiency	Relative Efficiency
	26507		
Fiducial Area	18095	100%	100%
Trigger Threshold	17988	99.4%	99.4%
$N_\mu > 0$	13998	77.3%	77.8%
Vertex Association	13496	74.5%	96.4%
$E_1^\mu > 4.5$ GeV	12669	70.0%	93.8%
$N_\mu = 2$	3287	18.1%	25.9%
$E_2^\mu > 4.5$ GeV	3072	16.9%	93.4%
Spatial Correlation	3009	16.6%	97.9%
Identification Algorithm	2807	15.5%	93.2%
Stack 4			
Cut	Number of events	Efficiency	Relative Efficiency
	21766		
Fiducial Area	14799	100%	100%
Trigger Threshold	11869	80.2%	80.2%
$N_\mu > 0$	8621	58.3%	72.6%
Vertex Association	8339	56.3%	96.7%
$E_1^\mu > 4.5$ GeV	8024	54.2%	96.2%
$N_\mu = 2$	2223	15.0%	27.7%
$E_2^\mu > 4.5$ GeV	2011	13.5%	90.4%
Spatial Correlation	1971	13.3%	98.0%
Identification Algorithm	1842	12.4%	93.4%

Table 5.16: ν_μ opposite sign dimuon event selection efficiency for events generated by FADE beginning stacks 1 and 2.

5.7 Dimuon Rates and the Charm Threshold

Instead of the absolute dimuon cross-section, dimuon analyses tend to focus upon the ratio of the dimuon to single muon rates. The reason for this is three-fold : this quantity is more directly obtained, is insensitive to the description of the beam profile, and the energy dependence of the rates provides information on the charm mass and other parameters (CKM elements, amount of strangeness in the nucleon). This section studies the relative rate and presents comparisons with several other experiments. The comparison will be made only on the neutrino sample, due to the low statistics of the antineutrino events.

5.7.1 Extraction of the Relative Rates

The dimuon rate was calculated using the following procedure:

1. Background subtracted dimuon and single muon data were binned in five E^{ν}_{vis} bins.

2. Both samples were corrected for acceptance and kinematic cuts. In the dimuon case the correction also takes the ν-$\overline{\nu}$ misidentification and the missing energy due to the unobserved neutrino in the meson decay into account.

3. The corrected dimuon data is divided by the corrected single muon data for each E^{ν}_{vis} bin.

The correction factor used for the dimuon and single muon samples was:

$$\mathcal{A}(E^{\nu}_{vis}) = \frac{N(E^{\nu})_{gen}}{N(E^{\nu}_{vis})_{obs}} \tag{5.15}$$

where $N(E^{\nu})_{gen}$ represents the number of events generated in bins of incident neutrino energy and $N(E^{\nu}_{vis})_{obs}$ represents the number of events observed in bins of visible neutrino energy. The dimuon to single muon cross section ratios are displayed in Table 5.17 and shown in Figure 5.11. Also shown in Figure 5.11 are the acceptance corrected results from the CCFR experiment [62] and the CDHS experiment [75]. The three experiments agree well in the energy ranges to which they are sensitive. The NOMAD and CCFR results agree with the theoretical prediction based on the slow rescaling mechanism at zeroth order in α_s. The CDHS results are systematically lower than both the NOMAD and CCFR data and the theoretical prediction, indicating a possible further threshold effect in the CDHS data at low energies. The

Monte Carlo was generated with a charm mass of 1.3 (GeV/c^2). Both the single muon and dimuon Monte Carlo samples used the CCFR structure functions.

It should be noted that, although the relative rate is independent of the neutrino beam profile when it is studied as a function of the neutrino energy, the total rate is not. The number of neutrino charged current interactions observed in a phase space element $(x + dx, y + dy, E_\nu + dE_\nu)$ is

$$\frac{d^3\mathcal{N}_{CC}}{dxdydE_\nu} = N^T N^\nu \Phi^\nu(E_\nu) \frac{d^3\sigma^{CC}}{dxdydE_\nu} \tag{5.16}$$

where N^T is the number of target nucleons in the experimental fiducial volume, N^ν is the number of neutrinos passing through the fiducial volume over the course of the experiment, $\Phi^\nu(E_\nu)$ is the shape of the neutrino flux as a function of the neutrino energy, normalised such that $\int \Phi^\nu(E_\nu)dE_\nu = 1\text{m}^{-2}$, and $d^3\sigma/dxdydE_\nu$ is the neutrino-nucleon interaction differential cross section. Similarly, the number of neutrino induced dimuon events observed is

$$\frac{d^3\mathcal{N}_{DIM}}{d\xi dydE_\nu} = N^T N^\nu \Phi^\nu(E_\nu) \frac{d^3\sigma^{DIM}}{d\xi dydE_\nu} \tag{5.17}$$

The beam profile dependence cancels when the relative rate, $\mathcal{R}$, as a function of energy is calculated

$$\mathcal{R}(E) = \frac{d\mathcal{N}_{DIM}/dE_\nu}{d\mathcal{N}_{CC}/dE_\nu} = \frac{\int\int(d^3\sigma^{DIM}/d\xi dydE_\nu)d\xi dy}{\int\int(d^3\sigma^{CC}/dxdydE_\nu)dxdy} \tag{5.18}$$

However, when calculating the integrated relative rate, the beam profile must still be taken into account

$$\mathcal{R} = \frac{\mathcal{N}_{DIM}}{\mathcal{N}_{CC}} = \frac{\int\int\int \Phi^\nu(E_\nu)(d^3\sigma^{DIM}/d\xi dydE_\nu)d\xi dydE_\nu}{\int\int\int \Phi^\nu(E_\nu)(d^3\sigma^{CC}/dxdydE_\nu)dE_\nu dxdy} \tag{5.19}$$

This beam dependence changes the rate from the value that is, näively, predicted by the ratio of the integrated differential cross sections. In the case of NOMAD, the effect of the low energy beam is to decrease the number of observed dimuon events to yield a rate of $(4.14 \pm 0.05) \times 10^{-3}$. The opposite effect occurred in CCFR which had a high energy beam (an average neutrino energy of 140 GeV) and measured a higher total rate of $(7.13 \pm 0.23) \times 10^{-3}$.

As a check the same exercise may be performed using the dimuon sample generated by NEGLIB. Figure 5.12 compares the NOMAD data corrected for acceptance and kinematic effects using the charm production model in NEGLIB. The neutrino energy dependence of the dimuon selection efficiency

Neutrino Opposite Sign Dimuon Rates ($m_c = 1.3$ (GeV/c^2))					
Energy Bin (GeV)	μ^- Data	$\mu^-\mu^+$ Data	μ^- Accept. Corr.	$\mu^-\mu^+$ Accept. Corr.	$\sigma_{\mu^-\mu^+}/\sigma_{\mu^-}$ $\times 10^{-3}$
0 - 20	178,677	24 ± 7	5.7 ± 0.1	71 ± 10	1.6 ± 0.5
20 - 40	687,246	458 ± 50	2.02 ± 0.03	13.8 ± 0.4	4.5 ± 0.5
40 - 70	467,932	722 ± 96	1.42 ± 0.02	5.4 ± 0.1	5.8 ± 0.8
70 - 100	229,358	563 ± 82	1.33 ± 0.03	3.4 ± 0.1	6.2 ± 0.9
100 - 200	187,799	604 ± 91	1.86 ± 0.04	4.6 ± 0.1	8 ± 1
200 - 300	7,372	25 ± 12	3.2 ± 0.2	5.3 ± 0.3	6 ± 3
Total	1,751,012	2396 ± 133	2.09 ± 0.03	6.35 ± 0.07	4.14 ± 0.05

Table 5.17: Neutrino induced opposite sign dimuon rates corrected for acceptance and kinematic cuts by a dimuon simulation with a charm mass of 1.3 (GeV/c^2). Columns represent : (1) energy bin, (2) raw single muon data after all cuts, (3) background subtracted dimuon data after all cuts, (4) acceptance correction to the single muon data (5) acceptance correction to the dimuon data and (6) dimuon to single muon ratio.

in FADE differs markedly from that in NEGLIB. This behaviour of the rates is a furthur indication that NEGLIB does not describe charm quark production kinematics appropriately.

The charm analysis presented in the following chapter uses FADE rather than NEGLIB for several other reasons:

- Charm production and the subsequent meson decay is correctly modelled.
- The program can generate large event samples much faster than if the NOMAD Monte Carlo chain were to be used.
- It is straightforward to vary parameters in both the cross section and the description of the fragmentation and
- FADE better describes the available FCAL dimuon data.

5.8 Previous Experiments

The phenomenon of charm production by neutrinos had been investigated by a number of experiments since 1974[77]. Dimuons have been studied by three types of detectors :

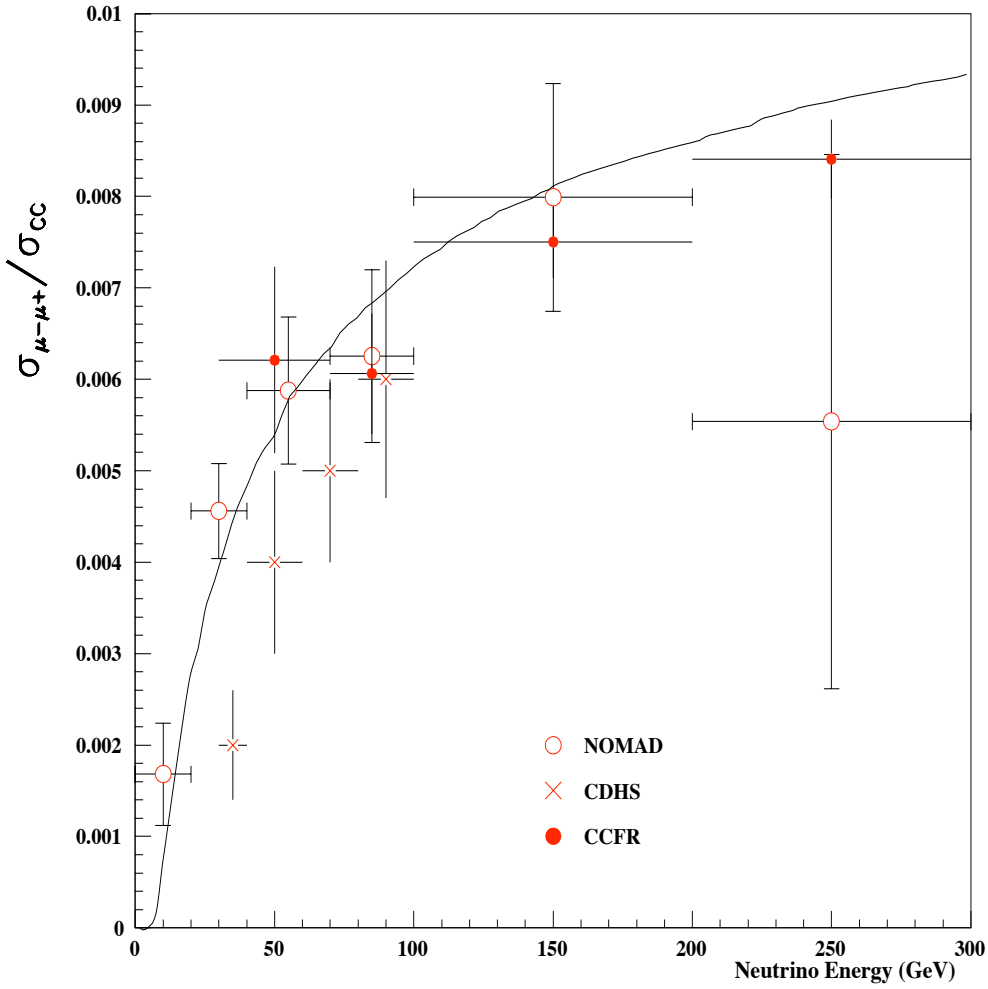

Figure 5.11: Neutrino-induced opposite sign dimuon rates corrected for acceptance and kinematic effects using FADE and assuming a charm mass of 1.3 (GeV/c^2). The NOMAD results are displayed as open circles. Also shown are the CCFR results (closed circles) and CDHS results (crosses). The line is the theoretical ratio of cross sections assuming the slow rescaling mechanism in Leading Order QCD, a charm mass of 1.3 (GeV/c^2), and the validity of the CCFR structure functions.

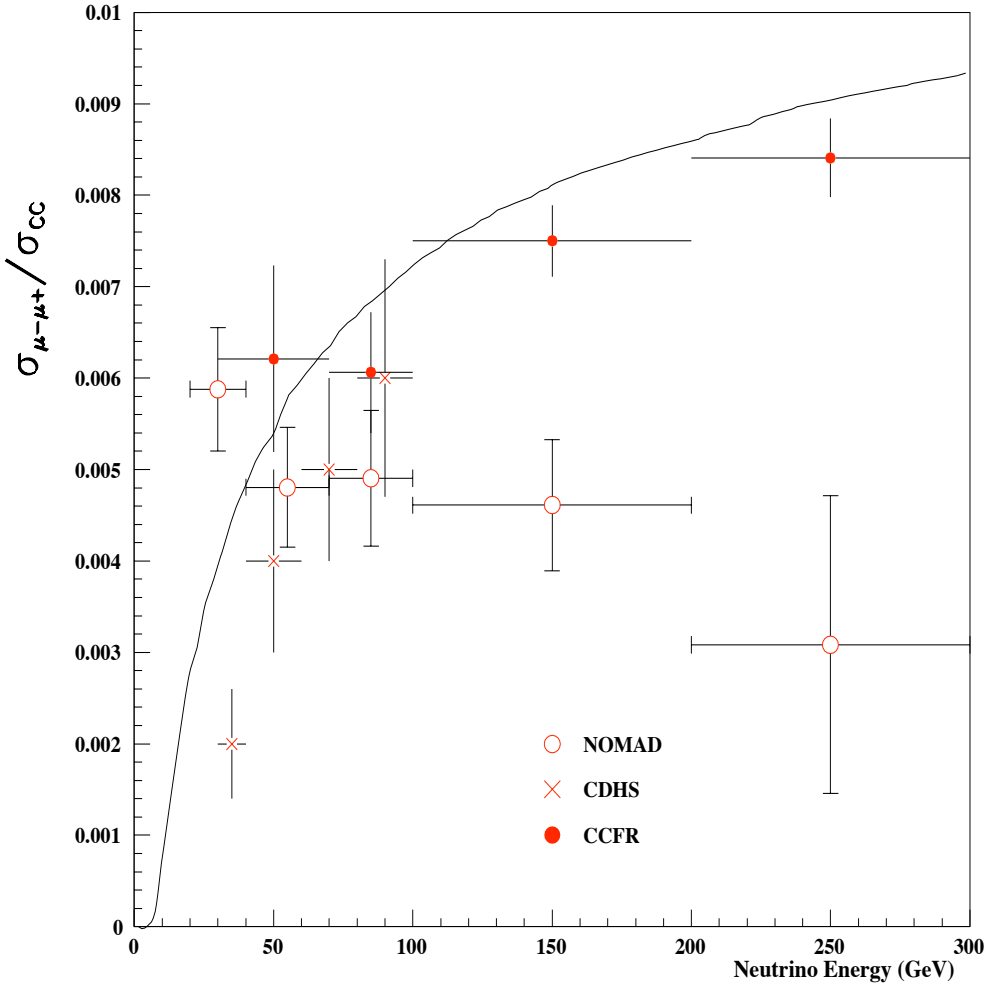

Figure 5.12: Neutrino-induced opposite sign dimuon rates corrected for acceptance and kinematic effects using the standard NOMAD Monte Carlo program, NEGLIB. The program assumes a charm mass of 1.35 (GeV/c^2) and uses the GRV-HO structure functions. The NOMAD results are displayed as open circles. Also shown are the CCFR results (closed circles) and CDHS results (crosses). The line is the theoretical ratio of cross sections assuming the slow rescaling mechanism in Leading Order QCD and a charm mass of 1.35 (GeV/c^2). The GRV-HO structure functions have also been used.

- **Counter Experiments :**
  - **FMMF Collaboration :** This detector was a low density sand-steel calorimeter which used flash chambers for particle tracking. It ran in the Quad-Triplet beam at the Fermilab Tevatron [78]. The dimuon sample consisted of events in which the momentum of both muons was greater than 10 GeV/c.
  - **CDHS Collaboration :** Running at the CERN SPS, the CERN-Dortmund-Heidelberg-Saclay detector accumulated the largest sample of opposite sign dimuons to date [75]. The experiment was a calorimeter using a magnetized steel target with drift chamber tracking and required that both muon momenta be greater than 5 GeV/c.
  - **CCFR Collaboration :** The CCFR group also used a high density target calorimeter, this one made of iron plates interleaved with scintillator planes, and drift chambers for tracking. It ran in the Quad-Triplet beam at the Fermilab Tevatron and has presented many results on opposite sign dimuons, including the first analysis using Next-to-Leading order QCD[63, 64]. The analysis imposed a cut of 9 GeV/c on the momentum of the primary muon and 5 GeV/c on the secondary muon momentum.
  - **CHARM II Collaboration :** The CHARM II detector was a massive, fine-grained and low density detector designed for the study of muon neutrino scattering on electrons. It used glass as the neutrino target and streamer tubes instrumented with cathode strips as both the calorimeter and tracking detector. The dimuon analysis imposed a cut on the momenta of both muons of greater than 6 GeV/c.
- **Bubble Chamber Experiments :**
  - **Columbia-BNL-Rutgers :** The highest statistics dilepton ($\mu^- e^+$) sample from a bubble chamber experiment was gathered by the Columbia-BNL-Rutgers collaboration. The experiment used the Fermilab 15-ft bubble chamber filled with a Ne-H_2 mixture[80] and accepted events in which the momentum of the secondary positron was above 300 MeV/c.
  - **E632 :** This experiment also used the 15-ft bubble chamber at Fermilab with a Ne-H_2 mix [81]. Their dimuon sample required both muons to have greater than 4 GeV/c of momentum.

Counter Experiments			
Experiment	E_ν (GeV)	$\mu^-\mu^+$	$\mu^+\mu^-$
FMMF	30-600	393	
CDHS	0-300	11041	3685
CCFR	30-600	5030	1060
CHARM II	30-300	3100	700
NOMAD	0-300	3116	112
Bubble Chamber Experiments			
Experiment	E_ν (GeV)	μ^-l^+	μ^+l^-
Col-BNL	0-200	461 (μ^-e^+)	
E632	10-450	40 ($\mu^-\mu^+$)	8($\mu^+\mu^-$)
NOMAD	0-300	320 (μ^-e^+)	
Emulsion Experiment			
Experiment	E_ν (GeV)	Charmed Hadron Events	
E531	0-250	122	

Table 5.18: Summary of data samples from previous neutrino charm production experiments.

- **Other Experiments :**
  - **E531 :** Although only accumulating a small number of events, the Fermilab E531 experiment is unique in being an emulsion experiment [66, 67]. This detector measured charm particle production directly by identifying and reconstructing the charm particle decay in the emulsions. Much of the information used in opposite sign dimuon Monte Carlo codes comes from this experiment.

A summary of the results obtained from these experiments is given in Table 5.18. NOMAD appears in two places in the table in order to emphasize the hybrid nature of the NOMAD detector. The detector is capable of studying dimuon production in the FCAL and both dimuon and μ^-e^+[74] production in the main target.

Chapter 6

Charm Analysis

6.1 Introduction

Information about the parameters involved in the production of charm quarks may be extracted through the study of opposite sign dimuon events. The shapes and sizes of the distributions of the various kinematic variables may, through comparison with Monte Carlo simulations, be used to extract parameters such as the amount of the strange quark in the nucleon, the charm quark mass and the CKM matrix element, V_{cd}. This chapter describes the analysis of the dimuon data and presents the results of that analysis.

6.2 Philosophy of the Analysis

The production of an opposite sign dimuon event is governed by four parameters :

- m_c : The mass of the charm quark which appears in the cross section and helps determine, through the slow rescaling mechanism, the shapes of the final kinematic distributions.

- κ : Let ρ be the ratio of strange quarks and antiquarks to non-strange quarks and antiquarks in the nucleon sea :

$$\rho = \frac{\int xs(x)dx + \int x\overline{s}(x)dx}{\int xu(x)_{sea}dx + \int x\overline{u}(x)dx + \int xd(x)_{sea}dx + \int x\overline{d}(x)dx} \quad (6.1)$$

  where the function $xq(x)\{q \in s, \overline{u}, \overline{d}\}$ represents the momentum distribution of quark q in the proton and the integrals are performed over

Bjorken x. The size of the sea quark and sea antiquark components must be identical

$$\begin{aligned} \int xu(x)_{sea}dx &= \int x\overline{u}(x)dx \\ \int xd(x)_{sea}dx &= \int x\overline{d}(x)dx \\ \int xs(x)dx &= \int x\overline{s}(x)dx \end{aligned} \tag{6.2}$$

so Equation 6.1 becomes

$$\rho = \frac{\int x\overline{s}(x)dx}{\int x\overline{u}(x)dx + \int x\overline{d}(x)dx} \tag{6.3}$$

which can be rearranged to yield the proportion of strange antiquarks in the total antiquark sea

$$\frac{\rho}{\rho+1} = \frac{\int x\overline{s}(x)dx}{\int x\overline{s}(x)dx + \int x\overline{u}(x)dx + \int x\overline{d}(x)dx} \tag{6.4}$$

The proportion of strange quarks and antiquarks in the nucleon sea is expected to be $\frac{1}{3}$ if the sea were SU(3) flavour symmetric. Conventionally, Equation 6.4 is expressed in terms of a variable κ, defined by

$$\kappa = 2\rho \tag{6.5}$$

With this substitution, Equation 6.4 becomes

$$\frac{\kappa}{\kappa+2} = \frac{\int x\overline{s}(x)dx}{\int x\overline{s}(x)dx + \int x\overline{u}(x)dx + \int x\overline{d}(x)dx} \tag{6.6}$$

A value of κ=1 would imply that the nucleon sea is made up of $\frac{1}{3}$ s and $\overline{s}$ quarks and $\frac{2}{3}$ u,$\overline{u}$,d and $\overline{d}$ quarks.

- V_{cd} : As already discussed in Chapter 1 the Cabibbo-Kobayashi-Maskawa matrix element, V_{cd}, controls the fraction of d-quarks that will produce charm. Once V_{cd} is known, the unitarity of the CKM mixing matrix may be used to constrain the value of V_{cs}.

- B_c : The semileptonic branching ratio of charmed mesons into muons.

The information available for a fit to these parameters may be separated into two categories : (a) the shape of the distributions and (b) the normalisation i.e. the number of opposite sign dimuon events per charged current event.

The shape of a distribution is at most a function of three parameters, m_c, κ and V_{cd}, which hereafter will be collectively referred to as "the shape parameters", since the branching ratio merely affects the overall normalisation. On the other hand the normalisation is a function of all four parameters[1]. Necessarily any fit involving the normalisation must be a four parameter fit in order that the statistical errors on the results be correct.

A full four parameter fit not only would have been too computationally intensive, but also less sensitive due to the correlation between the variables, leading to larger systematic errors. To avoid this the underlying principle of the following analysis was to fit m_c, κ and V_{cd} using only the shape of the available distributions. In this way the inevitable high degree of correlation with B_c was avoided. Once the shape parameters had been ascertained, the normalisation could be used to determine the branching ratio.

6.3 Analysis Method

Any fit of a theoretical model to data involves varying the free parameters in the theory until a good fit has been achieved. There are two methods for doing this in the context of the charm analysis.

1. **Grid Analysis :**

   The first approach to the charm analysis involves dividing the phase space defined by the shape parameters into a fine grid and then generating a Monte Carlo sample at each set of parameters on the grid points. The sample at each point is then compared to the data and an estimate of the goodness of fit is calculated. The benefit of this method is that the sample generated at any particular point is statistically independent of the samples at the other grid points. The liabilities are that, as the samples are only defined at the grid point, some form of interpolation algorithm is required in order to map the region between the grid points. The use of interpolation contains a number of hidden traps; in the context of fitting, the most dangerous is that one is usually searching for a maximum or minimum in the goodness of fit parameter. It is possible for interpolation algorithms, especially those which use methods based on interpolating polynomials, to generate false minima or maxima between the grid points resulting in a distorted fit. A way around this danger is to make the grid points close enough that only a linear interpolation is required to move from one grid point to another.

[1]The set of all parameters: m_c, κ, V_{cd} and B_c will hereafter be referred to as the "charm parameters".

However, this requires a formidable amount of computation. To obtain some understanding of the degree of computation involved, suppose that there are N points to test for each shape parameter, defining a space containing N^3 grid points. In order to fit for three free parameters one needs to study the distributions of at least three experimental variables, each of which may be split into M bins. The total number of bins is, therefore, M^3N^3. Suppose $M = N = 10$; then the number of bins is 1×10^6. If each bin is required to contain at least 10 events after cuts, so that the statistical error on the bin follows a Gaussian distribution, and assuming a selection efficiency of approximately 20% (as it is in the case of opposite sign dimuons) then the required number of generated events is on the order of 5×10^7 events. For this study one would require somewhat finer bins, so that only a linear interpolation method is required, increasing the required number of events even further. This level of computation was not considered to be feasible.

2. **Weighted Analysis:**

   Consider an event generated at a point in phase space defined by (x_{Bj}, y_{Bj}, E_ν) with charm parameters (m_c,κ,V_{cd},B_c). The contribution this event makes to an event sample (or the "weight" for the event) is

$$\frac{\mathcal{D}(m_c, \kappa, V_{cd}, B_c)}{\mathcal{N}(m_c, \kappa, V_{cd}, B_c)} \tag{6.7}$$

   where $\mathcal{D}(m_c, \kappa, V_{cd}, B_c)$ is the value of the differential cross section at the phase space point (x_{Bj}, y_{Bj}, E_ν) weighted by the beam flux, $\Phi(E_\nu)$ and $\mathcal{N}(m_c, \kappa, V_{cd}, B_c)$ is the integral of the flux weighted differential cross section for the set of charm parameters (m_c,κ,V_{cd},B_c), which is effectively the total number of generated events.

$$\mathcal{D}(m_c, \kappa, V_{cd}, B_c) = \Phi(E_\nu)\frac{d^3\sigma}{d\xi dy dE}(m_c, \kappa, V_{cd}, B_c) \tag{6.8}$$

$$\mathcal{N}(m_c, \kappa, V_{cd}, B_c) = \int\int\int \Phi(E_\nu)\frac{d^3\sigma}{d\xi dy dE}(m_c, \kappa, V_{cd}, B_c)\, d\xi dy dE \tag{6.9}$$

   In these equations ξ is the slow-rescaling parameter defined in Equation 1.26 of Chapter 1.

   The contribution of an event generated at the same point in phase space (x_{Bj}, y_{Bj}, E_ν) but with different charm parameters, (m_c^N,κ^N,V_{cd}^N,B_c^N) in an event sample is

$$\frac{\mathcal{D}(m_c^N, \kappa^N, V_{cd}^N, B_c^N)}{\mathcal{N}(m_c^N, \kappa^N, V_{cd}^N, B_c^N)} \tag{6.10}$$

and so the result of moving to a new set of charm parameters has been to *reweight* the event by a factor of

$$\mathcal{W} = \frac{\mathcal{D}(m_c^N, \kappa^N, V_{cd}^N, B_c^N)/\mathcal{N}(m_c^N, \kappa^N, V_{cd}^N, B_c^N)}{\mathcal{D}(m_c, \kappa, V_{cd}, B_c)/\mathcal{N}(m_c, \kappa, V_{cd}, B_c)} \tag{6.11}$$

Now suppose that there exists a large set of events generated with a single set of charm parameters. Then the distributions for another set (m_c^N,κ^N,V_{cd}^N,B_c^N) may be calculated by reweighting each individual event in the sample by the factor defined in Equation 6.11.

The charm analysis proceeds as follows if the weighting method is used :

- Generate a large event sample with one specific set of charm parameters. This is the "seed sample".
- For any other set of parameters, give each event a reweighting factor defined by Equation 6.11.
- Vary the charm parameters, and hence the individual event reweighting factors, until the best fit of the simulated distributions to the measured data distributions in achieved.

The subtlety with this procedure is that the set of charm parameters used to generate the seed sample must ensure that no region of phase space is empty. Otherwise, the fit becomes biased. For instance, if the seed sample were to be generated with a high charm mass then the neutrino energy distribution would be skewed to high values. There would be an unpopulated region at low energy, purely because the charm mass is too high for events to exist there. Since one cannot weight events which do not exist, this region would be empty, even if a weighted analysis for low masses were to be attempted, and the mass resulting from the fit would be biased to high values.

Due to both the computation time and uncertainties in the interpolation involved using the grid method the following analysis was performed using the weighting approach.

6.4 Charm Quark Mass Analysis

This section presents a determination of the mass of the charm quark using the opposite sign dimuon data. The mass appears implicitly in the cross

section as part of the slow rescaling formalism, in which the scaling parameter is changed from x_{Bj} to $\xi = x_{Bj} + m_c^2/2M\nu$ in the presence of a heavy quark.

In order to extract the charm mass parameter one must compare a mass sensitive distribution in the data with the same distribution in the simulation for different masses. The charm production cross section may be expressed in terms of y_{Bj}, the neutrino energy, E_ν, and the slow rescaling variable, ξ, which is itself a function of x_{Bj}. This suggests that kinematic quantities which are most sensitive to the value of the charm quark mass are:

- **The visible y_{Bj} spectrum :** The charm mass imposes a lower limit on the value of the hadronic energy in a dimuon event. The visible y_{Bj} may be written as

$$y_{vis} = \frac{E_{\mu_2} + E_{had}}{E_{\mu_1} + E_{\mu_2} + E_{had}} = \frac{1}{1 + \frac{E_{\mu_1}}{E_{\mu_2}+E_{had}}} \tag{6.12}$$

  The heavier the charm quark, the larger is the mean hadronic energy and so the mean y_{vis} should increase. The low y region of the spectrum is most sensitive to differences in charm mass.

- **The visible x_{Bj} spectrum :** Since the correct scaling variable is ξ and not x_{Bj} the shape of the x_{Bj} distribution is dependent on the charm mass.

- **The visible neutrino energy spectrum :** As already mentioned the slow rescaling mechanism introduces a heavy quark threshold in the hadronic energy spectrum and hence also in the neutrino energy spectrum.

The opposite sign dimuon sample was extracted with a deposited hadronic energy cut of 5 GeV, below which the calibration was not considered to be reliable, and a cut on the secondary muon energy of 4.5 GeV. Combined, these represent a cut on the total hadronic energy of the event of at least 9.5 GeV. Kinematically this translates into a low y cut which severely reduces the sensitivity of the y distribution to the charm quark mass.

As the charm mass increases, the mean of the x_{vis} distribution also becomes larger. If the amount of strange sea, κ, increases the mean of the x_{vis} distribution decreases. It is obvious, then, that the charm mass and κ are strongly anticorrelated through the x_{vis} distribution. However, the amount of the strange sea has only a small effect on the visible neutrino energy spectrum. Figure 6.1 shows a comparison between the visible energy spectra of two Monte Carlo dimuon samples generated with two extreme values for κ.

There is very little shape difference between the two distributions, justifying the claim that an analysis of the shape of the visible energy distribution is insensitive to the value of κ. The charm quark mass fit will proceed by studying the visible neutrino energy spectrum.

The fit was carried out by comparing background subtracted data in E_{vis} bins with the prediction from FADE. The data and Monte Carlo was split into six E_{vis} bins (0 - 20 - 30 - 50 - 80 - 100 - 300 GeV). In the seed Monte Carlo the fragmentation parameter (cf Section 5.6.1) was fixed at 0.64, the CCFR structure functions were used and κ was fixed at 0.373, which was determined by a Leading Order analysis by CCFR [62]. The sample was generated with a charm mass of 0.1 (GeV/c^2) and contained 1×10^6 events. The sample was generated with such a low mass in order that the low energy region of the energy spectrum be populated and hence that the weighted analysis gives a non-biased result (see the discussion concerning the weighted analysis method above).

A χ^2 function was used as measure of the goodness of fit of the Monte Carlo to the data. The functional form of the χ^2 was

$$\chi^2 = \sum_i \frac{(D_i - (S \cdot B_i + F_i))^2}{(\sigma^2_{DATA_i} + \sigma^2_{MC_i})} \tag{6.13}$$

where the index i runs over the six energy bins. In Equation 6.13, D_i, $S \cdot B_i$, and F_i represent the $\mu^-\mu^+$ data, background data and FADE Monte Carlo event numbers respectively and the quantity $S = 1.5 \pm 0.3$ is the background scale used to convert the number of observed like sign dimuon events to the number of opposite sign dimuon background events (see Section 5.3). In the denominator $\sigma^2_{MC_i}$ is the statistical variance on the simulation and $\sigma^2_{DATA_i}$ is the variance in the data. Since the background scale must be taken into account, this has the form :

$$\sigma^2_{DATA_i} = D_i + S^2 \cdot B_i \tag{6.14}$$

obtained by combining the statistical errors in quadrature. The uncertainty in the background scale appears below in the form of a systematic error.

A fit to the shape of the visible neutrino energy spectrum yields

$$m_c = 1.3^{+0.2}_{-0.3} \ (\mathrm{GeV/c^2}) \tag{6.15}$$

The χ^2 of the fit was 6.1 with 5 degrees of freedom. The χ^2 as a function of the charm mass is shown in Figure 6.2.

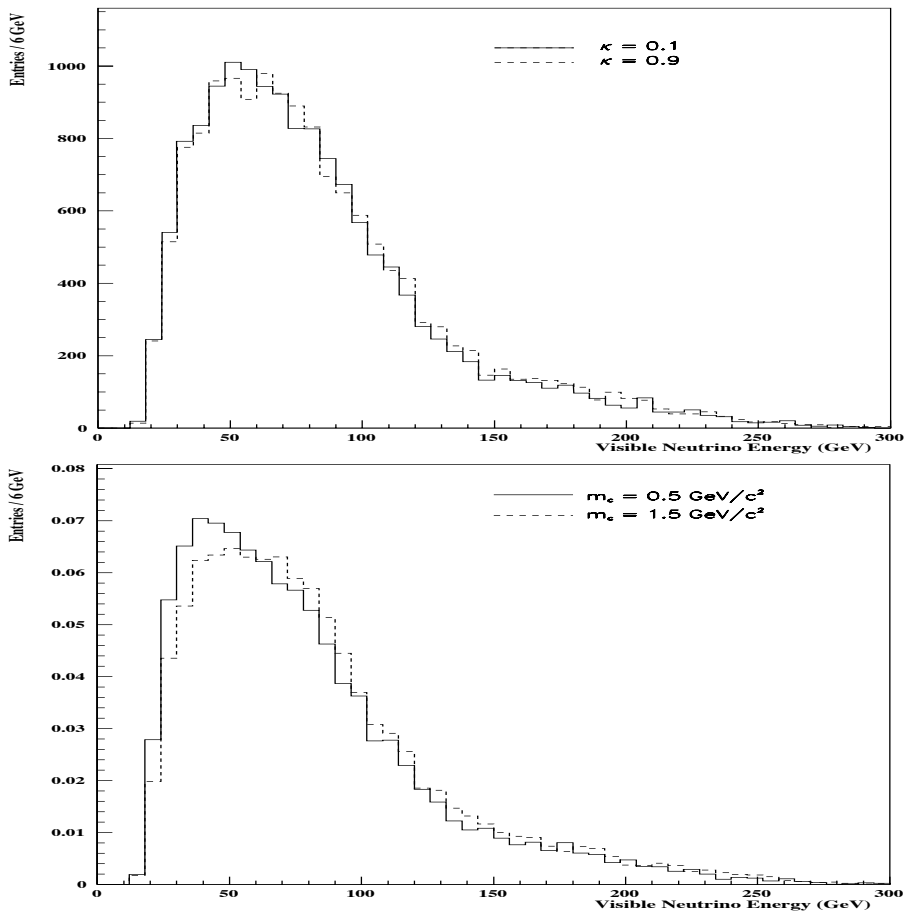

Figure 6.1: Comparison between two visible neutrino energy spectra for different values of κ and m_c. The top plot was generated with $m_c = 1.5$ (GeV/c^2) and two different values of κ. The bottom plot was generated with $\kappa = 0.37$ and different values for m_c. The shape of the energy spectrum changes substantially for different charm masses. No significant shape difference is observed for different values of κ.

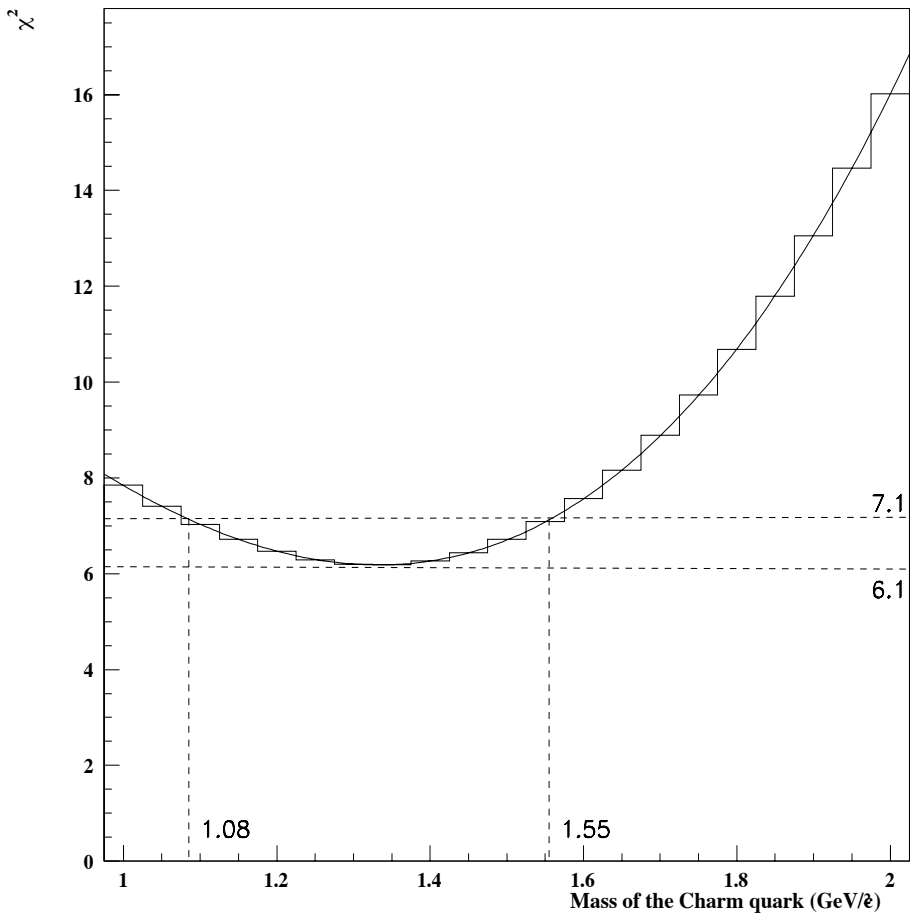

Figure 6.2: The χ^2 of the charm mass fit as a function of the charm mass. The central value is 1.3 (GeV/c^2) at a χ^2 of 6.1 with 5 degrees of freedom. The statistical error is determined by the points on either side of the central mass value at which the χ^2 is one unit above the minimum. The curve is a fit of a third order polynomial to the histogram and the 68% confidence limits are shown on the charm mass axis.

6.4.1 Systematic Uncertainties

Systematic uncertainties arise from uncertainties in parameters within the model and by finite resolution on the experimental variables. Estimates of the uncertainties were obtained by varying each parameter and observing the shift in the fitted charm mass. The sources of uncertainty are described below and the contribution from each is outlined in Table 6.1.

- **Background Scale, S:** The scale used to estimate the background was (1.5 ± 0.3) (cf Section 5.3). The uncertainty in the mass due to the background scale was found by varying the scale between 1.2 and 1.8.

- **Fragmentation :** The uncertainty due to the fragmentation was estimated by changing the fragmentation parameter from 0.55 to 0.75, a variation of 15%.

- **Structure Functions :** Different structure functions lead to different kinematics. Since NOMAD has not parametrised its own structure functions the uncertainty involved in the choice of the underlying parton distributions was estimated by regenerating the seed Monte Carlo file with different structure functions and repeating the dimuon fit. It should be noted that the results of this analysis are based on the CCFR structure functions[62]. Other structure functions used were the GRV-HO [55] and the MRS-S0 [56] functions. Any systematic effect resulting from a change to different structure functions is an indication of difference between these and the functions parametrised by CCFR.

- **ν-$\overline{\nu}$ Misidentification :** The separation of the data into neutrino and antineutrino induced dimuons involves the identification of the primary muon based on a transverse momentum criterion. The transverse momentum of the secondary muon is determined by that of the D meson, which in turn is parametrised by

$$\frac{dN}{dp_T^2} \propto e^{-\beta p_T^2} \tag{6.16}$$

  where the parameter β was measured to be $\beta = 1.1 \pm 0.3$[70]. The uncertainty from the identification procedure was estimated by performing the fit using seed samples generated with β equal to 0.8 and 1.4.

- **The size of the strange sea :** The size of the strange sea was varied from 0.3 to 0.45.

- **The CKM matrix elements V_{cd} and V_{cs} :** The current best values of these two CKM matrix elements are $|V_{cd}| = 0.221 \pm 0.003$ and $|V_{cs}| = 0.974 \pm 0.001$ [82]. Input values of the CKM elements were separately varied by their uncertainties and the mass fit was repeated. As Table 6.1 shows, the systematic error attributed to uncertainty in the CKM matrix elements was negligible.

- **Cut values :** The value of a cut is known only up to the experimental resolution. To estimate the uncertainty deriving from this finite resolution each cut on a specific variable was varied around its central value taking into account the experimental resolution in that variable.

- **Beam profile :** An estimate of the uncertainty on the charm mass due to a non-optimal beam profile on the calibration was made by weighting the Monte Carlo neutrino events by the relative flux predictions of two different beam profiles in much the same way as in Section 3.4.4.

The charm quark mass from the fit is $1.3^{+0.2}_{-0.3}{}^{+0.3}_{-0.3}$ (GeV/c^2) where the systematic errors have been added in quadrature. It should be noted that the assumption of independence of some of the error contributions in Table 6.1 is not strictly justified. For example, the background scale is a function of cuts in the secondary muon energy. This indicates that the errors quoted above are, most probably, overestimates and so the total error is a conservative estimate of the actual uncertainty.

The charm quark mass measured above is compared to the results of other experiments in Table 6.2. The results are consistent within the uncertainties.

6.5 The Strange Quark Content of the Nucleon

Charm production from neutrinos is an excellent probe of the strange component of the nucleon sea. The differential cross sections for charm production in neutrino and antineutrino interactions are given in Equations 1.33 and 1.34. Reproducing them here for convenience they are

$$\frac{d^2\sigma^{\nu\mathcal{N}}}{d\xi dy} = \frac{G^2 m E_\nu \xi}{\pi}\left[\left(u(\xi,Q^2)+d(\xi,Q^2)\right)|V_{cd}|^2 + 2s(\xi,Q^2)|V_{cs}|^2\right]\left(1-y+\frac{xy}{\xi}\right) \quad (6.17)$$

Theoretical Uncertainties			
Source of Uncertainty	Δm_c	Source of Uncertainty	Δm_c
Background Scale = 1.2	+0.16	Background Scale = 1.8	-0.17
Fragmentation; $\epsilon = 0.55$	+0.03	Fragmentation; $\epsilon = 0.75$	-0.04
GRV-HO Structure Functions	-0.06	MRS-S0 Structure Function	-0.07
$\beta = 0.8$	-0.03	$\beta = 1.4$	+0.02
$\kappa = 0.3$	+0.07	$\kappa = 0.45$	-0.03
$V_{cd} = 0.218$	-0.01	$V_{cd} = 0.224$	+0.01
$V_{cs} = 0.973$	-0.01	$V_{cs} = 0.975$	+0.01
Beam profile	-0.20		
Experimental Uncertainties			
Source of Uncertainty	Δm_c	Source of Uncertainty	Δm_c
Fiducial; $\|X\|, \|Y\| < 65$ cm	-0.03	Fiducial; $\|X\|, \|Y\| < 75$ cm	+0.15
$\Delta T < 4$ ns	-0.01	$\Delta T < 6$ ns	+0.01
Radial distance < 8 cm	+0.11	Radial distance < 12 cm	-0.09
$Q^2_{vis} > 0.8$ GeV/c^2	-0.03	$Q^2_{vis} > 1.2$ GeV/c^2	+0.01
$x_{Bj} < 0.8$	+0.01	$x_{Bj} < 1.2$	-0.01
$E_{had} > 4.0$ GeV	-0.07	$E_{had} > 6.0$ GeV	+0.09
$E_{\mu^1} > 4.3$ GeV	-0.03	$E_{\mu^1} > 4.7$ GeV	+0.07
$E_{\mu^2} > 4.3$ GeV	-0.10	$E_{\mu^2} > 4.7$ GeV	+0.20

Table 6.1: The variation of the fitted value of the charm mass for different sources of systematic uncertainty.

Experiment	m_c (GeV/c^2)
CCFR	$1.3 \pm 0.2 \pm 0.1$ (LO Analysis)[76] $1.70 \pm 0.19 \pm 0.02$ (NLO Analysis)[64]
CHARM II	$1.79^{+0.26}_{-0.28} \pm 0.27$ [79]

Table 6.2: Results on m_c from previous experiments. Both the Leading Order and Next-to-Leading Order results are shown for CCFR.

for neutrino interactions and

$$\frac{d^2\sigma^{\overline{\nu}\mathcal{N}}}{d\xi dy} = \frac{G^2 m E_\nu \xi}{\pi}\left[\left(\overline{u}(\xi,Q^2)+\overline{d}(\xi,Q^2)\right)|V_{cd}|^2 + 2\overline{s}(\xi,Q^2)|V_{cs}|^2\right] \left(1-y+\frac{xy}{\xi}\right) \quad (6.18)$$

for antineutrino events and where terms proportional to the nucleon mass have been neglected for the sake of clarity. Due to the relative size of the CKM elements ($|V_{cs}|^2 = 0.95 \gg 0.05 = |V_{cd}|^2$) 88% of the antineutrino dimuon sample comes from the strange quark component of the nucleon sea[61]. This implies that the number of observed events is a direct probe of the size of strange part of the nucleon sea, κ (Equation 6.6). Unfortunately, as reported in Chapter 5, the antineutrino induced dimuon sample in NOMAD is extremely small and hence is not useful for this sort of analysis. We must, then, turn to the neutrino induced sample in order to estimate the size of the strange sea.

The distribution which is most sensitive to κ is the visible Bjorken x distribution in which shape and magnitude are controlled by five variables : m_c, κ, V_{cs}, V_{cd}, and B_c. The high degree of correlation with B_c is avoided if only the shape of the x_{vis} distribution is considered. In addition, the charm mass has been constrained by the fit to the visible energy distribution and so the anticorrelation with m_c (see the discussion in the previous section) no longer has to be considered. It is expected that κ and V_{cd} are strongly correlated and so the analysis may be carried out either by allowing both κ and V_{cd} to be free parameters and fitting for both, or by fixing one parameter to its current best value and varying the other. Without the information from the antineutrino sample it is not expected that the result for V_{cd} will be more precise than the current value, and so the strange content of the nucleon will be determined by fixing V_{cd}.

Fixing the CKM elements to be $|V_{cd}| = 0.220 \pm 0.003$ and $|V_{cs}| = 0.974 \pm 0.001$[82], the background subtracted data and the Monte Carlo were split into five x_{vis} bins (0.0 - 0.05 - 0.1 - 0.3. - 0.5 - 1.0). The goodness of fit function was the same χ^2 function as that used in the mass analysis. The result of the fit is

$$\kappa = 0.46^{+0.09}_{-0.07} \quad (6.19)$$

with a χ^2 of 3.3 with 4 degrees of freedom. The χ^2 as a function of κ is shown in Figure 6.3.

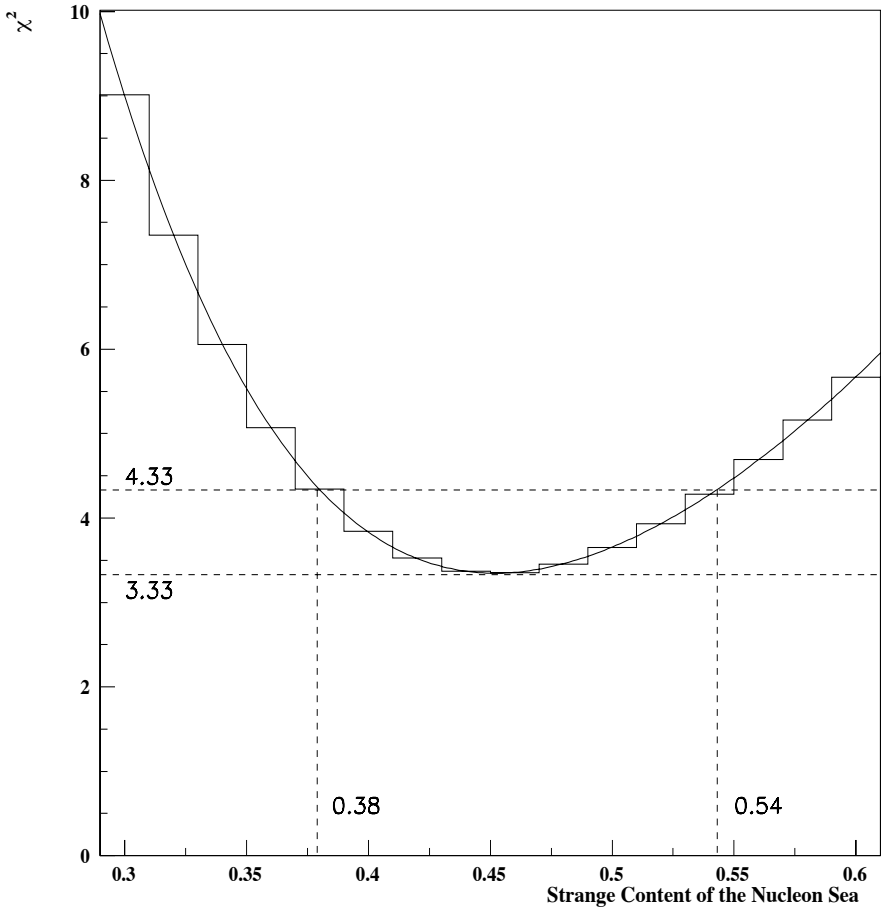

Figure 6.3: The χ^2 of the of the fit to the strange content of the nucleon sea as a function of κ. The central value is 0.45 with a χ^2 of 3.3 with 4 degrees of freedom. The statistical error is determined by the points on either side of the central value at which the χ^2 is one unit above the minimum. The curve is a fit of a fourth order polynomial to the histogram and the 68% confidence limits are shown on the κ axis.

Theoretical Uncertainties			
Source of Uncertainty	$\Delta\kappa$	Source of Uncertainty	$\Delta\kappa$
Background Scale = 1.2	-0.06	Background Scale = 1.8	+0.10
Fragmentation; $\epsilon = 0.55$	+0.005	Fragmentation; $\epsilon = 0.75$	-0.002
$\beta = 0.8$	-0.007	$\beta = 1.4$	+0.004
$m_c = 0.9$ (GeV/c^2)	-0.05	$m_c = 1.8$ (GeV/c^2)	+0.07
$V_{cd} = 0.218$	-0.02	$V_{cd} = 0.224$	+0.06
$V_{cs} = 0.973$	-0.007	$V_{cs} = 0.975$	+0.01
Beam profile	+0.05		
Experimental Uncertainties			
Source of Uncertainty	$\Delta\kappa$	Source of Uncertainty	$\Delta\kappa$
Fiducial; $\|X\|, \|Y\| < 65$ cm	-0.02	Fiducial; $\|X\|, \|Y\| < 75$ cm	+0.017
$\Delta T < 4$ ns	+0.003	$\Delta T < 6$ ns	-0.001
Radial distance < 8 cm	+0.04	Radial distance < 12 cm	-0.02
$Q^2_{vis} > 0.8$ GeV/c^2	+0.01	$Q^2_{vis} > 1.2$ GeV/c^2	-0.03
$E_{had} > 4.0$ GeV	+0.001	$E_{had} > 6.0$ GeV	-0.005
$E_{\mu^1} > 4.3$ GeV	+0.006	$E_{\mu^1} > 4.7$ GeV	-0.006
$E_{\mu^2} > 4.3$ GeV	-0.003	$E_{\mu^2} > 4.7$ GeV	+0.004

Table 6.3: The variation of the fitted value of κ for different sources of systematic uncertainty.

6.5.1 Systematic Uncertainties

The factors contributing to the systematic uncertainty in the measurement of κ are essentially identical to those in the charm quark mass analysis. The only differences are that the systematic effect of variations in κ is replaced by the effect of varying the charm mass and the variation in κ obtained by changing the cut on x_{vis} is omitted. The error attributed to different structure functions has also been omitted, since the manner in which κ is included in packaged structure functions, such as those from PDFLIB, is highly dependent on the particular function sets. The systematic errors are tabulated in Table 6.3 and, when added in quadrature, yield a final result of

$$\kappa = 0.46^{+0.09+0.15}_{-0.07-0.09} \tag{6.20}$$

6.5.2 Results from previous experiments

Results on the strange content of the nucleon sea from previous experiments are tabulated in Table 6.4. The value of κ shows that the nucleon sea is *not* SU(3) symmetric. In fact, it can be seen that the nucleon sea is composed of 20 % s and $\bar{s}$ quarks, 40% u and $\bar{u}$ quarks and 40% d and $\bar{d}$ quarks, assuming the up and down components of the nucleon have the same magnitude. This assumption is not necessarily justified as data from NMC[83, 84] suggests that the up and down quark content of the nucleon sea is not identical.

As with the charm quark mass, the current measurement is consistent with previous experiments, although the total systematic error is larger. As Tables 6.1 and 6.3 show, the major contributions to the systematic error are the uncertainty in the background scale and the beam profile.

The only way to reduce the error attributed to the background would be to generate at least four times the number of events as are contained in the current ν_μ^{CC} Monte Carlo sample. As already discussed in Chapter 5, the simulation of an event sample of this size (approximately 1×10^6 events) is a highly non-trivial exercise. The production rate of simulated events is on the order of 10,000 events per day and so sample of 1×10^6 events would have required about 3 months of uninterrupted processing. The processing facility used for the FCAL simulation production is also utilised by other experimental groups and so it is conceivable that the processing time could have increased by a factor of two or more.

In the case of the beam profile, the SPY results[36] indicate that the current beam profile does not model the beam precisely. The use of a beam profile in which the SPY results have been included has the potential to significantly decrease the systematic error attributed to the beam.

6.6 The Average Semileptonic Branching Ratio

The last parameter which can be extracted from the data is the semileptonic branching ratio, B_c. Having constrained m_c and κ, the branching ratio may be determined by studying the rate of dimuons observed with respect to the number of ν_μ^{CC} events. The observed rate was (0.0015 ± 0.0001) dimuons per ν_μ^{CC} event. The rate obtained from the Monte Carlo, after kinematic cuts and acceptance functions were applied, was (0.01587 ± 0.0001) dimuons per ν_μ^{CC} events, assuming a branching ratio of 100%. Dividing the observed rate by the predicted rate gives a branching ratio of $(9.5 \pm 0.7)\%$. This is slightly smaller than the value of $(10.9 \pm 0.8 \pm 0.6)\%$ obtained by CCFR[63]. However,

Experiment	κ
CCFR	$0.44^{+0.09+0.07}_{-0.07-0.02}$ (LO Analysis)[76] $0.536^{+0.03+0.11}_{-0.03-0.07}$ (NLO Analysis)[64]
FMMF	$0.41 \pm 0.08^{+0.103}_{-0.069}$ [78]
CHARM II	$0.39^{+0.07}_{-0.06} \pm 0.07$ [79]
CDHS	$0.47 \pm 0.08 \pm 0.05$ [75]

Table 6.4: Results on κ from previous experiments. Both the Leading Order and Next-to-Leading Order results are shown for CCFR.

studies of charm production by neutrinos in emulsion show that the average branching ratio is a weakly rising function of the neutrino energy. The average neutrino energy of the CCFR experiment was 140 GeV, compared to the NOMAD average energy of 24.4 GeV and so a lower branching ratio is expected.

The parameter being measured in this section is the semileptonic branching ratio averaged over the production rates of charmed mesons and baryons produced in neutrino charm quark production. That is, if H is the set of charmed hadrons that are produced in neutrino-nucleon interactions (i.e. the set $\{H : H \in D^0, \overline{D^0}, D^+, D^-, D_s^+, D_s^-, \Lambda_c\}$), then

$$B_c = \frac{\sum_{h \in H} R_h B_h}{\sum_{h \in H} R_h} \tag{6.21}$$

where R_h is the rate of production of charmed hadron h, with respect to the total rate of charm production, and B_h is the semi-inclusive branching ratio for the process $h \to \mu^+ + anything$. Hence, if the production rates of any of the different charmed hadrons change with neutrino energy then the *average* branching ratio becomes energy dependent.

Figure 6.4 compares the average semileptonic branching ratio measured in the NOMAD data with that calculated from production rates measured in E531[66]. Also shown is the contribution to the branching ratio from different

Experiment	Branching Fraction	Average Neutrino Energy (GeV)
CCFR	$0.109 \pm 0.008 \pm 0.006$	140.0
E531	0.099 ± 0.012	140.0
CHARM II	0.091 ± 0.010	23.7
CDHS	0.078 ± 0.013	12.0

Table 6.5: The average semileptonic branching ratio obtained from previous experiments.

charmed hadron species : D^0,D^+,Λ_c and other mesons (D^-,$\overline{D}^0$,D_s). As the figure shows, below a neutrino energy of 30 GeV, the production rates of the Λ_c and rarer mesons increase with a corresponding decrease in the D meson rate of production. Since the semi-inclusive process $\Lambda_c \rightarrow \mu^+ + anything$ has a small branching ratio more weight is given to the Λ_c component in Equation 6.21 resulting in a decrease of the average semileptonic branching ratio as well.

The majority of the CCFR dimuon data was above a neutrino energy of 40 GeV, due to the high energy neutrino beam at Fermilab. Hence, CCFR was unable to directly observe the decrease in the branching ratio. NOMAD, however, operates in a lower energy range, and the energy dependence of the branching ratio is observable, as Figure 6.4 shows.

If only data above a visible neutrino energy of 30 GeV is analysed, the measured branching ratio becomes $(10.5 \pm 0.7)\%$, entirely consistent with that measured by previous experiments (see Table 6.5). The value for B_c determined by CDHS is smaller than any of the other neutrino experiments and also differs from that obtained by e^+e^- collider experiments. It is thought that this may have been caused by difficulties in the correction for experimental acceptance in that analysis[85] but, due to the low mean neutrino energy, there may also have been a substantial contribution from Λ_c decay.

Systematic uncertainties were estimated in the same manner as used in the rest of the analysis. The results are compiled in Table 6.6 and the final result, with the systematic errors added in quadrature, is

$$B_c = 0.095 \pm 0.007^{+0.015}_{-0.013} \tag{6.22}$$

at an average neutrino energy of 24.4 GeV.

6.7 Future Prospects

- **Inclusion of 1997 and 1998 Data :** The data comprising the work

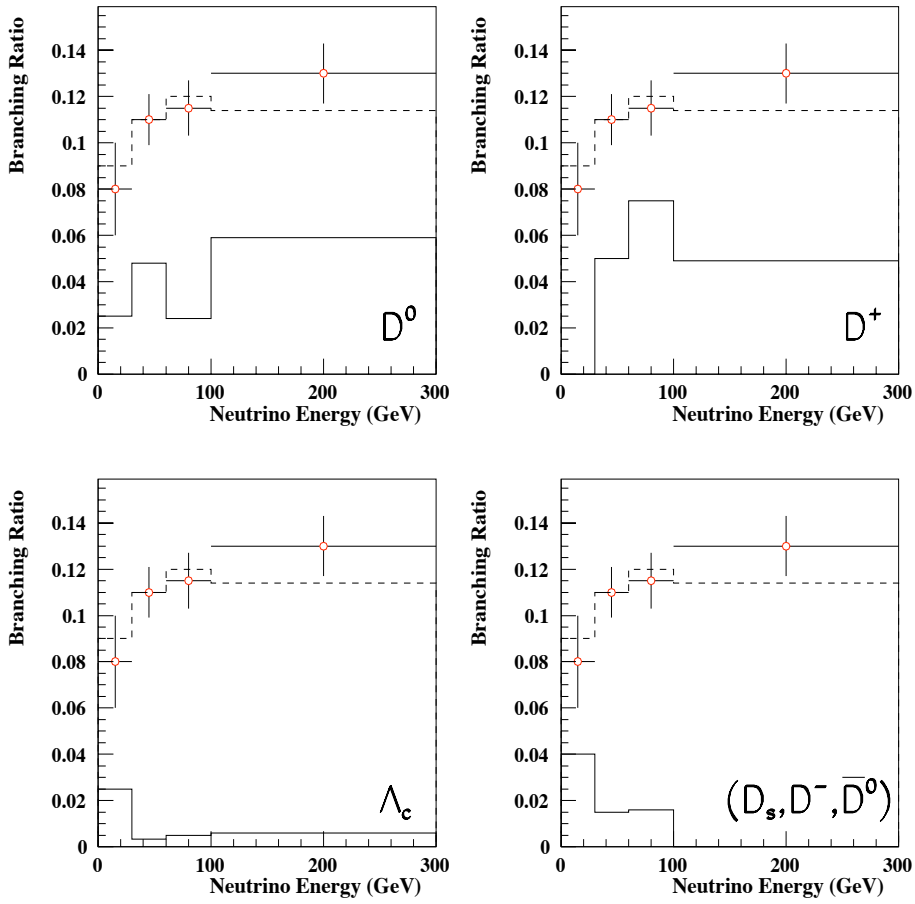

Figure 6.4: The average semileptonic branching ratio as a function of the neutrino energy. The dotted line in each plot is the average semileptonic branching ratio calculated from production rates measured at E531[66]. The points represent the average semileptonic branching ratio measured in NOMAD in energy bins. The errors are statistical only. The solid line in each plot displays the contribution of a particular charmed hadron to the total average semileptonic branching ratio. Shown are (top left) the contribution from D^0 mesons, (top right) the contribution from D^+ mesons, (bottom left) the contribution from Λ_c baryons and (bottom right) the contribution from other mesons (D^-,$\overline{D}^0$,D_s).

Theoretical Uncertainties			
Source of Uncertainty	ΔB_c	Source of Uncertainty	ΔB_c
Background Scale = 1.2	+0.0070	Background Scale = 1.8	-0.0080
Fragmentation; $\epsilon = 0.55$	-0.0023	Fragmentation; $\epsilon = 0.75$	+0.0011
$\beta = 0.8$	+0.0013	$\beta = 1.4$	-0.0005
$m_c = 0.9$ (GeV/c^2)	+0.0002	$m_c = 1.8$ (GeV/c^2)	-0.0003
$\kappa = 0.35$	+0.012	$\kappa = 0.55$	-0.0095
GRV-HO Structure Function	+0.004	MRS-S0 Structure Function	-0.0030
$V_{cd} = 0.218$	+0.0001	$V_{cd} = 0.224$	-0.0001
$V_{cs} = 0.973$	+0.0001	$V_{cs} = 0.975$	-0.0001
Beam Profile	+0.00001		
Experimental Uncertainties			
Source of Uncertainty	ΔB_c	Source of Uncertainty	ΔB_c
Fiducial; $\|X\|, \|Y\| < 65$ cm	-0.0002	Fiducial; $\|X\|, \|Y\| < 75$ cm	+0.0002
$\Delta T < 4$ ns	-0.0001	$\Delta T < 6$ ns	+0.00001
Radial distance < 8 cm	-0.0033	Radial distance < 12 cm	+0.0017
$Q^2_{vis} > 0.8$ GeV/c^2	+0.0003	$Q^2_{vis} > 1.2$ GeV/c^2	-0.0008
$E_{had} > 4.0$ GeV	+0.0003	$E_{had} > 6.0$ GeV	-0.0002
$E_{\mu^1} > 4.3$ GeV	-0.0001	$E_{\mu^1} > 4.7$ GeV	+0.0002
$E_{\mu^2} > 4.3$ GeV	+0.0008	$E_{\mu^2} > 4.7$ GeV	-0.0009

Table 6.6: The variation of the fitted value of the average semileptonic branching ratio for different sources of systematic uncertainty.

in this thesis represents approximately 30 % of the total amount of data taken with the FCAL since 1995. Neither the 1997 nor the 1998 FCAL data sets have undergone reconstruction. The inclusion of this data would represent a significant increase in the size of the opposite sign dimuon sample. Extrapolation from the available data set indicates an expected number of observed dimuons of the order of 10,000, competitive with CDHS which has recorded the largest data set to date.

- **Monte Carlo Generation :** The precision of the results presented above is limited by the systematic uncertainties. In each case the largest source of systematic uncertainty is the error on the background scale. The generation and reconstruction of at least four times the amount of Monte Carlo events is required to ensure that the statistical uncertainty in the background scale is at least halved.

- **Inclusion of the Antineutrino Sample :** The lack of an appreciable antineutrino sample imposes a constraint on the analyses that can be performed using the opposite sign dimuon data. If a reasonable value were assumed for the average semileptonic branching ratio, a sample of opposite sign dimuon events produced in an antineutrino beam would provide a direct measurement of κ whilst the neutrino sample would be used to determine V_{cd}. Due to the high degree of correlation between the two variables this analysis method is impossible with only the neutrino induced sample. NOMAD ran with an antineutrino beam for two short periods in 1998. Although not yet reconstructed, the number of opposite sign dimuon events expected to be observed is approximately 250. Even with this small sample it would be possible to decrease the error on κ by a factor of 1.5 and provide an independent measurement of V_{cd}. With the number of events in the current neutrino induced sample, an accuracy of 5% in the measurement of V_{cd} would be possible, making the κ and V_{cd} measurements comparable with those from CCFR.

- **NLO Analysis :** The only experiment to analyse charm production by neutrinos at Next-to-Leading Order was CCFR[64]. There are, however, some reservations about this analysis in the literature. CCFR reported that the amount of the strange sea in the nucleon extracted using a NLO formalism was almost twice that extracted using a LO formalism. However, Reference [88] suggests that this result was attained through the inconsistent application of an acceptance correction and that, if a consistent analysis were to be performed, the resulting

size of the strange sea would be closer to that attained at Leading Order. Furthermore, reference [89] states that the theory used by CCFR was only an approximation to the true NLO theory. Briefly, CCFR used a differential cross section in which the fragmentation process was factorized from the hard scattering process :

$$\frac{d^3\sigma_{NLO}^{\nu(\overline{\nu})}}{dxdydz} = \frac{d^3\sigma_{NLO}^{\nu(\overline{\nu})}}{dxdy} D_c(z) \tag{6.23}$$

In Reference [89], Kretzer points out that opposite sign dimuon production is really a semi-inclusive process in which the fragmentation function cannot be factorized from the rest of the cross section. An independent analysis of the neutrino production of charm at Next-to-Leading Order would aid in either verifying the results of CCFR or provide alternatives based on a consistent theoretical model.

Conclusion

The NOMAD experiment at the CERN SPS was constructed in 1994. In mid-1995 the front iron support was instrumented with scintillators to form an iron-scintillator sampling calorimeter. The proposed method of calibration of this calorimeter, the FCAL, was based on distortions in the Bjorken y distribution. However, this method was seen to possess shortcomings and so a straight-forward comparison with Monte Carlo was used. The absolute energy scale was determined to be

$$1[\mathrm{GeV}] = (2.95 \pm 0.02(stat) \pm 0.27(sys))[\mathrm{mip}]$$

About 500,000 events from the 1995 run and 3,000,000 events from the 1996 run were found to be useful for analysis. The reconstruction of the visible neutrino energy in charged current neutrino interactions shows good agreement with the Monte Carlo prediction, as does the reconstruction of the various kinematic variables. The energy resolution of the FCAL was estimated to be approximately $104\%/\sqrt{E}$.

From the sample of charged current neutrino interactions, an opposite sign dimuon sample of 4,953 events was reconstructed. After accidental overlaps of beam muons with charged current events were eliminated, 35 % of these were found to be background events from muonic hadron decays and hadron punchthrough. There were (2966 ± 236) neutrino induced and (263 ± 24) antineutrino induced dimuons after background subtraction. The description of these events by the NOMAD Monte Carlo was found to be inadequate, prompting the construction of FADE, a dedicated dimuon generator for FCAL interactions which adequately described the dimuon data. Using FADE, the rate of opposite sign dimuon production with respect to the production of charged current events was measured to be $(4.14 \pm 0.05) \times 10^{-3}$ after correction for experimental acceptance.

Analysis of the opposite sign dimuon data was performed using a method based on event weighting. The results obtained for the charm mass, the strange sea content of the nucleon and the average semileptonic branching

ratio were :

$$m_c = 1.3^{+0.2\,+0.3}_{-0.3\,-0.3}$$
$$\kappa = 0.46^{+0.09+0.15}_{-0.07-0.09}$$
$$B_c = 0.095 \pm 0.007^{+0.015}_{-0.013}$$

where the first error is statistical and the second combines all systematic errors in quadrature. Improvements on and extensions to these results could be achieved by

- Generating more charged current Monte Carlo to decrease the statistical error on the background.
- Reconstructing and analysing the 1997 and 1998 data sets.
- Reconstructing the antineutrino data so that an independent measurement of κ and V_{cd} may be made.
- Performing the analysis at Next-to-Leading Order in QCD in order to verify, or disprove, the results of CCFR.

Appendix A

Code Versions

The data sets used in this thesis were reconstructed with the following code versions :

	1995 Data	1996 Data and Monte Carlo
Code	Version	
Recon	Recon64	v7r5
Veto	v7r0	v7r3
Drift Chamber	v7r0	v7r4
Extrapolator	v2r0	v7r4
DcTrd	v7r0	v7r3
Trd	trd64	v7r4
Prs	prs62	
Cal	cal64	v7r4
Muo	muon63	v7r2
Sci	v7r0	v7r2
Hcal	hcal65	v7r1
Fcal	v7r0	v7r3
Phase2	v1r1	v7r3a
Util	v7r0	v7r3
Sprec	v1r3	v7r0
Magfield	v1r4	v7r4
Engine	v3r0	v7r3

Table A.1: Versions of NOMAD Software used in the 1995 and 1996 data production. Note that the PRS code was merged with the CAL code for the 1996 data production.

Bibliography

[1] E.D.Commins and P.H.Bucksbaum, *Weak interactions of leptons and quarks*, Cambridge University Press, Cambridge (1983).

[2] D.H.Perkins, *Introduction to High Energy Physics*, Addison-Wesley Publishing Company (1987).

[3] W. Greiner, B. Müller, *Gauge Theory of Weak Interactions*, Springer (1996).

[4] W. Greiner, A. Schäfer, *Quantum Chromodynamics*, Springer (1994).

[5] F. Halzen and A. D. Martin, *Quarks and Leptons : An Introductory Course in Modern Particle Physics*, John Wiley and Sons (1984).

[6] J.D.Bjorken, *Phys Rev.* **163**, 1767 (1967).

[7] H. Georgi and H. D. Politzer, *Phys. Rev.* **D14**, (1976) 1829.

[8] C. Athanassopoulos *et al.*, *Phys. Rev. Lett.* **77**, (1996) 3082.

[9] J. Altegoer *et al*, *A search for $\nu_\mu \to \nu_\tau$ oscillations using the NOMAD detector*, CERN-EP/98-57 (submitted for publication in Phys. Lett. B) (1998)

[10] E. Eskut *et al.*, CERN-PPE/97-149 (submitted for publication in Phys. Lett. B) (1998)

[11] B. Pontecorvo, *JETP* **6** (1958) 429.

[12] C. W. Kim and A. Pevsner,*Neutrinos in Physics and Astrophysics*, Harwood Academic Publishers (1993).

[13] GEANT Detector Description and Simulation Tool, CERN Program Library Q123.

[14] B. Schmidt,*Study of ν_μ - Charged Current Interactions and Search for $\nu_\mu \leftrightarrow \nu_\tau$ oscillations in the channel $\tau^- \rightarrow \mu^- \overline{\nu_\mu} \nu_\tau$ with the NOMAD Detector*, Ph.D Thesis, Universität Dortmund, Germany (1997).

[15] J. Altegoer *et al.*, *Nucl. Inst. and Meth.* **A404**, (1998) 96.

[16] C. Brome, T.G. Dignan and M. E. Hill, NOMAD By Numbers, NOMAD Internal Note, 1995, NOMAD Collaboration, CERN, Geneva.

[17] G. Bassompierre *et al.*, *Nucl. Inst. and Meth.* **A403** (1998) 363.

[18] M. Anfreville *et al*, *The drift chambers of the NOMAD detector*, submitted for publication to Nucl. Instr. and Meth. (1997)

[19] W. W. M. Allison and J. H. Cobb, *Ann. Rev. Nucl. Part. Sci.*, **30** (1980) 253-98.

[20] M. L. Cherry *et al*, *Phys. Rev.* **D10**, No. 11 (1974) 3594-3607.

[21] M. Barranco-Luque *et al*, *Nucl. Instr. and Meth.* **A176** (1980) 175.

[22] LabView User Manual for Sun (September 1994 Edition), National Instruments Corporation, Austin, TX, 1992, 1994

[23] D. Autiero *et al*, *Nucl. Instr. and Meth.* **A372**, (1996) 556.

[24] D. Autiero *et al*, *Nucl. Instr. and Meth.* **A373**, (1996) 358.

[25] S.R. Mishra *et al*, *Phys.Rev.Lett.*, **66**, (1991) 3117.

[26] P.H. Sandler *et al*, *Z. Phys.* **C57**, Vol.#1, (1993) 1.

[27] D. Geiregat *et al*, *Phys. Lett.* **B 245**, (1990) 271.

[28] J. Altegoer *et al*, *Instrumenting the Front "I"s of NOMAD*, NOMAD Internal Note 95-011, NOMAD Collaboration, 1995, CERN, Geneva

[29] D. Geppert, *Bau von Komponenten eines Szintillator-Hadron-Kalorimeters und dessen Kalibrierung im NOMAD-Experiment*, Diplomarbeit, Universität Dortmund, Germany (1995)

[30] K. S. Kölbig and B. Schorr, *Comp Phys. Comm.*, **31**, (1984) 97.

[31] A. Geiser, *Summary of muon reconstruction efficiencies*, NOMAD Muon Analysis Working Group Meeting ,1996, CERN, Geneva

[32] A. Geiser, J. C. Long, *Study of ν_μ^{CC} Events and Comparison with NUBEAM, NEGLIB and GENOM*, NOMAD Internal Note 97-005, NOMAD Collaboration, 1997, CERN, Geneva.

[33] I.G.Bird, *RECON - NOMAD reconstruction manual*, NOMAD Internal Note No.37, NOMAD Collaboration, 1995, CERN, Geneva

[34] F. Sauli *et al*, *Instrumentation in High Energy Physics*, World Scientific (1993).

[35] SPY Collaboration, G. Ambrosini *et al*, CERN-SPSLC/96-01

[36] SPY Collaboration, S. Ragazzi *et al*, *Secondary Particle Yields from 450 GeV/c protons on Beryllium*, SPSC Open Meeting (1997)

[37] G. Ambrosini *et al*, *Phys. Lett.* **B 420**, (1997)

[38] A. Ferrari and P.R. Sala, *GEANT Hadronic Event Generators : a comparison at the single interaction level*, ATLAS Internal Note PHYS-No-086 (1996)

[39] F.Weber *et al*, *The Construction and Use of the Flux Reweighting Tables*, NOMAD Internal Note 97-037, NOMAD Collaboration, 1997, CERN, Geneva.

[40] A. Fasso *et al.*, FLUKA92, in *Proc. of the Workshop on Simulating Accelerator Radiation Environments*, Santa Fe, USA, 1993.

[41] D. Daniels and E. Tsesmelis, *NUBEAM Documentation*, NOMAD Internal Note (1996).

[42] GEANT *Detector Description and Simulation Tool*, CERN Programming Library Long Writeup W5013.

[43] J. P. Meyer and A. Rubbia, *NOMAD Event Generator Offline Manual*, Version 5.00.

[44] G. Ingleman, A. Edin and J. T. Rathsman, *LEPTO 6.5 - A Monte Carlo Generator for Deep Inelastic Lepton-Nucleon Scattering*, DESY 96-057.

[45] T. Sjöstrand, *JETSET Physis and Manual*, Version 7.4, (1994)

[46] H. P. Besch, *Comp. Phys. Comm.*, **75**, (1993) 396.

[47] S. Jadach, J. H. Kühn and Z. Was, *Comp. Phys. Comm*, **64**, (1991) 267.

[48] S. Jadach, J. H. Kühn and Z. Was, *Comp. Phys. Comm*, **64**, (1991) 275.
S. Jadach, J. H. Kühn and Z. Was, *Comp. Phys. Comm*, **70**, (1992) 69.

[49] J. Altegoer *et al.*, *NOMAD GEANT Offline Manual*, Version 5.11.

[50] I. G. Bird, *NOMAD Reconstruction Program*, NOMAD Internal Note No. 37 (1993).

[51] K. Varvell, *NOMAD DST Package - Version v7r3*, NOMAD Internal Note 97-034 (1997).

[52] D. Nordmann, *Untersuchung der Akzeptanz für Myonen aus Frontkalorimeter Ereinissen im NOMAD-Experiment*, Diplomarbeit, Universität Dortmund, Germany (1996).

[53] T. Schmidt, *Untersuchung von Dimyon-Ereignissen im Frontkalorimeter des NOMAD-Detektors*, Diplomarbeit, Universität Dortmund, Germany (1998).

[54] W.T.Eadie *et al*, *Statistical Methods in Experimental Physics* North Holland, Amsterdam and London, (1971).

[55] M. Glück, E. Reya, and A. Vogt, *Z. Phys.* **C53**, (1992) 127.

[56] A. D. Martin *et al.*, *Phys. Lett.* **B 306**, (1993) 145.

[57] H. Burkhardt *et al.*, *Z. Phys.* **C 33**, (1987) 483.

[58] C. Baltay *et al.*, *Phys. Rev. Lett.* **55**, (1985) 2543.

[59] C. Foudas *et al.*, *Z. Phys.* **C 15**, (1982) 19.

[60] B.L.Young *et al.*, *Phys. Lett.* **B 74**, (1978) 111.

[61] S. A. Rabinowitz, *Opposite Sign Dimuon Production in Neutrino Interactions at the Fermilab Tevatron*, Ph.D Thesis, Columbia University (N.Y.) (1992).

[62] C. Foudas, *Neutrino Production of Opposite Sign Dimuons at the FNAL Tevatron*, Ph.D Thesis, Columbia University (N.Y.) (1989).

[63] A. Bazarko, *Determination of the Strange Quark Distribution from a Next-to-Leading-Order QCD Analysis of Neutrino and Antineutrino Production of Charm*, Ph.D Thesis, Columbia University (N.Y.) (1994).

[64] A.O.Bazarko *et al.*, *Z. Phys.* **C65**, (1995) 189.

[65] J. Chrin, *Z. Phys.* **C36**, (1987) 163-171.

[66] N. Ushida *et al.*, *Phys. Lett.* **B 121**, (1983) 287.

[67] N. Ushida *et al.*, *Phys. Lett.* **B 206**, (1988) 375.

[68] D. Bortoletto *et al.*, *Phys. Rev.* **D 37**, (1988) 1719.

[69] H. Albrecht *et al.*, *Phys. Lett.* **B 150**, (1985) 235.

[70] M. Aguilar-Benitez *et. al.*, *Phys. Lett.* **B 123**, (1983) 287.

[71] J. Adler *et al.*, *Phys. Rev. Lett.* **62**, (1989) 1821.

[72] J.D. Richman and P.R.Burchat *Rev. Mod. Phys.*, Vol# 67, (1995) No. 4.

[73] S. Mishra, Harvard Univ., USA, *priv. comm.* (1997).

[74] J. M. Vieira, *Production de quarks charmés et détermination de la mer étrange de quarks dans l'expérience NOMAD*, Ph.D Thesis, Université de Lausanne (1998).

[75] H. Abramowicz *et al.*, *Z. Phys.* **C15**, (1982) 19.

[76] S. A. Rabinowitz *et al.*, *Phys. Rev. Lett.* **70**, (1993) 134.

[77] A. Benvenuti *et al.*, *Phys. Rev. Lett.* **34**, (1975) 538.

[78] B. Strongin *et al.*, *Phys. Rev.* **D 43**, (1991) 2778.

[79] P. Vilain *et al.*, CERN-EP/98-128 (submitted for publication in European Physical Journal C) (1998)

[80] N.J.Baker *et al.*, *Phys. Rev.* **D 43**, (1991) 2765.

[81] V. Jain *et al.*, *Phys. Rev.* **D 41**, (1990) 2057.

[82] Review of Particle Properties, Particle Data Group, *Phys. Rev.* **D 45** (1992)

[83] P. Amaudruz *et al.*, *Phys. Rev. Lett.* **66**, (1991) 2712.

[84] J.T.Londergan and A.W.Thomas, *Prog. Part. Nucl. Pys.* **41**, (1998) 49.

[85] M. H. Shaevitz, *Nucl. Phys.* **B 19**, (1991) 270.

[86] M. A. G. Aivazis, F. I. Olness and W. K. Tung, *Phys. Rev.* **D 50**, (1994) 3085.

[87] M. A. G. Aivazis, F. I. Olness and W. K. Tung, *Phys. Rev.* **D 50**, (1994) 3102.

[88] M. Glück et al, *Phys. Lett.* **B 380**, (1996) 171.

[89] S. Kretzer and I. Schienbein, *Phys. Rev.* **D 56**, (1997), 1804.